

PERFORMANCE AND RELIABILITY OF NANOPARTICLES REINFORCED LEAD-FREE SOLDER JOINTS – A STUDY

Thesis

Submitted in partial fulfillment of the requirements for the degree of

DOCTOR OF PHILOSOPHY

by

SANJAY VINAYAK TIKALE



**DEPARTMENT OF METALLURGICAL AND MATERIALS
ENGINEERING**

**NATIONAL INSTITUTE OF TECHNOLOGY KARNATAKA,
SURATHKAL, MANGALORE – 575025**

January, 2021

DECLARATION

By the Ph.D. Research Scholar

I hereby *declare* that the Research Thesis entitled “**PERFORMANCE AND RELIABILITY OF NANOPARTICLES REINFORCED LEAD-FREE SOLDER JOINTS – A STUDY**” which is being submitted to the National Institute of Technology Karnataka, Surathkal in partial fulfilment of the requirements for the award of the Degree of **Doctor of Philosophy in Metallurgical and Materials Engineering** is a *bonafide report of the research work carried out by me*. The material contained in this Research Thesis has not been submitted to any University or Institution for the award of any degree.



155089MT15F06, **SANJAY VINAYAK TIKALE**

Department of Metallurgical and Materials Engineering

Place: NITK-Surathkal

Date: 10/06/2021

C E R T I F I C A T E

This is to *certify* that the Research Thesis entitled “**PERFORMANCE AND RELIABILITY OF NANOPARTICLES REINFORCED LEAD-FREE SOLDER JOINTS – A STUDY**” submitted by **Mr. SANJAY VINAYAK TIKALE**, (**Register Number: 155089MT15F06**) as the record of the research work carried out by him, is *accepted as the Research Thesis submission* in partial fulfillment of the requirements for the award of the degree of **Doctor of Philosophy**.

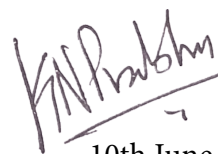


10th June 2021

Dr. K. Narayan Prabhu

Research Guide

(Signature with Date and Seal)



10th June 2021

Chairman - DRPC

(Signature with Date and Seal)

ACKNOWLEDGEMENTS

I would like to express my sincere and deep sense of gratitude to my research guide, Prof. K. Narayan Prabhu for his guidance, tireless help, and support throughout the research work. It has been an honor to do my Ph.D. under his supervision. I am deeply indebted to him for his patience, motivation, ideas, persistent encouragement and cheerfulness, and most importantly his devotion of time that helped me throughout this journey of research work. I also thank him for providing me with excellent experimental facilities during my research work. His professional attitude and human qualities will always serve as guidelines in my life.

I sincerely thank my RPAC members Prof. A. O. Surendranathan and Dr. Saumen Mandal, Department of Metallurgical & Materials Engineering, and Dr. Nagaraja H. S., Department of Physics for their insightful comments and valuable suggestions during the research work.

My heartfelt gratitude to Dr. Uday Bhat, Professor, and Chairman-CRF, Department of Metallurgical and Materials Engg., for allowing me to use the XRD, Scanning electron microscope, and FESEM facilities. I am grateful to Dr. Ravishankar K. S., Department of Metallurgical and Materials Engg., for allowing me to use mechanical testing lab facilities. I am grateful to Prof. Anandhan Srinivasan, former Head, and Dr. Jagannath Nayak, Professor and Dean (SW), Department of Metallurgical and Materials Engg., for their timely support.

I am sincerely grateful for the companionship of the fellow researchers in the Casting Research Center, Department of Metallurgical and Materials Engineering, NITK. I am deeply grateful to Dr. Mrunali Sona, for her constant guidance, help, and support from the beginning of my research work. I will be always grateful for her efforts and patience during the experiments and will always cherish the time spent together during my Ph.D. journey. I would like to thank my colleagues and friends from our research group Dr. Vignesh Nayak, Dr. Sudheer, Dr. Pranesh Rao K. M., Ms. Swati Agarwala, Mr. Augustine Samuel, and Mr. Kamal Nathan for their constant help, encouragement, suggestions, and support.

Carrying out my research work along with them will always be memorable. I would like to thank Mr. Ramakrishna and Mr. Kiran Bhat for their help and support.

My heartfelt thanks to Mrs. Sharmila for her timely help and tireless support. I am also obliged to lab technicians Mr. Satish, Mr. Dinesh, Mrs. Vinaya, Mr. Yashwanth, and Mr. Sundar Shettigara for helping me during sample preparation and experiments. I am thankful to all technical and non-technical staff of the Department of Metallurgical and Materials Engineering for their wholehearted help during my work. Special thanks to Mrs. Rashmi for helping with the scanning electron microscopy.

I am grateful to NITK for providing me with an opportunity to carry out my doctoral study in the Department of Metallurgical and Materials Engineering. I thank all faculty members of the Department who taught and helped me.

I would like to express my deepest gratitude to my parents, without their support I would not have pursued higher education. They have been a constant source of love and strength all these years.

Finally, I thank all those who directly or indirectly helped me to complete the research work successfully.

Sanjay Vinayak Tikale

ABSTRACT

The present study involved the development of Sn-3.6Ag, 99Sn-0.3Ag-0.7Cu (SAC0307), 96.5Sn-3Ag-0.5Cu (SAC305), and 96.5Sn-3Ag-0.5Cu-0.06Ni-0.01Ge (SAC305-NiGe) lead-free solders with the addition of Al₂O₃ nanoparticles and multi-walled carbon nanotubes (MWCNT). The effects of multiple reflow cycles and the addition of Al₂O₃ nanoparticles and MWCNT in 0.01, 0.05, 0.1, 0.3, and 0.5 weight percent concentration on microstructure development and mechanical strength of the solder joint were first investigated. The addition of nanoparticles in low weight percent concentration improved the wettability and solder joint shear strength. Based on superior shear strength and improved ductility compared to the original solder, nanocomposites containing 0.01 and 0.05 wt. pct. Al₂O₃ nanoparticles were selected and tested for the performance and reliability of the joint. The surface mount 2220 capacitor joint and single-lap-shear joint assemblies reflowed on bare copper and electroless Ni-coated Cu substrates were used in this study. The reliability of the solder joint was assessed in terms of the joint shear strength under varying thermal environments like thermal shock, multiple heating cycles, and aging. The nanocomposite with 0.05 wt.% nanoparticles addition yielded the most significant increase in the joint strength compared to the unreinforced solder. The Ni-substrate coating significantly suppressed the IMC growth under different thermal conditions. The joint reliability of nanocomposites improved for samples reflowed on Ni-coated substrate compared to that on bare Cu substrate. The Weibull analysis showed that the performance and reliability of the solder joint can be greatly improved by the addition of Al₂O₃ nanoparticles in small weight percent concentrations and Ni-coating on the substrate. The ANOVA study suggests that the solder joint performance was majorly influenced by the operating environments, solder composition, and the substrate coating. SAC305-NiGe and SAC0307 based nanocomposites were found to be better than all solder compositions studied in the present study. The low-silver content SAC0307+0.05Al₂O₃ nanocomposite will be an effective alternate solder composition in place of high silver content Sn-Ag-Cu solders.

Keywords: Sn-Ag-Cu solder; Al₂O₃ nanoparticles; MWCNT; 2220-capacitor joint; lap-shear-joint; multiple reflows; Ni-coating; joint shear strength; reliability.

CONTENTS

LIST OF FIGURES	v
LIST OF TABLES	xiv
NOMENCLATURE	xvi
Chapter 1 INTRODUCTION	1
1.1 Scope of the Investigation	3
1.2 Objectives of the Research Work	4
1.3 Organization of the Thesis	5
Chapter 2 LITERATURE REVIEW	7
2.1 Soldering	7
2.2 Soldering Techniques	7
2.2.1 Wave soldering	8
2.2.2 Reflow soldering	8
2.3 Solders	10
2.3.1 Lead-free solders	11
2.3.1.1 Sn-Ag-Cu solders	15
2.4 Wettability of the Solder Alloys	17
2.5 Evolution of the Solder Joint Microstructure and Growth of Intermetallic Compounds	18
2.6 Factors Affecting the Microstructure and Strength of the Solder Joint	20
2.7 Development of Lead-free Solder for Better Mechanical Performance and Reliability of the Joint	23
2.7.1 Alloying of solder	23
2.7.1.1 Rare earth elements (RE)	27
2.7.1.2 Multi-component solder system	28
2.7.2 Nanocomposites	29
2.7.2.1 Metallic nanoparticles	29
2.7.2.1.1 Nickel (Ni)	29
2.7.2.1.2 Aluminium (Al)	30
2.7.2.1.3 Cobalt (Co)	31
2.7.2.1.4 Molybdenum (Mo)	31

2.7.2.1.5 Zinc (Zn)	32
2.7.2.2 Intermetallic nanoparticles	33
2.7.2.3 Oxides nanoparticles	34
2.7.2.3.1 Titanium dioxide (TiO ₂)	34
2.7.2.3.2 Zirconium dioxide (ZrO ₂)	35
2.7.2.3.3 Iron oxide (Fe ₂ O ₃)	35
2.7.2.3.4 Cerium oxide (CeO ₂)	37
2.7.2.3.5 Alumina (Al ₂ O ₃)	38
2.7.2.4 Carbon nanotubes (CNT)	40
2.7.3 Surface coating	42
2.8 Summary	43
Chapter 3 EXPERIMENTAL DETAILS	47
3.1 Preparation of Solder Nanocomposites	47
3.2 Assessment of the Melting Characteristics of Nanocomposites	49
3.3 Preparation of the Solder Joint Assemblies	50
3.4 Assessment of the Wettability of Nanocomposites	52
3.5 Assessment of the Effect of Nanoparticles Addition on Microhardness of Solders	54
3.6 Assessment of the Joint Shear Strength under Multiple Reflow Cycles	54
3.7 Electroless Nickel Coating on Copper Substrate and Specimen Preparation	54
3.8 Assessment of the Reliability of the Solder Joint	57
3.9 Microstructural Investigation	58
3.10 Fractography	59
Chapter 4 RESULTS	61
4.1 Melting Parameters of Nanoparticles Reinforced Solder Alloys	61
4.2 Wettability of Nanocomposite Solders	63
4.3 Microstructure Development and Intermetallic Layer Growth at the Solder Joint under Multiple Reflow Cycles	68
4.4 Microhardness, Joint Shear Strength and Ductility of Nanocomposites under Multiple Reflow Cycles	77
4.5 Solder Joint Microstructure on Cu and Ni-P Coated Substrate for Al ₂ O ₃ Nanoparticle Reinforced Select Nanocomposites under Different Thermal Conditions	83

4.6 Joint Shear Strength, Ductility and Microhardness of Nanocomposite Solders under Different Thermal Conditions	91
4.7 Fracture Behavior of the Solder Joints under Multiple Reflows and Different Thermal Conditions	96
Chapter 5 DISCUSSION	101
5.1 Effect of Addition of Nanoparticles on Melting Behavior and Wettability of Lead-free Solders	101
5.2 Effect of Addition of Nanoparticles on Microstructure Evolution and Intermetallic layer Growth under Multiple Reflow Condition	103
5.3 Shear Strength and Ductility of the Solder Joint under Multiple Reflow Condition	111
5.4 Microstructure Development and IMC layer Growth on Bare Cu and Ni-P Coated Substrate for Select Solder Nanocomposites	115
5.5 Performance and Reliability of the Solder Joints	118
5.5.1 Weibull distribution analysis of the joint shear strength	121
5.5.2 Analysis of variance (ANOVA) experiment	125
5.6 Fractography	128
Chapter 6 CONCLUSIONS	135
REFERENCES	141
APPENDIX A: MELTING PARAMETERS OBTAINED FROM THE DSC TEST FOR DIFFERENT SOLDER NANOCOMPOSITES	155
APPENDIX B: WETTING AREA AND TIN-CLIMB FOR DIFFERENT SOLDER NANOCOMPOSITES	157
APPENDIX C: MICROSTRUCTURE OF SOLDER JOINT FOR DIFFERENT SOLDER NANOCOMPOSITES UNDER MULTIPLE REFLOW CYCLES	159
APPENDIX D: STRESS-STRAIN CURVES AND MICROHARDNESS FOR DIFFERENT SOLDER NANOCOMPOSITES UNDER VARYING THERMAL CONDITIONS	161
APPENDIX E: WEIBULL PLOTS OF JOINT SHEAR STRENGTH FOR DIFFERENT SOLDER NANOCOMPOSITES	163
APPENDIX F: ANOVA TABLES FOR JOINT SHEAR STRENGTH	165
LIST OF PUBLICATIONS	167
BIO-DATA	169

List of Figures

Figure No.	Caption	Page No.
2.1	A schematic diagram for the wave soldering technique	8
2.2	A schematic diagram for the typical reflow soldering process	9
2.3	A typical reflow cycle profile	9
2.4	Binary (a) Sn-Cu and (b) Sn-Ag phase diagram, and a projection of the liquidus surfaces for the Sn-Ag-Cu phase diagram showing (c) ternary eutectic reaction and (d) Sn-rich corner	15
2.5	The microstructure of a typical eutectic Sn-Ag-Cu solder alloy	16
2.6	A schematic diagram for the interaction of the moving grain boundary and the second-phase particles (a) encountering, (b) interacting	36
3.1	(a) SEM image, (b) XRD pattern, (c) TEM image of Al ₂ O ₃ nanoparticles, and (d) TEM image showing the size of Al ₂ O ₃ nanoparticles	48
3.2	(a) SEM image, (b) XRD pattern, (c) TEM image of MWCNT, and (d) TEM image showing the inner and outer diameter of MWCNT strand	48
3.3	Process flowchart for the surfactant treatment of nanoparticles and the preparation of nanocomposites	49
3.4	A schematic diagram for the preparation of a single-lap-shear solder joint	51
3.5	Photograph of an IC Reflow oven	51
3.6	Reflow cycle profile	51
3.7	Surface roughness profile for the copper substrate	52
3.8	SMT 2220 capacitor component with dimensions and structural details	52
3.9	Schematics for preparation of capacitor joint assembly	52

3.10	2220-capacitor joint assembly (a) stereomicroscopic image, (b) cross-sectional view of the joint	52
3.11	Photograph of the Zeiss stereomicroscope	53
3.12	Photograph of the KRUSS drop shape analyzer	53
3.13	Stereomicroscopic images showing wetting area measurement for the reflowed solder samples	54
3.14	(a) Stereomicroscopic image and (b) drop shape analyzer image showing measurement of the tin-climb on reflowed capacitor joint	54
3.15	Photograph of the Shimadzu Micro Vickers hardness tester	55
3.16	Photograph of the INSTRON 5967 tensile testing machine	55
3.17	Flowchart for the electroless nickel plating process	56
3.18	SEM micrograph and EDS plot for electroless Ni-P coating on copper substrate	56
3.19	Heating cycle profile	58
3.20	Thermal shock profile	58
3.21	Photograph of the Nordson DAGE 4000plus bond tester and schematics for the bond shear testing	58
3.22	Representative SEM micrograph showing the IMC layer thickness measurement for an uneven interfacial IMC layer at the joint interface	59
4.1	DSC heating and cooling curves for (a) SAC305-NiGe, (b) SAC305-NiGe+0.01Al ₂ O ₃ , and (c) SAC305-NiGe+0.05Al ₂ O ₃ solder compositions	62
4.2	DSC heating curves for SAC305 solder with different weight percent addition of (a) Al ₂ O ₃ nanoparticles and (b) MWCNT	62
4.3	Wetting area for (a) SAC0307, (b) SAC0307+0.05Al ₂ O ₃ , (c) SAC0307+0.1Al ₂ O ₃ and (d) SAC0307+0.5Al ₂ O ₃ solder compositions reflowed on bare copper substrate	64

4.4	Wetting area for (a) SAC0307, (b) SAC0307+0.05Al ₂ O ₃ , (c) SAC0307+0.1Al ₂ O ₃ , and (d) SAC0307+0.5Al ₂ O ₃ solder compositions reflowed on Ni-coated Cu substrate	64
4.5	Wetting area for (a) SAC0307+0.01MWCNT, (b) SAC0307+0.05MWCNT, (c) SAC0307+0.1MWCNT, and (d) SAC0307+0.5MWCNT solder compositions reflowed on bare copper substrate	65
4.6	Wetting area versus Al ₂ O ₃ nanoparticles concentration addition for (a) Sn-3.6Ag, (b) SAC0307, and (c) SAC305 solders reflowed on bare copper and Ni-coated copper substrate	65
4.7	Wetting area versus MWCNT concentration addition for (a) Sn-3.6Ag, (b) SAC0307, and (c) SAC305 solders reflowed on bare copper substrate	66
4.8	The stereomicroscopic images of capacitor samples showing tin-climb on the capacitor terminals for SAC305-NiGe, SAC305-NiGe+0.01Al ₂ O ₃ , and SAC305-NiGe+0.05Al ₂ O ₃ solder compositions reflowed on (a), (b), (c) bare copper substrate, and (d), (e), (f) Ni-coated substrate	66
4.9	Tin-climb height for select nanocomposites of SAC0307 solder reflowed on bare Cu and Ni-coated substrate	67
4.10	Tin-climb height for select nanocomposites of SAC305-NiGe solder reflowed on bare Cu and Ni-coated substrate	67
4.11	Tin-climb height for select nanocomposites of SAC305 solder and plain Sn-37Pb solder reflowed on bare Cu and Ni-coated substrate	68
4.12	SEM micrographs of the joint interface for SAC0307 solder with the addition of Al ₂ O ₃ nanoparticles in different weight percent concentrations on the copper substrate under multiple reflow cycles	69
4.13	SEM micrographs of the joint interface for SAC0307 solder with the addition of MWCNT in different weight percent concentrations on the copper substrate under multiple reflow cycles	70

4.14	SEM micrographs of the joint interface for SAC305 solder with the addition of Al ₂ O ₃ nanoparticles in different weight percent concentrations on the copper substrate under multiple reflow cycles	71
4.15	SEM micrographs of the joint interface for Sn-3.6Ag solder with the addition of Al ₂ O ₃ nanoparticles in different weight percent concentrations on the copper substrate under multiple reflow cycles	72
4.16	(a) SEM micrograph showing different IMCs at the solder joint interface, (b) XRD plot showing peaks for different IMCs at the joint interface, EDS plot and elemental compositions for, (c) β-Sn matrix, (d) Ag ₃ Sn, (e) Cu ₆ Sn ₅ , and (f) Cu ₃ Sn IMC	73
4.17	Cu ₆ Sn ₅ and Ag ₃ Sn IMC precipitates in solder matrix for (a) unreinforced SAC305 solder and (b) SAC305+0.05Al ₂ O ₃ nanocomposite	74
4.18	IMC thickness under multiple reflow cycles for SAC0307 solder joint on the copper substrate with different weight percent addition of, (a) Al ₂ O ₃ nanoparticles and (b) MWCNT	76
4.19	IMC thickness under multiple reflow cycles for SAC305 solder joint on the copper substrate with different weight percent addition of, (a) Al ₂ O ₃ nanoparticles and (b) MWCNT	76
4.20	IMC thickness under multiple reflow cycles for Sn-3.6Ag solder joint on the copper substrate with different weight percent addition of, (a) Al ₂ O ₃ nanoparticles and (b) MWCNT	76
4.21	Joint shear strength under different reflow cycles for SAC0307 solder on Cu substrate with varying weight percent addition of (a) Al ₂ O ₃ nanoparticles and (b) MWCNT	78
4.22	Joint shear strength under different reflow cycles for SAC305 solder on Cu substrate with varying weight percent addition of (a) Al ₂ O ₃ nanoparticles and (b) MWCNT	79
4.23	Joint shear strength under different reflow cycles for Sn-3.6Ag solder on Cu substrate with varying weight percent addition of (a) Al ₂ O ₃ nanoparticles and (b) MWCNT	79

4.24	Stress-strain curves for SAC0307 solder with varying weight percent addition of (a) Al ₂ O ₃ nanoparticles and (b) MWCNT	80
4.25	Stress-strain curves for SAC305 solder with varying weight percent addition of (a) Al ₂ O ₃ nanoparticles and (b) MWCNT	81
4.26	Stress-strain curves for Sn-3.6Ag solder with varying weight percent addition of (a) Al ₂ O ₃ nanoparticles and (b) MWCNT	81
4.27	SEM micrographs of capacitor assembly, (a) cross-sectional view showing the microstructure of the capacitor joint, (b) magnified region of terminal/SAC305 solder interface, (c) magnified region of terminal/Sn-37Pb solder interface, and interfacial microstructure for (d) SAC305/Cu substrate, (e) SAC305/Ni-P coating, and (f) Sn-37Pb/Cu substrate	84
4.28	SEM images of interfacial microstructure for SAC305 solder and SAC305+0.05Al ₂ O ₃ composite on bare Cu and Ni-P coated substrate under varying high-temperature environments	85
4.29	(a) SEM micrograph of the SAC305 solder joint on Ni-P coated substrate, and EDS plot with elemental compositions for (b) (Cu, Ni) ₆ Sn ₅ and (c) (Cu, Ni) ₃ Sn ₄ IMC layers	86
4.30	SEM micrographs for Sn-37Pb/Cu joint interface under different thermal conditions, (a) as-reflowed, (b) heating cycles, and (d) aging at 150 °C	87
4.31	Average IMC thickness under varying thermal conditions for SAC305 solder nanocomposites and Sn-37Pb solder reflowed on (a) Cu substrate, and (b) Ni-P coated substrate	87
4.32	SEM images of interfacial microstructure for SAC305-NiGe solder and SAC305-NiGe+0.05Al ₂ O ₃ composite on bare Cu and Ni-P coated substrate under varying high-temperature environments	88
4.33	SEM micrograph of SAC305-NiGe solder joint on Cu substrate and EDS plot for Cu ₆ Sn ₅ IMC layer at the joint interface	89

4.34	Average IMC thickness under varying thermal conditions for SAC305-NiGe solder nanocomposites reflowed on (a) Cu substrate, and (b) Ni-P coated substrate	89
4.35	SEM images of interfacial microstructure for SAC0307 solder and SAC0307+0.05Al ₂ O ₃ composite on bare Cu and Ni-P coated substrate under varying high-temperature environments	90
4.36	Average IMC thickness under varying thermal conditions for SAC0307 solder nanocomposites reflowed on (a) Cu substrate, and (b) Ni-P coated substrate	91
4.37	Stress-strain plots for single-lap-joint samples under different thermal conditions for (a) SAC305 on Cu substrate and (b) SAC305+0.05Al ₂ O ₃ solder composition on Ni-P coated substrate	95
4.38	Microhardness for SAC305 solder nanocomposites and plain Sn-37Pb solder under varying high-temperature environments	95
4.39	SEM images of a fractured surface showing (a) characteristics of mixed-mode failure on the sheared surface, (b) ductile fracture area, and (c) brittle fracture area	97
4.40	SEM micrographs of fractured surfaces showing various fracture details, (a) ductile fracture surface with shear markings, (b) mixed-mode of fracture with transition ridge, (c) fractured surface with a high density of micro-dimples, and (d) fractured surface with coarse dimples	97
4.41	SEM images of fractured surface for nanocomposites with a high concentration of nanoparticles showing (a) ductile fracture area with coarse dimples, (b) magnified dimple area showing broken IMC precipitates, and (c) coarse dimples with the agglomeration of MWCNT at the dimple area	98
4.42	SEM micrographs of the fracture surfaces for (a) as-reflowed SAC305 solder joint, and SAC305+0.05Al ₂ O ₃ under (b) as-reflowed, (c) heating cycles, and (d) aging at 150 °C conditions, respectively, and EDS plots (e) confirming the presence of β-Sn in the bulk matrix and	99

	(f) exposed Cu_6Sn_5 IMC inside the dimple with traces of Al_2O_3 nanoparticles	
5.1	Cu_6Sn_5 IMC thickness versus reflow cycle time plots for (a) SAC305, (b) SAC305+0.05 Al_2O_3 , (c) SAC305+0.1 Al_2O_3 , and (d) SAC305+0.5 Al_2O_3 composition reflowed on Cu substrate	105
5.2	Schematic diagram of possible diffusion paths in the solder joint	107
5.3	Secondary electron mode SEM micrographs for (a) unreinforced SAC305 solder joint and (b) SAC305+0.05 Al_2O_3 nanocomposite sample showing the refinement of the β -Sn grains in the matrix	109
5.4	FESEM images of bulk microstructure for Al_2O_3 nanoparticle reinforced SAC305 solder joint showing the presence of Al_2O_3 nanoparticles in the matrix	109
5.5	(a) SEM image of the selected area at the joint interface, (b) EDS scan showing peaks for Al_2O_3 , (c) elemental mapping scan for the selected area showing Al_2O_3 nanoparticles adsorption on Cu_6Sn_5 IMC and dispersion in grain boundaries of the solder matrix	110
5.6	EDS scan for elemental mapping of Al_2O_3 nanoparticles for (a) SAC0307+0.05 Al_2O_3 , and (b) SAC0307+0.5 Al_2O_3 compositions showing uniform dispersion and agglomeration of nanoparticles in the solder matrix	111
5.7	SEM micrographs at the joint interface after multiple reflows showing (a) IMC spalling and micro-cracks in IMC layers, (b) micro-voids at IMC-substrate interface in overgrown IMC layer	114
5.8	Natural log of Cu_6Sn_5 IMC thickness versus different thermal conditions for SAC305-NiGe solder nanocomposites on (a) uncoated-Cu substrate and (b) Ni-P coating	117
5.9	Natural log of Cu_6Sn_5 IMC thickness versus different thermal conditions for nanocomposites on the uncoated-Cu substrate and Ni-P coating for (a) SAC305 and (b) SAC0307 solder	117

5.10	IMC thickness versus joint shear strength plot for plain SAC305 solder and SAC305+0.05Al ₂ O ₃ composite reflowed on bare Cu and Ni-P coated substrate under different thermal conditions	120
5.11	Weibull plots of joint shear strength for SAC0307, SAC0307+0.01Al ₂ O ₃ , and SAC0307+0.05Al ₂ O ₃ solder compositions reflowed on (a), (c), (e) bare Cu substrate; and (b), (d), (f) on Ni-P coated substrate	123
5.12	Main effect plots for (a) thermal condition, (b) substrate coating, (c) solder composition, and interaction plot for (d) substrate coating-solder composition	128
5.13	Different modes of failure in solder joint	129
5.14	SEM images showing characteristics features of ductile failure for unreinforced solder and nanocomposites under different thermal conditions	130
5.15	SEM micrographs showing (a) solder-IMC separation plane on fracture surface showing Ag ₃ Sn IMC particles inside the rough dimple, (b) deep dimples with exposed Cu ₆ Sn ₅ IMC, and (c) FESEM images of the regional organization of micro dimples on the ductile fracture surface, (d) magnified view of deep dimple showing internal details of broken Cu ₆ Sn ₅ and Ag ₃ Sn IMCs	132
B.1	The stereomicroscopic images of reflowed samples on bare Cu substrate for SAC305 solder nanocomposites reinforced with (a) 0, (b) 0.05, (c) 0.1, (d) 0.5 wt.% Al ₂ O ₃ nanoparticles, and (e) 0.01, (f) 0.05, (g) 0.1, (h) 0.5 wt.% MWCNT	157
B.2	The stereomicroscopic images of reflowed samples on bare Cu substrate for Sn-3.6Ag solder nanocomposites reinforced with (a) 0, (b) 0.05, (c) 0.1, (d) 0.5 wt.% Al ₂ O ₃ nanoparticles, and (e) 0.01, (f) 0.05, (g) 0.1, (h) 0.5 wt.% MWCNT	157
B.3	The stereomicroscopic images of capacitor samples showing tin-climb on the capacitor terminals for SAC0307, SAC0307+0.01Al ₂ O ₃ , and SAC0307+0.05Al ₂ O ₃ solder compositions reflowed on (a), (b), (c) bare copper substrate, and (d), (e), (f) Ni-coated substrate, respectively	158

B.4	The stereomicroscopic images of capacitor samples showing tin-climb on the capacitor terminals for SAC305, SAC305+0.01Al ₂ O ₃ , and SAC305+0.05Al ₂ O ₃ solder compositions reflowed on (a), (b), (c) bare copper substrate, and (d), (e), (f) Ni-coated substrate, respectively	158
C.1	SEM micrographs of the joint interface for SAC305 solder with the addition of MWCNT in different weight percent concentrations on the copper substrate under multiple reflow cycles	159
C.2	SEM micrographs of the joint interface for Sn-3.6Ag solder with the addition of MWCNT in different weight percent concentrations on the copper substrate under multiple reflow cycles	160
D.1	Stress-strain plots for single-lap-joint samples under different thermal conditions for (a) SAC0307 on Cu substrate and (b) SAC0307+0.05Al ₂ O ₃ solder composition on Ni-P coated substrate	161
D.2	Stress-strain plots for single-lap-joint samples under different thermal conditions for (a) SAC305-NiGe on Cu substrate and (b) SAC305-NiGe+0.05Al ₂ O ₃ solder composition on Ni-P coated substrate	161
D.3	Microhardness for SAC0307 solder nanocomposites under varying high-temperature environments	162
D.4	Microhardness for SAC305-NiGe solder nanocomposites under varying high-temperature environments	162
E.1	Weibull plots of joint shear strength for SAC305, SAC305+0.01Al ₂ O ₃ , and SAC305+0.05Al ₂ O ₃ solder compositions reflowed on (a), (c), (e) bare Cu substrate; and (b), (d), (f) on Ni-P coated substrate	163
E.2	Weibull plots of joint shear strength for SAC305, SAC305+0.01Al ₂ O ₃ , and SAC305+0.05Al ₂ O ₃ solder compositions reflowed on (a), (c), (e) bare Cu substrate; and (b), (d), (f) on Ni-P coated substrate	164

List of Tables

Table No.	Caption	Page No.
2.1	Potential lead-free solder candidates with their applications and concerns	12
2.2	Characteristics, advantages, and application concerns of different additive elements in solder	24
3.1	Lead-free solder alloy composition	47
3.2	Electroless nickel coating bath composition and operating conditions	56
4.1	Melting parameters of SAC305 solder with the addition of Al ₂ O ₃ nanoparticles in different weight percent concentrations	63
4.2	Melting parameters of SAC305 solder with the addition of MWCNT in different weight percent concentrations	63
4.3	Microhardness of different solders with varying weight percent addition of Al ₂ O ₃ nanoparticles and MWCNT	77
4.4	Failure strain and work of fracture (WOF) for different solder nanocomposites	82
4.5	Capacitor joint shear strength for different nanocomposites of SAC0307 solder on bare Cu and Ni-P coated substrate under different thermal conditions	93
4.6	Capacitor joint shear strength for different nanocomposites of SAC305 and Sn-37Pb solder on bare Cu and Ni-P coated substrate under different thermal conditions	93
4.7	Capacitor joint strength for different nanocomposites of SAC305-NiGe solder on bare Cu and Ni-P coated substrate under different thermal conditions	94
5.1	IMC growth exponent (n), growth constant (k) and adjusted R ² values for different nanocomposites of SAC305 solder	106

5.2	IMC growth exponent (n), growth constant (k), and adjusted R ² values for different nanocomposites of SAC0307 solder	106
5.3	IMC growth exponent (n), growth constant (k), and adjusted R ² values for different nanocomposites of Sn-3.6Ag solder	106
5.4	Characteristic parameters of Weibull analysis calculated from the fitting line for different nanocomposites of SAC305 solder reflowed on bare Cu and Ni-P coating	124
5.5	Characteristic parameters of Weibull analysis calculated from the fitting line for different nanocomposites of SAC305-NiGe solder reflowed on bare Cu and Ni-P coating	125
5.6	Analysis of Variance (ANOVA) table for joint shear strength of SAC305 solder nanocomposites	127
A.1	Melting parameters for Sn-3.6Ag solder with the addition of Al ₂ O ₃ nanoparticles and MWCNT in different weight percent concentrations	155
A.2	Melting parameters for Sn-3.6Ag solder with the addition of Al ₂ O ₃ nanoparticles and MWCNT in different weight percent concentrations	156
A.3	Melting parameters for SAC305-NiGe solder with the addition of Al ₂ O ₃ nanoparticles in different weight percent concentrations	156
F.1	Analysis of Variance (ANOVA) table for joint shear strength of SAC0307 solder nanocomposites	165
F.2	Analysis of Variance (ANOVA) table for joint shear strength of SAC305-NiGe solder nanocomposites	166

NOMENCLATURE

A	Area (μm^2)
k	Growth constant ($\mu\text{m}^2/\text{s}$)
l	Length (μm)
m	Weibull modulus
N	Total number of samples
n	Growth exponent
P_f	Probability of failure
R_a	Average surface roughness (μm)
S	Survival probability
t	Time (s)
y	Intermetallic layer thickness (μm)
ε	Strain (mm/mm)
Φ	Diameter (mm)
γ_{gs}	Interfacial energy between the solid surface and gas (J)
γ_{ls}	Interfacial energy between the solid and the liquid (J)
γ_{gl}	Interfacial energy between the gas and liquid/ surface tension of the liquid (J)
σ	Stress (MPa)
σ_f	Failure stress (MPa)
σ_0	Characteristic stress (MPa)
σ_f	Failure stress at 60% of survivability (MPa)
θ	Equilibrium contact angle ($^\circ$)

Chapter 1 INTRODUCTION

Sn-Pb solders have been extensively used in electronic assemblies for more than 70 years due to their excellent solderability, manufacturability, good mechanical properties, and low cost. However, the toxicity of lead (Pb) and its severe hazardous effects on human health as well as on the ecological system led to the ban on its usage. The legislation on end-of-life disposal and directives from EPA, EUWEEE, and RoHS led to the elimination of Sn-Pb from consumer electronics. The restrictions on the use of lead-based solders motivated researchers for the development of reliable and high-performing lead-free solders for the electronics packaging industry. The binary and ternary Pb-free solder alloys based on Sn-Cu, Sn-Ag, and Sn-Ag-Cu alloy systems provide promising alternatives for the replacement of conventional Sn-Pb solders (Ting Tan et al. 2015). Several environmental-friendly Sn-based alloys with different elemental additives like Cu, Ag, Ni, In, Bi, Zn, and Co have been considered the most promising candidates to replace the toxic Sn-Pb alloy (Kotadia et al. 2014). Among these, the Sn-Ag-Cu (SAC) solder alloys are the most preferred lead-free solders in the electronics industry due to their good solderability and adequate mechanical strength. Especially high-silver (Ag >3 wt.%) bearing SAC alloys are mostly used in electronic applications owing to their better physical, thermal and mechanical properties. However, high melting temperatures (i.e. 217-221 °C) and high tin (Sn) content compared to Sn-Pb solders give rise to problems like high intermetallic compound (IMC) growth rate and accelerated Cu dissolution from the substrate (Amagai 2008; Xu et al. 2019). The high-silver content in solder promotes the formation and coarsening of large Ag_3Sn IMC particles in the solder bulk under high-temperature working conditions, which increases the brittleness of the joint, deteriorates its mechanical strength and drop-impact reliability. Reducing Ag content in SAC solder is an effective method to weaken this potential threat by minimizing the amount of Ag_3Sn IMCs and changing their morphology from plate to particle type. Constant efforts have been put into the development of the low-Ag content Sn-Ag-Cu alloys to improve their thermal and mechanical properties to substitute the high-Ag solders. In comparison with commonly used Sn3.0Ag0.5Cu (SAC305) solder alloy, the low-Ag content solders have good ductility

and drop-impact reliability but have low mechanical and thermal fatigue strength which restrict their widespread usage in the electronic industries (Che et al. 2010; Shnawah et al. 2012b).

In recent times, the increased compactness of the microelectronics devices has increased the complexity and density of components in the high-end devices, which constantly requires high-performing and reliable solder joints for the better performance and long-term reliability of the assembly. The reliability of the solder joint is crucial in the electronic industry. The solder joint reliability is the ability to sustain its mechanical integrity and satisfactorily perform the intended functions during its course of operation under different working conditions. The reliability of the joint can be assessed by combining the service environment and system design. The service environment includes multiple reflows to which assembly is exposed during manufacturing and rework, long exposure to the high-temperature environment and frequent exposure to extreme temperature fluctuations that product must withstand, possible mechanical stresses, and frequent power on/off cycles that product may undergo. The integrity and reliability of the electronic components under different working atmospheres largely depend on the quality and stable bonding of the solder joint (Abtey and Selvaduray 2000; Cheng et al. 2017). A thin and uniform IMC layer at the joint interface provides an essential electrical continuity, thermal support, and mechanical integrity to the attached components in the assembly. The electronic components are repeatedly exposed to different thermal and mechanical stresses during their complete service life. Re-melts and prolonged exposure of joint to the high-temperature environments accelerates interfacial IMC growth and microstructure coarsening, which makes joint weak. The excessive IMC growth is detrimental to the joint strength due to its inherent brittle nature and strong tendency to develop structural defects like Kirkendall voids and micro-cracks (El-Daly et al. 2015c; Xu et al. 2019). Therefore, the study of IMC layer growth and the development of the solder matrix under multiple reflows and different thermal conditions have paramount importance to improve the performance and reliability of the solder joint. The suppression of IMC growth and

strengthening of the solder joint matrix under different thermal conditions can significantly improve the service life of the electronic components.

The conventional lead-free solders fall short in providing optimal performance and better long-term reliability to the solder interconnects. The continuous development in new devices constantly demands improved properties and high performance from the lead-free solders. Various properties of the solder can be tailored by purposefully incorporating various second-phase foreign particles in the solder to fabricate the multi-composite solder. The development of lead-free solders with the addition of nanoparticles proved to be a potentially viable and cost-effective approach to improving the physical, microstructural and mechanical properties of the solder. Owing to their smaller size and high surface free energy, the addition of nanoparticles suppress the IMC growth, refines the microstructure, and improves the wetting, tensile strength, hardness, and creep properties of the solder which in turn enhances the performance and reliability of the solder joint. Among several types of metallic and ceramic nanoparticles, carbon nanotubes and Al_2O_3 nanoparticles were found to be prominent materials for reinforcement. The exceptional physical, thermal, and mechanical properties exhibited by these nanoparticles make them more promising candidates for the development of lead-free solders.

1.1 Scope of the Investigation

Many studies have explored the effects of the addition of nanoparticles on different individual properties of lead-free solders. However, the effects of nanoparticle addition, multiple reflow cycles, substrate metallization, and varying high-temperature working environments on the performance and reliability of solder joints have not been studied extensively. The present study aims at the assessment of the effect of MWCNT and Al_2O_3 nanoparticles addition in varying weight percent on the joint shear strength of Sn-3.6Ag, Sn-3.0Ag-0.5Cu, Sn-0.3Ag-0.7Cu, and Sn-3.0Ag-0.5Cu-0.06Ni-0.01Ge lead-free solders under the effect of multiple reflow cycles. The assessment of the solder joint performance under multiple reflow cycles helps in selecting the best suitable solder composition for manufacturing and repair works of microelectronics assembly. The best performing

nanocomposites under multiple reflows were selected to study the solder joint reliability using 2220-capacitor/solder interconnects under different thermal conditions. The influence of substrate metallization on the performance and reliability of the joint can be investigated by selecting copper and nickel-coated copper substrates. The assessment of the solder joint strength under different thermal conditions like multiple heating cycles, thermal shocks, and aging brings out the role of the developed nanocomposites in electronic packaging applications. The assessment of the effect of different process parameters on solder joint strength using analysis of variance (ANOVA) technique and Weibull distribution provides a better understanding of the significance of the effect of variables and their interaction on the performance and long-term reliability of the solder joint.

1.2 Objectives of the Research Work

- 1] To study the effect of the addition of MWCNT and Al₂O₃ nanoparticles in varying weight percent concentrations on the melting parameters, wettability, microhardness, microstructure development, and joint shear strength under multiple reflow cycles for Sn-3.6Ag, Sn-3.0Ag-0.5Cu, and Sn-0.3Ag-0.7Cu lead-free solders.
- 2] To develop the low-silver content SAC0307 solder and high-silver content Sn-3.0Ag-0.5Cu and Sn-3.0Ag-0.5Cu-0.06Ni-0.01Ge lead-free solders with the addition of nanoparticles and study the performance and reliability of the solder joints under multiple heating cycles, thermal shocks, and isothermal aging conditions.
- 3] To investigate the effect of Ni-P coated substrate on microstructure evolution and joint reliability of SAC0307, SAC305, and SAC305-NiGe lead-free solders.
- 4] To assess the effect of different process parameters and their interaction on shear strength performance of nanocomposite solder joints using factorial experiments.

1.3 Organization of the Thesis

The thesis is divided into six chapters. Chapter 1 presents the introduction, followed by the scope and objectives of the present research work. Chapter 2 provides the literature review on lead-free solders, factors affecting the reliability of the solder joint, and different approaches to improve the reliability of the solder joint. Chapter 3 describes the experimental details, materials used, and the methodology adopted for the investigation. Chapter 4 presents the results of the experiments carried out. Chapter 5 gives a detailed analysis of the results, interpretation, and related discussion. Chapter 6 lists the conclusions drawn based on the discussion and experimental findings. The experimental results not presented in Chapter 4 are presented in the Appendix.

Chapter 2 LITERATURE REVIEW

Metal joining is a controlled process used to connect two metal parts to form an assembly. Welding, soldering, brazing, etc. are some important metal joining processes used in the manufacturing industry. Soldering is the most important joining process exclusively used in the electronics industry to join the different electronic components to the circuit board.

2.1 Soldering

Soldering is the metal joining process where two base metals joined together through the use of a filler metal having a melting point well below the base metals. The filler metal is known as solder and the process is carried out generally at temperatures below 450 °C. During soldering, adequate heat is applied to the parts to be joined to melt the solder and the molten solder gets drawn into the joint by capillary action. The actual joining is achieved by wetting action and formation of a metallurgical bond between solder and substrate. The soldering process is known to mankind for a very long time. However, since the dawn of the electronic age, soldering has been the most prominent assembly and interconnection technology in electronic packaging industries and it will remain so in the foreseeable future. Solder joints provide the necessary mechanical, thermal, and electrical integrity to the attached components of the electronic assembly; however, solder joints have been also recognized as the weak links in electronic products under mechanical and thermal stresses. The performance and quality of the solder are crucial to the integrity of a solder joint, and the reliability of each joint can control the overall lifespan of an electronic product (Abtey and Selvaduray 2000; Kumar and Prabhu 2007; Laurila et al. 2005).

2.2 Soldering Techniques

Soldering in the microelectronics packaging industry is predominantly done by two techniques namely, wave soldering and reflow soldering, to attach the different electronic components on printed circuit boards (PCBs) of the assembly.

2.2.1 Wave soldering

Wave soldering is used in a bulk soldering process for manufacturing the printed circuit boards. This technique is mainly used in pin-through-hole soldering. A schematic diagram for the wave soldering process is shown in Figure 2.1 (Liukkonen et al. 2011). The assembly of temporarily attached components is passed over a pot of molten solder in which a pump circulates the molten solder and produces an upwelling of solder, which looks like a standing wave. The component ends come in contact with molten solder and form the solder joint by capillary action. The viscosity and density of the molten solder significantly affect the wave soldering process (Abtey and Selvaduray 2000). The recent developments in electronics components technologies largely replaced the through-hole components with surface mount components, therefore, wave soldering has been superseded and replaced by the reflow soldering technique in many large-scale electronics applications.

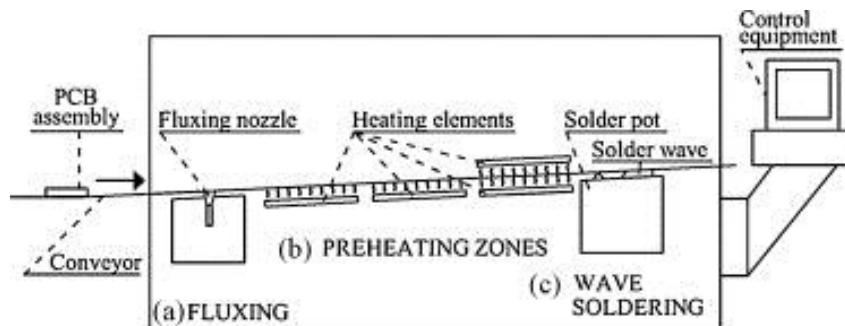


Figure 2.1: A schematic diagram for the wave soldering technique

2.2.2 Reflow soldering

The reflow soldering technique is predominantly used for attaching the surface mount technology (SMT) electronic components to the PCB. A solder paste (a sticky mixture of solder alloy powder, flux, binder, and additives) is used to temporarily attach the electronic components to the contact pads on PCB and the entire assembly is passed through the reflow oven where it is subjected to the controlled heating called a reflow cycle. The molten solder exhibits the properties like cohesion and adhesion which helps to form the metallurgical bond with the contact pad as well as component thus, forms the solder joint.

A schematic diagram for a typical reflow soldering process and a reflow cycle used in the reflow oven to manufacture the assemblies is shown in Figure 2.2 and Figure 2.3 (Optronics 2015), respectively.

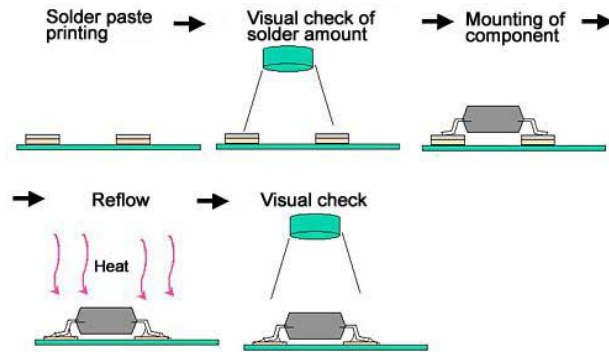


Figure 2.2: A schematic diagram for the typical reflow soldering process

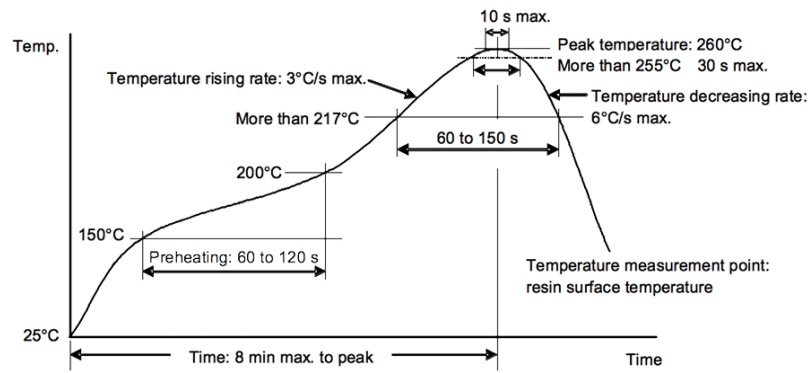


Figure 2.3: A typical reflow cycle profile

A typical reflow cycle consists of different zones namely, pre-heat zone, thermal soak zone, reflow zone, and cooling zone. In the first zone of the reflow process i.e. preheat zone the assembly is continuously subjected to the increasing temperature (50-100 °C below the liquidus temperature of the solder) till the target soak/pre-reflow temperature is reached. All the volatile solvents in solder paste get outgas at this stage. The rate of change of temperature (ramp-up rate) in this zone is adjusted according to the allowable temperature that a most sensitive component on the assembly can withstand. The thermal soak zone helps in the activation of flux in the solder, which helps in the oxide reduction of the contact pad and component terminals. The activated flux helps in preparing the proper contact

surfaces for the joint formation and supports the spreading of the molten solder in the reflow zone. In the reflow zone, the soldering temperature ramps up till the maximum temperature of the reflow cycle is reached (30-50 °C above the liquidus temperature of solder), where solder paste completely melts and spreads over the contact area of the substrate and component terminal (reactive wetting) to form a metallurgical bond. The preferred peak temperature for SAC solder is usually 250 °C as the melting temperature of SAC solders is generally falls around 217 °C. In the cooling zone, solder joints gradually cool and solidify. A proper cooling rate (ramp-down rate) hinders the excessive intermetallic formation at the joint interface and prevents the thermal shock to the attached components (Tan et al. 2015).

2.3 Solders

Tin-lead (Sn-Pb) solders are conventionally used for metal interconnections due to their desirable outstanding soldering properties, such as low melting temperatures (180-188 °C range), good workability, ductility, and excellent wetting combined with ease of manufacturing and low cost. The presence of Pb enhances several properties of the solder and improves the overall reliability of the joint. Lead-bearing solders, especially the eutectic, Sn63Pb37 (63% of tin, 37% of lead by weight), or near-eutectic tin-lead alloys (i.e. Sn60Pb40), has become indispensable for the interconnection and packaging of electronic devices and circuits, and have been used extensively in the assembly of modern electronic circuits. For the past several decades, tin-lead alloys have been the solder material of choice for the interconnecting and packaging electronic components (Abtew and Selvaduray 2000; Ma and Suhling 2009a).

Lead and lead-based compounds have been declared as chemicals posing the greatest threat to human beings and the environment by the environmental protection agency (EPA). The widespread utilization and disposal of components containing leaded solder allow lead (Pb) to enter into the food chain and ecosystem, which causes several problems to human health and the ecosystem. Environmental concerns over the use of toxic Pb have led to its ban in the electronics industry in most countries. End-of-life disposal has been cited as a driving

factor for the elimination of lead. Several directives namely, WEEE (Waste Electrical and Electronic Equipment), RoHS (Restriction of use of Hazardous Substances) and ELV (End of Life Vehicle) have put the restriction on the use of Pb for consumer electronics applications (Desmarest 2012; Ramli et al. 2016; Tseng et al. 2013; Zeng and Tu 2002). The increased concerns regarding the toxicity and environmental impacts of lead and the strict restrictions on the use of lead-based solders motivated researchers for the development of reliable and high-performing lead-free solders for the electronics packaging industry. The research and development of substitute solder alloys have been directed towards Sn containing binary or ternary alloys.

2.3.1 Lead-free solders

To fulfill the solder requirement of microelectronic industries caused due to ban on Sn-Pb solder, several novel lead-free alternatives have been developed from the past few decades. The newly developed lead-free solder alloy is constantly compared with conventional eutectic or near eutectic Sn-Pb solder and is expected to perform equally well or better in most respects. The alternative lead-free solder alloys necessarily meet the following minimum requirements to replace the Sn-Pb solder (Abteu and Selvaduray 2000; Laurila et al. 2005, 2010a; Yu et al. 2000):

- The new lead-free solders should have melting temperatures close to eutectic Sn-Pb solder (183 °C).
- Low toxicity and should not have present or future negative environmental impact.
- Electrical conductivity and the reliability of the alloy, which involves factors such as strength, ductility, the ability to withstand thermal and mechanical fatigue, creep, and shock resistance.
- Rework ability of the soldering alloy is also important. This involves the resistance to the formation of undesirable alloys or intermetallic structures upon multiple re-melts.
- Good wetting is another important requirement of lead-free solders. A favorable surface energy difference with common bonding metals is necessary to prevent the solder from balling up and falling off.

- Improved mechanical properties as creep resistance, thermo-mechanical fatigue strength, vibration, and mechanical shock resistance, shear strength, and thermal stability.
- Prevent the transformation of β -Sn to α -Sn, which causes unwanted volume change and degrades structural integrity and reliability of solder.
- Low alpha particle emission should also be taken into account for sensitive devices, such as flip-chip configuration (Suganuma 2001).

Researchers have developed a large number of lead-free solders in the past few decades to meet the various requirements of the electronic packaging industry. The binary and ternary Pb-free solder alloys based on Sn-Cu, Sn-Ag, and Sn-Ag-Cu alloy systems provide promising alternatives for the replacement of conventional Sn-Pb solders (Ting Tan et al. 2015). Several environmental-friendly Sn-based alloys such as Sn-3.0Ag-0.5Cu, Sn-14Bi-5In, Sn-0.3Ag-0.7Cu, Sn-0.7Cu, Sn-3.5Ag, Sn-9Zn Sn-8Zn-3Bi, and Sn-58Bi, etc. have been considered the most promising candidates to replace the toxic Sn-Pb alloy (Kotadia et al. 2014). Among them, the Sn-Ag-Cu (SAC) solder alloys are the most preferred lead-free solders in the electronics industry due to their comparable melting point, electrical performance, good solderability, and mechanical properties compared to Sn-Pb solder. Some potential lead-free solder candidates with their applications and concerns are summarized in Table 2.1 (Fallahi et al. 2012; Keller et al. 2011b; Laurila et al. 2005, 2010b; Yuan and Lee 2013).

Table 2.1: Potential lead-free solder candidates with their applications and concerns

Alloy system	Composition	Melting range (°C)	Application remark
Melting temperature below 180 °C			
Bi-In	Bi-33In (eutectic)	109	<ul style="list-style-type: none"> • Bi content may cause the soldered area to peel off. • The melting point too low for some applications.
In-Ag	In-3Ag (eutectic)	143	<ul style="list-style-type: none"> • Good wettability and low-temperature malleability. • Specifically good for cryogenic applications.

Sn–In	Sn–52In	118	<ul style="list-style-type: none"> • In increases the cost of solder. • Specialized applications for wetting ceramics and glasses.
	Sn–50In	118–125	
Sn–Bi	Sn–58Bi (eutectic)	138	<ul style="list-style-type: none"> • Low melting point eutectic solder. • Bi produce brittle phase in the matrix. • Potential segregation problems. • Low melting phase with Pb traces. • Poor creep resistance.
Melting temperature range 180-200 °C			
Sn–Bi–In	Sn–20Bi–10In	143–193	<ul style="list-style-type: none"> • Replacement candidates for near-eutectic SnPb alloys. • Potential segregation and cracking problems with increasing Bi content. • Low melting phase with Pb traces.
Sn–Zn–Bi	Sn–8Zn3Bi	189–199	<ul style="list-style-type: none"> • Zn imparts poor corrosion resistance. • Poor wettability. • Zn forms brittle intermetallic, which deteriorates mechanical strength.
Sn–Zn	Sn–9Zn (eutectic)	198.5	
Melting temperature range 180-230 °C			
Sn–Ag	Sn–3.5Ag (eutectic)	221	<ul style="list-style-type: none"> • Primary replacement candidates for near eutectic SnPb alloys. • High melting point. • Very large Ag₃Sn platelets formation increases the brittleness of the joint. • Poor wettability.
	Sn–2Ag	221–226	
Sn–Ag–Cu	Sn–3.8Ag–0.7Cu (SAC387) (near eutectic)	217	<ul style="list-style-type: none"> • Preferred for reflow soldering. • Tends to dissolve copper at high temperature, which has detrimental effects.
	Sn3.9Ag0.6Cu (eutectic)	217	<ul style="list-style-type: none"> • Used for BGA/CSP and CBGA components attachments and rework of BGA board. • Relatively expensive.

	Sn-1Ag-0.5Cu (SAC 105) (near eutectic)	220-225	<ul style="list-style-type: none"> • Contains the least amount of silver. • Compatible with all flux types. • Relatively inexpensive. • Good fatigue resistance, wetting, and joint reliability.
	Sn-3Ag-0.5Cu (SAC305) (near eutectic)	217-220	<ul style="list-style-type: none"> • Recommended alloy for wave and reflow soldering. • Good wettability and mechanical strength. • Tends to dissolve copper at high temperature. • Weak strength under thermal cycling. • Large Ag₃Sn intermetallic particles growth causes mechanical weakening and poor shock/drop performance. • Tendency to creep. • Relatively expensive.
	Sn-4Ag-0.5Cu (SAC405) (eutectic)	217	<ul style="list-style-type: none"> • Specifically designed for copper and stainless steel plumbing. • High Ag₃Sn intermetallic particles growth increases the brittleness of the joint. • Relatively expensive.
	Sn-0.3Ag-0.7Cu	217-228	<ul style="list-style-type: none"> • Good ductility. • Lower Ag₃Sn intermetallic particle growth. • Less expensive. • Low mechanical and thermal fatigue strength.
Sn-Cu	Sn-0.7Cu (eutectic)	227	<ul style="list-style-type: none"> • Low cost. • Plumbing alloy. • Poor mechanical properties. • Application for wave soldering.
Sn-Cu multicomponent system	Sn-0.7Cu-0.05Ni-0.009Ge (eutectic)	227	<ul style="list-style-type: none"> • Silver-free solder. • Nickel stabilizes solder alloy and lowers copper erosion. • The presence of Ge improves wettability and reduce dross formation.

2.3.1.1 Sn-Ag-Cu solders

The near eutectic SAC alloys with a composition of 3-4 % Ag and 0.5-1 % Cu are the most popular and widely accepted solder alloys in microelectronic packaging industries. Sn–Ag–Cu ternary alloys have the advantage of acceptable wettability, good interfacial properties, and low coarsening rate, and have relatively low melting temperatures compared to binary Sn–Ag and Sn–Cu eutectic alloys. The presence of Cu lowers the melting temperature and improves the wettability of SAC solder alloys. The binary phase diagrams of Sn–Cu and Sn–Ag solder systems and ternary phase diagram of Sn–Ag–Cu solder system are shown in Figure 2.4 (Kotadia et al. 2014; Li et al. 2014; Liang et al. 2007).

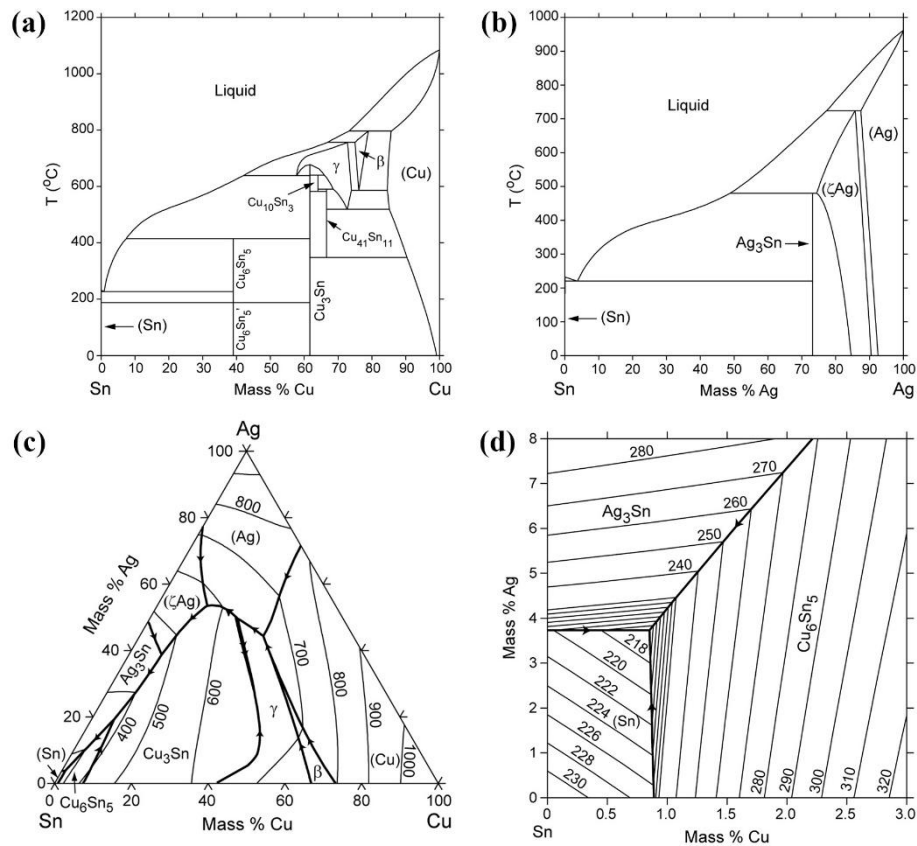


Figure 2.4: Binary (a) Sn–Cu and (b) Sn–Ag phase diagram, and a projection of the liquidus surfaces for the Sn–Ag–Cu phase diagram showing (c) ternary eutectic reaction and (d) Sn-rich corner

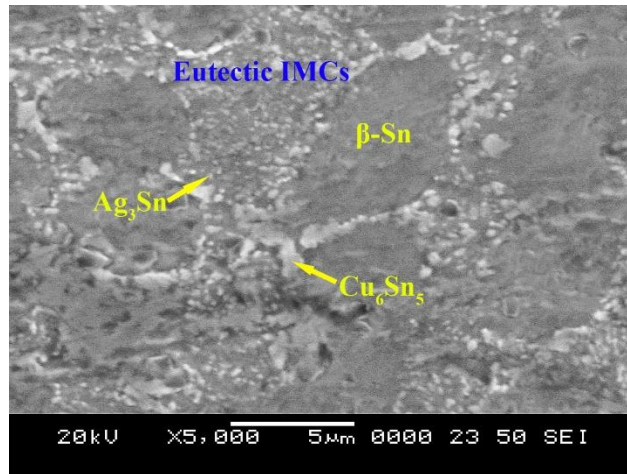


Figure 2.5: The microstructure of a typical eutectic Sn-Ag-Cu solder alloy

The area in the Sn-rich corner shows the near eutectic region. The majority of the commercially available SAC alloy compositions are within this region (Ma and Suhling 2009b). The ternary eutectic reaction takes place at a temperature of 217.2 °C. A typical microstructure for eutectic Sn-Ag-Cu solder alloy is shown in Figure 2.5. Under equilibrium solidification conditions, the microstructure of SAC solder mainly consists of three phases, a high volume fraction of β -Sn matrix with small, rod/needle-shaped Ag_3Sn and disc-shaped Cu_6Sn_5 IMC precipitates dispersed in the matrix (Chen et al. 2016; Lalonde et al. 2004; Lee and Mohamad 2013; Lewis et al. 2002; Moon et al. 2000). However, due to a typical large undercooling (10-50 °C) associated with the nucleation of the β -Sn phase, the suppression in equilibrium ternary eutectic phase transformation was observed in Sn-Ag-Cu alloys. Therefore, the Ag_3Sn and Cu_6Sn_5 intermetallic precipitates sometimes can grow to large sizes before the whole joint solidifies. These particles are said to be primary precipitates and the remaining fine intermetallic precipitates between the β -Sn dendrites are referred to as secondary precipitates (Yin et al. 2012). In the suppressed eutectic transformation condition, the Ag and Cu contents of the liquid solder reach far below equilibrium values due to the formation of a primary Ag_3Sn or Cu_6Sn_5 phases. Once the β -Sn nucleation begins, the liquid alloy composition exists within the primary β -Sn region due to large constitutional supercooling. This makes the β -Sn to adopt a dendritic morphology, and during dendrite growth, the interdendritic regions become enriched in Ag

and Cu and eventually solidify as monovariant or invariant eutectic micro constituents, depending on local composition (Lalonde et al. 2004).

The structural integrity and reliability of the solder joint majorly depend on the wettability of the solder, solder microstructure, type and sizes of intermetallic precipitation formed in the microstructure, and morphology and thickness of intermetallic compounds (IMCs) layers formed at the joint interface. The performance and reliability of the electronic assembly under different service conditions can be greatly improved by developing the solder alloy for better wettability, refine microstructure, and enhanced physical, thermal and mechanical properties.

2.4 Wettability of the Solder Alloys

Wettability of the solder is the first and most important property in selecting the lead-free solder for the intended application. Wettability can be defined as the tendency of the liquid to spread on a solid substrate. Wetting of a solid substrate by liquid is a surface phenomenon in which the surface of a solid is covered by liquid by spreading over it. The wetting process involves a continuous decrease in contact angle and a continuous increase in spreading area with time. Wetting can be broadly classified into two categories as reactive wetting and non-reactive wetting. Reactive wetting is characterized by the chemical reaction of the substrate and liquid with the formation of intermetallic compounds e.g soldering. The non-reactive wetting does not involve any chemical reaction between the substrate and liquid, e.g spreading of water on the glass surface. A metric of wettability is the contact angle, θ , formed at the edge of the spreading solder with the substrate. The contact angle is defined as the angle formed by the intersection of the liquid-solid interface and the liquid-vapor interface. The contact angle is decided by the balance of three interfacial energies of the solid surface/gas interface (γ_{gs}), solid and the liquid interface (γ_{ls}), and surface tension of the molten solder (γ_{gl}). The relationship between the contact angle and surface energies can be represented by Young's equation (Equation 2.1), where θ is the equilibrium contact angle (Arenas and Acoff 2004). The lower the value of θ , the better is the wettability.

$$\gamma_{gs} = \gamma_{ls} + \gamma_{gl} \cos \theta$$

2.1

Wetting of substrates by molten solders is a complex and important phenomenon that affects the interfacial microstructure and hence the reliability of a solder joint. The reactive wetting of solder and substrate is accomplished by the dissolution of the substrate in molten solder and by complex interfacial reactions leading to the formation of intermetallic compound (IMC) layers. The formation of an optimum layer of IMC indicates a better solder joint/bond. Wetting is significantly affected by the factors like surface roughness of the substrate, flux, reflow temperature, viscosity of the liquid, diffusion, interfacial reaction, solidification, adsorption, surface tension, etc (Kumar and Prabhu 2007). The good wettability of the solder improves the metallurgical bonding between component and substrate, thus, improves the mechanical integrity of the solder joint, thereby improves the quality and mechanical strength of the joint.

2.5 Evolution of the Solder Joint Microstructure and Growth of Intermetallic Compounds

The mechanical properties of the solder joint largely depend on the joint microstructure and growth of intermetallic compound (IMC) layers at the joint interface. The typical bulk microstructure of SAC solder consists of Ag_3Sn and Cu_6Sn_5 IMC precipitates dispersed in the β -Sn matrix. The reaction between copper and Sn produces Cu_6Sn_5 IMC precipitates, while the reaction between Ag and Sn forms the Ag_3Sn precipitates in the matrix. There is no reaction product formation between Cu and Ag in the microstructure, as the affinity of Cu towards Sn is more than Ag. Ag_3Sn and Cu_6Sn_5 IMC precipitates have much higher strength but have low fracture toughness than the β -Sn phase in the microstructure. Hence, the presence of a large amount of Ag_3Sn and Cu_6Sn_5 phases result in a stiff bulk solder; whereas, a high fraction of the primary β -Sn phase yields a soft and highly compliant bulk solder. An increase in the amount of Ag content in SAC solders results in a quantitative increase of Ag_3Sn IMC particles in the solder matrix (Reid et al. 2008). The metallurgical reaction between the copper substrate and molten solder primarily produces Cu_6Sn_5 IMC layer at the joint interface. The long exposure of solder joint to high-temperature environments like longer reflow time, multiple reflows, and aging results in decomposition

of the existing Cu₆Sn₅ IMC layer, which produce a more thermodynamically stable Cu₃Sn IMC layer underneath Cu₆Sn₅ IMC layer at the interface. Moreover, the activation energy required to form the Cu₃Sn IMC is much higher (114.7 kJ mol⁻¹) compared to Cu₆Sn₅ IMC (58.3 kJ mol⁻¹), which indicates that Cu₃Sn IMC is more thermodynamically stable than the Cu₆Sn₅ IMC layer (Ting Tan et al. 2015). There is no formation of Cu₃Sn IMC precipitates in the matrix as the concentration of Cu in the bulk solder is insufficient for the precipitation.

The growth kinetics of the intermetallic layer at the joint interface can be diffusion or interfacial reaction controlled. The largest product of the Gibbs free energy change and the rate of growth determines the formation of the first phase, which means the phase with the largest interdiffusion flux forms first. The difference in IMC growth rates depends on various growth kinetics (Zeng 2009). The IMC growth rate is controlled by diffusion rates of the participating elements, while the nucleation kinetics and coarsening of IMC grains are controlled by solder/IMC interface energies. The IMC growth at the joint interface is considered to be an ordinary diffusion growth controlled by the interdiffusion of elements of the solder and substrates. Due to low activation energy, the interfacial IMCs continue to grow even at room temperature (Chen et al. 2007; Dutta et al. 2009). If the IMC layer growth is a diffusion dominant process, then the isothermal growth of the IMC layer should follow the square root time law given by Equation 2.2 (Yu et al. 2005)

$$y = y_0 + \sqrt{kt} \quad 2.2$$

where y_0 is the initial IMC layer thickness (cm), t is the aging time (s), and k is the growth rate constant (cm²/s), which strongly depends on the diffusion coefficient of participating elements in the IMC formation and can be obtained through linear regression. For plotting, Equation 2.2 can be written as shown in Equation 2.3.

$$y - y_0 = k^{1/2}t^{1/2} \quad 2.3$$

The value of k can be obtained from the slope of the linear regression of the measured average IMC thickness ($y - y_0$) versus $t^{1/2}$ plot. The activation energies for the IMC layer

growth on substrates can be calculated using the Arrhenius relationship (Tu et al. 2001) as shown with Equation 2.4.

$$k = k_0 \exp\left(-\frac{Q}{RT}\right) \quad 2.4$$

For plotting purpose the Equation 2.4 can be rearranged as per Equation 2.5

$$\ln k = \ln k_0 - \frac{Q}{RT} \quad 2.5$$

Where k_0 is the layer growth constant (cm^2/s), Q is the activation energy for IMC layer growth (kJ/mol), R is the ideal gas constant (8.314 J/mol K), and T is the absolute temperature (K). The Q for the layer growth can be obtained from the slope of the $\ln k$ versus $1/T$ plot multiplied by R .

2.6 Factors Affecting the Microstructure and Strength of the Solder Joint

Introduction of surface mount electronics in hostile environments as in an automobile, defence and space, miniaturization and extensive use of portable electronic products are the motivations for the importance of solder joint reliability. Solder interconnects in electronics assembly continuously go through the mechanical and thermal stresses during their service life. The IMC layer formed at the joint interface determines the mechanical strength and reliability of the joint. The frequent exposure to elevated temperature environments during manufacturing, repair, and service of the electronic components often coarsen the IMC precipitates in the bulk microstructure and increase the interfacial IMC layer growth beyond the desired level, which ultimately affects the strength and reliability of the joint. Depending on the thickness and morphology of the layer, it can act as a good foothold for the components. A thin and uniform intermetallic compound (IMC) layer at the joint interface provides an essential electrical continuity, thermal support, and mechanical integrity to the attached components in the assembly. The thin and planar IMC layer has a strengthening effect on the joint but a thicker and irregular layer makes the joint hard and brittle. The excessive IMC growth is detrimental to the joint strength due to its inherent brittle nature and strong tendency to develop structural defects like Kirkendall

voids and micro-cracks (Amagai 2008; El-Daly et al. 2015c; Liu et al. 2016; Xu et al. 2019).

The increasing complexity of the components such as stacked Package-on-Package (POP) or System-in-Package (SiP) and circuit board assembly (e.g., stacked, double-sided boards, etc.) makes it impossible to form all the solder joints in a single reflow. In a typical electronic assembly, many of the solder joints undergo multiple reflow cycles during a complete manufacturing process from wafer bumping to the board level assembly. Rework and repair are essential practices for high-cost electronic commodities. Every time a solder joint is attached to a metallic surface by soldering, an intermetallic layer (IMC) is formed at the solder/substrate interface. During both reflow and rework, the temperature is well above 100 °C. A component, and thereby its joints, often go through multiple reflow cycles since various components are mounted at different levels on the circuit boards. The growth rate depends on the design of the component, the chemical composition of the solder, and also the time and temperature above the liquidus. The longer time the solder is in a liquidus phase and the higher the temperatures it is exposed to, the thicker the intermetallic layer is created. Solder joints formed in the first reflow further evolve during the subsequent reflows. The thickness of the intermetallic layer increases with the increasing number of soldering cycles. Therefore, it is important to understand the impact of multiple reflows on solder joint formation, microstructure growth, and reliability (Deng et al. 2005; Zhang et al. 2003).

The Ag content in the solder alloy and formation of Ag₃Sn IMC precipitates significantly affects the solder matrix strength, thus, affects the mechanical strength of the solder joint. The main disadvantages of high Ag-content SAC solder are the undesirable formation of a large volume fraction of Ag₃Sn IMC particles and a fast reaction rate with the metallization layer. Moreover, the high cost of Ag limits its use for large production (Abdelhadi and Ladani 2012). Studies showed that the microstructure of the SAC solder alloy with high Ag content consisted of sparse, huge primary precipitations, large areas of β-Sn dendrites, and interdendritic regions, in which fine intermetallic particles were dispersed in the Sn matrix. The finer Ag₃Sn particles (~140 nm dia.) in interdendritic regions affect the

mechanical properties of the solder than coarser Cu_6Sn_5 particles ($\sim 1 \mu\text{m}$ dia.). The mechanical properties were controlled by particle hardening within the interdendritic zones. The shear strength, microhardness, elastic modulus, yield stress, and UTS were obtained highest for hypoeutectic Ag content of 3 wt.%. However with increasing the Ag content further showed huge Ag_3Sn plate formation in the solder matrix. These primary precipitates limit the amount of finely dispersed Ag_3Sn particles, causing solder hardening and reduction in elongation at UTS point and total elongation at the fracture point. Solders without Ag content (Sn-0.4Cu) showed the highest plasticity, while the addition of small weight percent (1 wt.%) Ag reduced the ductility significantly (Che et al. 2010; Keller et al. 2011a). The study found that large Ag_3Sn platelets did not form in alloys with less than 3.2 wt. % Ag content (Kim et al. 2003). Ag_3Sn is the only Ag bearing phase present in the SAC solder. An increase in the amount of Ag content results in a high amount of Ag_3Sn IMC particles formation in SAC solders (Kariya et al. 2004) and also increases the cost of the solder. Large Ag_3Sn platelets should be avoided as they provide crack initiation sites under tensile and shear stresses and induce brittle fracture. The presence of a large quantity of Ag_3Sn IMC particles in the microstructure reduces the drop-impact reliability of the solder joint (Zhao et al. 2016a). Many studies have attributed the failure of the SAC305 solder joint to the large platelets of Ag_3Sn IMC under impact and thermal cycling conditions (Kim et al. 2003; Song et al. 2007; Zeng and Tu 2002).

The potential threat to the drop impact reliability of the solder caused by high-Ag content can be effectively minimized by reducing the Ag content in the SAC solder. The low Ag content (<1 wt.%) SAC solders have a low volume fraction of Ag_3Sn IMC particles formation in the matrix, good ductility, and plasticity, and relatively lower cost compared to high-Ag solders. Reducing the Ag content of SAC alloy increased its elastic compliance and plastic energy dissipation ability, which have been identified as key factors for improving the drop resistance. The low Ag-solders have better drop impact reliability and ductility compared to eutectic and near eutectic high-Ag SAC solders. However, the decrease in Ag content compromises solderability and mechanical strength of the solder, which restricts their widespread usage in the electronic industries (Che et al. 2010; Cheng

et al. 2011; Kanlayasiri and Ariga 2010; Shnawah et al. 2012b). Thus, it is important to seek solutions to compensate for the performance deficiencies arising from decreasing Ag content.

2.7 Development of Lead-free Solder for Better Mechanical Performance and Reliability of the Joint

The microelectronic packaging companies select the solders based on their applications on the assembly processes, cost, and reliability requirements of the components, as well as requests by their customers. The development of new solder alloy or improving the properties and performance of the solder with the addition of reactive or non-reactive elements/particles into the solder is widely used by researchers and manufacturers. The commonly used additives are either different suitable alloying elements or second-phase particles like different nano-metals, nano-ceramics, intermetallic nanoparticles, and carbon-based nanoparticles.

2.7.1 Alloying of solder

The common elements considered for addition in solders for the improvement of desired properties include Copper (Cu), Silver (Ag), Nickel (Ni), Indium (In), Bismuth (Bi), Zinc (Zn), Gold (Au), Germanium (Ge), Chromium (Cr), Iron (Fe), Manganese (Mn), Silicon (Si), Titanium (Ti), Palladium (Pd), Platinum (Pt), Cobalt (Co), Cadmium (Cd), Antimony (Sb), and rare earth elements. The Cadmium and Antimony present toxicity concerns. The different characteristics, advantages, and application concerns of the addition of different alloying elements in solder are summarized in Table 2.2 (Lim 2010).

Table 2.2: Characteristics, advantages, and application concerns of different additive elements in solder

Element	Melting point (°C)	Characteristics and application concerns
Tin (Sn)	232	<ul style="list-style-type: none"> • Serves as the base alloy metal. • Low melting temperature. • Less expensive and readily available. • Formation of tin whiskers and tin pest in solder joint is problematic.
Copper (Cu)	1084	<ul style="list-style-type: none"> • Inexpensive and least affected by lead impurities. • Removal of the oxide layer is more challenging.
Nickel (Ni)	1453	<ul style="list-style-type: none"> • Inhibits Cu dissolution from the substrate. • Substitute Cu in Cu₆Sn₅ IMC to form a complex and more stable (Cu, Ni)₆Sn₅ IMC phase. • Improves the strain-rate performance of the solder and enhance the drop strength of low-Ag SAC alloys. • Inhibits the diffusion and inhibits the growth of interfacial Cu₃Sn IMC phase (Wang et al. 2009; Watanabe et al. 2011; Yang et al. 2011). • Does not significantly improves creep performance.
Bismuth (Bi)	217.5	<ul style="list-style-type: none"> • Lowers melting temperature of the solder. • Reduce surface tension and improves the wettability of the solder. • Along with Ni, it reduces Cu dissolution more effectively. • Improves the strength of the bulk solder through precipitation hardening. • Suppresses the formation of large Ag₃Sn intermetallics in the bulk solder. • Improves drop shock and shear performance of low-Ag solders (Pandher et al. 2007). • Suppress the degradation of microstructure and mechanical properties during aging (Ahmed et al. 2016). • Increases brittleness of the joint due to Bi precipitation and prone to thermal fatigue (Liu et al. 2010). • Expands on solidification. • When contaminated with lead, becomes more brittle. • Some toxicity concerns in animals.
Indium (In)	156.6	<ul style="list-style-type: none"> • Lowers melting temperature. • Very expensive and scarce. • Refines Sn-rich phase in the microstructure.

		<ul style="list-style-type: none"> • Improves uniformity in distribution of intermetallic compounds in the matrix, which enhances microhardness and tensile strength of the low-Ag Sn–0.3Ag–0.7Cu solder (Kanlayasiri et al. 2009). • Extremely soft and lacks mechanical strength in alloys with high indium contents (Fallahi et al. 2012). • Corrosion-prone. • Fast oxide formation during melting.
Gold (Au)	1063	<ul style="list-style-type: none"> • Increases melting temperature of the solder. • Embrittlement problem with increasing gold content. • Very expensive.
Chromium (Cr)	1857	<ul style="list-style-type: none"> • Improves shear ductility of high-Ag SAC solder (Anderson and Harringa 2006). • Could suppress the void formation and coalescence at the Cu/Cu₃Sn interface (Kim et al. 2009).
Iron (Fe)	1535	<ul style="list-style-type: none"> • Slightly decreased the Cu₃Sn IMC layer but does not suppress the total IMC thickness (Fallahi et al. 2012). • No significant effect in reducing the melting point of solder (Shnawah et al. 2012a). • Fe-modified SAC solder showed ductile failure after aging (Laurila et al. 2009). • Suppressed the diffusion rate of Sn to minimize the formation and coalescence of voids at the Cu₃Sn/Cu interface and prevent interfacial weakening (Anderson and Harringa 2006).
Manganese (Mn)	1245	<ul style="list-style-type: none"> • Effective at reducing the growth of the Cu₃Sn layer and the combined (Cu₃Sn + Cu₆Sn₅) intermetallic layer. • Improves ductility at high-temperature aging (Anderson and Harringa 2006). • Could suppress Kirkendall void formation at the Cu/Sn3.5Ag solder joints (Kim et al. 2009).
Zinc (Zn)	419.5	<ul style="list-style-type: none"> • Minor Zn doping could effectively retard IMC growth, including Cu₆Sn₅ and Cu₃Sn. • Could also increase the interface quality after multi-reflow and aging on the Ni/Au surface finish (Jiang et al. 2006). • Refines the bulk IMC precipitates and improves the solder strength. The high concentration of Zn could deteriorate the microstructure and increase the brittleness of the joint (El-Daly et al. 2015b). • Oxides and corrodes readily. • Requires strong fluxes.

Cobalt (Co)	1495	<ul style="list-style-type: none"> • Active chemically and forms many compounds. • Have a higher affinity with Sn than Cu. • The addition <0.1 wt.% improves the properties of the Sn-Cu eutectic solder (Cheng et al. 2008). • Minor substitution of Co for Cu in high-Ag SAC solder could refine the joint-matrix microstructure and increase the shear strength (Anderson et al. 2002; Gao et al. 2006). • Promote nucleation and reduce the Cu₃Sn layer after annealing. • Micro-alloying with Co could significantly refine the grain structure (Ma et al. 2016).
Germanium (Ge)	937.4	<ul style="list-style-type: none"> • (Ge) acts as an antioxidant and enhances the properties and behavior of Sn-Cu-Ni alloys. • The presence of Ge decreases the dissolution of Cu (Hamilton et al. 2007). • Expensive and adds cost to the solder.
Palladium (Pd)	1552	<ul style="list-style-type: none"> • Effectively suppress the growth of Cu₃Sn in the Cu/Sn-Ag-Cu solder joints and reduced the formation of Kirkendall voids to improve mechanical reliability (Ho et al. 2012). • Soluble to Cu₆Sn₅ and especially dissolves to Cu sublattice. • Can refine the grain structure of (Cu, Pd)₆Sn₅ and inhibits its grain growth (Laurila et al. 2010b).
Silicon (Si)	1410	<ul style="list-style-type: none"> • Can suppress the void formation at the IMC interface.
Titanium (Ti)	1660	<ul style="list-style-type: none"> • Suppresses void formation and coalescence at the Cu (substrate)/Cu₃Sn interface and embrittlement after aging (Anderson and Haringa 2006).
Platinum (Pt)	1772	<ul style="list-style-type: none"> • Can dissolve to Cu sublattice of Cu₆Sn₅ and refined the grain structure of (Cu, Pt)₆Sn₅ after one reflow, and slowed down grain growth after 4 reflows (Amagai 2008).
Antimony (Sb)	630.5	<ul style="list-style-type: none"> • Increases mechanical properties of solder. • Slightly reduces thermal and electrical conductivity. • Improves test reliability of SAC solders. • Does not improve wettability (Kanlayasiri and Kongchayasukawat 2018). • Considered toxic (listed on the EACEM list of “not to be used” substances)
Cadmium (Cd)	321.1	<ul style="list-style-type: none"> • Cadmium and its compounds are listed in the RoHS directive and therefore are considered hazardous substances.

2.7.1.1 Rare earth elements (RE)

Rare earth elements have been regarded as the vitamins of metals, which means that a very small amount of a RE element may greatly enhance the properties of metals. The mechanical and physical properties of SAC solder alloys can be improved with the addition of rare earth elements such as Ce, La, Lu, and Y, etc. Rare earth elements can reduce the melting point of the solder, improve the wettability, retard the IMC growth, and improve the shear strength and creep resistance of Sn-Ag-Cu solder alloys (Zhang et al. 2012). RE-doped solders are found to have better mechanical and thermal performances than plain solders. The addition of RE in trace amount showed improvement in wettability, creep strength, and tensile strength properties of the solder. In particular, the creep resistance in RE-doped alloys showed about four times growth in creep rupture time for Sn-Ag and seven times for Sn-Cu and Sn-Ag-Cu solders. Addition of 0.25 % RE elements, mainly cerium (Ce) and lanthanum (La), to Sn-3.5Ag-0.7Cu solder showed prominent refinement in the β -Sn grains and the IMC. (Wu et al. 2004).

Studies done by Dudek et al. showed that the addition of a trace amount of La, Ce, and Y elements in Sn-3.9Ag-0.7Cu lead-free solder results in refined microstructure, reduced Cu_6Sn_5 IMC layer thickness, and, most importantly, significantly increased ductility compared with plain Sn-3.9Ag-0.7Cu alloy. The RE-containing particles i.e. RESn_3 formed in solder matrix, allow microscopic voids to nucleate throughout the solder volume and homogenize the strain in the solder joint (instead of localized strain at the solder-intermetallic interface), thereby increasing the ductility of the solder (Dudek et al. 2006; Dudek and Chawla 2010). An investigation on the effect of Ce addition in high-Ag content SAC solder with Cu and Ni-P coated substrate showed the microstructure refinement and suppression in IMC layer thickness on both types of substrate. The study also highlights that the Ce-reinforced SAC solder has excellent oxidation resistance, and the mechanical performance of joints does not degrade on isothermal aging (Xie et al. 2012). The addition of rare earth elements results in better solder properties and joint strength but significantly increases the cost of the solder, which limits their usage.

2.7.1.2 Multi-component solder system

Researchers and manufacturers have used multi-component solder system for intended purposes by introducing one or more elements in small amounts to the Sn-Ag, Sn-Cu, and Sn-Ag-Cu solder systems. Zhao et al. has studied the different properties of five types of multicomponent lead-free solders, i.e. Sn-2Cu-0.5Ni, Sn-2Cu-0.5Ni-0.5Au, Sn-3.5Ag-0.5Ni, Sn-3.5Ag-1Cu-0.5Ni, and Sn-3.5Ag-2Cu-0.5Ni. The study showed minimal change in melting points of multicomponent solder systems compared to base eutectic solder alloys. The solder microstructure appeared refined with the dispersion of different complex IMC particles in the bulk. When only Ni is involved, the composition of Cu_6Sn_5 IMC particles changed to $(\text{Cu, Ni})_6\text{Sn}_5$, and when both Au and Ni were involved, then both $(\text{Cu, Au})_6\text{Sn}_5$, $(\text{Cu, Ni, Au})_6\text{Sn}_5$ and $(\text{Cu, Ni, Au})_6\text{Sn}_5$ IMC particles appeared in the matrix. Besides, the presence of Ag_3Sn and Ni_3Sn_4 IMC particles were also observed in the matrix. The multicomponent solders showed preferable or at least equivalent tensile properties and ductile failure compared with respective eutectic solders (Zhao et al. 2013). The Sn-Cu-Ni-Ge lead-free solder (or SN100C) is an improved version of the low-cost Sn-Cu (SC) eutectic solder by doping small amounts of Ni and Ge. The introduction of Ni produced a more refined bulk microstructure and helps in forming the more stable Cu_6Sn_5 intermetallic phase of the soldered joint (Nogita et al. 2009; Nogita and Nishimura 2008). Ni addition also helps in reducing the corrosion of Cu on the printed circuit board. The presence of Ge lowers the oxidation and prevents bridging formation during soldering and improves the wettability of the solder (Shohji et al. 2005; Yen et al. 2011). However, the Sn-Cu-Ni-Ge solder exhibits a relatively high melting temperature.

The addition of selected elements in the SAC solder improves the intended properties of the solder and the reliability of the joint. However, the multicomponent systems are difficult to analyze as the phase diagram gets complicated and the formation of different intermetallics in the microstructure became difficult to control under different high-temperature working environments. Moreover, the extra elemental addition increases the cost of the solder alloy.

2.7.2 Nanocomposites

The miniature designs and high functionality of devices have pushed the demand for more reliable lead-free solder compositions (Ma et al. 2018; Nai et al. 2006). The compactness of electronic devices and increased component density on electronic packages has reduced the solder joint size on PCBs, which puts interconnects under increased thermal and mechanical stresses during service. The optimal functionality of the interconnects and long-term reliability of the micro joints requires excellent solder properties (Desmarest 2012; El-Daly et al. 2015a; Gao et al. 2019; Nai et al. 2008; Nakata et al. 2017; Tsao et al. 2013a; Yakymovych et al. 2016). It is evident that various properties of the solder can be tailored by purposefully incorporating various foreign additives to fabricate multi-composite solder. Due to the smaller pitch sizes and miniature solder joints, micrometer size particulate reinforced composite solder are out of consideration because of the size limitation. Hence, the only option for particle reinforcement in solder is with nano-length scale materials.

The particulate reinforcement in solder can be of active or inert types. Active reinforcements generally react with the solder elements to form respective intermetallic phases; whereas, inert reinforcements do not react with the solder elements and retain their primitive nature in molten solder. The development of lead-free solders with the addition of nanoparticles has proved to be a potentially viable and effective approach to improving the different properties of the solder. Owing to their smaller size, large specific surface area and high surface energy, the addition of nanoparticles improves the physical, microstructural and mechanical properties of the solder (Chen et al. 2016; Ramli et al. 2016). Some of the preferred reactive nanoparticle additives for lead-free solders with their properties, advantages, and concerns are discussed below.

2.7.2.1 Metallic nanoparticles

2.7.2.1.1 Nickel (Ni)

Nickel is most favored as an alloying elemental as well as particle reinforcement in Sn-Ag and SAC solders by researchers and manufacturers. Studies have shown that the addition

of Ni particles into lead-free solders could refine the microstructure and enhance the mechanical properties of the solder joint. An investigation by Yao et al. reported that Ni-containing composite solders possessed better wettability. Niranjani et al. observed that the hardness and creep resistance of the composite solder have been improved with the addition of 0.5 wt% Ni nanoparticles (Niranjani et al. 2012; Yao et al. 2008). Ni particles substitute the Cu atoms in the Cu_6Sn_5 IMC and form complex and more stable $(\text{CuNi})_6\text{Sn}_5$ IMC. Because of the close atomic size and similar face-centered cubic (fcc) lattice structure, the Ni atoms can substitute the Cu atoms in the IMC lattice without distorting the lattice structure. Besides, the activation energy required to form the $(\text{Cu, Ni})_6\text{Sn}_5$ IMC is lower (49.3 kJ mol^{-1}) than the Cu_6Sn_5 IMC (58.3 kJ mol^{-1}), which indicates that the $(\text{Cu, Ni})_6\text{Sn}_5$ IMC possesses higher stability (Gain et al. 2010; Laurila et al. 2010a; Yoon et al. 2009). According to Liu et al., the morphology of $(\text{CuNi})_6\text{Sn}_5$ IMC grains is also similar to Cu_6Sn_5 IMC grains but is more refined and the IMC layer is thinner compared to Cu_6Sn_5 IMC (Liu et al. 2009). The grain refinement is contributed by the stronger affinity of Ni towards Sn than Cu atoms and lower activation energy of formation of the $(\text{CuNi})_6\text{Sn}_5$ IMC over Cu_6Sn_5 IMC. In summary, the addition of Ni particles can significantly suppress the growth of the Cu_3Sn IMC layer during thermal aging and prolonged soldering (Amagai 2008).

2.7.2.1.2 Aluminium (Al)

Aluminium (Al) has been proposed as an additive element in SAC solder due to its low cost and non-hazardousness towards the environment. The IMC growth can be significantly reduced with 1 wt.% of Al element alloyed in the SAC solder by reducing the activity of Sn and Cu during soldering and thermal aging. When Al is added into solder as nanoparticles instead of an alloying element, these nanoparticles do not dissolve or interact with the Cu_6Sn_5 IMC to form the AlCu IMC layer (Li et al. 2012). Sun et al. showed that the addition of small amounts of Al nanoparticles into the Sn-1.0Ag-0.5Cu solder could refine the eutectic microstructure and Cu_6Sn_5 , Ag_3Sn IMCs, thus, enhancing the mechanical properties of the solder. However, the mechanical properties of the solder would decrease once the content of Al nanoparticles exceeded 0.1 wt.% (Sun et al. 2016). The effectiveness of Al nanoparticles in suppressing the IMC growth is found lower than

that of Ni nanoparticles. This is because Al does not dissolve in the Cu_6Sn_5 IMC and thus, the IMC layer does not inhibit the diffusion of Cu atoms as effectively as $(\text{Cu}, \text{Ni})_6\text{Sn}_5$ IMC (Gain et al. 2010).

2.7.2.1.3 Cobalt (Co)

The Co-containing lead-free solders were observed to have better shear ductility, strength, thermal fatigue and creep resistance. This could be attributed to the formation of a $(\text{Cu}, \text{Co})_3\text{Sn}_2$ IMC precipitates in the solder matrix, which strengthens the solder by its dispersion effect. Lin et al. investigated the effects of Co addition into Sn–1Ag–0.5Cu/Cu solder joint. It was found that the addition of Co could remarkably suppress the copper atoms of solder matrix diffusing to the interface, thus decreased the growth of $(\text{Cu}, \text{Ni}, \text{Co})_6\text{Sn}_5$ IMC (Lin et al. 2009). The addition of Co nanoparticles to a SAC/Cu solder joint promotes the substitution of Cu atoms by Co atoms in the Cu_6Sn_5 IMC lattice structure, forming a new IMC layer, $(\text{Cu}, \text{Co})_6\text{Sn}_5$ at the interface (Anderson et al. 2002). The substitution of Cu by Co atoms is the same as in the case by Ni atoms. The only difference is, the lattice structure of Co is a hexagonal close-packed (hcp) structure, which is different from Ni and Cu (both in fcc lattice structure). Hence, the thermodynamic affinity between Sn and Co is weaker than that between Sn and Ni but higher than that between Sn and Cu. In other words, the $(\text{Cu}, \text{Co})_6\text{Sn}_5$ IMC is more thermodynamically stable than Cu_6Sn_5 IMC but less stable than $(\text{Cu}, \text{Ni})_6\text{Sn}_5$ IMC. In summary, the influence of Co nanoparticles in the SAC/Cu solder joint is very similar to that of Ni nanoparticles but the effectiveness of Co in suppressing the Cu_3Sn IMC is slightly weaker due to weaker thermodynamic affinity. From the research of Yen et al. and Amagai, we can conclude that even a very small addition of Co nanoparticles (as little as 0.03 wt%) is sufficient to induce beneficial changes in the growth of an IMC at the joint interface. However excessive addition of Co may cause excessive growth of the IMC and degrade the joint reliability (Amagai 2008; Yen et al. 2011).

2.7.2.1.4 Molybdenum (Mo)

The addition of Mo nanoparticle up to 2.0 wt.% in SAC solder is capable of improving the solder hardness and strength due to the formation of small and regularly shaped Mo–Sn

IMC particles. These IMC particles are dispersed in the β -Sn solder matrix which can prevent grain boundary sliding and restrict the dislocation movement of the bulk solder (Mohan Kumar et al. 2006). The refinement of the IMC increased while the layer thickness decreased with increasing amounts of addition. Mo nanoparticles tend to accumulate on the surface of Cu_6Sn_5 IMC scalloped grains and the channel between them rather than disperse in the solder matrix. Therefore, it can be said that Mo nanoparticles can effectively retard the growth of both Cu_6Sn_5 and Cu_3Sn IMCs but its effectiveness in retarding the Cu_3Sn IMC is much weaker compared to Ni and Co (Arafat et al. 2011). Studies done by Yang et al. indicates that the addition of Mo nanoparticles has a refinement effect on Ag_3Sn precipitates and significantly suppresses the Cu_6Sn_5 IMC layer growth during aging. Mo nanoparticles act as a diffusion barrier, causing an increase in the activation energy for diffusion in the composite solder, thereby reducing the Cu_6Sn_5 IMC growth rate (Yang et al. 2019). However, the study on the influence of Mo nanoparticles on IMC growth and joint reliability of SAC/Cu joint is still very limited.

2.7.2.1.5 Zinc (Zn)

The addition of Zn as an alloying element and nanoparticle reinforcement have shown benefits in improving the solder strength but deteriorated the solder elongation and wettability (Song et al. 2010). El-Daly et al. reported that the superior creep resistance could achieve with the addition of a 0.5 wt.% Zn in SAC solder. The tensile strength of the Zn-containing solder is found higher than plain SAC solder with the addition of 2 wt.% Zn; however, the ductility of the solder decreased drastically due to the presence of large Ag_5Zn_8 IMC particles (El-Daly et al. 2014b; a). Studies reported the reduction in undercooling of the solder with Zn addition, which may lead to a nonhomogeneous distribution of the unwanted phases in the solder joint. The deterioration of solder wettability may be caused by the oxidation of Zn nanoparticles during soldering, which increases the surface tension of the solder (Chan et al. 2013; Prasad and Mikula 2006). The addition of Zn either as an alloying element or nanoparticles in small weight percent could effectively retard the diffusion between Sn and Cu atoms in the solder joint and suppressed the IMC growth at the interface. However excessive amount of Zn nanoparticles (0.8 wt.%)

induced an additional IMC layer (Cu_5Zn_8) which increased the total IMC thickness and causes the reliability issue (Chan et al. 2013).

2.7.2.2 Intermetallic nanoparticles

Researchers have attempted to introduce the Cu_6Sn_5 , Ag_3Sn , and Cu_3Sn intermetallic nanoparticles into the solder to improve the solder properties. Intermetallic compounds are important phases that determine the long-term reliability of the solder joint. A study was done by Zhong et al. (Zhong et al. 2015) on the addition of Cu_6Sn_5 nanoparticles in solder showed that the intermetallic nanoparticles could be a promising low-temperature sintering material. An investigation done by Li et al. on the addition of nano-scale Cu_6Sn_5 particles into Sn-Bi solder showed the microstructure refinement and improvement in creep and corrosion resistance of the solder (Li et al. 2017). In recent times, researchers have studied the effect of the addition of Cu_3Sn , Ag_3Sn , and Cu_6Sn_5 intermetallic particles in SAC solders as well as in flux. Studies showed a positive effect in grain refinement and IMC growth inhibition; however, the desired amount of IMC suppression and improvement in mechanical properties of the solder joint could not be achieved (Shao et al. 2019; Wang et al. 2019). Nevertheless, the research on the development of solders with the addition of intermetallic nanoparticles is still relatively rare and several aspects need to be extensively investigated before the use of intermetallic particles in solder for industrial application.

The biggest concern with the addition of reactive nanoparticles such as metallic and intermetallic nanoparticles is that the active reinforcements generally dissolve in molten solder to form related intermetallic compound (IMC) particles with the constituent elements of solder itself. These IMCs are prone to coarsening when the solder joint is subjected to high-temperature working conditions, thereby weaken the advantages of nanoparticle addition in solder and deterioration in the joint properties. The complex IMC formation and their growth under working conditions limit the usage of reactive nanoparticles in many industrial applications where solder joints are exposed to a high-temperature service environment and long-term reliability of the components is the main concern.

The reinforcements such as nano-ceramics and carbon-based nanoparticles are the unreactive type of reinforcement, which retain their original nature in molten solder and effectively contribute to modifying properties of the solder. The inert nanoparticle reinforcement offers a feasible and cost-effective solution for the improvement of solder properties under high-temperature service conditions. Some of the preferred non-reactive nanoparticle additives in lead-free solders with their properties, advantages, and concerns are discussed below.

2.7.2.3 Oxides nanoparticles

2.7.2.3.1 Titanium dioxide (TiO₂)

TiO₂ nanoparticles being the favorite inert nanoparticles for the reinforcement in solders. Researchers reported the improvement in mechanical properties of the composite solder such as ultimate tensile strength, yield strength, and micro-hardness with the addition of TiO₂ nanoparticles up to 1.0 wt.%. The dispersed TiO₂ nanoparticles in the solder matrix refine the IMC particles (such as Cu₆Sn₅ and Ag₃Sn) and improve the matrix strength by dispersion strengthening. However, researchers observed the deterioration in the ductility of the composite solder with the increase in TiO₂ content (Leong et al. 2011; Lin et al. 2003). Leong and Tsao observed that the Cu₆Sn₅ IMC thickness at SAC/Cu solder joint interface was suppressed by about 50% when 0.5 wt.% TiO₂ nanoparticles were added to the solder. Moreover, the morphology of the Cu₆Sn₅ IMC remained scallop-like instead of whisker-like during prolonged reflow times as the adsorption of nanoparticles reduced the ripening rate of the IMC grains (Leong et al. 2011; Tsao and Chang 2010). The TiO₂ nanoparticles doped SAC305 solder nanocomposites showed a significant reduction in Ag₃Sn IMC particle size and enhanced distribution in the matrix. The microhardness and tensile strength were improved with nanoparticle reinforcement in the solder (Tang et al. 2014). Mohd Salleh et al. investigated the performance of TiO₂ reinforced Sn–0.7Cu solder under multiple reflow cycles. The results showed a relative suppression of the Cu₆Sn₅ phase, both as primary crystals and as an interfacial layer compared to unreinforced solder. The authors suggest that the TiO₂ nanoparticles promote nucleation and decrease the amount of molten solder contact time with the interfacial layer, which results in IMC

suppression. The TiO_2 particles appear to stabilize the interfacial Cu_6Sn_5 layer and result in a more planar morphology. The IMC suppression in TiO_2 reinforced solder joints yielded a higher shear strength after multiple reflow cycles compared to unreinforced Sn–0.7Cu solder joints (Mohd Salleh et al. 2016). In conclusion, the addition of TiO_2 nanoparticles can effectively retard the growth of the Cu_6Sn_5 IMC and improve the solder joint strength in different working conditions. However, precautions should be taken to ensure the proper amount of addition of nanoparticles, as the higher content of the nanoparticles tend to agglomerate and could be detrimental for the solder joint properties.

2.7.2.3.2 Zirconium dioxide (ZrO_2)

The addition of 1-2 wt.% ZrO_2 nanoparticles in the lead-free solder could reduce the size of the β -Sn grains and effectively restricts the growth of Ag_3Sn IMC particles in the solder matrix due to the adsorption effect (Gain et al. 2011a; Shen et al. 2006). Studies found that ZrO_2 reinforced Sn-0.7Cu solder has a higher hardness, yield strength, and ultimate tensile strength (UTS) than ZrO_2 -free solder but the composite solder suffered the problem of formation of pores in the matrix. The ZrO_2 -added composite joints showed suppression in interfacial IMC layer under thermal-cycling conditions; however, the effective IMC suppression was rather weak compared to TiO_2 and Al_2O_3 nanoparticle addition (Gain et al. 2011b; Gain and Zhang 2016; Zhong and Gupta 2008a).

2.7.2.3.3 Iron oxide (Fe_2O_3)

The wettability of solder was improved and the growth of the IMC layer was suppressed with the addition of small amounts of Fe_2O_3 nanoparticles (Che Ani et al. 2018; Zhao et al. 2016a; b). Zhao et al. studied the effect of the addition of Fe_2O_3 nanoparticles in different sizes on the properties of Sn-1.0Ag-0.5Cu nanocomposite solders and joints. The investigation revealed that the size of the added Fe_2O_3 nanoparticles in the composite solders is critical to the properties of the solder alloys and solder/Cu joints. When the size of added Fe_2O_3 nanoparticles changed from 200 nm to 20 nm, improvements in the microstructure refinement, reduction in the liquidus temperature, and enhancement in solder wettability of the composite solder were observed. The addition of smaller-size Fe_2O_3 nanoparticles effectively suppressed the interfacial IMC formation during reflow

and impeded the interfacial IMC growth during thermal aging. The addition of nanoparticles in small size improved the shear strength and the ability of plastic deformation of the solder joints more effectively compare to large size particles (Zhao et al. 2016b). Che Ani et al. studied the influence of Fe_2O_3 nanoparticle reinforced SAC solder for the ultrafine microelectronics assembly. The results showed the suppression in the IMC layer at the joint interface and an improvement in the fillet height of the joint with the addition of Fe_2O_3 nanoparticles in 0.05 wt.%. The addition of over 0.05 wt.% showed the accumulation of nanoparticles in the matrix and deterioration of the joint properties (Che Ani et al. 2018).

The grain refinement due to the addition of Fe_2O_3 nanoparticles in the solder can be explained by the classical theory of growth inhibition by second-phase particles (Anderson et al. 1989). The second-phase Fe_2O_3 nanoparticles gathered at the grain boundaries of β -Sn, then produced great pinning force at the grain boundaries to inhibit grain growth and finally refined the β -Sn grain. A schematic diagram of the moving grain boundary and particle interaction based on the relationship theory between grain growth and second-phase particles given by Smith (Rohrer 2010) is shown in Figure 2.6 (Zhao et al. 2016b).

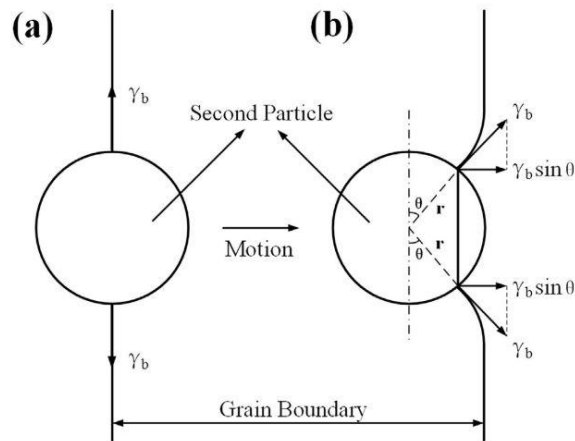


Figure 2.6: A schematic diagram for the interaction of the moving grain boundary and the second-phase particles (a) encountering, (b) interacting

Assuming the second phase particles are spherical with radius r and the interface energy per unit area of the grain boundary is γ_b . During grain growth, if a moving grain boundary encounters a second-phase particle, it will first cling to particles as shown in Figure 2.6-a,

and then the surface of the grain boundary will curve because of the role of the surface tension of the grain boundary. For each second phase particles, the restraining force of boundary migration is $2\pi r \gamma_b \sin\theta \cos\theta$, where θ is the angle between the average surface of the grain boundary and the surface at the point where it joins the second phase particles. When θ is 45° , the maximum restraining effect of the second phase particles on boundary migration is obtained. Thus, the maximum restraining force of boundary migration for a second phase particles equals $\pi r \gamma_b$. Considering the effect of all second phase particles on the migration of grain boundary, the total restraining force (F_{total}) acting on the boundary is given as in Equation 2.6:

$$F_{\text{total}} = n_i \pi r r_b = \frac{3 f \gamma_b}{2 r} \quad 2.6$$

Where n_i is the number of second phase particles per unit area of grain boundary and f is the fraction of the total volume occupied by the second phase particles. From the above equation, it can be seen that the total restraining force (F_{total}) is directly proportional to the fraction of the total volume of second phase particles on grain boundary (f) and is inversely proportional to the radius of the second phase particles (r). This analysis illustrates the size of the second phase particles on the grain boundary affects grain growth. The smaller the size of the second phase particles is, the larger the restraining force (F_{total}) and the smaller the grain size in the composite solder matrix.

2.7.2.3.4 Cerium oxide (CeO₂)

Studies done by Fouzder et al. reported the improvement in the microhardness of the solder and microstructure refinement of the solder joint with the addition of CeO₂ particles in low-Ag content SAC0307 solder (Fouzder et al. 2014). Li, tang, and Guo studied the effects of CeO₂ nanoparticles on the shear strength of the SAC0307 solder. The study reveals that the appropriate addition i.e. up to 0.5 wt.% of CeO₂ nanoparticles can improve the shear strength of the composite solder; however, excessive addition degrades the mechanical properties of the solder (Z.H. Li, Y. Tang, Q.W.Guo 2019). The research on the effect of the addition of rare earth oxides on different properties and joint reliability of SAC solders

is still limited and also the higher cost of nanoparticles limits their widespread usage for microelectronic packaging applications.

2.7.2.3.5 Alumina (Al_2O_3)

It is well known that Al_2O_3 has many exceptional properties such as a high melting point, excellent mechanical strength, and good abrasion resistance. Al_2O_3 nanoparticles have been widely used as an inert reinforcement to fabricate composite materials due to their superiorities in heat stability, availability as well as low cost. Studies showed that the addition of Al_2O_3 nanoparticles had a positive effect on the microstructure and mechanical strengths of composite solder alloys. Being hard material, the addition of Al_2O_3 nanoparticles helps in improving the hardness and bulk strength of the solder. Composite lead-free solders with added Al_2O_3 nanoparticles have been reported to possess better micro-hardness, wettability, tensile strength, creep resistance, and a lower coefficient of thermal expansion (CTE).

Mavoori and Jin (Mavoori and Jin 1998) studied the effect of ultrafine Al_2O_3 on Sn-37Pb alloy and found a significant increase in creep resistance and mechanical properties of the solder. The findings of studies done by Zhong and Gupta indicated that the growth of the Cu_6Sn_5 IMC layer was retarded by the addition of Al_2O_3 nanoparticles (Zhong and Gupta 2008b). An investigation done by Tsao et al. on the influence of the addition of Al_2O_3 nanoparticles in Sn3.5Ag0.5Cu solder showed a significant decrease in the β -Sn phase, Ag_3Sn IMC particles size, and lamellae spacing in the solder microstructure. Studies found improvement in wettability and microhardness of the solder with the ceramic nanoparticles reinforcement (Tsao et al. 2010). The application of composite solder on ball grid array joints showed suppression in the IMC layer growth, improvement in the shear strength, and ductile failure of the joints (Tsao et al. 2013b). Tsao et al. reported that the growth of the Cu_6Sn_5 IMC layer was retarded when the SAC-(0.5–1.0 wt.%) Al_2O_3 /Cu soldered joints were subjected to multiple reflow cycles. The Cu_6Sn_5 IMC morphology changed from scallop-like to prism-like. The IMC thickness was thinner in the composite solder joint when compared to the SAC/Cu joint. The addition of Al_2O_3 ceramic nanoparticles results in enhanced wettability, suppression of the IMC layer, improvement in shear strength, and

microhardness of the solder. Al₂O₃ nanoparticles did not react with Cu or Sn atoms to form a new IMC at the interface but altered the morphology of the Cu₆Sn₅ IMC layer. A discontinuous scallop-shaped Cu₆Sn₅ IMC layer was changed to a continuous scallop-shape and become thinner after Al₂O₃ nanoparticles were added in the SAC/Cu joint. The Al₂O₃ nanoparticles can effectively retard the growth of the Cu₆Sn₅ IMC in general soldering conditions (Chen et al. 2016; Chuang et al. 2011a).

Researchers have studied the application of Al₂O₃ nanoparticles reinforced solders for interconnects in microelectronics packaging. The study on the effect of Al₂O₃ nanoparticles on microstructure and electro-migration behavior of SAC305 solder showed that the presence of nanoparticles effectively suppressed the IMC dissolution at the cathode and the IMC growth at the anode. The addition of nanoparticles reduced the diffusion flux of Cu and suppressed the diffusion of Cu in the bulk matrix (Peng et al. 2015). Several studies have stressed using nanoparticles in minor weight percent to obtain the best results from the composite solders. Excessive addition of nanoparticles may drastically deteriorate the solder properties (Chuang et al. 2011b; Ramli et al. 2016; Yakymovych et al. 2016).

The improvement in the solder properties is attributed to the refinement of β-Sn grains and the dispersion of the refined Ag₃Sn IMC particles in the solder matrix. The refinement of the β-Sn and Ag₃Sn grains in the composite solder matrix is resulted due to the adsorption of Al₂O₃ nanoparticles on the Ag₃Sn IMC grain surface and grain boundaries in the matrix during solidification of the solder. The improvement in the solder matrix strength due to the reduction in the size of the β-Sn grains can be explained by the Hall-Petch relationship for grain boundary strengthening. The relationship is shown in Equation 2.7.

$$\sigma_y = \sigma_i + kd^{-0.5} \quad 2.7$$

where σ_y is the yield strength of the polycrystalline material; σ_i is the constant for the material, which represents the overall resistance of the lattice to dislocation movement; k is a constant which measures the contribution of hardening due to grain boundaries, and d represents the grain size. The Hall-Petch theory states that the decrease in grain size increases the strength of materials. The decrease in grain size increases the number of grain

boundaries, and the presence of more grain boundaries resists the movement of dislocations. This increases the hardening of the material leading to an increase in the material strength.

The dispersion strengthening of the solder joint achieved due to the presence of fine particles and nanoparticles in the solder matrix can be explained by Orowan strengthening mechanism. The Orowan equation is given in Equation 2.8 (Liu et al. 2018)

$$\Delta\sigma_{\text{Orowan}} = \frac{\phi G_m b}{d_p} \left(\frac{6V_p}{\pi} \right)^{1/3} \quad 2.8$$

where G_m , b , V_p and d_p are the shear modulus of the matrix, the Burgers vector, the volume fraction, and the size of nanoparticles, respectively and ϕ is a constant. It is evident from the Orowan equation that the smaller the size of dispersed particles in the matrix the higher will be the strengthening effect.

2.7.2.4 Carbon nanotubes (CNT)

The exceptional mechanical and thermal properties of CNT have made them a suitable candidate for reinforcement to develop the composite solder alloy. A study on SAC–CNT composite solder did by Nai, Wei, and Gupta showed that the CNT composite solder has better wettability and dimensional stability over plain SAC solder. The composite solder possesses a lower coefficient of thermal expansion, improved tensile strength, and creep resistance (Nai et al. 2006). Investigation on the addition of single-wall carbon nanotubes (SWCNT) in SAC solders showed a reduction in the size of the secondary phases of the composite solder. The composite solder exhibited enhanced hardness and ultimate tensile strength with an increase in SWCNT wt.% addition but at the cost of the reduction in the solder joint ductility (Kumar et al. 2008). In another study by Nai et al. showed that the addition of CNT in various amounts improves the microhardness and overall strength of the solder matrix and has minimal influence on intermetallic compounds (IMC) growth during the soldering (Nai et al. 2009). Xu et al. studied the effect of CNT addition on electroless nickel-phosphorous under bump metallization for lead-free solder interconnections. The results showed an enhancement in bond strength because of CNT

addition under multiple reflows (Xu et al. 2014b). Investigation on the addition of multi-walled carbon nanotubes (MWCNT) in tin-5 antimony (Sn-5Sb) lead-free solder showed a slight decline in melting temperature of the composite solder alloy. The study also indicates the retardation of IMC growth at Sn-5Sb/copper joint interface under thermal aging (Dele-Afolabi et al. 2015). The effect of CNT addition on the intermetallic formation and shear strength of tin-3.5 silver (Sn-3.5Ag) solder alloy was investigated by Mayappan et al. and the study showed the retardation of Cu_6Sn_5 and Cu_3Sn IMC growth rate and improvement in the joint shear strength with CNT addition (Mayappan et al. 2016). Researchers have made efforts to improve the thermal and electrical properties along with mechanical properties of lead-free solder alloys with CNT addition to make composite lead-free solders more suitable for microelectronic applications. Lee et al. have reported the improvement in thermal conductivity of tin-MWCNT-reinforced tin-58 bismuth (Sn-58Bi) composite solder alloy (Lee et al. 2017). Studies by Kim et al. showed an improvement in electrical conductivity and thermo-mechanical properties for MWCNT/In-Sn-Bi composite solder alloy reflowed on polyethylene terephthalate substrate (Kim et al. 2017). In recent studies, Yang, Liu, and Zhang reported that the addition of CNT refined the solder microstructure and suppressed the IMC thickness at the joint interface. The study also highlights that the improvement in tensile creep resistance of composite Sn-Bi solder is superior to plain solder alloy (Kim et al. 2017).

Increasing the concentration of CNTs in the solder could increase the yield strength and ultimate tensile strength of the composite solder but deteriorate its ductility. Deterioration in solder ductility was attributed to the agglomeration of CNTs, which acted as crack nucleation sites. Excessive addition of CNTs would reduce the solder wettability as the interaction between solder and substrate elements could be severely blocked by excessive CNTs (Huang et al. 2013; Yang et al. 2018). In summary, the addition of CNTs in small weight percent (up to 0.05 wt.%) demonstrated better mechanical, electrical, and thermal properties of composite solder. However excessive addition of CNTs could negatively affect the solder properties.

2.7.3 Surface coating

In addition to the development of lead-free solder alloys, it is equally important to develop a reliable surface finish for the component assembly while using lead-free solders. The conventional copper metallization has been widely used in electronic packaging owing to its good solderability characteristic and excellent thermal conductivity performance. However, lead-free solders cause rapid consumption of Cu to form Sn-Cu intermetallic compounds at the joint interface. The rapid IMC growth develops micro-cracks and Kirkendall void in the IMC layer, which significantly deteriorates the mechanical strength and shock reliability of the solder joint (Peng et al. 2007; Tu and Zeng 2001; Zeng and Tu 2002). Tin-whisker growth is another potential problem for electronic product reliability. Various surface finishes on contact pads are used by researchers and manufacturers to overcome these problems. To retard the interaction between Sn and Cu at the interface, a nickel layer is often deposited on copper metallization which serves as a diffusion barrier at the solder-Cu substrate interface. Typical pad metallizations include electroless nickel immersion gold (ENIG), organic solderability preservative (OSP), Ni–Au, Ni–Pd, immersion Sn (ImSn), immersion Ag (ImAg), etc. In particular, an electroless Ni-P coating is widely used as a surface finish on Cu metallization due to its low cost, excellent solderability, uniformity, corrosion resistance, and simplicity of the process (He et al. 2004; Lin et al. 2010; Sohn et al. 2004). However, the presence of phosphor in Ni-P coating forms additional P-rich layers like Ni₃P and Ni-Sn-P along with Sn-Cu and Ni-Sn IMCs at the interface, which leads to the IMC spalling causing brittle fracture of the joint (Mei et al. 1998; Sohn et al. 2004; Yoon et al. 2007). Studies were done by Wang (2003) and Yoon (2010) (Wang and Liu 2003; Yoon et al. 2010) showed that the use of copper-bearing lead-free solders is an effective way to suppress the formation of P-rich layers at the interface. The presence of Cu in the solder preferentially forms the Cu-Sn intermetallic layer on the Ni₃P layer and significantly retard its growth by slowing down the Ni out-diffusion which further prevents the IMC spalling. The effectiveness of Ni-P coating on Cu substrate in improving the solder joint reliability was observed more pronounced for Cu-bearing lead-free solders over solders without Cu addition (Tseng et al. 2013). The Ni-P coating acts as

a strong diffusion barrier at the joint interface, therefore a thin IMC layer obtain on Ni-P coating compared to bare Cu substrate. The SAC solders generally form a complex $(\text{Cu}, \text{Ni})_6\text{Sn}_5$ IMC layer on Ni-P coated substrate which has lower activation energy than Cu_6Sn_5 IMC layer, hence, the $(\text{Cu}, \text{Ni})_6\text{Sn}_5$ IMC layer is more thermodynamically stable (Laurila et al. 2010a). Besides, the morphology of $(\text{CuNi})_6\text{Sn}_5$ IMC grains is more refined and thin than Cu_6Sn_5 IMC grains, therefore, a thin IMC layer obtain at the joint interface compared to Cu_6Sn_5 IMC layer on Cu substrate (Liu et al. 2009).

2.8 Summary

Soldering is an essential joining process in microelectronic packaging industries. Solder joints attaché the various components on electronic assembly, provides essential electrical continuity, thermal support, and mechanical integrity to the attached components in the assembly. In the light of several environmental and human health concerns over the toxicity of lead (Pb), the restriction on the use of Sn-Pb solders has accelerated the research and development for reliable and high-performing lead-free solders for the electronics packaging industry.

The development of lead-free solders for reliable joints needs a proper understanding of the microstructure evolution of the solder joint and the effect of various factors influencing the electrical, mechanical, thermal, and microstructural properties of the solder. The wettability of the solder on substrate influences the formation of a metallurgical bond between component-solder-substrate interfaces. A thin and uniform intermetallic compound (IMC) layer formation is essential for proper bonding and mechanical strength of the solder joint. However, the excessive growth of the IMC is detrimental to the joint properties. The growth of the IMC layer and coarsening of precipitates in the matrix are the most common problems that affect the performance and reliability of solder joins under different working conditions. Sn-Ag-Cu (SAC) solder alloys are the most preferred lead-free solders for microelectronic packaging applications because of their comparable electrical performance, modest melting point, good solderability, and better mechanical properties and thermal fatigue behavior compared to conventional Sn-Pb solder. The high-Ag content (>3 wt.%) SAC solders have good strength, wettability, and thermal stability

but have a high content of brittle phase (Ag_3Sn) particles in the bulk microstructure and poor drop reliability. The low-Ag (<2 wt.%) bearing SAC solders have good ductility and drop reliability but have low solderability and mechanical strength than high-Ag SAC solders. Therefore, most microelectronic packaging manufacturers need to use different lead-free solders as per the assembly requirement and intended performance.

The performance of the SAC solder can be improved either by alloying or by composite approach. Elemental addition can bring down the melting point of the solder, refine the microstructure, and forms a complex stable IMC layer at the interface. The addition of rare earth elements can reduce the melting point of the solder, improve the wettability, suppress the IMC growth, and improve the ductility, shear strength, and creep resistance of Sn-Ag-Cu solder alloys. However, elemental addition and use of rare earth elements promote the formation of complex brittle precipitates in the microstructure and increases the cost of the solder.

The miniaturization and increased component density in modern electronic devices demand high-performing and reliable lead-free solders. The development of solders for enhanced properties and joint reliability can be achieved with second-phase foreign particulate reinforcement. Considering the size restrictions of the miniature solder joints in modern assemblies, the reactive or non-reactive nanoparticles are the effective and viable options for reinforcement to achieve the desired improvement in the solder properties. The addition of second-phase particles can refine the solder microstructure, suppress the IMC layer growth, and improve the joint strength under different high-temperature working conditions. The ceramic nanoparticles and CNTs adsorb on the IMC surface and grain boundaries, thereby reducing the IMC growth kinetics and refine the microstructure. The dispersion of nanoparticles and refined IMC precipitates strengthen the solder joint. Nickel coating on substrate acts as a good diffusion barrier and slows down the growth rate of IMC layers, which are prone to crack formation. The development of lead-free solders with the addition of non-reactive oxide nanoparticles appears to be the most suitable, efficient, and economical approach.

A better understanding of the influence of varying working conditions on microstructural and mechanical properties of the solder is essential to develop the solder for better performance and joint reliability. The effect of the addition of non-reactive nanoparticles on microstructure and joint strength under different thermal conditions needs to be investigated systematically to optimize the properties of the solder alloy. The effect of various process parameters and their interaction on microstructure development and performance of the solder joint needs to be statistically analyzed for the better prediction of long-term reliability of the solder joint.

Chapter 3 EXPERIMENTAL DETAILS

3.1 Preparation of Solder Nanocomposites

Commercially available binary Sn-3.6Ag, ternary 96.5Sn-3Ag-0.5Cu (SAC305), 99Sn-0.3Ag-0.7Cu (SAC0307), and multicomponent 96.5Sn-3Ag-0.5Cu-0.06Ni-0.01Ge (SAC305-NiGe) (all in wt.%) lead-free solder pastes having the particle size of 30-40 μm and added with mildly activated rosin flux were used as the base alloys for preparation of nanocomposites. The alloy composition for all lead-free solders used in this study is given in Table 3.1. The Al_2O_3 nanoparticles with the average particle size of 20-30 nm (Sisco Research Laboratories Pvt. Ltd. Mumbai, Maharashtra, India) and Multi-walled carbon nanotubes i.e. MWCNT (Chengdu Organic Chemical Co. Ltd. Chinese Academy of Sciences, China) having an inner and outer diameter of about 10 nm and 25 nm, respectively with an average length of 100 to 300 nm, were used for the reinforcement in solders. The scanning electron microscope (SEM, JEOL JSM 6380LA) and transmission electron microscope (TEM, JEOL JEM-2100) images with x-ray diffraction pattern (XRD, JEOL-JPX8) for Al_2O_3 nanoparticles and MWCNT used in this study are shown in Figure 3.1 and Figure 3.2, respectively.

Table 3.1: Lead-free solder alloy composition

Solder name	Alloy composition (wt.%)					Manufacturer
	Sn	Ag	Cu	Ni	Ge	
Sn-3.6Ag	96.4	3.6	--	--	--	Multicore, UK
SAC305	96.5	3.0	0.5	--	--	Persang Alloy Industries, India
SAC0307	99	0.3	0.7	--	--	Persang Alloy Industries, India
SAC305-NiGe	96.5	3.0	0.5	0.06	0.01	Persang Alloy Industries, India

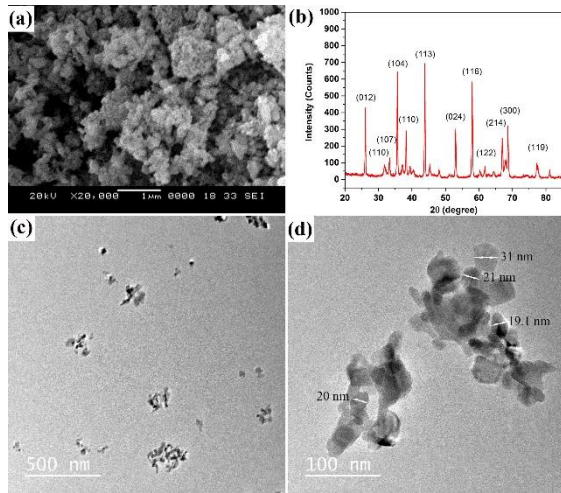


Figure 3.1: (a) SEM image, (b) XRD pattern, (c) TEM image of Al₂O₃ nanoparticles, and (d) TEM image showing the size of Al₂O₃ nanoparticles

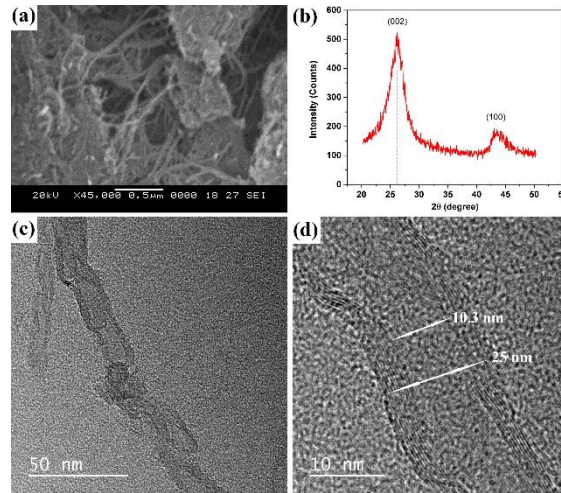


Figure 3.2: (a) SEM image, (b) XRD pattern, (c) TEM image of MWCNT, and (d) TEM image showing the inner and outer diameter of MWCNT strand

The Al₂O₃ nanoparticles and MWCNT were treated with the surfactant-assisted process before blending with the solder paste to prepare nanocomposites. As-procured nanoparticles were first purified in the acid bath (38 wt% HCl) for 30 minutes under ultrasonic agitation to remove any metallic impurities. Nanoparticles were recovered after the centrifuging operation. Cleaned nanoparticles in the desired amounts were uniformly dispersed into the surfactant dissolved solution [1:5 parts of Polyvinylpyrrolidone (PVP-10) surfactant dissolved into Dimethylacetamide (DMAc) solution; Sigma-Aldrich, USA] using ultrasonication for 30 min. The end of the molecular chain of PVP-10 establishes the hydrogen bonding on the surface of the nanoparticle while the molecular chain expands into the DMAc solution and forms a thin adsorption layer around the nanoparticle. The coated layer prevents the agglomeration of nanoparticles by suppressing the attraction between particles (Wu et al. 2018). The colloidal of dispersed nanoparticles were centrifuged for about 30 min to recover the stabilized and surfactant-treated nanoparticles. The paste of the treated nanoparticles in the desired weight percent was mixed with the solder paste to obtain the nanocomposite solder system using mechanical stirring for a minimum of 45 min. The process flowchart of the surfactant treatment of nanoparticles and the preparation of nanocomposites is illustrated in Figure 3.3. The residue of DMAc and

PVP in solder can help as partial protective-film forming agents during the reflow process (Han et al. 2012; Wu et al. 2018). The prepared solder nanocomposite systems are designated hereafter as, solder+ x Al₂O₃ and solder+ x MWCNT, where $x = 0.01, 0.05, 0.1, 0.3,$ and $0.5,$ represents the weight percent concentration of respective nanoparticles added in the solder. Experiments were also conducted with unreinforced solders for comparative analysis.

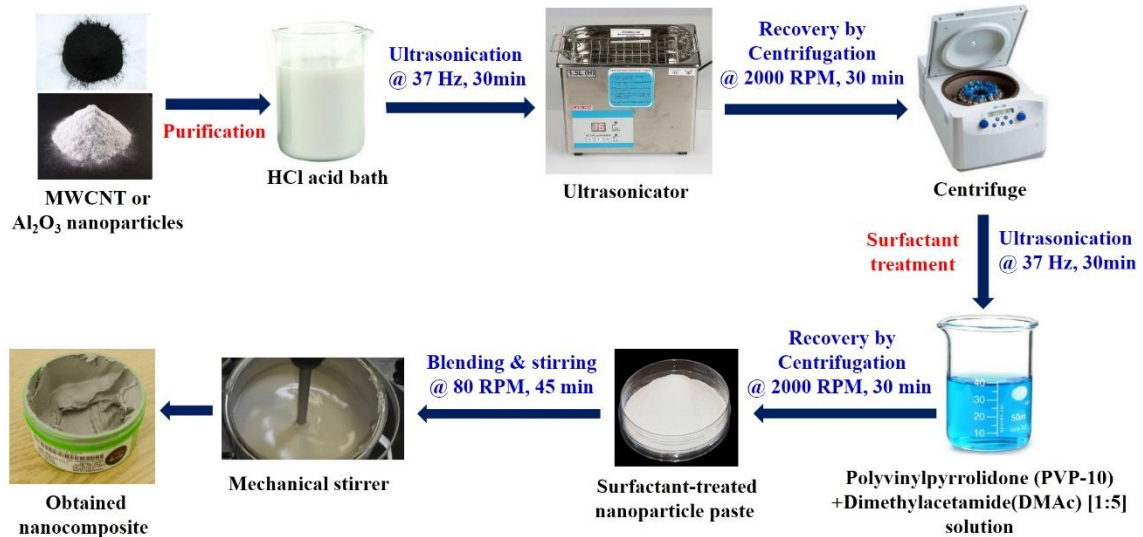


Figure 3.3: Process flowchart for the surfactant treatment of nanoparticles and the preparation of nanocomposites

3.2 Assessment of the Melting Characteristics of Nanocomposites

The effect of the addition of nanoparticles on the melting and solidification behavior of solders was studied using differential scanning calorimetry (DSC, 404 F1 Pegasus NETZSCH). A sample weighed about 15.5 mg was placed in a hermetically sealed aluminum crucible. The lid was punctured to ventilate the gases formed during the healing process. Samples were heated and cooled in the temperature range of 30 °C to 300 °C at the rate of 10 °C/min under the inert N₂ atmosphere. The onset, peak, and end temperatures, pasty range, and undercooling of the different solder nanocomposites were characterized through the heating (endothermic) and cooling (exothermic) curves obtained from the DSC test. The difference between solidus (onset) and liquidus (end) temperatures of the heating

curve gives the pasty range of the solder. The degree of undercooling for different solder compositions was determined through the difference between onset temperatures of heating and cooling curves.

3.3 Preparation of the Solder Joint Assemblies

To assess the shear strength of nanoparticle reinforced solder joints under multiple reflow conditions, a single-lap-shear solder joint was designed and prepared based on literature and standards (ASTM Standards 1999; Crawla et al. 2004; Goh et al. 2015; Hu et al. 2014; Siewert and Handwerker 2002). Figure 3.4 shows the schematic representation for the preparation of a single-lap-shear solder joint used in this study. A 10 mm long, 6 mm wide, and 0.2 mm thick layer of the solder paste was sandwiched between the ends of two pure copper plates each with a dimension of 55 mm (l) \times 6 mm (w) \times 1.5 mm (t) using the mechanical fixture. The samples along with the fixture assembly were heated in an IC reflow oven (PUHUI T-962) shown in Figure 3.5 for the reflow time of 100 s by following the programmed trapezoidal type reflow profile as shown in Figure 3.6 (J-STD-020D.1 2008). A heating rate (ramp-up rate) of about 1.4 °C/s and a cooling rate (ramp-down rate) of about 1.6 °C/s was used in the reflow profile.

Commercial SMT model 2220 capacitors [Syfer Technology, length (L) 5.7 ± 0.04 mm, width (W) 5 ± 0.4 mm, thickness (H) 1.45 ± 0.1 mm, contact terminal width (t) 0.6 ± 0.1 mm with more than 4 mm distance between two contact terminals] were procured from R. S. Components, India and capacitor joint assemblies were prepared as per the general SMT reflow process used in microelectronic industries. Pure (99.9%) EC grade copper substrates (studs with $\Phi 12$ mm \times 8 mm thickness) were polished to obtain a mirror finish surface by following standard metallographic polishing technique. The surface roughness (R_a value) of the substrate was measured using Form Talysurf 50 surface profiler. The surface roughness of substrates was maintained in the range of 0.02-0.04 μm throughout the study. A typical surface roughness profile for the substrates is shown in Figure 3.7. The measured amount of solder paste was placed over the substrate and the capacitor was mounted on the substrate with its metal connectors attached with solder paste. The assembly was reflowed

inside the reflow oven using the programmed reflow cycle. A schematic of the 2220 capacitor component and steps involved in capacitor joint assembly preparation are shown in Figure 3.8 and Figure 3.9, respectively. The reflowed capacitor joint assemblies were used to study the solder joint reliability under varying thermal conditions. Figure 3.10 shows a stereomicroscopic image and the SEM image of a cross-sectional view for actual capacitor joint assembly used in this study.

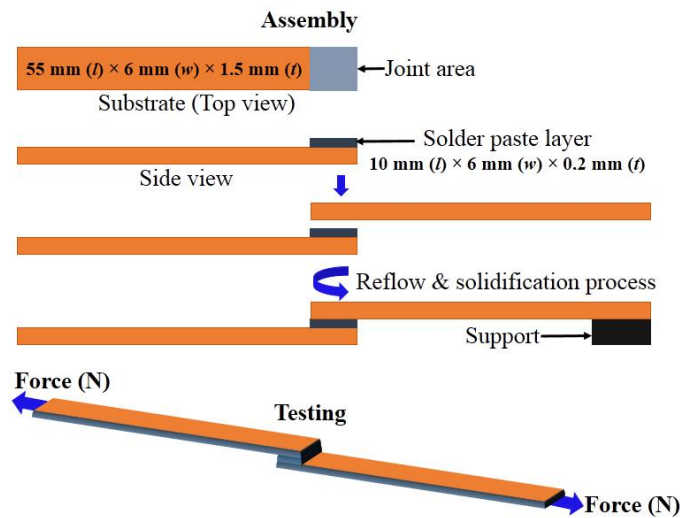


Figure 3.4: A schematic diagram for the preparation of a single-lap-shear solder joint



Figure 3.5: Photograph of an IC Reflow oven

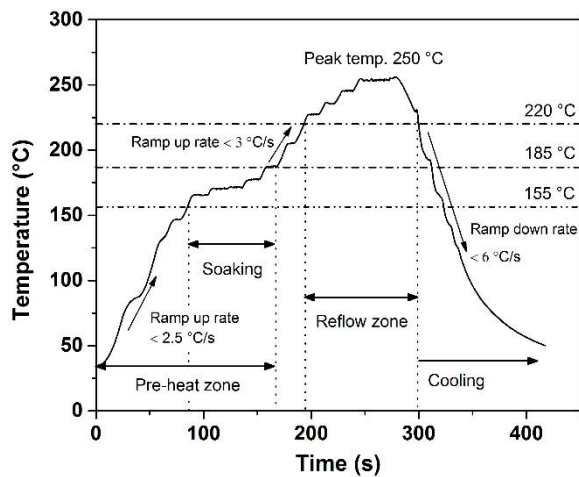


Figure 3.6: Reflow cycle profile

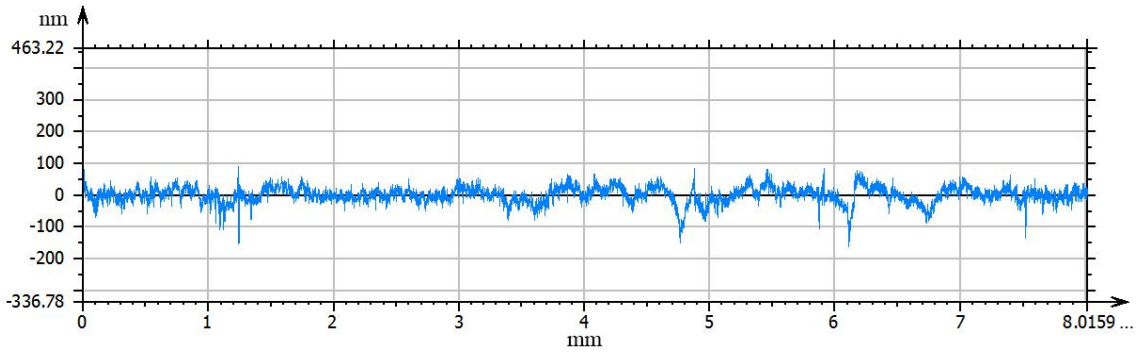


Figure 3.7: Surface roughness profile for the copper substrate

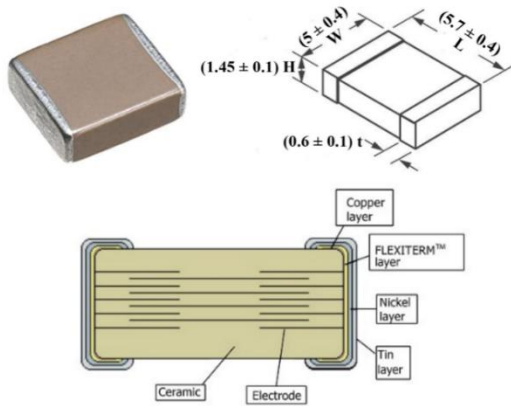


Figure 3.8: SMT 2220 capacitor component with dimensions and structural details

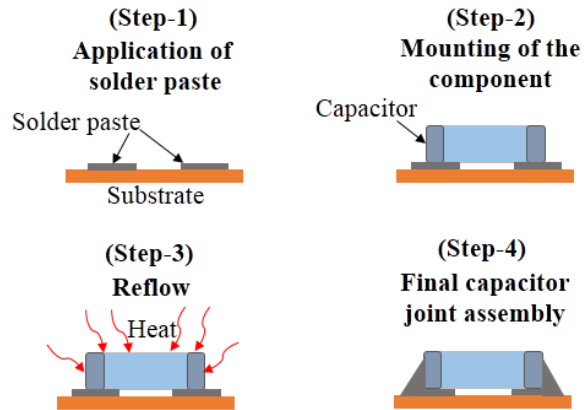


Figure 3.9: Schematics for preparation of capacitor joint assembly

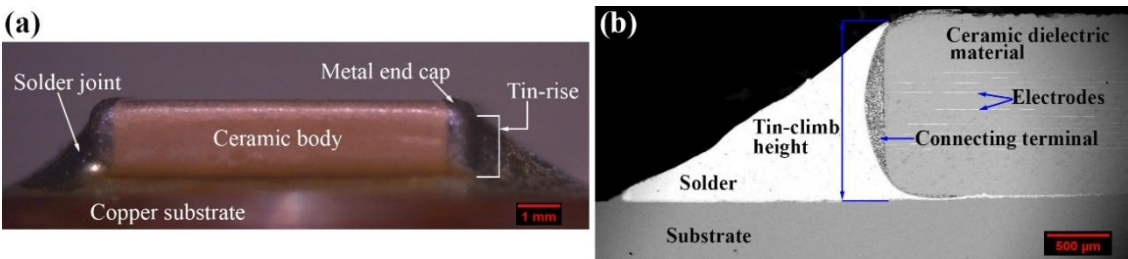


Figure 3.10: 2220-capacitor joint assembly (a) stereomicroscopic image, (b) cross-sectional view of the joint

3.4 Assessment of the Wettability of Nanocomposites

The extent of spreading of the molten solder alloy on the substrate after the reflow process reflects the wettability of the solder. The wettability of plain solders and nanocomposites was determined with respect to the change in the wetting area of reflowed solder samples.

The measured quantity (0.1 gm) of each nanocomposite solder paste was placed on the substrate using a solder dispenser. Samples were reflowed inside the reflow oven using the programmed reflow profile as shown in Figure 3.6. The spreading area of the reflowed sample was captured using the stereomicroscope (Zeiss, STEMI 2000-C) as shown in Figure 3.11. The wetting area was calculated with the help of image analyzer software Axio Vision SE64 Rel. 4.9. The average wetting area for each nanocomposite was determined from the measurement of at least three reflowed samples.

The reflowed capacitor joints showed the rising of the molten solder on the metal connectors of the capacitor assembly, which is known as a tin-climb phenomenon. The tin-climb height on the capacitor terminals reflect the wettability of the solder, hence, the change in tin-climb height was considered to assess the wettability of the select solder nanocomposites. The stereomicroscope and drop shape/contact angle analyzer (KRUSS DSA100) shown in Figure 3.12 were used to capture the images of capacitor joints and tin-climb height was measured using image analyzer software. Figure 3.13 and Figure 3.14 shows the typical spreading of the molten solder on the substrate and tin-climb on capacitor terminals for the reflowed samples, respectively.



Figure 3.11: Photograph of the Zeiss stereomicroscope



Figure 3.12: Photograph of the KRUSS drop shape analyzer

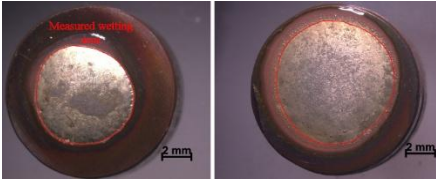


Figure 3.13: Stereomicroscopic images showing wetting area measurement for the reflowed solder samples

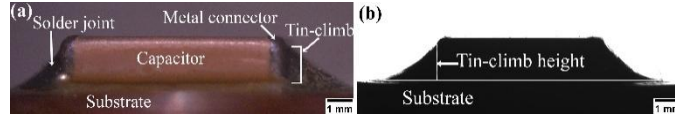


Figure 3.14: (a) Stereomicroscopic image and (b) drop shape analyzer image showing measurement of the tin-climb on reflowed capacitor joint

3.5 Assessment of the Effect of Nanoparticles Addition on Microhardness of Solders

The effect of nanoparticle addition on the bulk hardness of solders was analyzed using Micro Vickers hardness tester (Shimadzu HMV G20ST) as shown in Figure 3.15. Reflowed samples were sectioned and polished for a smooth surface finish. The microhardness testing was carried out with a 50 gf load and 10 s of dwell time. The change in hardness of solders with the addition of MWCNT and Al₂O₃ nanoparticles in different weight percent concentrations was assessed through a minimum of three trials for each solder composition.

3.6 Assessment of the Joint Shear Strength under Multiple Reflow Cycles

The assessment of the effect of multiple reflow cycles on joint shear strength and interfacial microstructure was studied by subjecting the lap-joint samples successively for 1, 2, 4, and 6 reflow cycles. Instron 5967 (30 kN) tensile tester as shown in Figure 3.16 was used for the tensile-shear test of single-lap-shear joint samples with a strain rate of $1 \times 10^{-2} \text{ s}^{-1}$. Stress-strain curves obtained from tensile-shear tests were analyzed to determine the joint shear strength and ductility of nanoparticle reinforced solders under the exposure of multiple reflow cycles.

3.7 Electroless Nickel Coating on Copper Substrate and Specimen Preparation

The polished copper substrates (studs and plates) were first cleaned for rust, oil, and greases in the alkaline bath (Sodium hydroxide in 7.5 g/L conc.) at 70 °C for 15 min using ultrasonic agitation. Specimens were rinsed with distilled water and immersed for about 15 min in the acid bath (10 wt.% HCl) for chemical etching, which removes any residual oxide

films on surfaces. The substrates were rinsed with distilled water and processed further for palladium-free surface activation. To activate the copper surface before electroless nickel plating, an electrolytic nickel strike was used in the bath containing nickel ions (Cotell et al. 1994; Li and An, 2008). Chemically etched specimens were tied to the pure copper wire and placed in the electrolyte dissolved with nickel sulfate. A pure nickel metal plate was attached to the positive terminal (anode) and copper substrates to the negative terminal (cathode) of the DC power supply machine. A small electric voltage was applied (3 V, 0.3 A) across the terminal for about 15 s. This developed an initial high-quality thin nickel coating, which provided a catalytic surface for the initiation of electroless nickel plating. The activated copper substrates were put inside the electroless nickel plating bath for about 8-10 minutes to obtain a uniform and void-free $3.5 \pm 0.25 \mu\text{m}$ thick layer of Ni-P coating on the copper surface with $>13\%$ phosphorus content (Pan et al. 2018). The details of bath composition and operating conditions for electroless Ni-P coating are presented in Table 3.2 (Cotell et al. 1994). Specimens were rinsed with distilled water and air-dried after the desired amount of Ni-P coating was achieved to use further for solder joint assembly preparation. A flowchart for the electroless nickel coating process is shown in Figure 3.17. The SEM image with an EDS plot for electroless Ni-P coating obtained on the copper substrate is shown in Figure 3.18.



Figure 3.15: Photograph of the Shimadzu Micro Vickers hardness tester

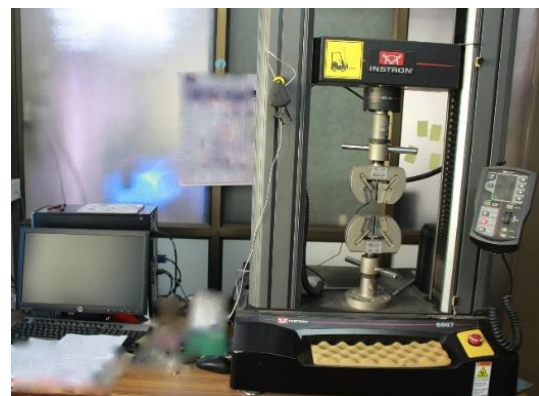


Figure 3.16: Photograph of the INSTRON 5967 tensile testing machine

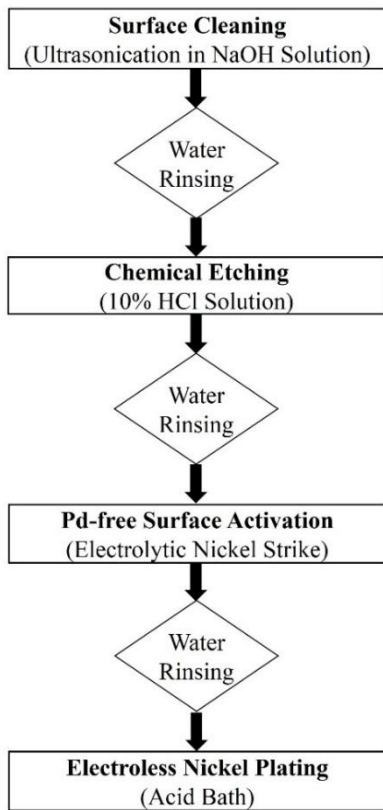


Figure 3.17: Flowchart for the electroless nickel plating process

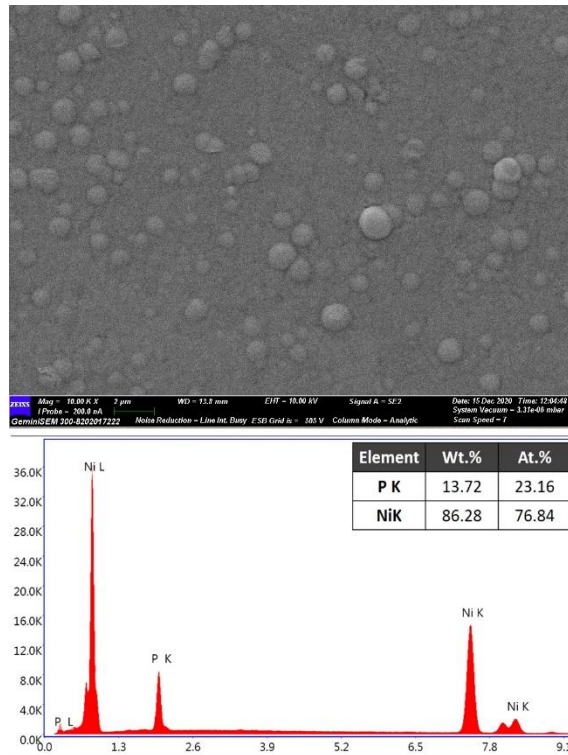


Figure 3.18: SEM micrograph and EDS plot for electroless Ni-P coating on copper substrate

Table 3.2: Electroless nickel coating bath composition and operating conditions

Bath Composition	
Reagent	Concentration
Nickel Sulphate	45 g/L
Sodium Hypophosphite	10 g/L
Amino-Acetic Acid (Glycine)	40 g/L
Acetic Acid	10 g/L
Sodium Hydroxide/HCl	To pH
Operating conditions	
Bath pH	4.5-5.5 (Acidic)
Bath temperature	88-95 °C
Plating rate	0.4 µm/min

3.8 Assessment of the Reliability of the Solder Joint

The performance and reliability of the solder joint for select nanocomposites reinforced with 0.01-0.05 wt.% Al₂O₃ nanoparticles were assessed in terms of the joint shear strength under as-reflowed, thermal shocks, multiple heating cycles, and thermal aging conditions. The capacitor joints were prepared using select nanocomposites with the bare copper and Ni-P coated Cu substrates. The single-lap-shear joint specimens were additionally used to study the shear strength and ductility behavior of joints under different high-temperature environments. Samples were prepared using two successive reflow cycles. Sets of prepared samples were exposed to different high-temperature environments. One set was exposed to 200 heating cycles (Figure 3.19), where the temperature ranges between 25 °C (R.T) to 150 °C. The other set was exposed to thermal shocks consecutively for 200 times, where temperature fluctuated from -15 °C to 150 °C, as shown in Figure 3.20. A combination of the hot plate and the deep freezer was used to achieve the desired environment for thermal shocks. A select solder alloy (SAC0307) and nanocomposites were tested under thermal shocks using cryogenic temperature to study the mechanical performance of developed nanocomposites under cryogenic conditions. The extremely low temperature (-173 °C) was achieved with the help of liquid nitrogen. Three independent sets were subjected to aging at 75 °C, 150 °C, and 200 °C, respectively, for 240 hours inside muffle furnaces. Some specimens were aged at room temperature for 720 hours to compare the performance of the solder joints under different aging conditions. The capacitor assemblies were tested for bond shear strength using Nordson Dage 4000plus bond tester as shown in Figure 3.21 with a 1 μm of tool height from the substrate surface and 200 μm/s of shear tool speed. The obtained shear force data for solder joint failure was used to determine the shear strength of the solder joints. The performance of developed nanocomposites was evaluated in comparison with the performance of solder joints using unreinforced solders and Sn-37Pb solder alloy under different thermal conditions.

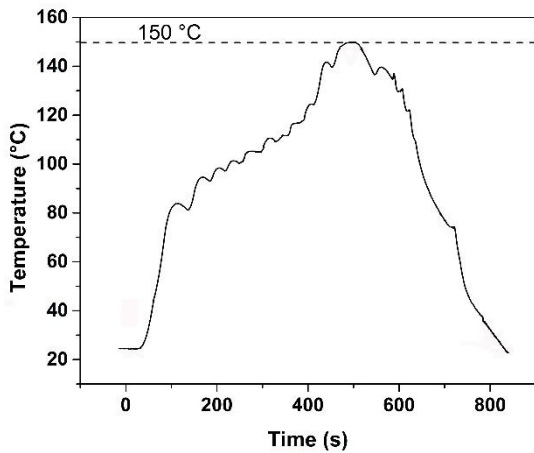


Figure 3.19: Heating cycle profile

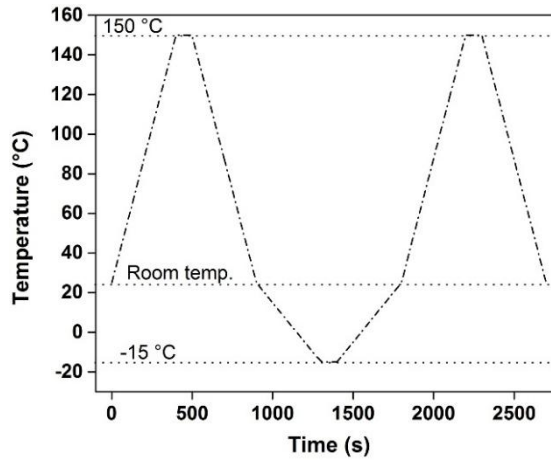


Figure 3.20: Thermal shock profile

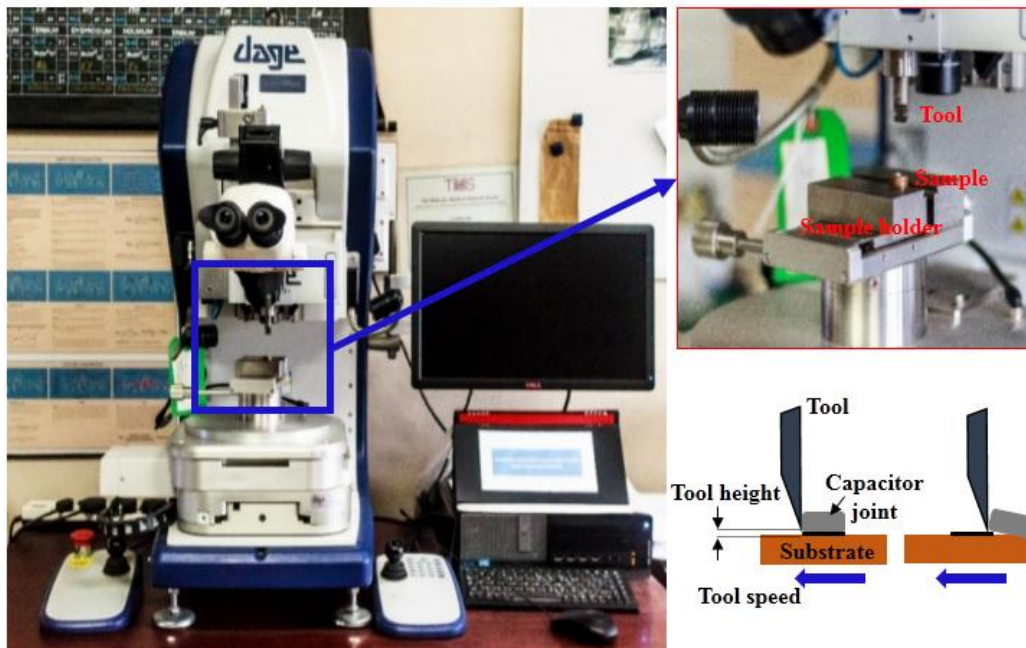


Figure 3.21: Photograph of the Nordson DAGE 4000plus bond tester and schematics for the bond shear testing

3.9 Microstructural Investigation

The effects of nanoparticle addition, multiple reflow cycles, Ni-P coated substrate, and different thermal conditions on microstructure evolution, morphology, and growth of the interfacial intermetallic compounds (IMCs) of the solder joint were studied using scanning electron microscopy. The elemental analysis of different phases in the solder joint was

carried out using energy dispersive spectroscopy (EDS) and X-ray diffraction spectroscopy (XRD). To study the IMC growth at the solder joint interface, reflowed samples were sectioned and polished with the standard metallographic procedure to obtain a highly polished surface. Polished surfaces were etched with 95% methanol (CH₃OH) + 3% hydrochloric acid (HCl) + 2% nitric acid (HNO₃) etchant solution for 1-2 seconds. The IMC layer obtained at the interface was uneven, hence, an average value of IMC thickness was determined by using an Equation 3.1

$$y = A/l \quad 3.1$$

where “y” is the average IMC thickness in μm , A is the area and l is the length of the IMC layer obtained from SEM micrograph. Figure 3.22 shows the representative SEM image of the solder joint interface and schematics for the IMC layer thickness measurement.

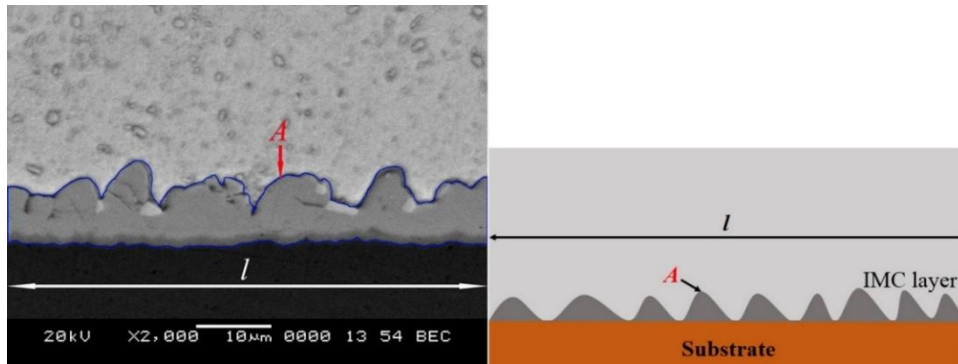


Figure 3.22: Representative SEM micrograph showing the IMC layer thickness measurement for an uneven interfacial IMC layer at the joint interface

3.10 Fractography

The fracture surface analysis reveals the failure characteristics of samples under applied stress and strain conditions. The fractured surfaces obtained after the shear test of different samples under varying thermal conditions were observed under the scanning electron microscope to determine the mode of failure. The different characteristics of fracture surfaces were investigated using SEM and EDS analysis.

Chapter 4 RESULTS

4.1 Melting Parameters of Nanoparticles Reinforced Solder Alloys

The heating (endothermic) and cooling (exothermic) cycle curves from the DSC test for SAC305-NiGe and SAC305-NiGe+0.05Al₂O₃ solder compositions are shown in Figure 4.1. The heating curves for SAC305 solders with different weight percent addition of Al₂O₃ nanoparticles and MWCNT are shown in Figure 4.2. A typical DSC heating curve for SAC305-NiGe solder showed the beginning of the melting point (onset temperature, T_{Solidus}) at 217.92 °C and end temperature (T_{Liquidus}) at 225.61 °C, which indicates the pasty range of about 7.69 °C for the SAC305-NiGe solder alloy. The pasty range for Sn-3.6Ag, SAC0307, and SAC305 solders was obtained at about 6.33 °C, 8.18 °C, and 8.39 °C, respectively. The DSC analysis showed about a 1-2 °C decrease in the onset temperature for the heating curve and an increase in the onset temperature for the cooling curve with the addition of nanoparticles in solders. The peak melting temperature of solders decreased marginally with the addition of MWCNT and Al₂O₃ nanoparticles in the small weight percentages (0.01-0.05 wt.%), whereas the addition of nanoparticles above 0.05 wt.% showed an increase in the melting parameters of solders. The different melting parameters like onset, peak and end temperatures, pasty range, and undercooling for SAC305 solder with the addition of Al₂O₃ nanoparticles and MWCNT in different weigh percent concentrations are shown in Table 4.1 and Table 4.2, respectively. The DSC heating curves appeared to be marginally shifted towards the lower temperature and cooling curves towards the higher temperature for nanocomposites, causing a decrease in the degree of undercooling for the SAC305 solder. A decrease in the degree of undercooling by about 1-4 °C was observed for all solders with the addition of Al₂O₃ nanoparticles and MWCNT in the 0.01-0.5 wt.% concentration range. The Sn-3.6Ag solder showed the highest degree of undercooling, while the SAC0307 solder showed the lowest degree of undercooling among all solder studied. The melting parameters obtained from the DSC test for SAC0307, Sn-3.6Ag, and SAC305-NiGe solders with the addition of Al₂O₃ nanoparticles and MWCNT in varying weight percent are provided in Appendix A. The DSC test for

SAC305-NiGe solder was carried out with only selected nanocomposites reinforced with the Al_2O_3 nanoparticles and not with MWCNT.

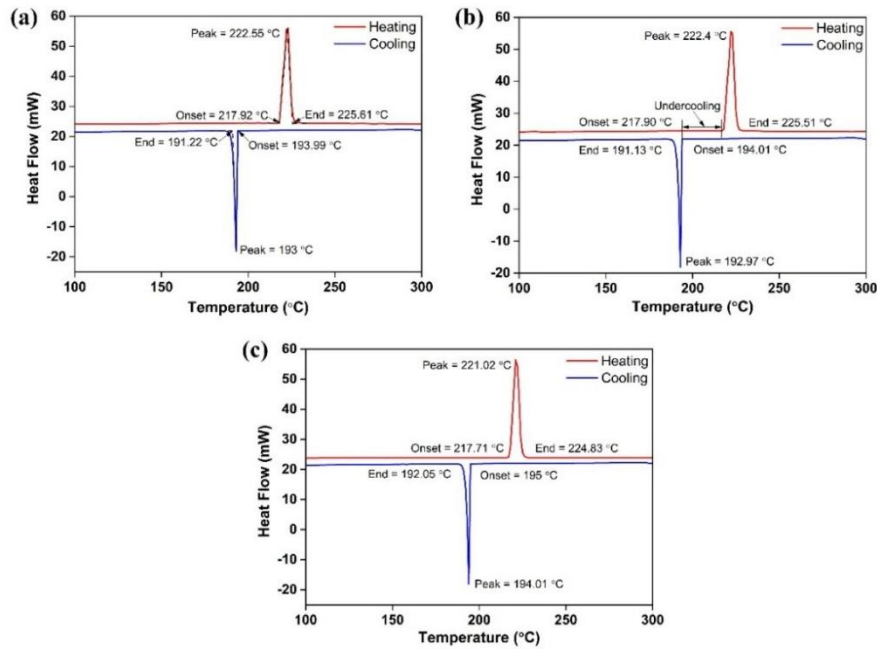


Figure 4.1: DSC heating and cooling curves for (a) SAC305-NiGe, (b) SAC305-NiGe+0.01Al₂O₃, and (c) SAC305-NiGe+0.05Al₂O₃ solder compositions

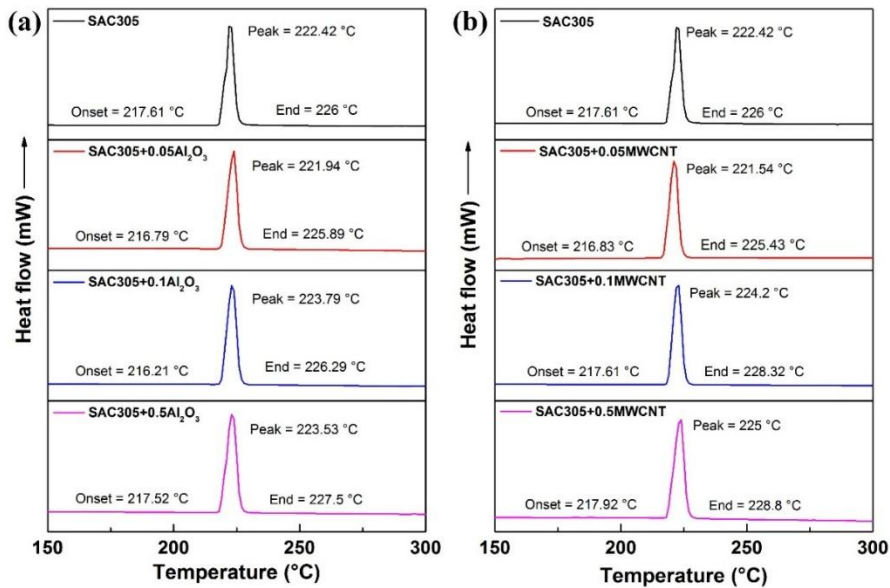


Figure 4.2: DSC heating curves for SAC305 solder with different weight percent addition of (a) Al₂O₃ nanoparticles and (b) MWCNT

Table 4.1: Melting parameters of SAC305 solder with the addition of Al₂O₃ nanoparticles in different weight percent concentrations

Solder Composition	T _{Onset, Heating} (°C) A	T _{Peak, Heating} (°C) B	T _{End, Heating} (°C) C	T _{Onset, Cooling} (°C) D	Pasty Range (°C) (C-A)	Undercooling (°C) (A-D)
SAC305	217.61	222.42	226	193	8.39	24.61
SAC305+0.01Al ₂ O ₃	217.44	222.03	225.29	194.97	7.85	22.47
SAC305+0.05Al ₂ O ₃	216.79	221.94	225.89	196.3	9.1	20.49
SAC305+0.1Al ₂ O ₃	216.21	223.79	226.29	197.55	10.08	18.66
SAC305+0.3Al ₂ O ₃	217.5	223.33	227	197.5	9.5	20
SAC305+0.5Al ₂ O ₃	217.52	223.53	227.5	197.77	9.98	19.28

Table 4.2: Melting parameters of SAC305 solder with the addition of MWCNT in different weight percent concentrations

Solder Composition	T _{Onset, Heating} (°C) A	T _{Peak, Heating} (°C) B	T _{End, Heating} (°C) C	T _{Onset, Cooling} (°C) D	Pasty Range (°C) (C-A)	Undercooling (°C) (A-D)
SAC305	217.61	222.42	226	193	8.39	24.61
SAC305+0.01MWCNT	217.22	221.91	225.82	193.8	8.6	23.42
SAC305+0.05MWCNT	216.83	221.54	225.43	194.35	8.6	22.48
SAC305+0.1MWCNT	217.61	224.2	228.32	195	10.71	22.61
SAC305+0.3MWCNT	217.56	224.69	228.51	195.6	10.95	21.96
SAC305+0.5MWCNT	217.92	225	228.8	195.78	10.88	22.14

4.2 Wettability of Nanocomposite Solders

The stereomicroscopic images of the reflowed samples for the SAC0307 solder with the addition of Al₂O₃ nanoparticles and MWCNT in different weight percent and reflowed on bare copper and Ni-P coated substrate are shown in Figure 4.3, Figure 4.4, and Figure 4.5, respectively. The change in the wetting area as a function of different weight percent addition of Al₂O₃ nanoparticles and MWCNT for different solders is plotted in Figure 4.6 and Figure 4.7, respectively. The spreading area of solders consistently increased with the addition of Al₂O₃ nanoparticles in 0.01-0.5 wt.% concentrations. The percentage increase in the wetting area with the 0.5 wt.% addition of Al₂O₃ nanoparticles was obtained about 29%, 47%, and 55% respectively for Sn-3.6Ag, SAC0307, and SAC305 solders compared

to respective unreinforced solders. The rate of increase in the wetting area was observed higher for the addition of Al_2O_3 nanoparticles in the range of 0.01-0.1 wt.% than 0.3-0.5 wt.% concentrations. The addition of MWCNT in the 0.01-0.05 wt.% concentration range showed an increase in the wetting area, whereas, addition above 0.05 wt.% significantly reduced the wettability of solders. The wetting area for nanocomposites with 0.05 wt.% addition of MWCNT showed about 13%, 32%, and 43% increase for Sn-3.6Ag, SAC0307, and SAC305 solders, respectively, compared to unreinforced solders. The addition of high content i.e. 0.5 wt.% MWCNT showed a decrease in the wetting area by about 30-50% compared to plain solders. The wetting behavior of solders and nanocomposites on Ni-P coated substrate was observed similar to that of the copper substrate. The wettability analysis for SAC305-NiGe solder and select nanocomposites was carried out with the help of tin-climb height instead of spreading area analysis.

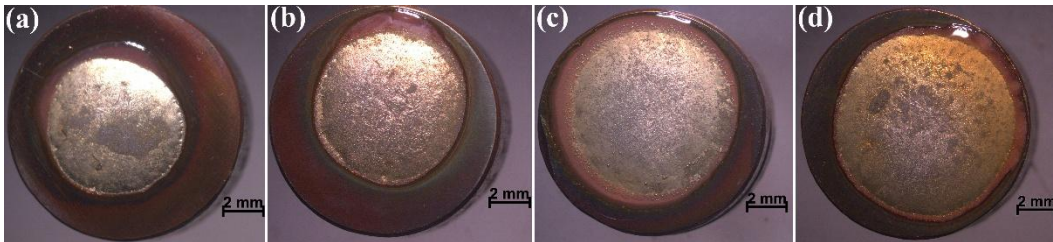


Figure 4.3: Wetting area for (a) SAC0307, (b) SAC0307+0.05 Al_2O_3 , (c) SAC0307+0.1 Al_2O_3 and (d) SAC0307+0.5 Al_2O_3 solder compositions reflowed on bare copper substrate

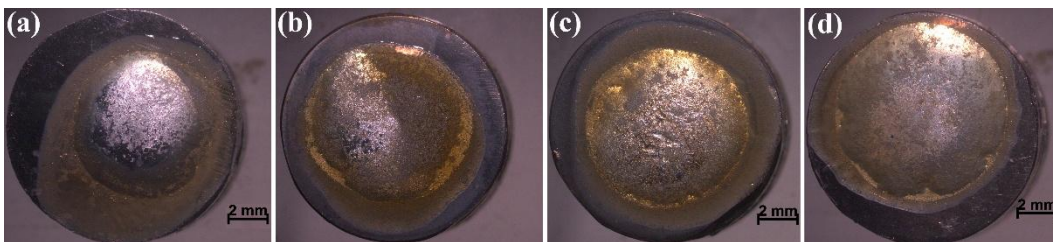


Figure 4.4: Wetting area for (a) SAC0307, (b) SAC0307+0.05 Al_2O_3 , (c) SAC0307+0.1 Al_2O_3 , and (d) SAC0307+0.5 Al_2O_3 solder compositions reflowed on Ni-coated Cu substrate

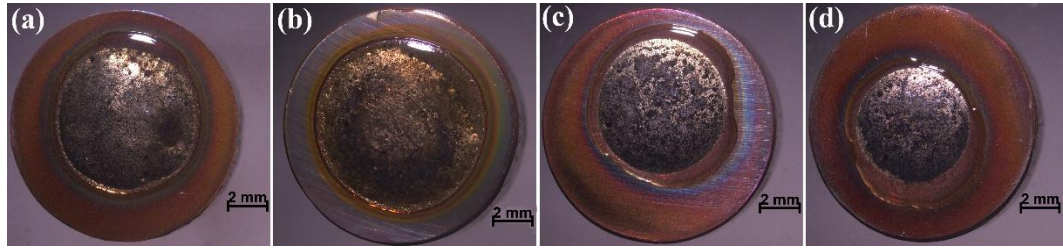


Figure 4.5: Wetting area for (a) SAC307+0.01MWCNT, (b) SAC307+0.05MWCNT, (c) SAC307+0.1MWCNT, and (d) SAC307+0.5MWCNT solder compositions reflowed on bare copper substrate

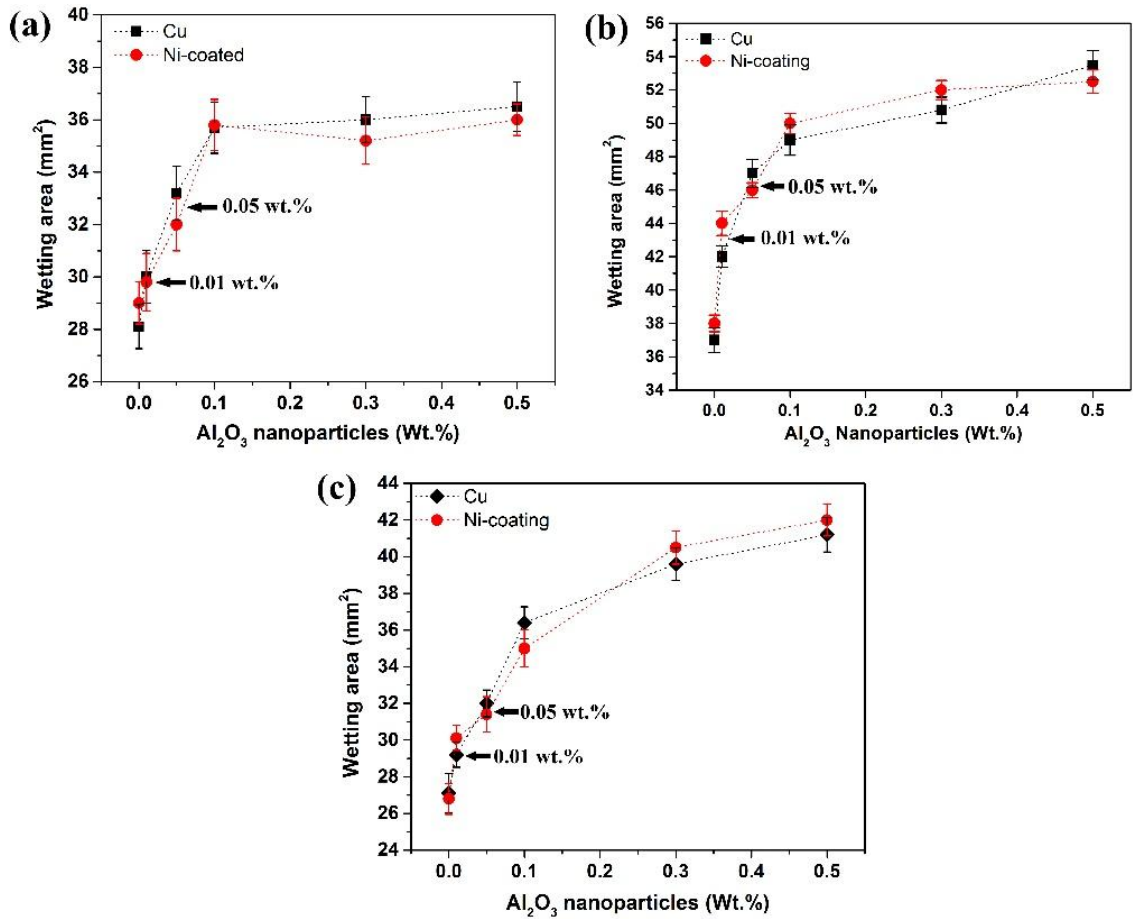


Figure 4.6: Wetting area versus Al₂O₃ nanoparticles concentration addition for (a) Sn-3.6Ag, (b) SAC307, and (c) SAC305 solders reflowed on bare copper and Ni-coated copper substrate

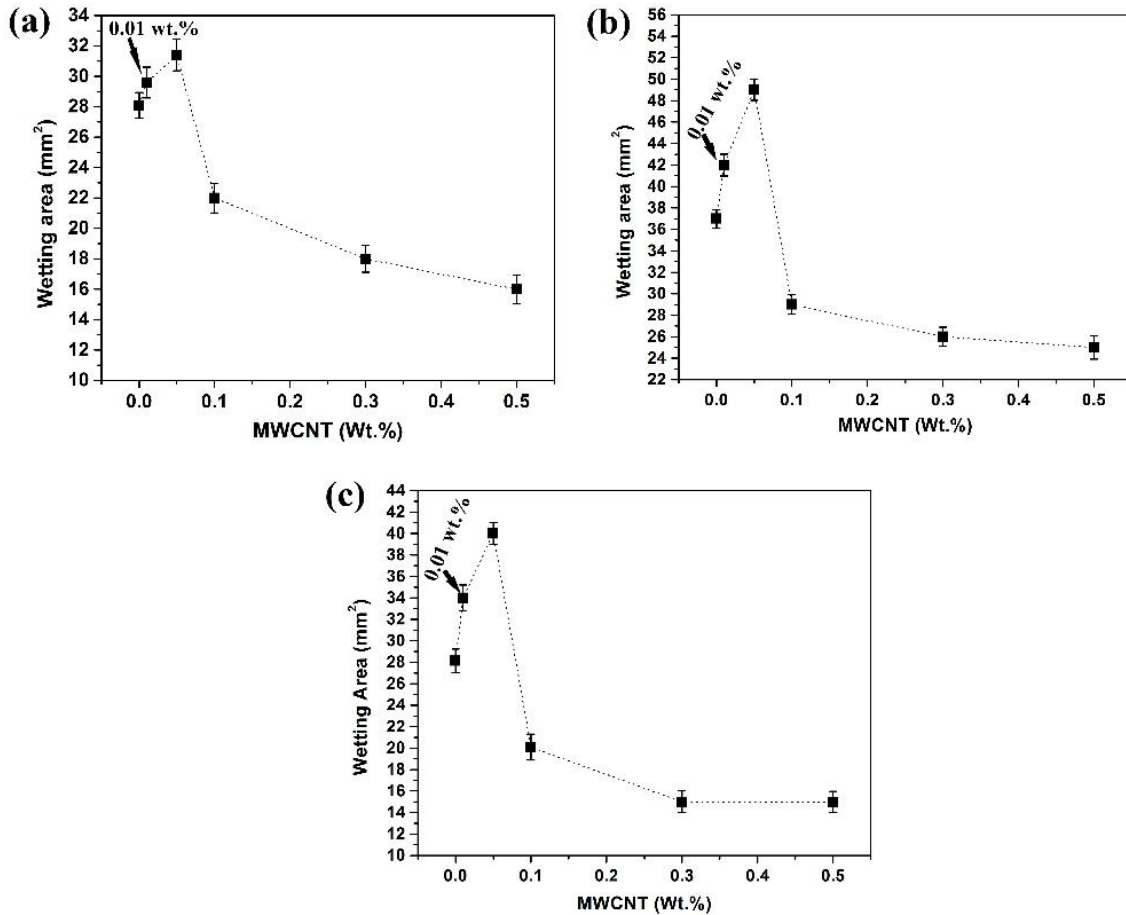


Figure 4.7: Wetting area versus MWCNT concentration addition for (a) Sn-3.6Ag, (b) SAC0307, and (c) SAC305 solders reflowed on bare copper substrate

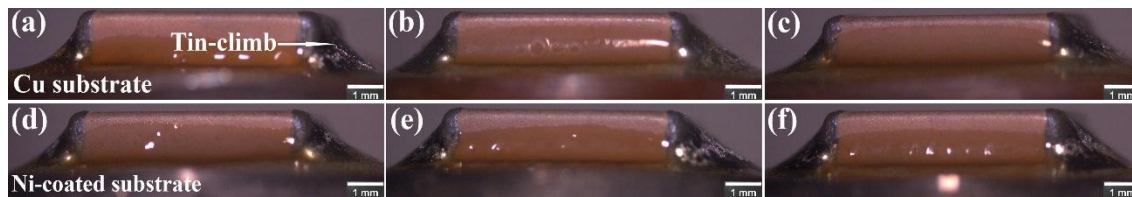


Figure 4.8: The stereomicroscopic images of capacitor samples showing tin-climb on the capacitor terminals for SAC305-NiGe, SAC305-NiGe+0.01Al₂O₃, and SAC305-NiGe+0.05Al₂O₃ solder compositions reflowed on (a), (b), (c) bare copper substrate, and (d), (e), (f) Ni-coated substrate

The tin-climb on capacitor terminals for SAC305-NiGe+0.01Al₂O₃ and SAC305-NiGe+0.05Al₂O₃ nanocomposites reflowed on bare Cu and Ni-coated substrate is shown in Figure 4.8. The measured tin-climb height for SAC0307, SAC305-NiGe, and

SAC305 solders with 0.01-0.05 wt.% concentration addition of Al_2O_3 nanoparticles on bare Cu and Ni-coated Cu substrate is shown with the bar plots in Figure 4.9, Figure 4.10, and Figure 4.11, respectively. The tin-climb height obtained for plain Sn-37Pb solder on the copper substrate is added in Figure 4.11 for comparison. The solder composites reinforced with 0.05 wt.% Al_2O_3 nanoparticles yielded about 36%, 26%, and 20% increase in tin-climb height respectively for SAC0307, SAC305, and SAC305-NiGe solders compared to unreinforced solders. The tin-climb for all the solders and nanocomposites on the Ni-coated substrate was observed nearly similar to that of the bare copper substrate. The tin-climb height for the plain Sn-37Pb solder obtained about 21% higher than unreinforced SAC305 solder; however, nanocomposites with 0.05 wt.% addition of Al_2O_3 nanoparticles showed higher tin-climb than Sn-37Pb solder. The stereomicroscopic images of reflowed samples for different solders and nanocomposites on bare Cu and Ni-coated substrate showing wetting area and tin-climb are provided in Appendix B.

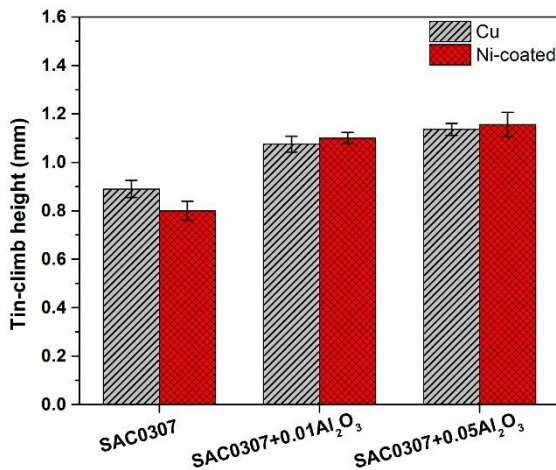


Figure 4.9: Tin-climb height for select nanocomposites of SAC0307 solder reflowed on bare Cu and Ni-coated substrate

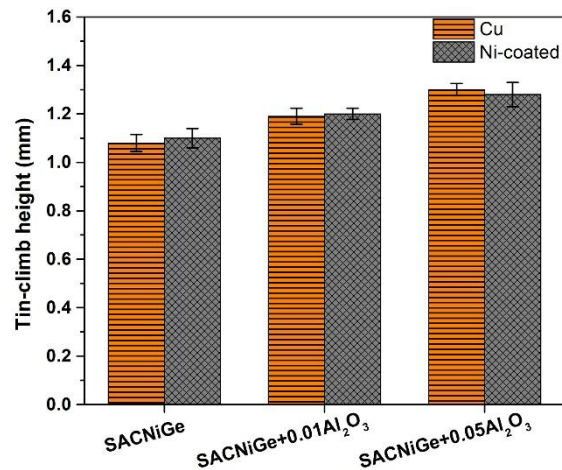


Figure 4.10: Tin-climb height for select nanocomposites of SAC305-NiGe solder reflowed on bare Cu and Ni-coated substrate

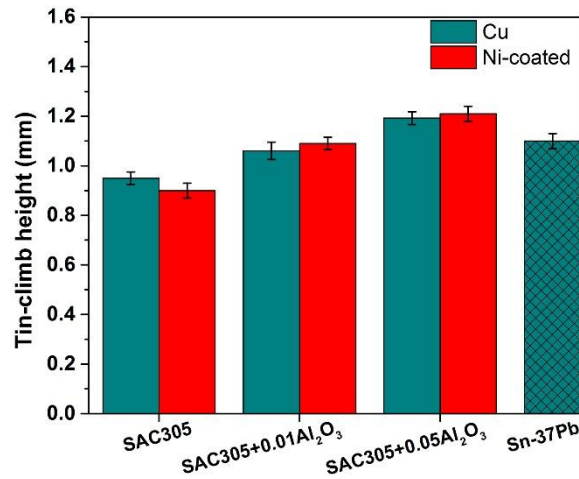


Figure 4.11: Tin-climb height for select nanocomposites of SAC305 solder and plain Sn-37Pb solder reflowed on bare Cu and Ni-coated substrate

4.3 Microstructure Development and Intermetallic Layer Growth at the Solder Joint under Multiple Reflow Cycles

The microstructure development of the solder joint with the addition of Al₂O₃ nanoparticles and MWCNT in different weight percent concentrations for SAC0307 solder on the bare copper substrate under multiple reflow cycles is shown with the SEM micrographs of the joint interface in Figure 4.12 and Figure 4.13, respectively. The SEM micrographs of the solder joint for different nanocomposites with the addition of Al₂O₃ nanoparticles for SAC305 and Sn-3.6Ag solders on the bare copper substrate under multiple reflow cycles are shown in Figure 4.14 and Figure 4.15, respectively. The SEM micrographs of the solder joint with MWCNT reinforced nanocomposites under multiple reflows for SAC305 and Sn-3.6Ag solders are provided in Appendix C. The elemental compositions of different phases in the microstructure were analyzed and confirmed with the EDS analysis. The XRD intensity plot and EDS plots for different phases in the solder joint microstructure are shown in Figure 4.16. The bulk microstructure of the solder joint for all solders mainly consisted of a high volume fraction of a β -Sn matrix with the rod-shaped Ag₃Sn IMC particles dispersed in it. The Cu₆Sn₅ IMC layer was predominantly formed at the solder/Cu substrate interface. A second IMC layer i.e. Cu₃Sn formed between the copper substrate and Cu₆Sn₅ IMC layer for the solder joints exposed beyond 2 reflow cycles.

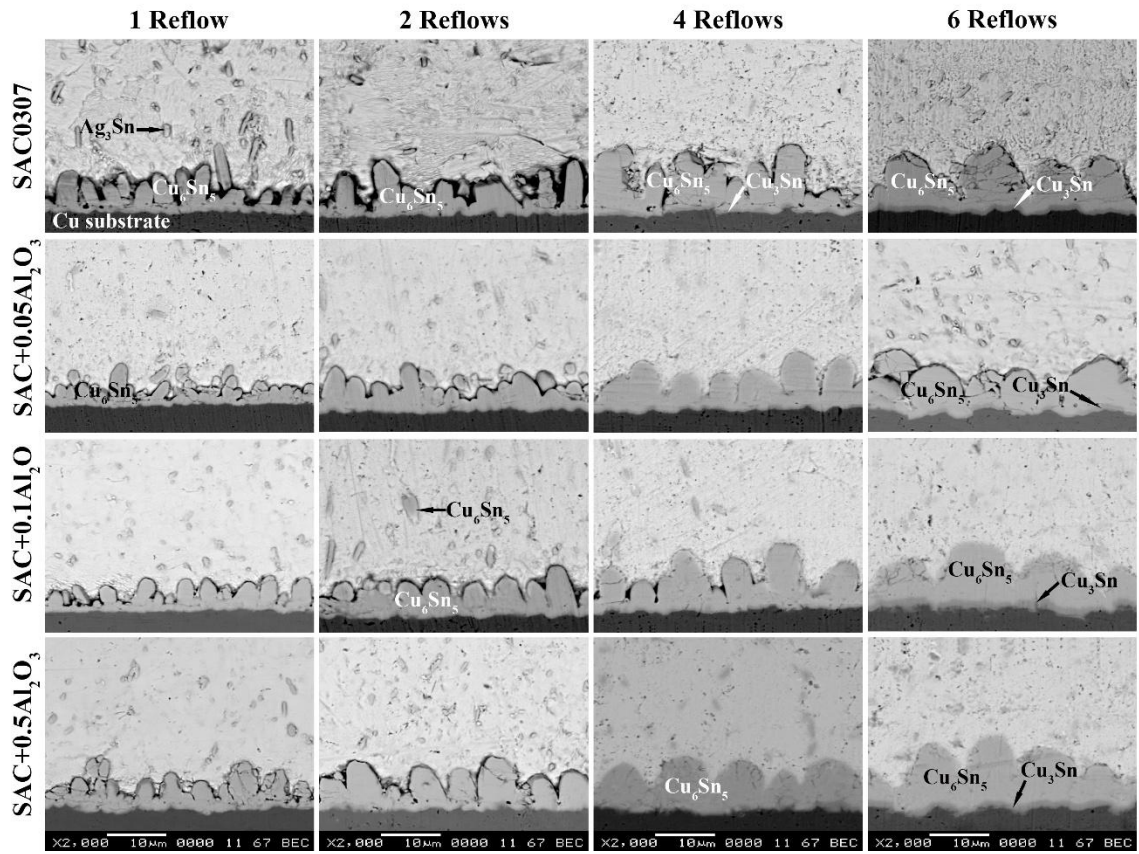


Figure 4.12: SEM micrographs of the joint interface for SAC0307 solder with the addition of Al₂O₃ nanoparticles in different weight percent concentrations on the copper substrate under multiple reflow cycles

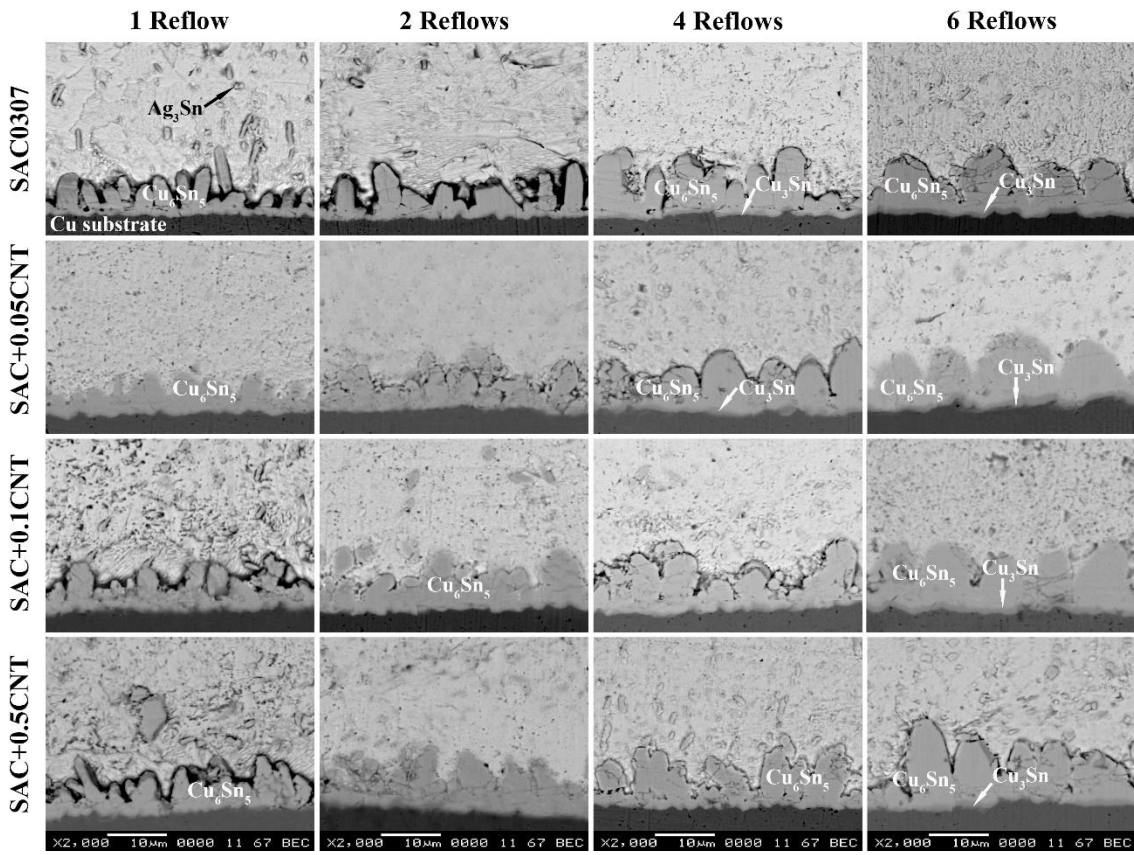


Figure 4.13: SEM micrographs of the joint interface for SAC0307 solder with the addition of MWCNT in different weight percent concentrations on the copper substrate under multiple reflow cycles

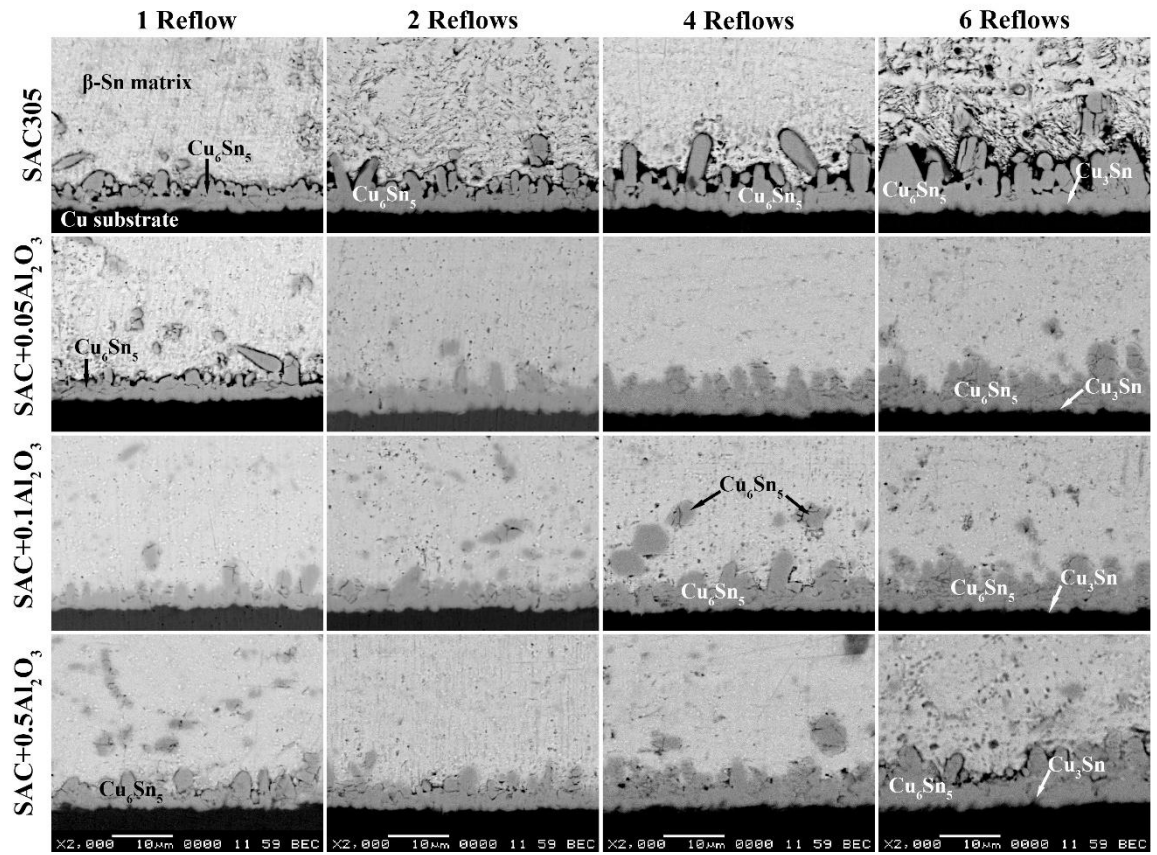


Figure 4.14: SEM micrographs of the joint interface for SAC305 solder with the addition of Al₂O₃ nanoparticles in different weight percent concentrations on the copper substrate under multiple reflow cycles

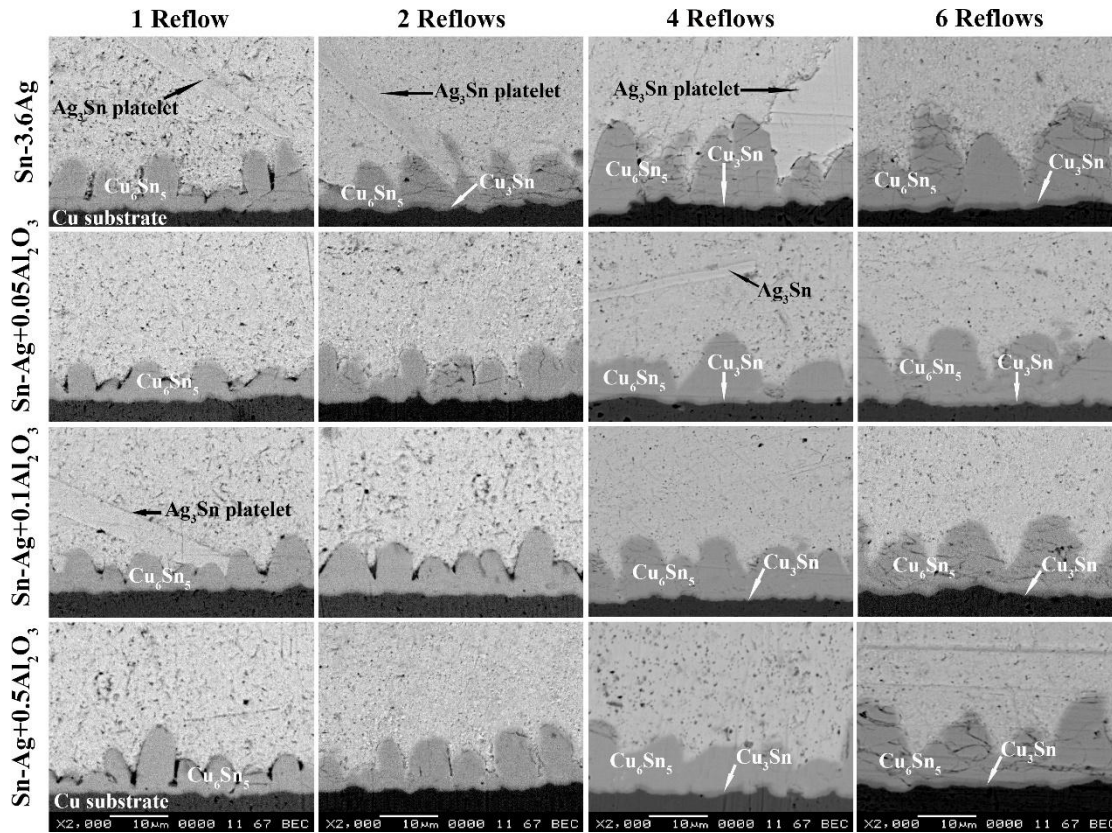


Figure 4.15: SEM micrographs of the joint interface for Sn-3.6Ag solder with the addition of Al₂O₃ nanoparticles in different weight percent concentrations on the copper substrate under multiple reflow cycles

The morphology of Cu₆Sn₅ IMC layer for the unreinforced SAC0307 solder joint was columnar in shape and became coarser scallop-shaped with the increase in the reflow cycles. The Cu₆Sn₅ IMC layer for SAC305 solder was found to be long-columnar and became thick and coarse with multiple reflow cycles. The unreinforced Sn-3.6Ag solder joint showed a coarser scallop-shaped Cu₆Sn₅ IMC layer formation at the joint interface and very large Ag₃Sn IMC platelets in the solder matrix compared to SAC305 and SAC0307 solders. The Ag₃Sn IMC precipitates appeared rod/fiber shaped for the SAC305 solder joint. The Ag₃Sn and Cu₆Sn₅ IMC particles in the matrix of the SAC0307 solder joint were appeared small and finer in shape compared to SAC305 and Sn-3.6Ag solders. A noticeable discontinuous Cu₃Sn IMC layer was formed between the Cu₆Sn₅ IMC layer and copper substrate after 4 reflows and appeared as a continuous layer after 6 reflows. In

the case of Sn-3.6Ag solder samples, the Cu_3Sn IMC layer formation was observed from 2 reflow cycles. The Ag_3Sn and Cu_6Sn_5 IMC precipitate in the matrix became coarser on exposure to multiple reflows. The SAC305-NiGe solder properties were only studied for the assessment of joint reliability under the influence of varying thermal conditions for select nanocomposites reinforced with only 0.01-0.05 wt.% Al_2O_3 nanoparticles, therefore the influence of multiple reflow cycles on microstructure development of SAC305-NiGe solder is not considered in this section.

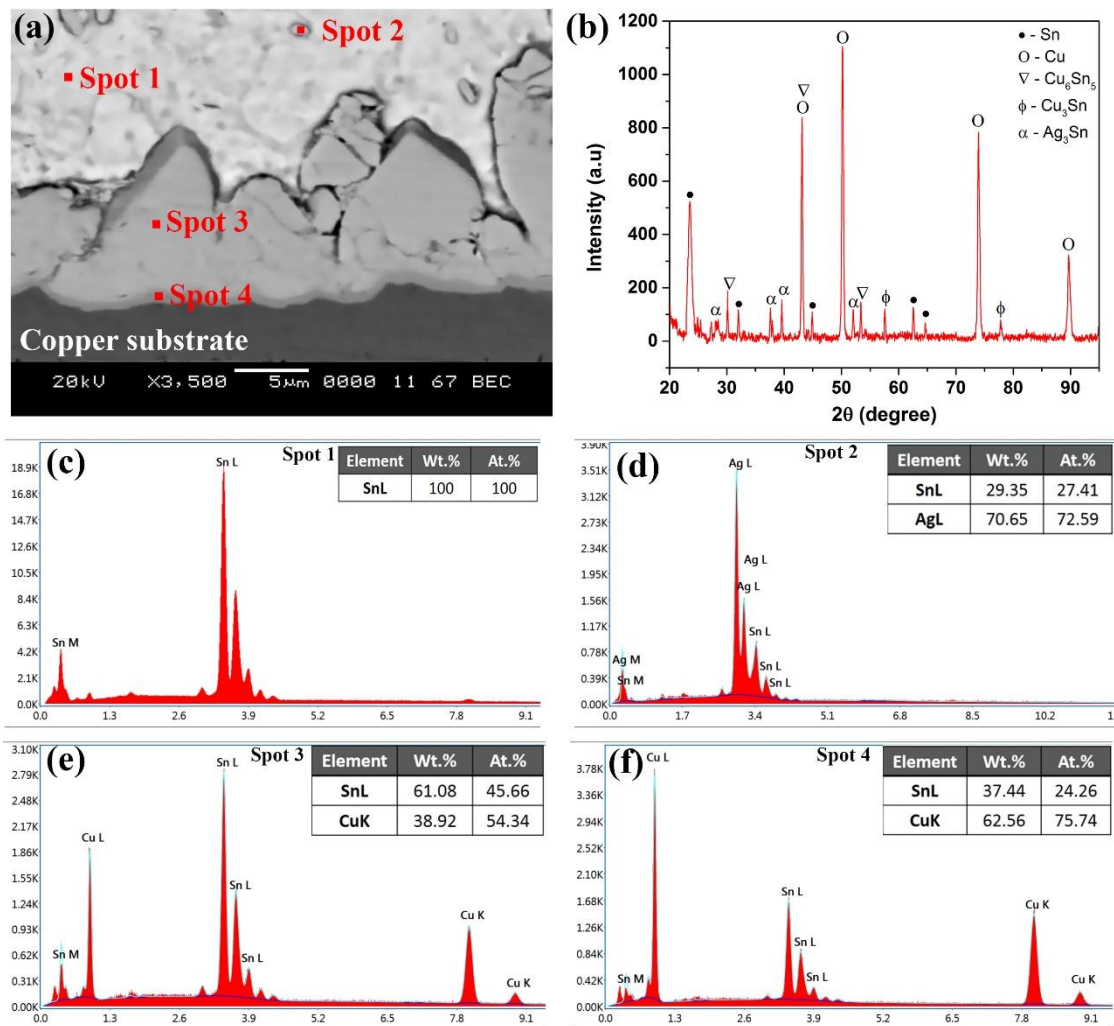


Figure 4.16: (a) SEM micrograph showing different IMCs at the solder joint interface, (b) XRD plot showing peaks for different IMCs at the joint interface, EDS plot and elemental compositions for, (c) β -Sn matrix, (d) Ag_3Sn , (e) Cu_6Sn_5 , and (f) Cu_3Sn IMC

The addition of Al_2O_3 nanoparticles in solder resulted in microstructure refinement and suppression of the IMC layer at the joint interface. The morphology of the IMC layer appeared more uniform, thin, and planar in shape for nanocomposite joints compared to unreinforced solder joints. The Al_2O_3 nanoparticles in small weight percentages i.e. 0.01-0.05 wt.% addition were found to be more effective in suppressing Cu_6Sn_5 IMC layer growth at the interface and refining the IMC precipitates in the matrix. The addition of 0.05 wt.% nanoparticles being the most effective in microstructure refinement and IMC suppression under multiple reflow cycles. The rod/fiber shaped Ag_3Sn IMC particles in the SAC305 solder joint matrix transformed into fine spheroidal particles with the addition of 0.05 wt.% Al_2O_3 nanoparticles. The extent of refinement in Ag_3Sn particles was measured up to 75%, while the area of Cu_6Sn_5 IMC precipitates was reduced by about 68% in the matrix. The SEM images showing the refinement of Ag_3Sn and Cu_6Sn_5 IMC particles in the bulk matrix of the SAC305 solder joint with the addition of Al_2O_3 nanoparticles are shown in Figure 4.17.

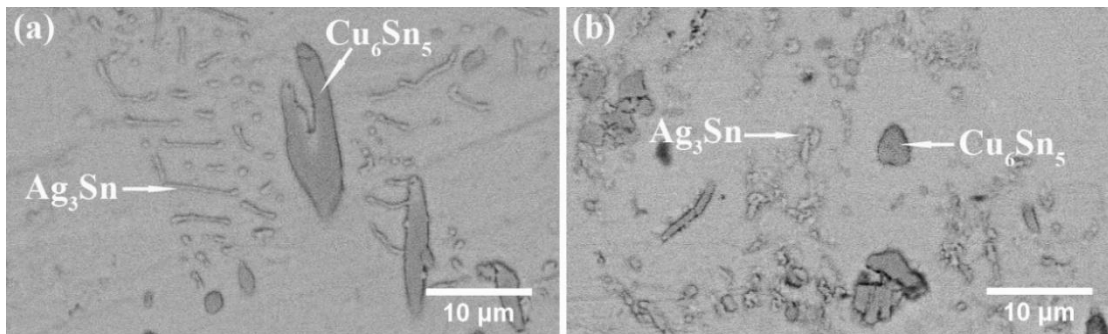


Figure 4.17: Cu_6Sn_5 and Ag_3Sn IMC precipitates in solder matrix for (a) unreinforced SAC305 solder and (b) SAC305+0.05 Al_2O_3 nanocomposite

The measured interfacial IMC thickness for SAC0307, SAC305, and Sn-3.6Ag solders with varying weight percent addition of Al_2O_3 nanoparticles and MWCNT under multiple reflow cycles is plotted in Figure 4.18, Figure 4.19, and Figure 4.20, respectively. In comparison with the SAC305 and SAC0307 solder nanocomposites, samples with Sn-3.6Ag solder showed about 50-70% higher IMC thickness under multiple reflow cycles. The IMC thickness for SAC0307+0.05 Al_2O_3 composite samples was obtained about 20% less compared to the unreinforced SAC0307 solder joint. The addition 0.05 wt.% Al_2O_3

nanoparticles resulted in about 19% and 13% reduction in Cu_6Sn_5 IMC thickness at the joint interface for SAC305 and Sn-3.6Ag solders, respectively. The effectiveness of small weight percent addition of Al_2O_3 nanoparticles on IMC retardation was observed even after 6 reflow cycles. The IMC layer at the interface for nanocomposite was obtained about 2 μm thinner compared to plain solder joints after 6 reflow cycles for all solders. However, the addition of high content i.e. >0.05 wt.% concentration of Al_2O_3 nanoparticles showed a decline in the effectiveness of the nanoparticle reinforcement on the microstructure refinement and IMC suppression. The addition of 0.5 wt.% Al_2O_3 nanoparticles resulted in about 14% and 7% reduction in IMC thickness for SAC0307 and SAC305 solders under multiple reflows, whereas, the high content of Al_2O_3 nanoparticles was ineffective in IMC retardation for Sn-3.6Ag solder under higher reflow cycles.

The addition of MWCNT in 0.05 wt.% yielded about 10-16% reduction in IMC thickness for SAC0307 solder joint under multiple reflows. The IMC retardation with the addition of 0.05 wt.% MWCNT for SAC305 and Sn-3.6Ag solders was about 14% and 10%, respectively. The increase in MWCNT addition beyond 0.05 wt.% was found to be ineffective in IMC retardation for all solders. The degree of refinement in Ag_3Sn precipitates and IMC layer suppression with nanoparticle addition for Sn-3.6Ag solder was achieved lesser compared to SAC305 and SAC0307 solders. The addition of Al_2O_3 nanoparticles and MWCNT in high weight percent was less effective in achieving any microstructure refinement and IMC suppression under higher reflow cycles. However, the effectiveness of Al_2O_3 nanoparticles addition on microstructure development was superior compared to MWCNT under multiple reflow cycles.

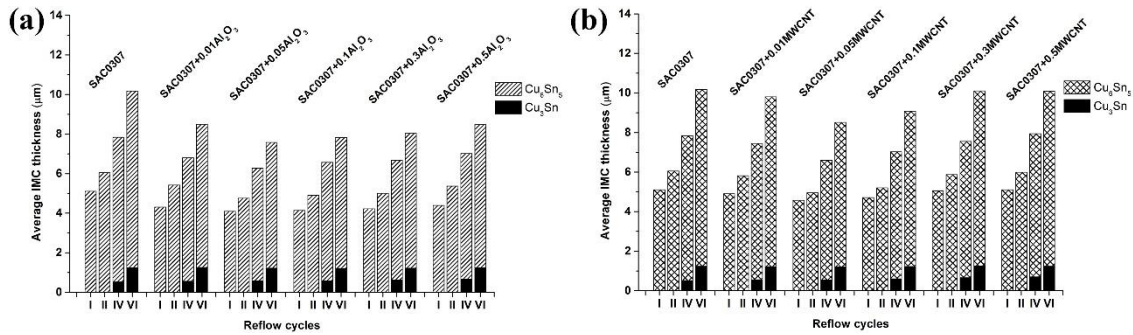


Figure 4.18: IMC thickness under multiple reflow cycles for SAC0307 solder joint on the copper substrate with different weight percent addition of, (a) Al_2O_3 nanoparticles and (b) MWCNT

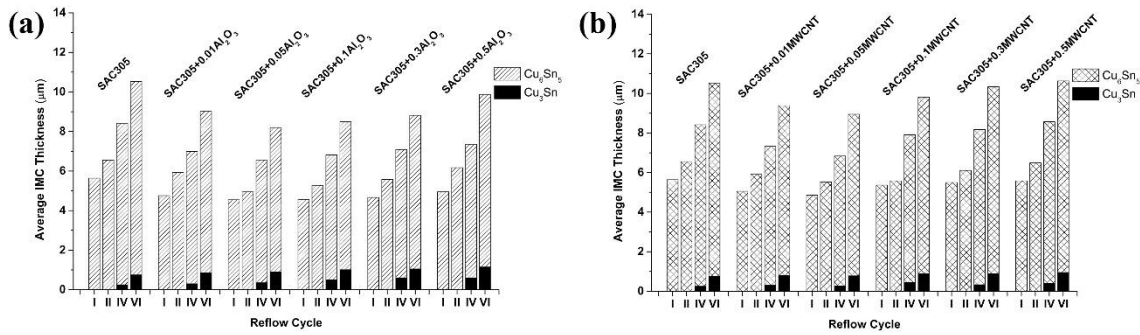


Figure 4.19: IMC thickness under multiple reflow cycles for SAC305 solder joint on the copper substrate with different weight percent addition of, (a) Al_2O_3 nanoparticles and (b) MWCNT

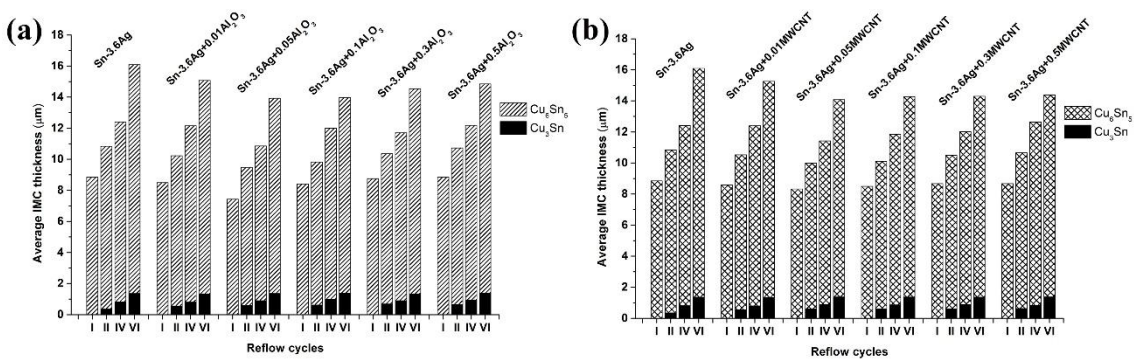


Figure 4.20: IMC thickness under multiple reflow cycles for Sn-3.6Ag solder joint on the copper substrate with different weight percent addition of, (a) Al_2O_3 nanoparticles and (b) MWCNT

4.4 Microhardness, Joint Shear Strength and Ductility of Nanocomposites under Multiple Reflow Cycles

The microhardness of the as-reflowed solder alloys with the addition of Al₂O₃ nanoparticles and MWCNT in different weight percent is tabulated in Table 4.3. The microhardness of solders increased with the increase in weight percent addition of nanoparticles. The data showed an increase in microhardness by about 53% for SAC0307, 20% for SAC305, and 25% for Sn-3.6Ag solder was achieved with the addition of 0.5 wt.% Al₂O₃ nanoparticles. The 0.5 wt.% addition of MWCNT resulted in about 59%, 31%, and 33%, increase in microhardness for SAC0307, SAC305, and Sn-3.6Ag solder, respectively. SAC305-NiGe+0.05Al₂O₃ nanocomposite solder showed about a 13% increase in the hardness compared to unreinforced solder. The microhardness for plain conventional Sn-37Pb solder was found to be 11.5 HVN.

Table 4.3: Microhardness of different solders with varying weight percent addition of Al₂O₃ nanoparticles and MWCNT

Solder composition	Microhardness (VHN)								
	Al ₂ O ₃ nanoparticles					MWCNT			
	Concentration (wt.%)								
	0	0.01	0.05	0.1	0.5	0.01	0.05	0.1	0.5
SAC0307	9.8	10.4	11.1	12.4	15	9.9	11.6	13.8	15.6
SAC305	13.8	14.3	15.6	15.9	16.6	14.2	14.8	16.6	18.1
Sn3.6Ag	13.4	13.7	14.5	15.3	16.8	13.6	14.4	16.0	17.8
SAC305-NiGe	14.3	15.1	16.2	--	--	--	--	--	--
Sn-37Pb	11.5	--	--	--	--	--	--	--	--

The average shear strength of the lap-shear solder joint under multiple reflow cycles for SAC0307, SAC305, and Sn-3.6Ag solders with the addition of Al₂O₃ nanoparticles and MWCNT in different weight percent is shown in Figure 4.21, Figure 4.22, and Figure 4.23, respectively. The joint shear strength for nanocomposites with small weight percent addition of nanoparticles was significantly higher than the unreinforced solders. The joint strength for all the solder compositions was observed increasing with the second reflow

and decreased with higher reflow cycles. Samples reflowed with 2 reflow cycles for nanocomposite with 0.05 wt.% Al_2O_3 nanoparticles content showed about a 53% increase in the joint strength for SAC0307 solder and about 12% increase for SAC305 and Sn-3.6Ag solders, respectively. The addition of a high concentration (0.5 wt.%) of Al_2O_3 nanoparticles showed a slight increase in the joint strength for SAC0307 solder; however, shear strength decreased by about 12-14% for SAC305 and Sn-3.6Ag solder joints under multiple reflow cycles. The improvement in the joint shear strength with the addition above 0.05 wt.% of Al_2O_3 nanoparticles was less significant compared to nanocomposites with small weight percent addition. The addition of 0.05 wt.% MWCNT increased the joint strength by about 21%, 18%, and 10% for SAC0307, SAC305, and Sn-3.6Ag solders, respectively. The high content (0.5 wt.%) addition of MWCNT caused a decrease in the joint shear strength by about 7% for SAC0307 solder, 25% for SAC305 solder, and about 27% for Sn-3.6Ag solder compared to unreinforced solders under multiple reflow cycles.

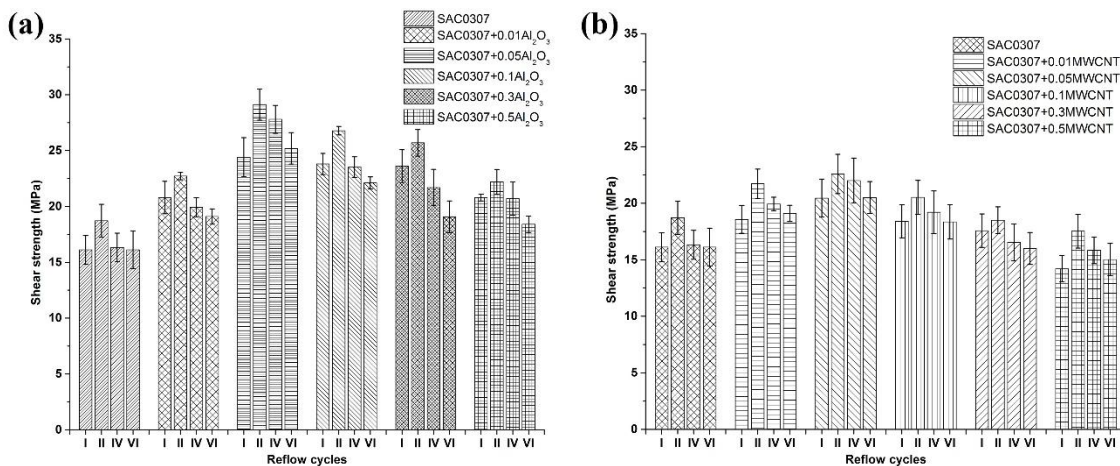


Figure 4.21: Joint shear strength under different reflow cycles for SAC0307 solder on Cu substrate with varying weight percent addition of (a) Al_2O_3 nanoparticles and (b) MWCNT

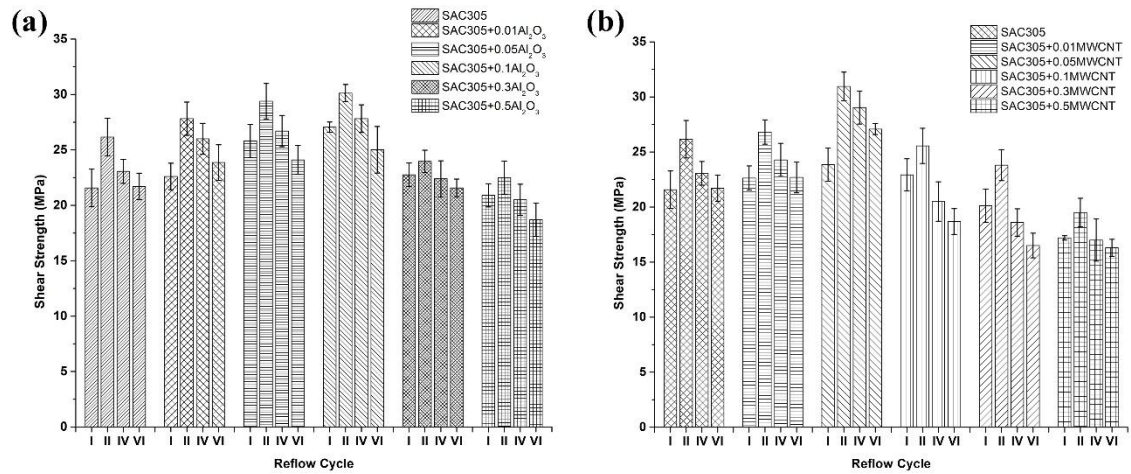


Figure 4.22: Joint shear strength under different reflow cycles for SAC305 solder on Cu substrate with varying weight percent addition of (a) Al_2O_3 nanoparticles and (b) MWCNT

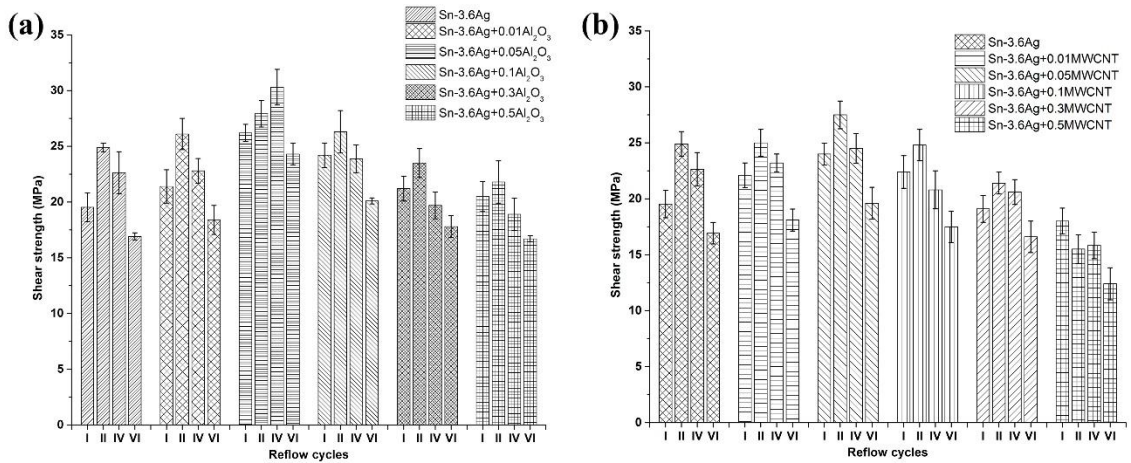


Figure 4.23: Joint shear strength under different reflow cycles for Sn-3.6Ag solder on Cu substrate with varying weight percent addition of (a) Al_2O_3 nanoparticles and (b) MWCNT

The ductility of the joint for different nanocomposites is reflected in the stress-strain curves obtained from the tensile-shear test of the single-lap joints. The stress-strain curves for different nanocomposites of SAC0307, SAC305, and Sn-3.6Ag solder samples reflowed with 2 reflow cycles are shown in Figure 4.24, Figure 4.25, and Figure 4.26, respectively. The percentage failure strain and work of fracture (WOF) for different solders and nanocomposites are tabulated in Table 4.4. The work of fracture (WOF) was determined

by calculating the area under the stress-strain curve for different solder composites. The stress-strain curves for nanocomposite samples with a small weight percentages (0.01-0.05 wt.%) addition of Al_2O_3 nanoparticles showed an increase in the joint failure stress and strain values, whereas the addition above 0.05 wt.% decreased the failure strain of the joint. Compared to unreinforced solder, the failure strain for nanocomposites with 0.05 wt.% Al_2O_3 nanoparticles showed about 16%, 27%, and 13% increase for SAC0307, SAC305 and Sn-3.6Ag solders, respectively. The increase in failure strain implies an improvement in the ductility of the joint. The increase in work of fracture and failure strain was observed prominent for nanocomposite samples with only 0.01-0.05 wt.% Al_2O_3 nanoparticles addition. The MWCNT addition in small weight percent has a marginal effect on increasing the failure strain and work of fracture of the joint. The addition of Al_2O_3 nanoparticles and MWCNT above 0.05 wt.% showed a reduction in the failure strain of the joint. The high content of MWCNT (>0.05 wt.%) significantly reduced the failure strain and WOF of the joint for all solders, which indicates a significant decrease in ductility of the joint. The degree of decrease in the joint ductility with a higher content of nanoparticles was observed lesser for Al_2O_3 nanoparticles compared to MWCNT. Amongst all solders studied, the failure strain was found to be highest for SAC0307 solder and lowest for Sn-3.6Ag solder.

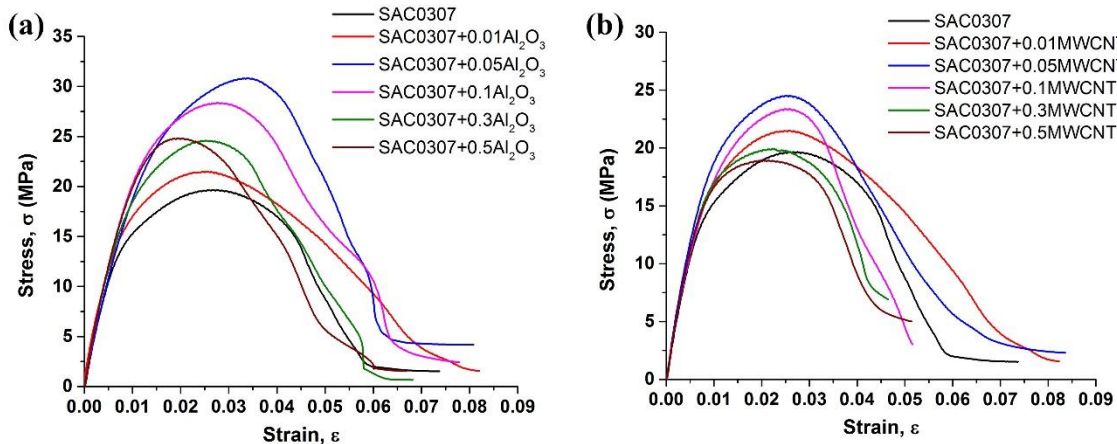


Figure 4.24: Stress-strain curves for SAC0307 solder with varying weight percent addition of (a) Al_2O_3 nanoparticles and (b) MWCNT

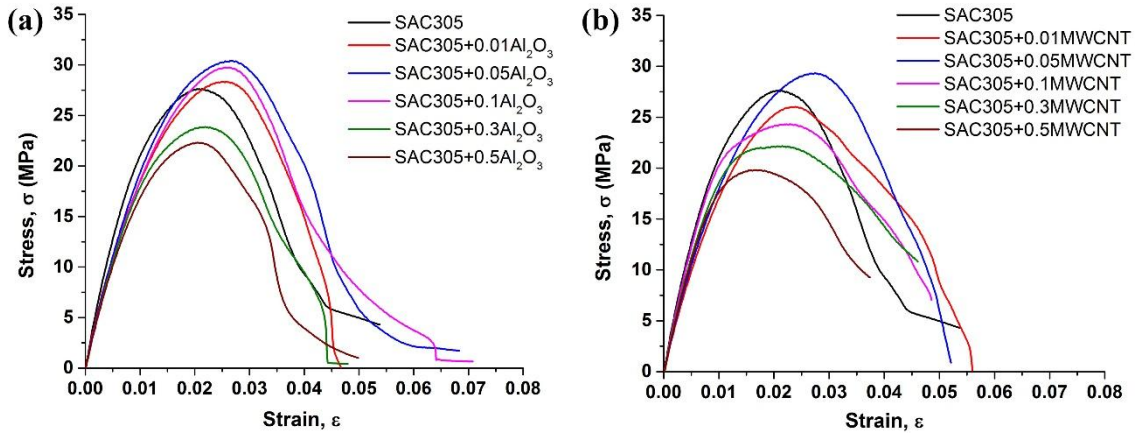


Figure 4.25: Stress-strain curves for SAC305 solder with varying weight percent addition of (a) Al_2O_3 nanoparticles and (b) MWCNT

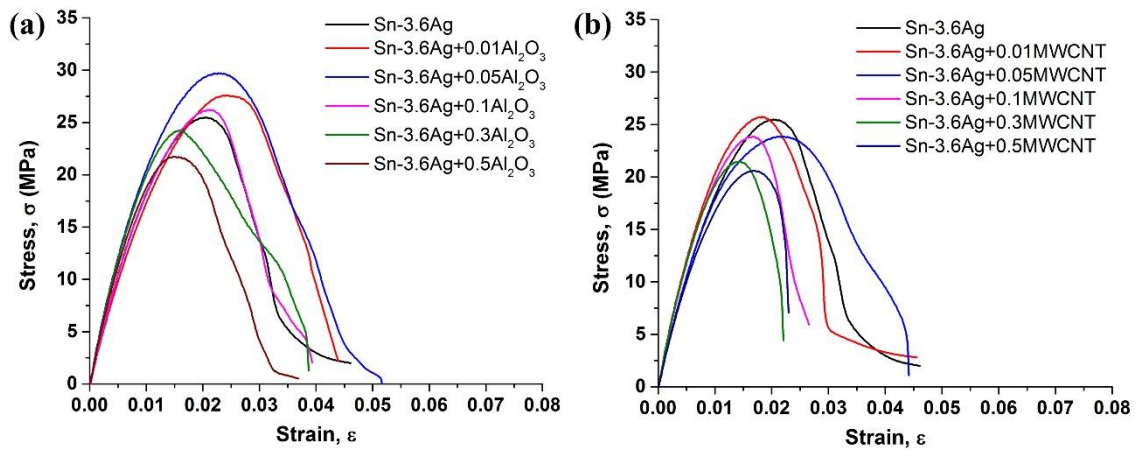


Figure 4.26: Stress-strain curves for Sn-3.6Ag solder with varying weight percent addition of (a) Al_2O_3 nanoparticles and (b) MWCNT

Table 4.4: Failure strain and work of fracture (WOF) for different solder nanocomposites

Solder composition	Failure Strain (%)	Work Of Fracture (WOF) (MJ/m ³)
SAC0307	7.34	0.852
SAC0307+0.01Al ₂ O ₃	8.19	1.086
SAC0307+0.05Al ₂ O ₃	8.04	1.430
SAC0307+0.1Al ₂ O ₃	7.77	1.308
SAC0307+0.5Al ₂ O ₃	6.68	0.923
SAC0307+0.01MWCNT	8.15	1.078
SAC0307+0.05MWCNT	8.32	1.089
SAC0307+0.1 MWCNT	5.15	0.813
SAC0307+0.5 MWCNT	5.11	0.68
SAC305	5.36	0.87
SAC305+0.01Al ₂ O ₃	4.65	0.886
SAC305+0.05Al ₂ O ₃	6.81	1.07
SAC305+0.1Al ₂ O ₃	6.42	1.037
SAC305+0.5Al ₂ O ₃	4.98	0.624
SAC305+0.01MWCNT	5.59	0.951
SAC305+0.05MWCNT	5.21	1.008
SAC305+0.1 MWCNT	4.85	0.859
SAC305+0.5 MWCNT	3.73	0.556
Sn-3.6Ag	4.59	0.622
Sn-3.6Ag +0.01Al ₂ O ₃	4.38	0.789
Sn-3.6Ag +0.05Al ₂ O ₃	5.17	0.894
Sn-3.6Ag +0.1Al ₂ O ₃	3.93	0.616
SAC305+0.5Al ₂ O ₃	3.68	0.447
Sn-3.6Ag +0.01MWCNT	4.55	0.603
Sn-3.6Ag +0.05MWCNT	4.42	0.7139
Sn-3.6Ag +0.1 MWCNT	2.65	0.42
Sn-3.6Ag +0.5 MWCNT	2.29	0.337

The effect of Al₂O₃ nanoparticles and MWCNT addition in different weight percent on melting behavior, wettability, microstructure development, joint shear strength, and ductility of Sn-3.6Ag, SAC0307, and SAC305 solders under multiple reflow cycles was thoroughly reviewed. The effectiveness of 0.01 wt.% and 0.05 wt.% addition of Al₂O₃ nanoparticles in developing the thermal, physical, microstructural, and mechanical properties of SAC0307 and SAC305 solders was found to be optimum. In the view of the development of low-silver content lead-free solders for improved solder joint performance

and viability in microelectronics packaging applications, more focus was given to the development of SAC0307 solder with small weight percent addition of Al_2O_3 nanoparticles in further study. The performance and reliability of SAC305 solder with the addition of the Al_2O_3 nanoparticles were assessed to study the development of high-silver content SAC305 solder with nanoparticles addition and to compare the performance of developed SAC0307 solder against the performance of most preferred SAC solder. The development of SAC305-NiGe super solder with the addition of Al_2O_3 nanoparticles was studied to investigate the effect of the addition of Ni, Ge elements, and Al_2O_3 nanoparticles in trace amounts on microstructure development and joint reliability of the SAC solder.

The addition of MWCNT in developing the thermal, physical, microstructural, and mechanical properties of solder was found to be less effective compared to Al_2O_3 nanoparticles and hence, the addition of MWCNT in solders was not considered for joint reliability assessment study. After considering the high IMC growth rate, poor ductility, and marginal effect of Al_2O_3 nanoparticles and MWCNT addition on improvement in Sn-3.6Ag solder properties, further study on joint reliability of Sn-3.6Ag solder was not considered.

4.5 Solder Joint Microstructure on Cu and Ni-P Coated Substrate for Al_2O_3 Nanoparticle Reinforced Select Nanocomposites under Different Thermal Conditions

A typical microstructure and IMC layer formation at the capacitor terminal/solder interface and terminal/substrate interface of the reflowed capacitor joint with SAC305 and Sn-37Pb solder alloys on bare Cu and Ni-P coated substrate is shown in Figure 4.27. The EDS investigation confirmed the formation of $(\text{Cu}, \text{Ni})_6\text{Sn}_5$ IMC layer at the connector/solder interface, Cu_6Sn_5 IMC layer at the solder/Cu substrate interface, and the $(\text{Cu}, \text{Ni})_6\text{Sn}_5$ IMC layer at the solder/Ni-coated substrate interface.

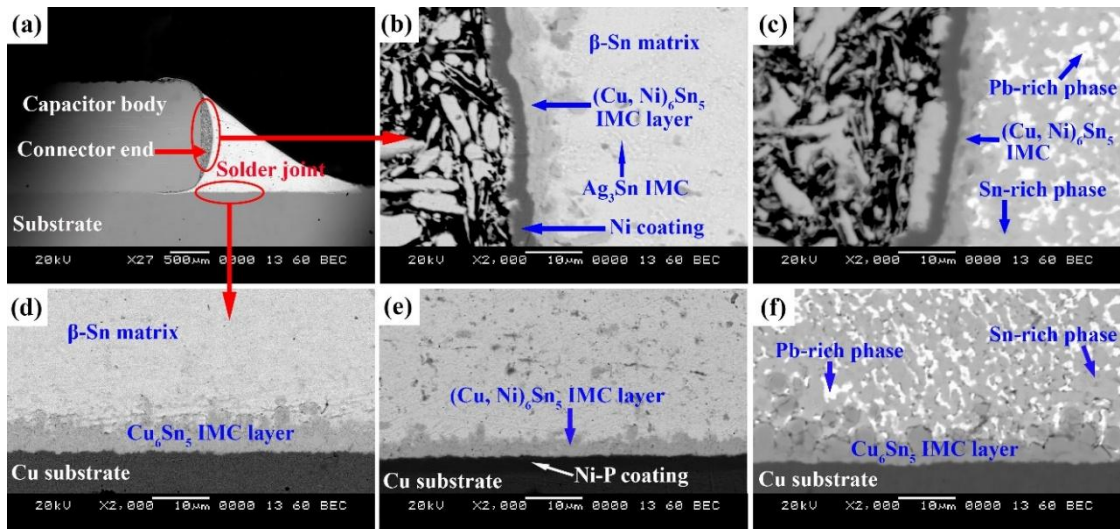


Figure 4.27: SEM micrographs of capacitor assembly, (a) cross-sectional view showing the microstructure of the capacitor joint, (b) magnified region of terminal/SAC305 solder interface, (c) magnified region of terminal/Sn-37Pb solder interface, and interfacial microstructure for (d) SAC305/Cu substrate, (e) SAC305/Ni-P coating, and (f) Sn-37Pb/Cu substrate

The interfacial microstructure development and IMC growth on bare Cu and Ni-P coated substrate under different thermal conditions for the select weight percent Al_2O_3 nanoparticle reinforced SAC305 solder nanocomposites are shown in Figure 4.28. The IMC layer composition, morphology, and growth at the joint interface were different on a nickel-coated substrate compared to the bare copper substrate. The Cu_6Sn_5 IMC layer was predominantly formed on the solder/Cu substrate interface, whereas a complex $(\text{Cu}, \text{Ni})_6\text{Sn}_5$ IMC formed on the solder/Ni-coated substrate interface. The elemental compositions of different IMCs developed on the SAC305-solder/Ni-coated substrate interface were analyzed and confirmed by the EDS analysis as shown in Figure 4.29. The microstructure development and IMC growth for plain Sn-37Pb solder under different thermal conditions on bare Cu substrate are shown by SEM micrographs in Figure 4.30. In the case of Sn-Pb solder, the Cu_6Sn_5 IMC layer was scallop in shape and became thick and planar under high-temperature aging conditions. The Cu_3Sn IMC layer appeared thick and continuous. The IMC thickness for the Sn-37Pb solder joint under aging was found to be very high compared to all SAC solders.

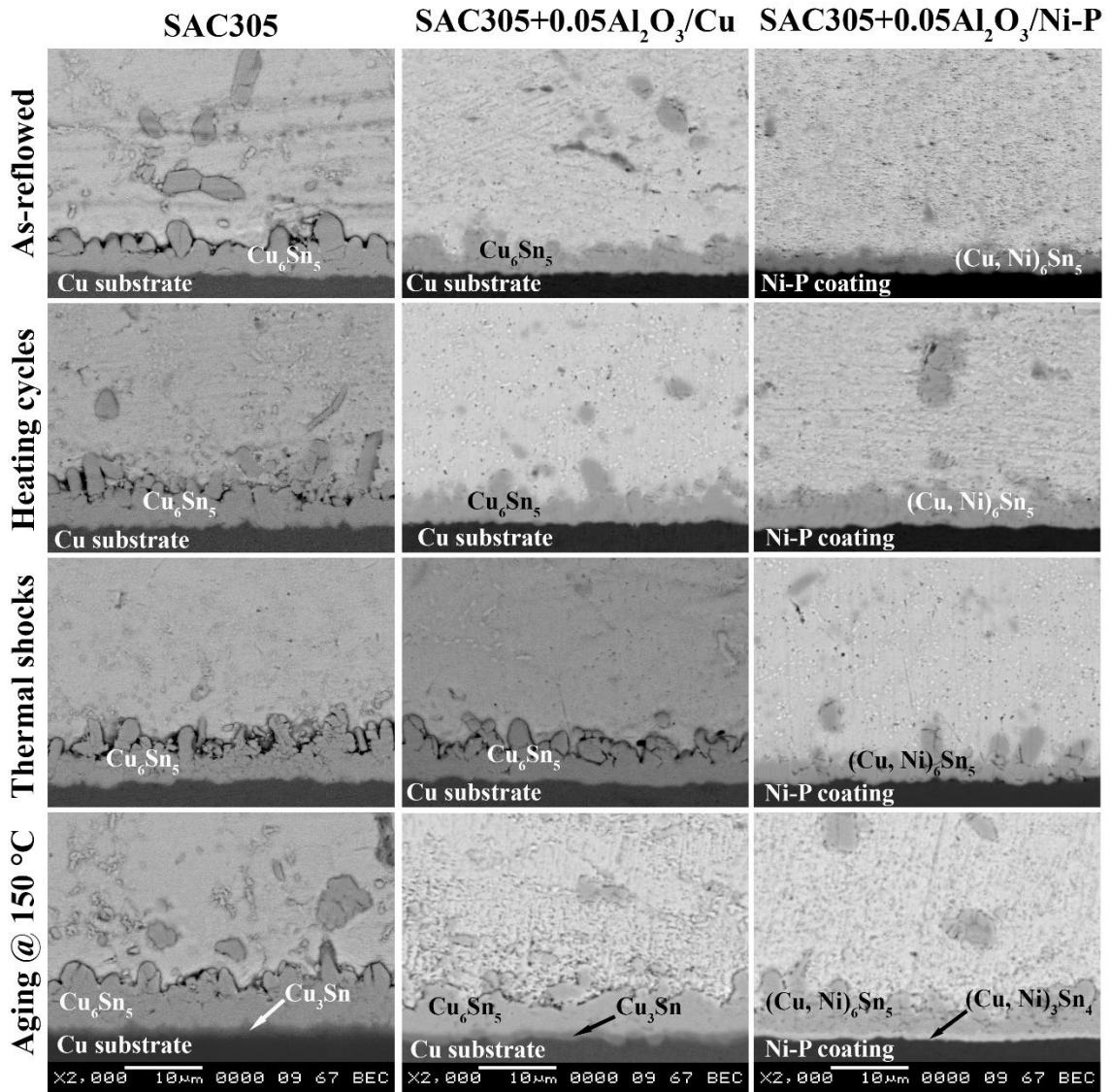


Figure 4.28: SEM images of interfacial microstructure for SAC305 solder and SAC305+0.05Al₂O₃ composite on bare Cu and Ni-P coated substrate under varying high-temperature environments

The morphology of the Cu₆Sn₅ IMC layer at the interface for unreinforced SAC305 solder became coarser on exposure to the different high-temperature environments. The IMC thickness for different nanocomposites of SAC305 solder on bare Cu and Ni-P coated substrate under varying thermal conditions is plotted in Figure 4.31. The thickness of the Cu₆Sn₅ IMC layer increased and coarsening of Ag₃Sn and Cu₆Sn₅ IMC precipitates in the matrix were observed under different thermal conditions. A noticeable Cu₃Sn IMC layer

formed between the Cu_6Sn_5 IMC layer and Cu substrate was observed only under high-temperature (150 °C and 200 °C) aging conditions. The addition of 0.05 wt.% Al_2O_3 nanoparticles transformed the Cu_6Sn_5 IMC layer morphology to a more uniform shape. The IMC layer thickness on the Cu substrate for SAC305+0.05 Al_2O_3 nanocomposite under aging (150 °C) was about 15% thinner compared to unreinforced SAC305 solder. The morphology of $(\text{Cu}, \text{Ni})_6\text{Sn}_5$ IMC layer formed on Ni-P coated substrate was continuous and planar than Cu_6Sn_5 IMC layer. In comparison with Cu_6Sn_5 IMC layer thickness on Cu substrate for SAC305+0.05 Al_2O_3 nanocomposite, the $(\text{Cu}, \text{Ni})_6\text{Sn}_5$ IMC layer on Ni-P coating was obtained about 28% thinner for as-reflowed condition and about 26% thinner for the aging condition. The formation of $(\text{Cu}, \text{Ni})_3\text{Sn}_4$ IMC layer between $(\text{Cu}, \text{Ni})_6\text{Sn}_5$ IMC layer and Ni-P coating was observed only under high-temperature aging conditions.

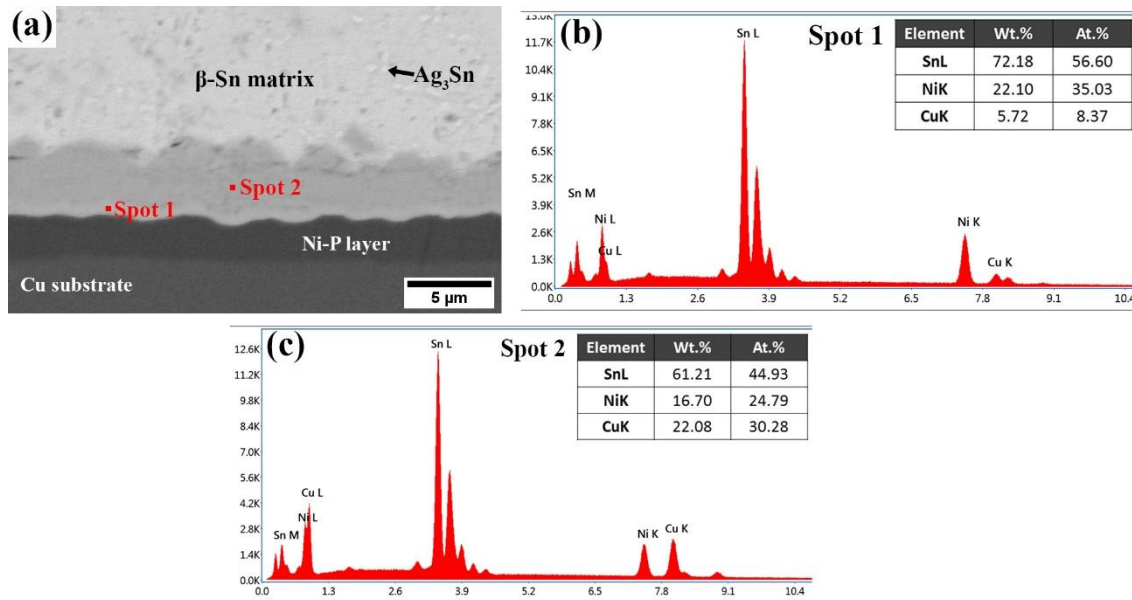


Figure 4.29: (a) SEM micrograph of the SAC305 solder joint on Ni-P coated substrate, and EDS plot with elemental compositions for (b) $(\text{Cu}, \text{Ni})_6\text{Sn}_5$ and (c) $(\text{Cu}, \text{Ni})_3\text{Sn}_4$ IMC layers

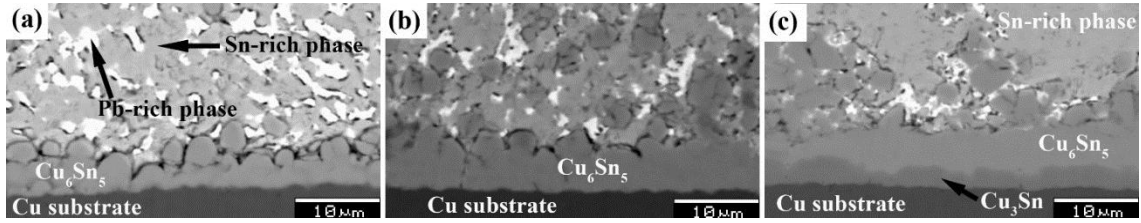


Figure 4.30: SEM micrographs for Sn-37Pb/Cu joint interface under different thermal conditions, (a) as-reflowed, (b) heating cycles, and (d) aging at 150 °C

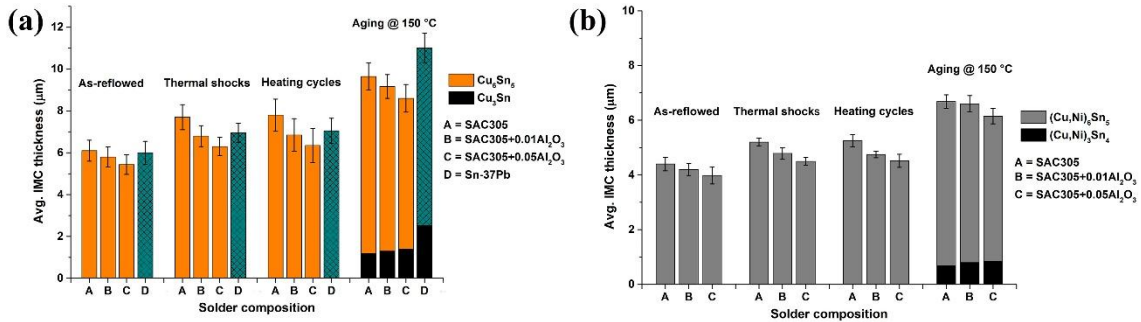


Figure 4.31: Average IMC thickness under varying thermal conditions for SAC305 solder nanocomposites and Sn-37Pb solder reflowed on (a) Cu substrate, and (b) Ni-P coated substrate

The SEM micrographs of the solder joints for select nanocomposites of SAC305-NiGe solder on Cu and Ni-P coated substrate under varying thermal conditions are shown in Figure 4.32. The Cu_6Sn_5 layer appeared thick and planar shape for SAC305-NiGe solder under aging. The EDS analysis showed the traces of nickel in the Cu_6Sn_5 layer formed on the SAC305-NiGe/Cu substrate interface as shown in Figure 4.33. The thickening of IMC layers and coarsening of IMC precipitates in the matrix were observed at high-temperature aging. The Cu_6Sn_5 and $(\text{Cu}, \text{Ni})_6\text{Sn}_5$ IMC layers showed faceted morphology for samples under aging. The Cu_3Sn and $(\text{Cu}, \text{Ni})_3\text{Sn}_4$ IMC layers formed under high-temperature environments and were discrete and thin compared to SAC305 and SAC0307 solders. The IMC thickness for SAC305-NiGe solder joints with 0.01-0.05 wt.% concentration addition of Al_2O_3 nanoparticles on bare Cu and Ni-coated substrate under different thermal conditions is plotted in Figure 4.34. The IMC thickness on the bare Cu substrate decreased by about 24% under different thermal conditions with the addition of 0.05 wt.% Al_2O_3 nanoparticles compared to unreinforced SAC305-NiGe solder. The $(\text{Cu}, \text{Ni})_6\text{Sn}_5$ IMC layer

thickness was about 30% and 26% thinner for unreinforced SAC305-NiGe and SAC305-NiGe+0.05Al₂O₃ nanocomposite, respectively compared to Cu₆Sn₅ IMC layer on bare Cu substrate for respective solder compositions.

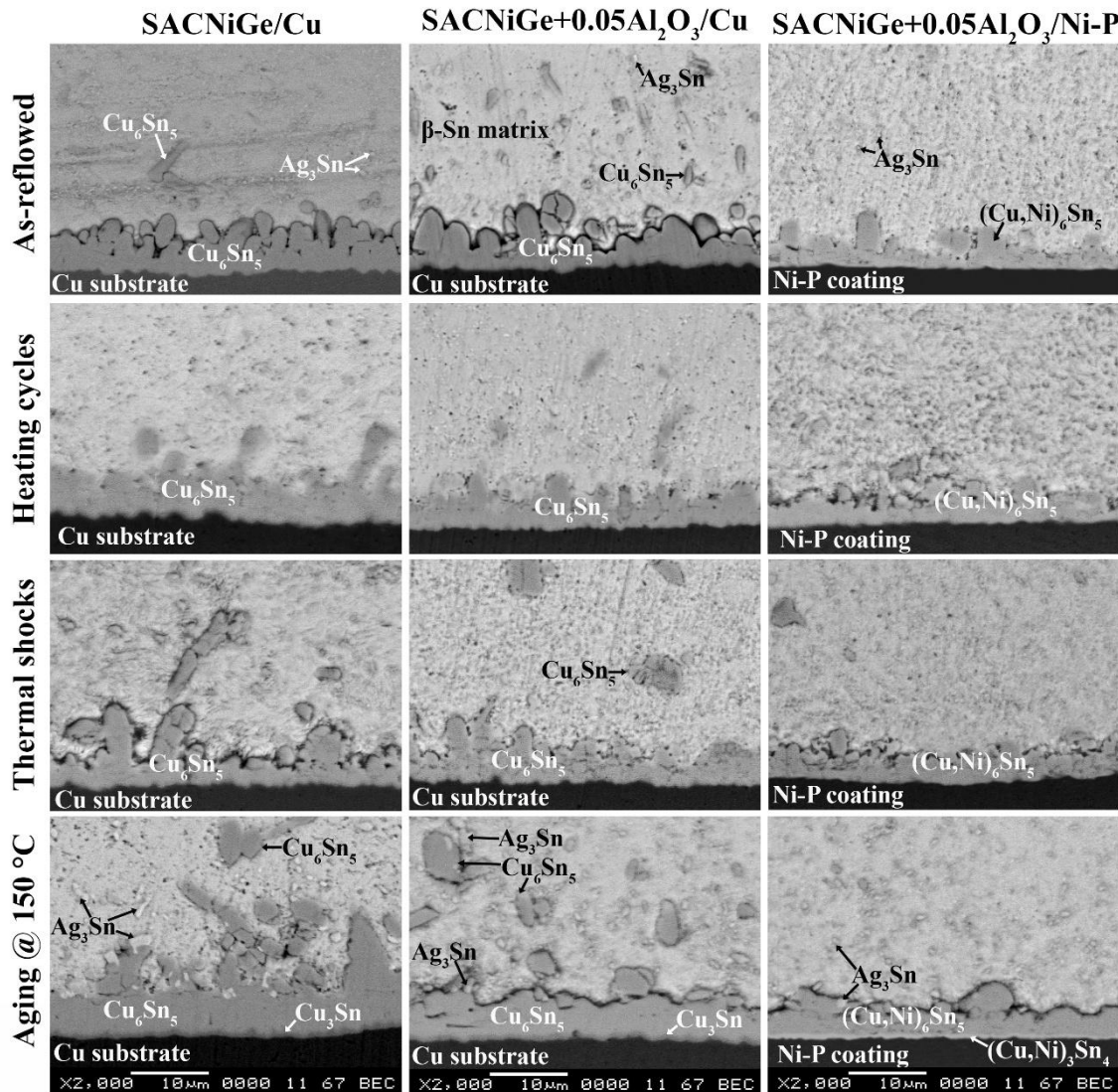


Figure 4.32: SEM images of interfacial microstructure for SAC305-NiGe solder and SAC305-NiGe+0.05Al₂O₃ composite on bare Cu and Ni-P coated substrate under varying high-temperature environments

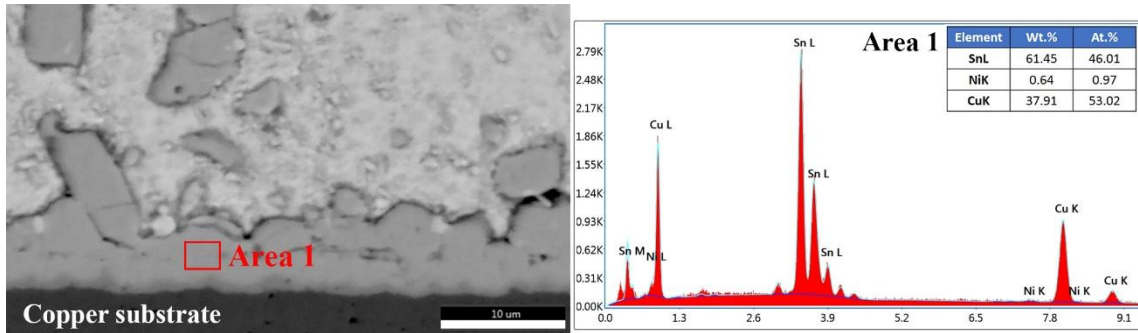


Figure 4.33: SEM micrograph of SAC305-NiGe solder joint on Cu substrate and EDS plot for Cu_6Sn_5 IMC layer at the joint interface

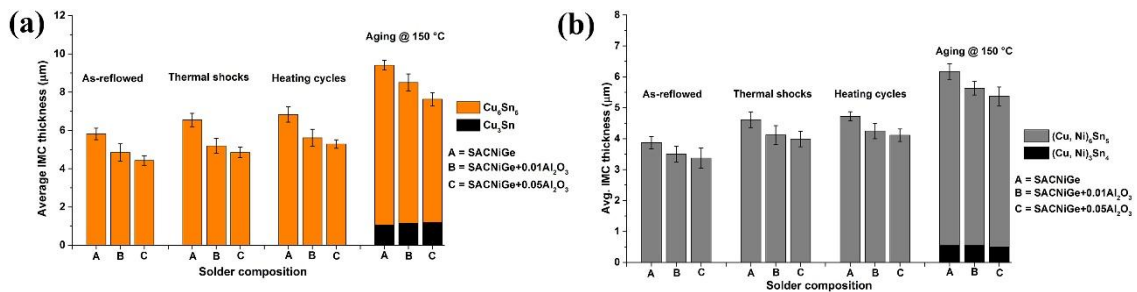


Figure 4.34: Average IMC thickness under varying thermal conditions for SAC305-NiGe solder nanocomposites reflowed on (a) Cu substrate, and (b) Ni-P coated substrate

The SEM micrographs of the solder joints for select nanocomposites of SAC0307 solder on Cu and Ni-P coated substrate under varying thermal conditions are shown in Figure 4.35. The morphology of Cu_6Sn_5 IMC layer for SAC0307 solder was observed columnar shape under as-reflowed, heating cycles, and thermal shock conditions and became coarse scallop-shaped with aging. The morphology of $(\text{Cu}, \text{Ni})_6\text{Sn}_5$ IMC layer was observed more uniform in shape and thinner for SAC0307+0.05 Al_2O_3 nanocomposite on Ni-P coated substrate. The IMC thickness for SAC0307 solder nanocomposites on bare Cu and Ni-coated substrate under different thermal conditions is shown in Figure 4.36. Under the aging condition, the morphology of Cu_6Sn_5 IMC layer became faceted and the thickness was obtained about 20% lesser for nanocomposites compared to unreinforced SAC0307 solder on bare Cu substrate. The $(\text{Cu}, \text{Ni})_6\text{Sn}_5$ IMC layer morphology was thin and planar compared to the Cu_6Sn_5 IMC layer under different thermal conditions. Under the high-temperature aging condition, the thickness of $(\text{Cu}, \text{Ni})_6\text{Sn}_5$ IMC layer was about 31% lesser

than Cu_6Sn_6 IMC layer for unreinforced SAC0307 solder and about 26% thinner for SAC0307+0.05 Al_2O_3 nanocomposite. The formation of Cu_3Sn and $(\text{Cu}, \text{Ni})_3\text{Sn}_4$ IMC layers was observed only under high-temperature aging conditions. The coarsening of Ag_3Sn and Cu_6Sn_5 IMC precipitates in the matrix under different thermal conditions was less significant compared to SAC305, SAC305-NiGe solders.

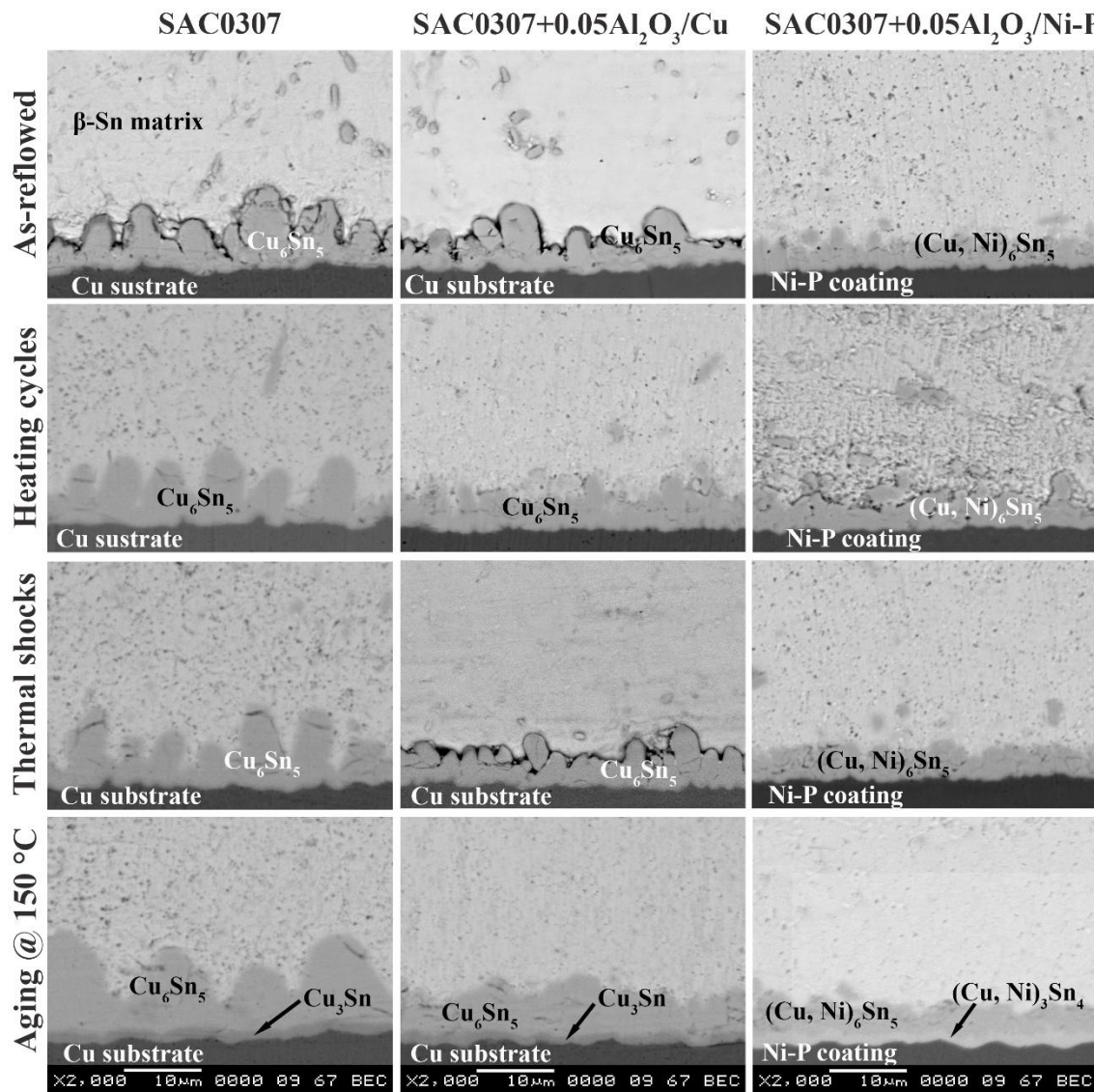


Figure 4.35: SEM images of interfacial microstructure for SAC0307 solder and SAC0307+0.05 Al_2O_3 composite on bare Cu and Ni-P coated substrate under varying high-temperature environments

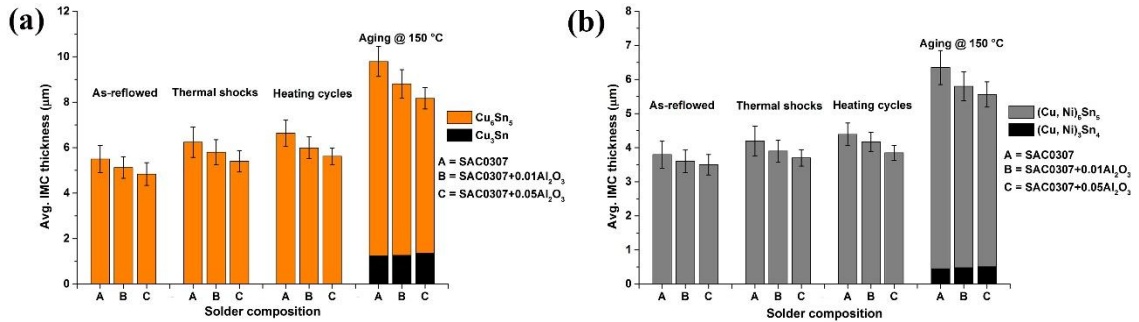


Figure 4.36: Average IMC thickness under varying thermal conditions for SAC0307 solder nanocomposites reflowed on (a) Cu substrate, and (b) Ni-P coated substrate

4.6 Joint Shear Strength, Ductility and Microhardness of Nanocomposite Solders under Different Thermal Conditions

The shear strength data of capacitor joints for select nanocomposites of SAC0307, SAC305, and SAC305-NiGe solders under different thermal conditions are tabulated in Table 4.5, Table 4.6, and Table 4.7, respectively. The data showed a decrease in joint shear strength on exposure to the elevated temperature environments. However, under all different thermal conditions, SAC0307 solder nanocomposites with 0.01 wt.% and 0.05 wt.% Al₂O₃ nanoparticles content reflowed on the copper substrate yielded about 10% and 28% higher strength, respectively, compared to unreinforced SAC0307 solder joints. The shear strength performance for SAC305 and SAC305-NiGe solder joints with the copper substrate under different thermal conditions was improved by about 17% and 20%, respectively for nanocomposites with 0.05 wt.% Al₂O₃ nanoparticles content. The joint strength for developed nanocomposites of all SAC solders under varying thermal conditions was found to be higher than that of corresponding unreinforced solder as well as the conventional Sn-Pb solder.

The joint shear strength decreased on exposure to the heating cycles, thermal shocks, and low-temperature aging. Samples treated with multiple heating cycles showed less decrease in shear strength compared to samples under thermal cycling and aging conditions. The joint failure stress was observed higher for samples aged at 75 °C and 150 °C compared to samples aged at room temperature but with a high deviation in the measurement of the failure stress value and a significant decrease in failure strain of the joint. The high

deviation in failure stress indicates the uncertain fracture behavior of the solder joint possessing a thick IMC layer at the interface and coarse IMC precipitates in the matrix under high-temperature aging conditions. The failure stress and strain decreased drastically for samples aged at 200 °C. The SAC0307 solder joint strength deteriorated significantly under thermal shocks at cryogenic temperature (-173 °C) and aging at 200 °C temperature. The joint shear strength for samples with Ni-P coating was much higher than samples with the bare copper substrate. The SAC0307+0.05Al₂O₃ composite joints showed about a 26% rise in failure strength with Ni-P coated substrate compared to bare Cu substrate under all thermal conditions. The percentage increase in the shear strength for SAC305 and SAC305-NiGe solder joints with Ni-P coated substrate was about 27% and 32%, respectively. The extent of reduction in shear strength under different thermal conditions for nanocomposites was found to be lesser than respective unreinforced solders. A comparative analysis of samples with Cu substrates showed about a 41% decrease in shear strength for unreinforced SAC305-NiGe solder samples from as-reflowed to aging (@ 200 °C) condition, while it was about only a 27% drop in strength for the SAC305-NiGe+0.05Al₂O₃ nanocomposite. On the other hand, the reduction in shear strength for samples on Ni-P coated substrates from as-reflowed to aging (@ 200 °C) condition for plain SAC305-NiGe solder was found to be 32% and 22% for SAC305-NiGe+0.05Al₂O₃ nanocomposite. This shows that the solder joints with Ni-P coated substrate have better thermal stability compared to joints with the bare copper substrate.

Table 4.5: Capacitor joint shear strength for different nanocomposites of SAC0307 solder on bare Cu and Ni-P coated substrate under different thermal conditions

Thermal condition	Condition details	Avg. joint shear strength on bare Cu substrate (MPa)			Avg. joint shear strength on Ni-coated Cu substrate (MPa)		
		SAC0307	SAC0307 + 0.01Al ₂ O ₃	SAC0307 + 0.05Al ₂ O ₃	SAC0307	SAC0307 + 0.01Al ₂ O ₃	SAC0307+ 0.05Al ₂ O ₃
As-reflowed	2 Reflows	17.48±1	20.18±1.5	24.18±1.5	20.41±2	23.73±1	29.28±0.5
Heating cycles	200 cycles (25 °C to 150 °C)	16.66±1.5	19.78±2	23.53±2	20.1±1	23±1.5	28.12±1.5
Thermal shocks	200 cycles (-15 °C to 150 °C)	16.49±1	18.71±1.5	22.55±1	18.68±0.5	21.24±1.5	26.58±1
	30 cycles (25 °C to -173 °C)	9.86±2	11.01±1.5	12.05±2	12.15±1.5	12.89±1.5	14.88±1
Aging	At Room temp. for 720 hrs	16.14±1	19.89±2	24±2	20.21±0.5	22.18±1	28.4±1
	At 75 °C for 240 hrs	23.32±1.5	23.75±1.5	27.14±2.5	24.47±1	25.31±2.5	27.9±2
	At 150 °C for 240 hrs	20.27±3.5	20±3	25.8±2.5	25.44±1.5	27.89±2.5	29.85±3.5
	At 200 °C for 240 hrs	9.05±1.5	9.86±2.5	11.25±2.5	14.4±1.5	17.05±3.5	17.28±3.5

Table 4.6: Capacitor joint shear strength for different nanocomposites of SAC305 and Sn-37Pb solder on bare Cu and Ni-P coated substrate under different thermal conditions

Thermal condition	Condition details	Avg. joint shear strength on bare Cu substrate (MPa)				Avg. joint shear strength on Ni-coated Cu substrate (MPa)		
		SAC305	SAC305+ 0.01Al ₂ O ₃	SAC305+ 0.05Al ₂ O ₃	Sn-37Pb	SAC305	SAC305+ 0.01Al ₂ O ₃	SAC305+ 0.05Al ₂ O ₃
As-reflowed	2 Reflows	24±1.5	25.8±1	28±0.5	24.5±1.5	25.8±2.5	28.03±0.5	30.5±1
Heating cycles	200 cycles (25 °C to 150 °C)	23.8±1	24.9±1.5	26.8±2.5	23.6±1.5	25.2±1	27.22±1.5	29.17±1.5
Thermal shocks	200 cycles (-15 °C to 150 °C)	19.5±1	21.51±1.5	22.2±1	20.8±2	22.1±1.5	23.2±0.5	25.51±2.5
Aging	At Room temp. for 720 hrs	22.8±1.5	24.3±1.5	25.55±1	23.8±1.5	24.8±1	25.52±1	27.21±2
	At 75 °C for 240 hrs	23.62±1	25.2±1.5	27.23±1	24±1.5	25.4±0.5	26.3±1.5	28.31±2.5
	At 150 °C for 240 hrs	24.6±3.5	25.8±2.5	27.92±1.5	14.6±0.5	26.1±3.5	27.5±4	29.5±3
	At 200 °C for 240 hrs	13.5±2.5	15.2±3.5	17.2±1.5	--	15.2±1	16.4±2.5	20.12±3

Table 4.7: Capacitor joint strength for different nanocomposites of SAC305-NiGe solder on bare Cu and Ni-P coated substrate under different thermal conditions

Thermal condition	Condition details	Avg. joint shear strength on bare Cu substrate (MPa)			Avg. joint shear strength on Ni-coated Cu substrate (MPa)		
		SACNiGe	SACNiGe + 0.01Al ₂ O ₃	SACNiGe + 0.05Al ₂ O ₃	SACNiGe	SACNiGe + 0.01Al ₂ O ₃	SACNiGe+ 0.05Al ₂ O ₃
As-reflowed	2 Reflows	25.08±1	26.93±1.5	30.18±1	27.28±1.5	31.7±1	33.15±2
Heating cycles	(200 cycles) 25 °C to 150 °C	24.4±2	25.56±1.5	29.1±2.5	26.8±1.5	30.17±0.5	30.3±1.5
Thermal shocks	(200 cycles) -15 °C to 150 °C	20.77±1.5	22.61±1	25.5±1	23.82±2.5	24.4±1.5	26.67±1.5
Aging	At Room temp. for 720 hrs	24.51±2	26.23±1.5	28.8±0.5	26.14±1	29.89±1.5	31.93±2.5
	At 75 °C for 240 hrs	24.57±1	27.78±1.5	29.2±1.5	28.14±0.5	31.82±2	33.85±0.5
	At 150 °C for 240 hrs	26.74±2.5	28.43±1.5	32.2±3	28.26±2.5	30.1±3.5	35.15±1.5
	At 200 °C for 240 hrs)	14.84±2.5	17.63±2.5	22±2	18.51±3	21.91±2.5	25.83±1.5

The ductility of the solder joint decreased on exposure to the high-temperature environments. The stress-strain curves for unreinforced SAC305 solder on bare Cu substrate and SAC305+0.05Al₂O₃ solder compositions on Ni-P coated substrate under different thermal conditions are shown in Figure 4.37. Nanocomposites showed higher joint failure stress and strain than unreinforced solder regardless of the thermal condition. The ductility of the joint significantly decreased under thermal shock and high-temperature (150-200 °C) aging conditions. The work of fracture (WOF) obtained for SAC305+0.05Al₂O₃ nanocomposite was about 20-40% higher than unreinforced SAC305 solder under different thermal conditions. A similar trend in ductility and WOF was obtained for nanocomposites of SAC0307 and SAC305-NiGe solders under varying thermal conditions.

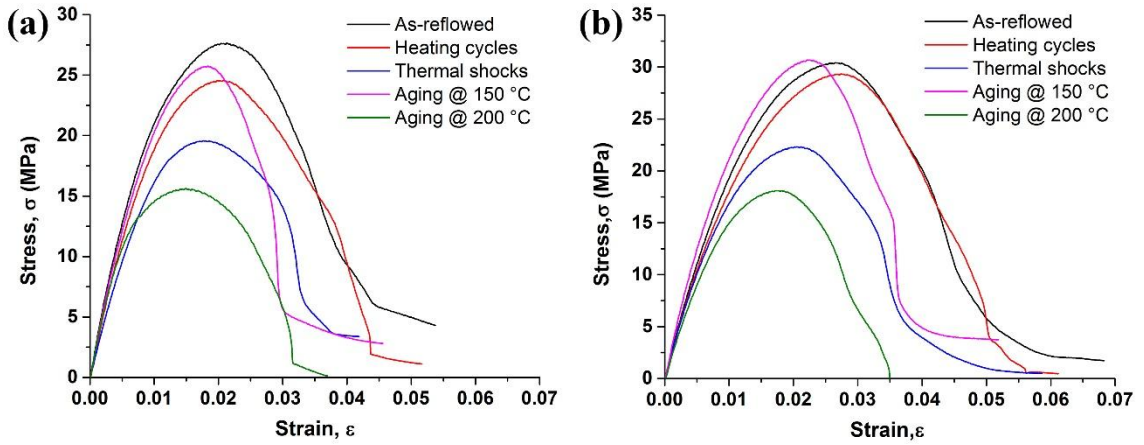


Figure 4.37: Stress-strain plots for single-lap-joint samples under different thermal conditions for (a) SAC305 on Cu substrate and (b) SAC305+0.05Al₂O₃ solder composition on Ni-P coated substrate

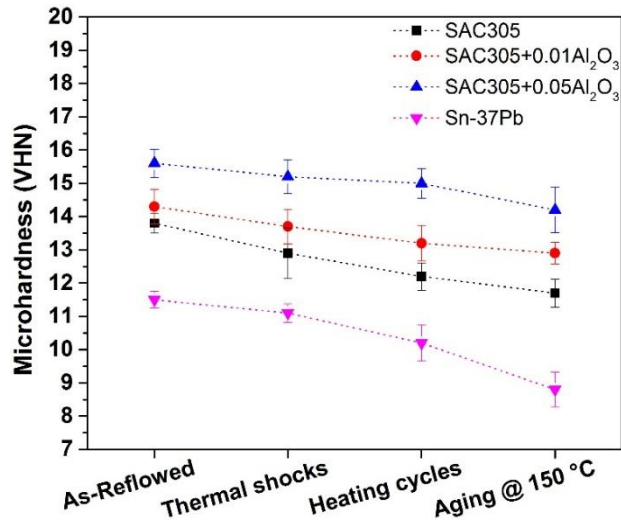


Figure 4.38: Microhardness for SAC305 solder nanocomposites and plain Sn-37Pb solder under varying high-temperature environments

The change in microhardness for SAC305 nanocomposites and plain Sn-37Pb solder under varying high-temperature environments is shown in Figure 4.38. The microhardness for nanocomposite with 0.05 wt.% Al₂O₃ nanoparticles were observed about 14% higher than unreinforced SAC305 solder. A decreasing trend was observed in the microhardness of the solder and nanocomposites with exposure to the high-temperature environments. However, nanocomposites showed about 11% and 21% higher hardness with the addition of 0.01 wt.% and 0.05 wt.% of Al₂O₃ nanoparticles, respectively, compared to plain SAC305

solder under all thermal conditions. The extent of decrease in the microhardness from as-reflowed to aging (@ 150 °C) condition was lower for nanocomposites compared to the unreinforced solder alloy. The microhardness for Sn-37Pb solder was obtained in the range of 11.5-8.6 VHN under different thermal conditions in the present study. The stress-strain plots and microhardness data under different thermal conditions for nanocomposites of SAC0307 and SAC305-NiGe solders are provided in Appendix D.

4.7 Fracture Behavior of the Solder Joints under Multiple Reflows and Different Thermal Conditions

The fractured surfaces after tensile-shear test of lap-joint samples for different solders and nanocomposites were studied to analyze the different failure mechanisms and characteristics of the joint failure under the applied stress and strain conditions. The solder joints showed a mixed-mode of failure with varying ductile and brittle fracture areas on the surface under different thermal conditions. A typical fracture surface showing the characteristic of the mixed-mode of failure on the sheared surface is shown in Figure 4.39. Samples reflowed with up to 2 reflow cycles showed predominantly a ductile fracture surface with shear marks and stretched dimples, whereas brittle failure increased with an increase in reflow cycles. The mixed-mode fracture surface was characterized by the separation plane of bulk solder and IMC interface known as transition ridge as shown in Figure 4.40-b. The ductile fracture area for nanocomposites samples with 0.01-0.05 wt.% nanoparticle content was characterized by the refined sheared grains and uniform distribution of micro-dimples over the fracture surface (Figure 4.40-c). The addition of high content of nanoparticles and increase in reflows promote brittle fracture and formation of coarse dimples on ductile fracture area (Figure 4.40-d). The fracture surface area for composites with a high content of nanoparticles under 6 reflow cycles showed the coarse shear dimple with an exposed IMC at the center and large brittle fracture region as shown in Figure 4.41-a. The magnified image of the coarse dimple area (Figure 4.41-b) clearly shows the presence of sheared Cu_6Sn_5 and Ag_3Sn IMC particles and a bulk solder-IMC interface separation region. The high MWCNT content nanocomposites showed the agglomeration of nanotubes at the coarse dimple area (Figure 4.41-c).

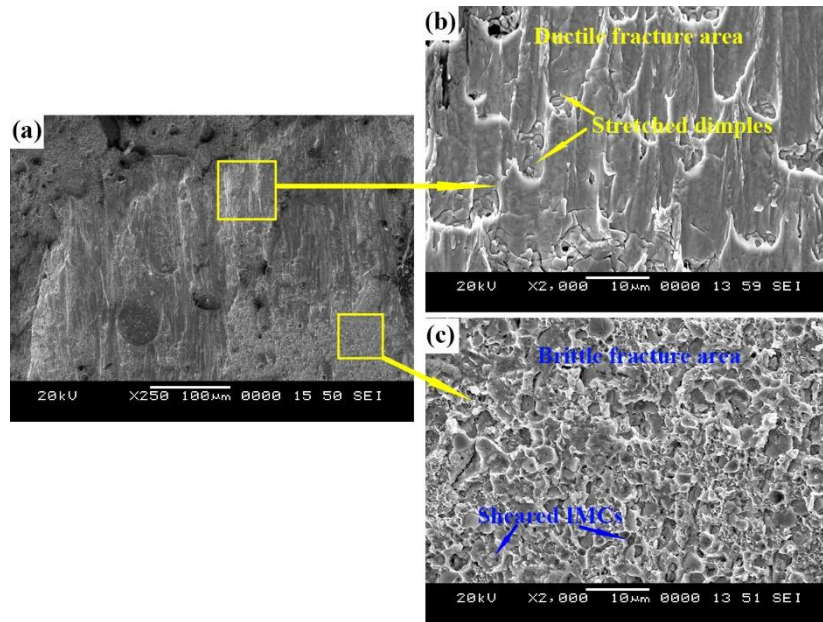


Figure 4.39: SEM images of a fractured surface showing (a) characteristics of mixed-mode failure on the sheared surface, (b) ductile fracture area, and (c) brittle fracture area

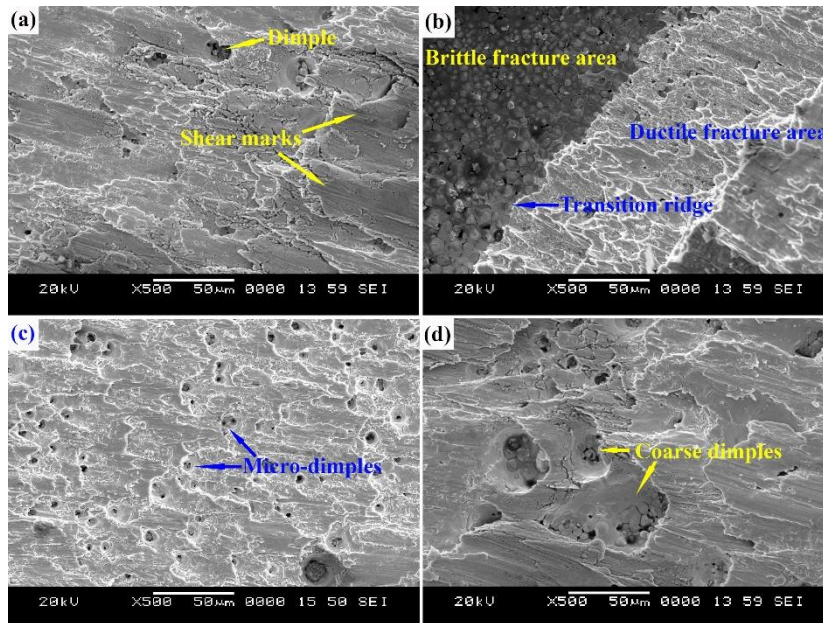


Figure 4.40: SEM micrographs of fractured surfaces showing various fracture details, (a) ductile fracture surface with shear markings, (b) mixed-mode of fracture with transition ridge, (c) fractured surface with a high density of micro-dimples, and (d) fractured surface with coarse dimples

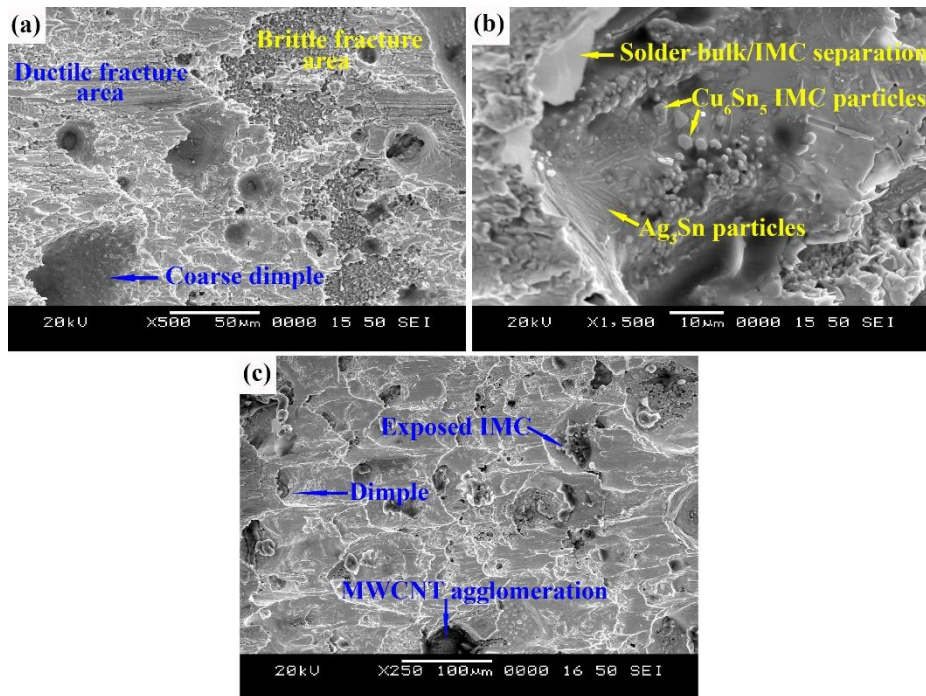


Figure 4.41: SEM images of fractured surface for nanocomposites with a high concentration of nanoparticles showing (a) ductile fracture area with coarse dimples, (b) magnified dimple area showing broken IMC precipitates, and (c) coarse dimples with the agglomeration of MWCNT at the dimple area

The fracture behavior for the select nanocomposite samples changed with different thermal conditions. Samples under as-reflowed and multiple heating cycle conditions showed predominantly a ductile fracture with shear markings and parabolic-shaped dimples on the fractured surface as shown in Figure 4.42-a. The nanocomposite samples exposed to multiple heating cycles and low-temperature aging (R.T and at 75 °C) showed ductile fracture with small dimples (Figure 4.42-b) uniformly spread over the fractured surface. Samples that underwent thermal shocks and high-temperature aging showed mixed-mode of failure with the varying brittle fracture area. The brittle fracture area was observed lesser for samples that underwent thermal shocks and were maximum for samples aged at 200 °C. Samples predominantly showed a brittle fracture under thermal shock conditions at cryogenic temperature. The dimple size on the ductile fracture surface increased for samples aged at the high-temperature aging condition. The ductile fracture surface under low-temperature aging showed dimples with plastic deformation along the shear direction,

while plastic deformation was considerably reduced for samples aged at high-temperature. The EDS analysis of the fractured surfaces confirms the presence of mostly Sn on the ductile fracture surface (Figure 4.42-b) and the presence of exposed Cu_6Sn_5 IMC with Al_2O_3 nanoparticles at the center of the coarse dimple (Figure 4.42-d).

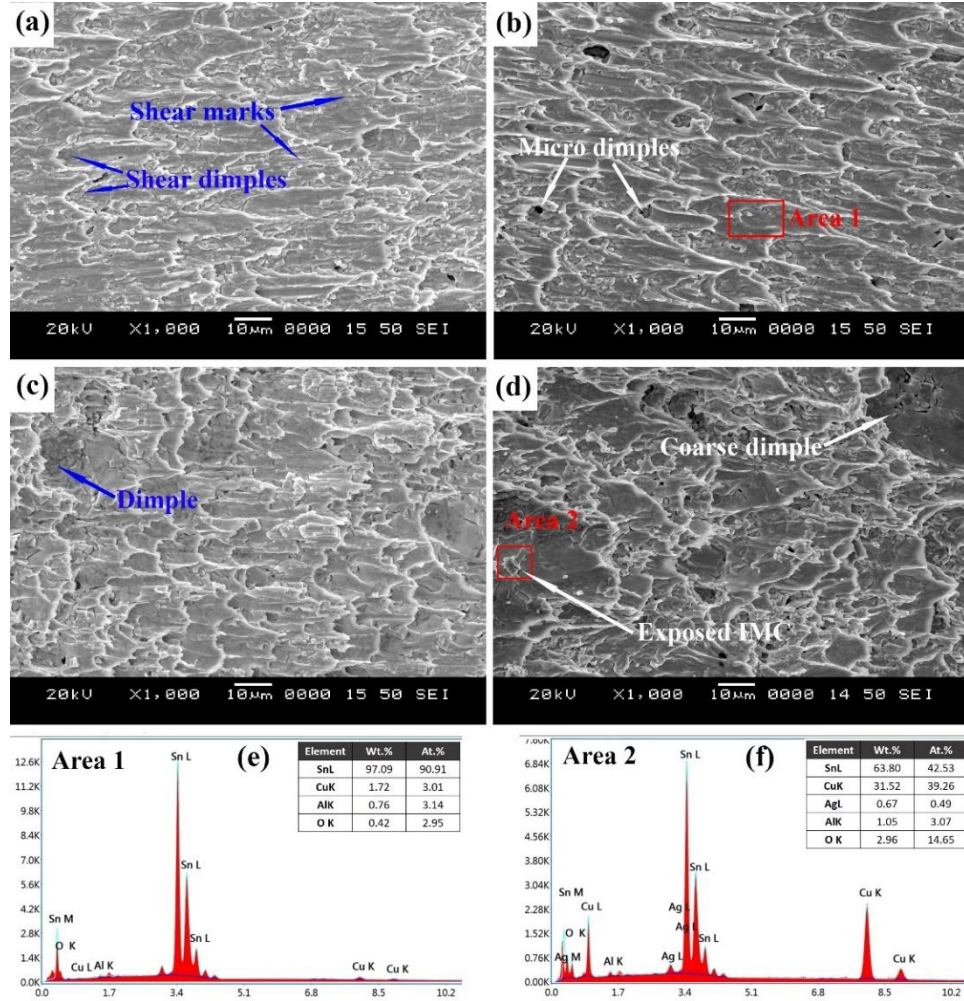


Figure 4.42: SEM micrographs of the fracture surfaces for (a) as-reflowed SAC305 solder joint, and SAC305+0.05 Al_2O_3 under (b) as-reflowed, (c) heating cycles, and (d) aging at 150 °C conditions, respectively, and EDS plots (e) confirming the presence of β -Sn in the bulk matrix and (f) exposed Cu_6Sn_5 IMC inside the dimple with traces of Al_2O_3 nanoparticles

Chapter 5 DISCUSSION

5.1 Effect of Addition of Nanoparticles on Melting Behavior and Wettability of Lead-free Solders

In general, the melting point of an alloy decreases with the addition of any second-phase particles. The marginal drop in thermal parameters of nanocomposite solders indicates the reduction in surface tension of the solder-melt due to the dispersion of nanoparticles, which reflects in the increased wettability of nanocomposites. The decrease in the degree of undercooling of solders with nanoparticles addition could be attributed to the increase in nucleation density in the melt, which promotes the solidification and helps in the formation of a finer microstructure and thin intermetallic layer at the solder joint interface. The impact of Al₂O₃ nanoparticles and MWCNT addition in small weight percent on melting parameters of different solders were not significant and hence, the developed nanocomposites are feasible for use with the existing developed reflow conditions and manufacturing process designs for lead-free solders in the microelectronic packaging industries.

The extent of spreading on the substrate and the rise in capacitor connectors of the molten solder directly depends on the wetting power of the solder composition. The increase in wetting area and tin-climb height for nanocomposites implies an improvement in the wettability of the solder with the addition of nanoparticles. The increase in the wettability of nanocomposite solders could be due to the interference of nanoparticles in the equilibrium between the molten solder and substrate. The nanoparticles possess high surface free energy. The reinforced nanoparticles reduced the surface tension of the melt and increased the surface instability of the molten solder, which alters the solder/substrate equilibrium (Wu et al. 2018; Xing et al. 2017; Zhao et al. 2016b). In general, the wetting process is accompanied by the spreading of molten solder. The driving force of wetting on substrates is mainly the interfacial energy that results from the imbalance of the surface and interface energies. Young's equation (Arenas and Acoff 2004) gives the balance of surface and interfacial tensions at equilibrium as shown in Equation 5.1 where, the γ_{gs} is

the interfacial energy between the solid surface/gas interface, γ_{ls} is the interfacial energy between the solid and the liquid and γ_{gl} is the surface tension of the molten solder or gas/liquid interface, and θ is the equilibrium contact angle.

$$\gamma_{gs} = \gamma_{ls} + \gamma_{gl} \cos \theta \quad 5.1$$

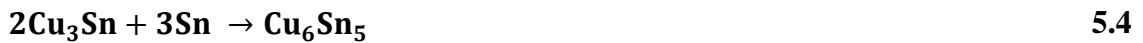
The addition of nanoparticles can reduce the γ_{gl} but does not affect the γ_{gs} and γ_{ls} , which disturbs the equilibrium of the system. To achieve a new level of equilibrium, the contact angle “ θ ” decreases. The reduction in the equilibrium contact angle implies an increase in the spreading of the molten solder on the substrate. Therefore, the wettability of the solder can be improved with the assistance of nanoparticle addition. However, the nanoparticle content should be kept under the limit to achieve the maximum increase in wettability. This is because the high content of the nanoparticles promotes the nanoparticle agglomeration in the melt, which reduces the effective content of surface-active nanoparticles in the system and decreases the surface free energy of the agglomerated nanoparticles. Hence, the spreading rate decreased for nanocomposites with more than 0.1 wt.% Al_2O_3 nanoparticles content. In the case of MWCNT addition, the high concentration (> 0.05 wt.%) leads to the increased agglomeration and entanglement of the nanotubes in the melt, which prevents the solder-melt flow on the substrate and therefore, a significant reduction in wettability of the solder was observed for nanocomposites with high concentration addition of MWCNT. The effective dispersion in solder-melt and finer size of Al_2O_3 nanoparticles yielded the higher wettability for nanocomposites reinforced with Al_2O_3 nanoparticles compared to nanocomposites with MWCNT. Amongst all solder studied, the Sn-3.6Ag solder showed the lowest wettability, while the SAC305-NiGe solder showed the highest wettability. It is noteworthy that nanocomposites with small weight percent addition of nanoparticles showed higher wetting power than conventional Sn-37Pb solder. The Ni-P coating on the substrate provides an equivalent wettable surface as bare copper and did not adversely affect the wettability of the solders and nanocomposites. The increase in wettability of the solder improves the metallurgical bonding and mechanical integrity of the solder joint, which helps in improving the quality and mechanical strength of the joint.

5.2 Effect of Addition of Nanoparticles on Microstructure Evolution and Intermetallic layer Growth under Multiple Reflow Condition

The IMC formation and growth at the interface is driven by dissolution, reaction, and diffusion of the elements. The Cu_6Sn_5 IMC was the prominent IMC layer formed at the joint interface for all solders reflowed on Cu substrate. The Sn atoms from the molten solder react with the Cu atoms on the substrate to form Cu_6Sn_5 and Cu_3Sn IMCs at the interface as shown with Equation 5.2 and Equation 5.3 (Laurila et al. 2005).



The Cu_6Sn_5 IMC being a kinetically favorable phase, therefore, the Cu_3Sn IMC immediately reacts with the available Sn atoms to form Cu_6Sn_5 IMC as shown by Equation 5.4 (Flanders et al. 1997; Mookam et al. 2018).



Under multiple reflow condition, the IMC growth rate increases due to the increase in the reaction kinetics and diffusion rate of the Sn and Cu atoms, which makes the primary Cu_6Sn_5 IMC layer to grow thicker. The IMC grains try to acquire the scallop-shaped morphology as the reflow cycles increases. This is mainly due to the interplay between interfacial, grain boundary energies, and large mass fluxes through the grain boundaries. The Cu_6Sn_5 IMC layer is thermodynamically unstable and decomposes on reaction with available Cu atoms from the substrate to form thermodynamically stable Cu_3Sn IMC as per the Equation 5.5 (Hu et al. 2014, 2016; Laurila et al. 2005) under the exposure of longer reflow times, multiple reflows, elevated temperature atmosphere or aging conditions.



The morphology of the IMC layer at the interface for nanocomposites appeared more uniform, thin, and scallop-shaped compared to unreinforced solder. The IMC layer growth

was suppressed with the addition of Al₂O₃ nanoparticles and MWCNT. The growth kinetics of IMC layer for solders reinforced with nanoparticles under multiple reflow condition was studied using a simple growth model as shown in Equation 5.6, where “y” is the average IMC layer thickness in μm, “k” is growth constant, “t” is the total reflow time calculated as the product of the number of reflow cycles and single reflow time of 100 s, and “n” is the growth exponent, which is indicative of the inter-metallic-growth mechanism. The value of n signifies the dominating diffusion phenomenon for the IMC growth under multiple reflow conditions. The value of n near to 0.33 indicates the grain boundary diffusion mechanism as the dominating factor for IMC growth, whereas n = 0.5 suggests volume diffusion is the governing phenomenon for IMC growth (Deng et al. 2005; Schaefer et al. 1998). The value of n and k can be obtained by fitting the IMC thickness (y) data versus reflow cycle time (t) in the power function.

$$y = kt^n \quad \text{5.6}$$

The obtained Cu₆Sn₅ IMC thickness values under multiple reflow cycles for different solders and nanocomposites with the addition of Al₂O₃ nanoparticles and MWCNT in different weight percent were fitted into the growth model using Origin 9 software and the values of n and k were obtained. The fitted curves for SAC305 solder with different weight percent addition of Al₂O₃ nanoparticles are shown in Figure 5.1. The obtained values of n and k with adjusted R² values for different nanocomposites of SAC305, SAC0307, and Sn-3.6Ag solders are tabulated in Table 5.1, Table 5.2, and Table 5.3, respectively. The IMC data for different solder compositions under multiple reflow cycles showed reliable fitting into the growth model with the R² value above 0.9. The value of growth exponent (n) for all the solder compositions was obtained <0.33, which suggests the grain boundary diffusion is the dominating mechanism in IMC growth under multiple reflow cycle conditions. The values of n and k were observed to decrease with the addition of Al₂O₃ nanoparticles and MWCNT in 0.01-0.05 wt.% and increased with further addition. The decrease in growth exponent and growth constant values implies the decrease in the IMC growth kinetics and suppression of IMC thickness at the joint interface. The increasing

trend in n and k values for the nanocomposites with more than 0.05 wt.% addition of nanoparticles suggest the reduction in net effectiveness of the nanoparticles in suppressing the IMC growth kinetics. Therefore, the IMC retardation was observed less effective for solders with more than 0.05 wt.% content of nanoparticles. The effectiveness of MWCNT addition at higher concentrations in reducing IMC growth kinetics was much weaker compared to that of Al_2O_3 nanoparticles.

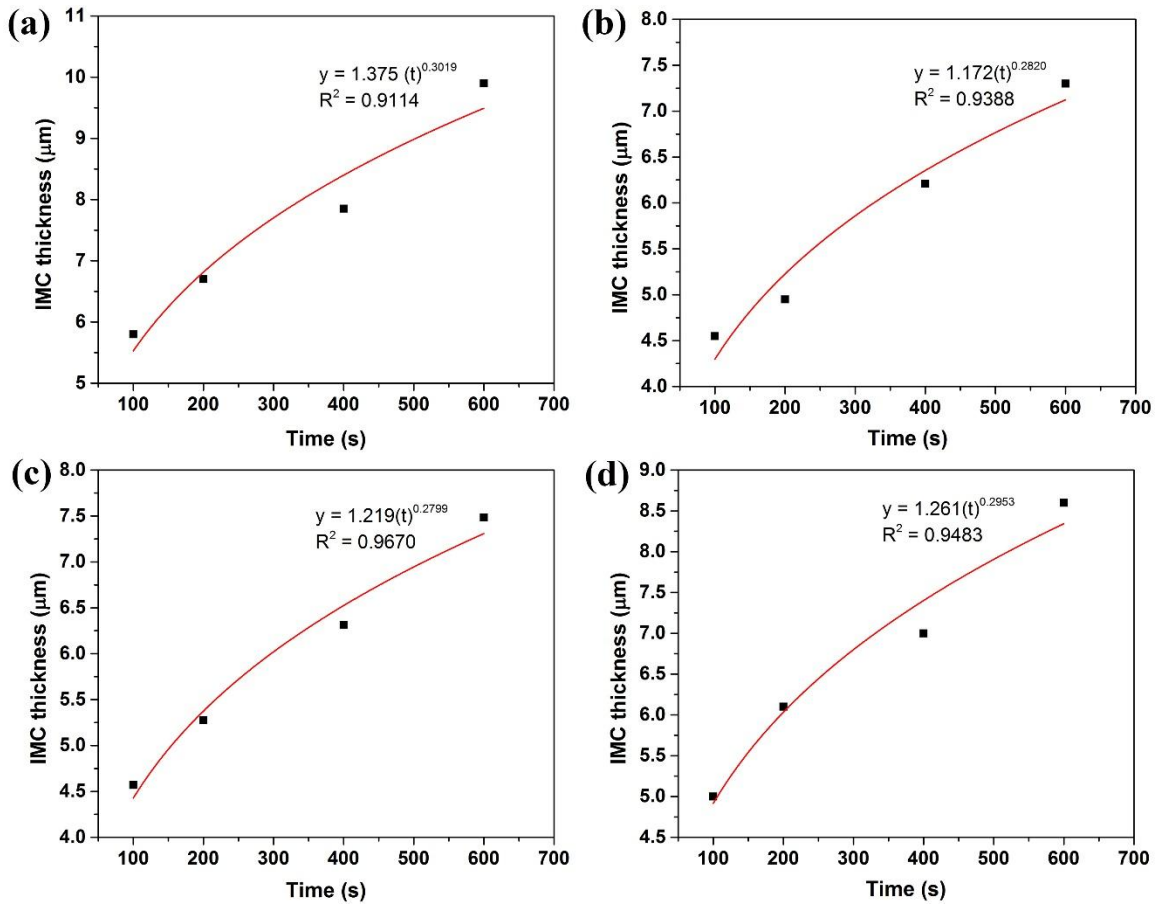


Figure 5.1: Cu_6Sn_5 IMC thickness versus reflow cycle time plots for (a) SAC305, (b) SAC305+0.05 Al_2O_3 , (c) SAC305+0.1 Al_2O_3 , and (d) SAC305+0.5 Al_2O_3 composition reflowed on Cu substrate

Table 5.1: IMC growth exponent (n), growth constant (k) and adjusted R² values for different nanocomposites of SAC305 solder

Solder Composition	n	k	R ²
SAC305	0.3019	1.375	0.9114
SAC0305+0.01Al ₂ O ₃	0.2835	1.254	0.9097
SAC0305+0.05Al ₂ O ₃	0.2820	1.172	0.9388
SAC0305+0.1Al ₂ O ₃	0.2799	1.219	0.9670
SAC0305+0.3Al ₂ O ₃	0.2974	1.157	0.9481
SAC0305+0.5Al ₂ O ₃	0.2953	1.261	0.9483
SAC0305+0.01MWCNT	0.2923	1.288	0.8636
SAC0305+0.05 MWCNT	0.2933	1.188	0.8457
SAC0305+0.1 MWCNT	0.2777	1.507	0.9087
SAC0305+0.3 MWCNT	0.2802	1.550	0.9370
SAC0305+0.5 MWCNT	0.2830	1.650	0.9649

Table 5.2: IMC growth exponent (n), growth constant (k), and adjusted R² values for different nanocomposites of SAC0307 solder

Solder Composition	n	k	R ²
SAC0307	0.3216	1.1518	0.9008
SAC0307+0.01Al ₂ O ₃	0.3101	1.0849	0.9289
SAC0307+0.05Al ₂ O ₃	0.3096	0.962	0.9807
SAC0307+0.1Al ₂ O ₃	0.3114	0.9816	0.9856
SAC0307+0.3Al ₂ O ₃	0.3167	0.9976	0.9608
SAC0307+0.5Al ₂ O ₃	0.3183	1.033	0.9842
SAC0307+0.01MWCNT	0.314	1.126	0.9191
SAC0307+0.05 MWCNT	0.3095	1.033	0.8812
SAC0307+0.1 MWCNT	0.3118	1.004	0.8872
SAC0307+0.3 MWCNT	0.3033	1.198	0.9123
SAC0307+0.5 MWCNT	0.3146	1.165	0.9220

Table 5.3: IMC growth exponent (n), growth constant (k), and adjusted R² values for different nanocomposites of Sn-3.6Ag solder

Solder Composition	n	k	R ²
Sn-3.6Ag	0.3314	1.884	0.9143
Sn-3.6Ag +0.01Al ₂ O ₃	0.3242	1.849	0.9308
Sn-3.6Ag +0.05Al ₂ O ₃	0.3143	1.789	0.9672
Sn-3.6Ag +0.1Al ₂ O ₃	0.3148	1.877	0.9178
Sn-3.6Ag +0.3Al ₂ O ₃	0.3166	1.9134	0.9852
Sn-3.6Ag +0.5Al ₂ O ₃	0.3122	2.058	0.9532
Sn-3.6Ag +0.01MWCNT	0.327	1.77	0.9625
Sn-3.6Ag +0.05 MWCNT	0.306	1.914	0.9706
Sn-3.6Ag +0.1 MWCNT	0.2977	2.031	0.9148
Sn-3.6Ag +0.3 MWCNT	0.2973	2.054	0.8754
Sn-3.6Ag +0.5 MWCNT	0.3045	2.035	0.9220

The decrease in IMC growth kinetics, microstructure refinement, and suppression of IMC layer thickness at the joint interface due to the addition of nanoparticles can be explained by the adsorption theory of nanoparticles on IMC surface and grain boundaries (Chen et al. 2016; Shen et al. 2006; Tang et al. 2014; Tsao et al. 2010; Wu et al. 2018; Yakymovych et al. 2016).

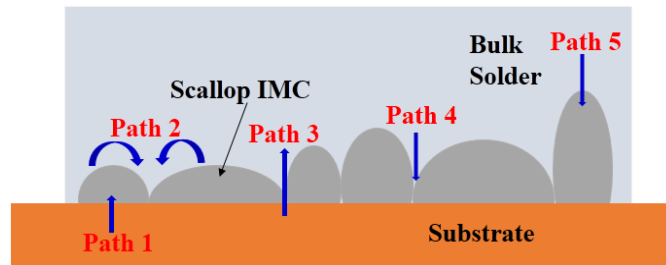


Figure 5.2: Schematic diagram of possible diffusion paths in the solder joint

The IMC growth at the joint interface under different thermal conditions is driven by diffusion between Cu and Sn atoms. In general, there are five possible paths for reaction, dissolution, and diffusion of Cu and Sn atoms at the interface as shown in Figure 5.2. The newly formed Cu_6Sn_5 IMC grains have a scallop shape and are generally separated from each other. The Cu atoms from the substrate diffuse in existing IMC at the interface through path 1 and IMC grows thicker. The rate of diffusion through path 1 is highest during the initial state of IMC formation as the substrate is the main source of Cu for IMC formation. Path 2 indicates the diffusion between two adjacent scallop grains. The Cu/Sn atoms migrate from the scallop peak to the valley area as the concentration gradient creates between two scallops, which makes the IMC layer morphology more planar. Through path 3, some Cu atoms from the substrate migrate directly to the molten solder through the interspace between two scallop grains. The diffusion through path 3 creates IMC particles in the solder bulk, which either present near the IMC area in particle form or redeposit on adjacent larger IMC grain and eventually close off the channel. Thus, the IMC grains grow upward and increase the IMC layer thickness. According to the Gibbs–Thomson effect, which states that the solubility of a particle is higher when the particle size or curvature is smaller. Under multiple reflow condition, the IMC layer coarsens due to Ostwald ripening

effect, which describes the dissolution of smaller adjacent IMC grains into melt and then re-deposition on adjacent larger grains (Ely et al. 2014; Perez 2005). Through diffusion paths 4 and 5, the Sn atoms from bulk solder react with atoms at IMC interspace and IMC surface and increase the IMC layer thickness. The adsorption of nanoparticles on IMC surface retard the migration of Cu atoms from adjacent scallops and through the interspace gaps, thus partially hinders the diffusion paths 2 and 3. Nanoparticles offer the barrier for the diffusion of Sn atoms from bulk solder to the IMC interspace as well as IMC surface. Thus the diffusion from paths 4 and 5 gets retarded. Under different thermal conditions, only diffusion path 1 i.e Cu atoms from the substrate to IMC layer diffusion majorly contributes to the IMC growth for nanocomposites. However, the diffusion of Cu atoms is hindered by the growth of the Cu_6Sn_5 and Cu_3Sn IMC layers.

Nanoparticles are most favorable to be adsorbed by grain surfaces of crystal phases due to their high surface free energy. During the solidification and grain growth process, the increasing interfacial energy between the solder matrix and reinforced nanoparticles played an important role in inhibiting the grain growth. In the grain growth process, when a grain boundary encounters the added nanoparticles, the interfacial energy between them increased, thus causing the enhanced thermodynamic resistance to the grain growth (Chen et al. 2015a; b). Moreover, the nanoparticles in grain boundaries act as the effective diffusion barrier to hinder the diffusion of respective atoms on grain, which contributed to suppressing the grain growth, leading to the finer microstructure. Figure 5.3 shows the secondary electron mode SEM micrographs for unreinforced and nanocomposite SAC305 solder samples showing the refinement of the β -Sn grains in the matrix with Al_2O_3 nanoparticles addition. The average area of β -Sn grain was reduced by about 64% with the addition of 0.05 wt.% Al_2O_3 nanoparticles. The reduction in the degree of undercooling of the solder with the small weight percent addition of nanoparticles also helps in microstructure refinement during solidification. The FESEM images of bulk microstructure for Al_2O_3 nanoparticle reinforced SAC305 solder (Figure 5.4) shows the presence of Al_2O_3 nanoparticles in the matrix.

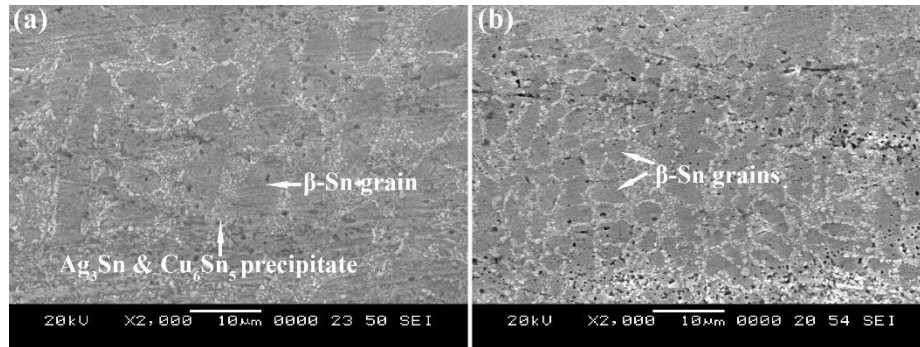


Figure 5.3: Secondary electron mode SEM micrographs for (a) unreinforced SAC305 solder joint and (b) SAC305+0.05Al₂O₃ nanocomposite sample showing the refinement of the β -Sn grains in the matrix

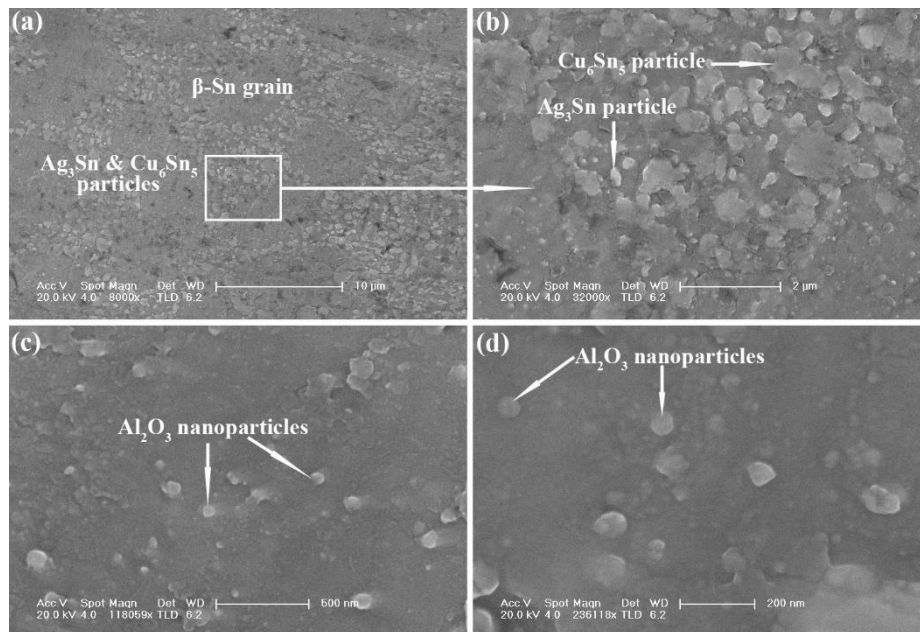


Figure 5.4: FESEM images of bulk microstructure for Al₂O₃ nanoparticle reinforced SAC305 solder joint showing the presence of Al₂O₃ nanoparticles in the matrix

The effective adsorption of nanoparticles on the IMC surface reduces the IMC growth kinetics and hinders the diffusion between Sn and Cu atoms, which resulted in the suppression of IMC thickness at the joint interface. The addition of Al₂O₃ nanoparticles and MWCNT in small weight percentages (0.01-0.05 wt.%) was more effective in suppressing the IMC layer growth at the interface; however, addition above 0.05 wt.% was less effective in microstructure refinement and IMC suppression. The EDS elemental mapping scan for Al₂O₃ at the joint interface for the SAC0307 nanocomposite sample in

Figure 5.5 shows the presence of Al_2O_3 nanoparticles on the IMC surface as well as in the matrix. These findings in this study support and validate the theory of adsorption of nanoparticles in suppressing the IMC growth.

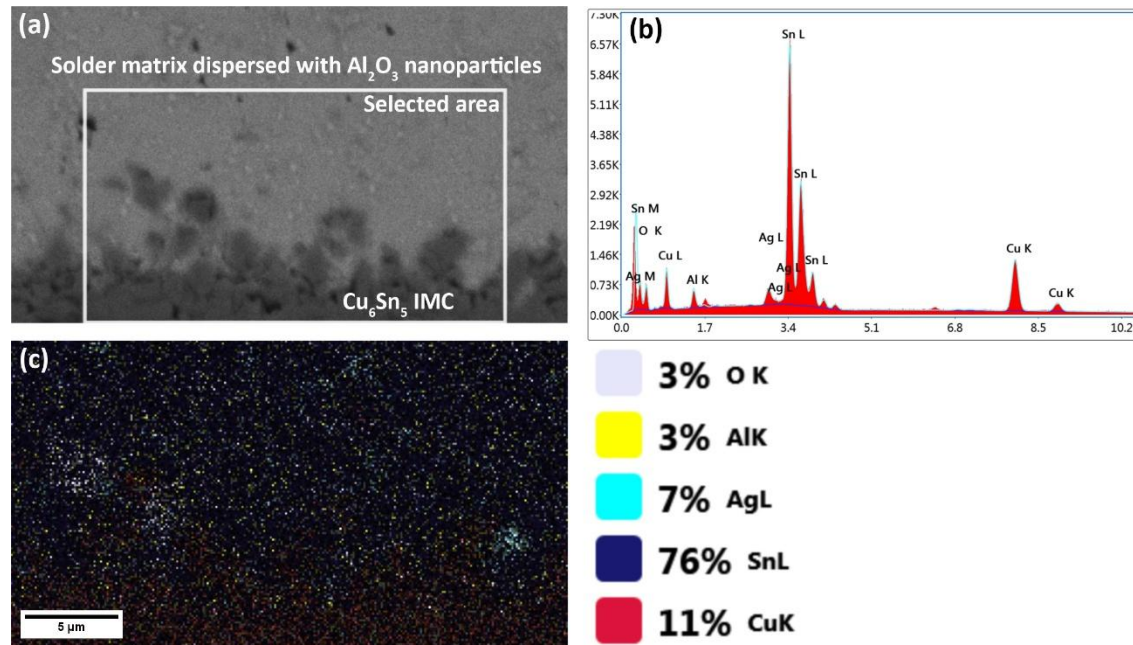


Figure 5.5: (a) SEM image of the selected area at the joint interface, (b) EDS scan showing peaks for Al_2O_3 , (c) elemental mapping scan for the selected area showing Al_2O_3 nanoparticles adsorption on Cu_6Sn_5 IMC and dispersion in grain boundaries of the solder matrix

The effectiveness of nanoparticle addition in suppressing the IMC growth and microstructure refinement was observed more prominent for SAC0307 solder, while least effective in the case of Sn-3.6Ag solder. The reason could be the high IMC growth rate of the binary high silver-content Sn-3.6Ag solder compared to Sn-Ag-Cu solders. The absence of Cu and high Ag content in Sn-3.6Ag solder promotes high Cu_6Sn_5 IMC layer growth at the joint interface and Ag_3Sn IMC precipitate coarsening in the matrix compared to other SAC solders. The Cu content in SAC solders preferentially forms the Cu_6Sn_5 IMC precipitates which reduce the concentration of Sn in the bulk, thus hinders the IMC growth at the joint interface.

The addition of nanoparticles beyond 0.05 wt.% showed a high tendency of agglomeration. Figure 5.6 shows the elemental mapping scan images for nanocomposites confirming the

uniform dispersion of Al_2O_3 nanoparticles in the matrix for small weight percent addition and agglomeration of nanoparticles with higher concentration addition. The effectiveness of nanoparticle addition on microstructure refinement and IMC suppression significantly reduced with the high content of nanoparticles owing to the increase in the agglomeration of nanoparticles. The nanoparticle clusters possess low surface-free energy. The formation of nanoparticle clusters in the solder matrix reduced the net available active nanomaterial in the melt required for effective adsorption, which significantly reduces the uniform adsorption of the nanoparticles on IMC surface and grain boundaries. This adversely affects IMC suppression and microstructure refinement. MWCNT addition beyond 0.05 wt.% promotes significantly high agglomeration than Al_2O_3 nanoparticles due to its larger size and tube structure. Therefore, the high content of MWCNT addition showed adverse effects on the thermal, physical, and mechanical properties of the solder.

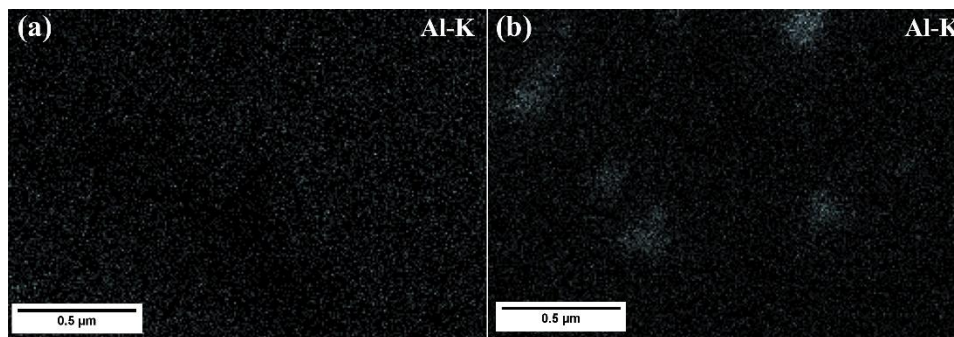


Figure 5.6: EDS scan for elemental mapping of Al_2O_3 nanoparticles for (a) SAC0307+0.05 Al_2O_3 , and (b) SAC0307+0.5 Al_2O_3 compositions showing uniform dispersion and agglomeration of nanoparticles in the solder matrix

5.3 Shear Strength and Ductility of the Solder Joint under Multiple Reflow Condition

The increase in the microhardness of nanocomposites could be attributed to the dispersion of hard nanoparticles in the matrix, microstructure refinement, and a higher constraint to localized matrix deformation during indentation due to the presence of hard second-phase particles like Ag_3Sn , Cu_6Sn_5 IMC precipitates, and nanoparticles. Nanocomposites with the addition of small amounts (0.01-0.05 wt.%) of nanoparticles showed an increase in the shear failure stress, failure strain, and work of fracture (WOF) of the joint. The increase in failure strain implies an improvement in the joint ductility. The work of fracture quantified

the ability of the solder material to absorb energy up to fracture under the applied load. Compared to unreinforced solder, the significant increase in the work of fracture for nanocomposite with 0.05 wt.% nanoparticles addition signified the potential application of nanocomposite in damage tolerant design.

The increase in the shear strength and ductility of the nanocomposite solder joints with small weight percent addition of Al_2O_3 nanoparticles and reflowed for 2 reflow cycles can be attributed to the IMC layer suppression at the interface and uniform dispersion of nanoparticles in the matrix, which provides strengthening in nanocomposites due to Orowan strengthening mechanism (Száráz et al. 2007). The fine grain structure, presence of ultrafine Ag_3Sn IMC particles in the inter-dendritic zone, and IMC suppression at the joint interface also contributed to strengthening the solder joint. The dislocation interaction with the fine Ag_3Sn precipitates and Al_2O_3 nanoparticles within the inter-dendritic zones plays an important role in solder strengthening. Fine precipitates and nanoparticles act as the pinning point for the dislocations. The dislocation movement can be affected either by particle shearing or bypassing around the precipitates (bowing of dislocations in the Orowan looping mechanism). Bowing leads to unpinning, leaving behind the dislocation loop around the particles. The enhancement in strength for nanocomposites was resulted due to the increased dislocation accumulation and resistance to dislocation by dispersed fine second-phase particles in the matrix. The uniform dispersion of refined precipitates and nanoparticles in the matrix allows effective load transfer from matrix to particles, which improves the joint strength. Nanoparticles provide higher interfacial surface area and uniform distribution of nanoparticles helps in increasing the ductility of the solder. The increase in failure strain for nanocomposites could be attributed to the combined effect of (i) fine grain structure of the matrix, which reduce the size of the nucleating flaws and increase the resistance to crack propagation, leading to higher failure strain; (ii) the reduced probability of particle cracking in dispersed Al_2O_3 nanoparticles and ultrafine Ag_3Sn precipitates during shear. The agglomerated nanoparticles and coarse IMC precipitates have a greater tendency of particle cracking and fragmentation during loading. The cracked particles can act as discontinuous flow localization, which initiates and propagate micro-

cracks directly in the matrix and reduce the failure strain. In the case of MWCNT added nanocomposites, the enhancement in the joint shear strength is mainly contributed by the refined microstructure and presence of nanotubes in the matrix, which carry the load during failure and increase the joint strength. The effectiveness of the MWCNT addition in improving the ductility of the joint was lesser compared to Al_2O_3 nanoparticles, which could be due to its larger size, shape, distribution, and dislocation interaction in the matrix during failure. The simultaneous increase in the strength and ductility of the metal matrix composites with the addition of nanoparticles is reported by many researchers (Kamrani et al. 2019; Liu et al. 2018; Paramsothy et al. 2012).

The clustering associated with the high content addition of nanoparticles significantly decreases the effective volume fraction of the reinforcement particles in the matrix. The Orowan strengthening effect significantly decreases with the increase in particle size and inter-particle distance. The large clustering of nanoparticles significantly reduces the Orowan strengthening effect. The ineffective microstructure refinement resulted due to the high content of nanoparticles increases the grain size and lowers the amount of matrix/reinforcement interfaces, which diminishes the effective load transfer between reinforcement and matrix and reduces the solder strength. Besides, the agglomeration of nanoparticles increases the de-bonding of the matrix/particle interface, which leads to the crack initiation and propagation, leading to a decrease in the failure strain of the solder joint. Nanocomposites with high weight percent addition of MWCNT showed higher de-bonding of particle/matrix interface, which significantly reduced the ductility of the joint. Besides, nanoparticle clusters acted as the preferred sites for micro-crack or micro-void nucleation under loading, which significantly reduced the ductility of the solder joint.

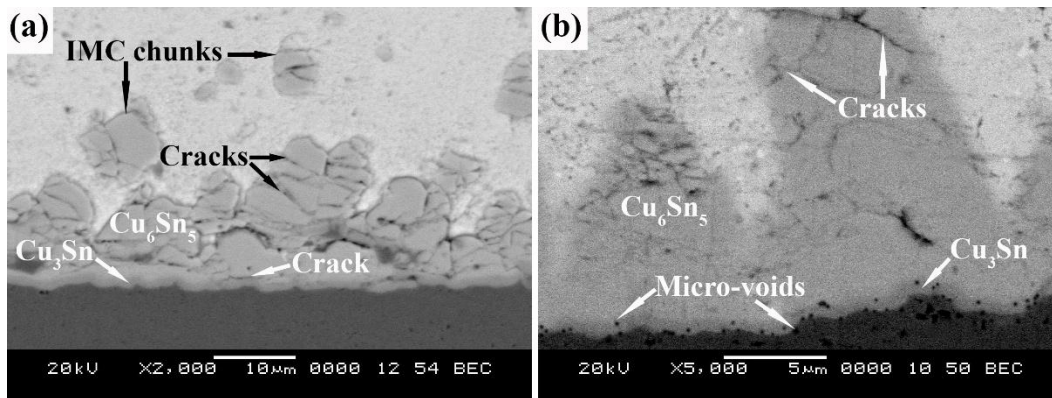


Figure 5.7: SEM micrographs at the joint interface after multiple reflows showing (a) IMC spalling and micro-cracks in IMC layers, (b) micro-voids at IMC-substrate interface in overgrown IMC layer

The decrease in shear strength and ductility of the joint after 2 reflow cycles was attributed to the coarsening of the IMC layer and bulk microstructure. The Cu_6Sn_5 and Cu_3Sn IMC layers at the interface and the Ag_3Sn , Cu_6Sn_5 IMC precipitates in the matrix significantly grow coarser on exposure to multiple reflow cycles due to the increase in the diffusion rate of elements. Samples exposed to 6 reflow cycles showed IMC spalling at the joint interface. Figure 5.7 shows the joint interfacial microstructure with IMC spalling, micro-cracks on the IMC layer, and micro-voids at the IMC interface for samples reflowed with 6 reflow cycles. Spalling resulted from the morphological change of the IMC layer at the interface. Spalling occurred mainly due to the inadequate quantity of any reactive element which forms the IMC layer and sensitivity of the IMC formation reaction towards the reactive elements (Kotadia et al. 2012). As the reflow cycle increases, more and more reactive atoms are taken out from the solder for the formation and growth of the intermetallic compounds at the interface. The increase in the growth of the intermetallic layer in successive reflows makes it a non-equilibrium phase and as the concentration of reactive element decreases in the solder, the falling of intermetallic chunks from the IMC layer takes place at the interface known as IMC spalling. The IMC spalling significantly decreases the strength and ductility of the joint. The thicker Cu_6Sn_5 and Cu_3Sn IMC layers at the interface resulted due to high reflow cycles often develops micro-cracks in the IMC layer. The difference between the coefficient of thermal expansion (CTE) values and crystal structure of Cu_6Sn_5 and Cu_3Sn IMC layers, bulk solder and copper substrate

produces stresses between the IMC layers, bulk, and substrate, leading to the formation of micro-cracks in the IMC layers. The diffusion speed of Cu and Sn at the copper substrate under successive reflow cycles promotes the formation of Kirkendall voids in the IMC layers. Since, IMCs are inherently brittle and have low fracture toughness, the increase in IMC thickness, presence of micro-voids and micro-cracks in IMC layers under multiple reflow cycles makes the joint more vulnerable to the brittle failure under loading condition and reduce the mechanical strength of the joint. Compared to SAC305 and SAC0307 solders, the high IMC growth rate of Sn-3.6Ag solder and large Ag_3Sn IMC precipitate formation in bulk were the major reasons behind its low ductility of the joint. The rate of degradation in mechanical properties of the solder joint under higher reflow cycles was lesser for nanocomposites reinforced with Al_2O_3 nanoparticles compared to unreinforced solders, owing to the positive effect of nanoparticles addition in microstructure refinement and IMC layer suppression. The effect of high concentration (>0.05 wt.%) addition of MWCNT in solders was more detrimental for shear strength and ductility of the solder joint than higher concentration addition of Al_2O_3 nanoparticles.

5.4 Microstructure Development and IMC layer Growth on Bare Cu and Ni-P Coated Substrate for Select Solder Nanocomposites

In real working conditions such as the continuous use of electronic equipment, temperature storage, and power on-off cycles, assemblies thereby soldered joints are subjected to solid-state aging conditions. The solid-state diffusion rate significantly increases under high-temperature working conditions like aging, which increases IMC growth rate, resulting in the IMC layer coarsening and thickening at the interface. The scallop morphology of the Cu_6Sn_5 IMC tends to become planar as the channels between scallops provide convenient paths for the diffusion of Cu atoms. Thus, the IMC grows faster at the channels between scallops rather than on the top surface of the scallops during the initial aging stage. The Cu_3Sn IMC layer growth during thermal aging is mainly governed by the inter-diffusion between Sn atoms diffused through the Cu_6Sn_5 IMC layer and Cu atoms from the metal substrate at the Cu/ Cu_3Sn interface. The diffusivity ratio of Cu to Sn in the Cu_6Sn_5 phase is about 0.35 (@150 °C-200 °C), while it is about 30 (@ 225 °C-350 °C) in the Cu_3Sn

phase, which suggest that Sn is the dominant diffusing species responsible for the growth of Cu_6Sn_5 , whereas, Cu becomes the dominant diffusing species for the growth of Cu_3Sn (Paul et al. 2011). The difference in the intrinsic diffusivities between Cu and Sn in the Cu_3Sn phase tends to induce the Kirkendall effect, and the Cu/ Cu_3Sn interface acts as a location for vacancy sinks, causing such defects to agglomerate into microvoids (or Kirkendall voids) at/near the interface. The thick Cu_6Sn_5 and Cu_3Sn IMC layers at the interface have different CTE values and crystal structures, which cause the development of stresses at the interface and promotes the formation of micro-cracks in IMC layers under high-temperature aging conditions. The IMC growth under thermal-cycling conditions often associated with the dynamic recrystallization of Sn atoms. The thermal cycling induces cyclic thermal stresses and strains, leading to thermal fatigue failures of the joint.

The IMC thickness obtained for plain solder and nanocomposites on bare Cu and Ni-P coated substrate were arranged in the order of increasing thickness and plotted against the respective thermal condition. The IMC thickness data fitted into a power-law growth model as given in Equation 5.6. By taking a natural log to both sides, the growth equation takes a form of a straight line equation as shown by Equation 5.7, where n is the slope of the line and k is the y-intercept.

$$\ln(y) = n \ln(t) + \ln(k) \quad 5.7$$

The linear fitting line equation obtained after fitting the average IMC thickness data for different nanocomposites under varying thermal conditions was compared with Equation 5.7 and the values of n and k were obtained. The values of n and k indicate the IMC growth kinetics for different nanocomposites on bare Cu and Ni-P coated substrate under different thermal conditions. The IMC thickness versus different thermal conditions fitting plots for select nanocomposites of SAC305-NiGe solder on bare Cu and Ni-P coated substrate are shown in Figure 5.8. The IMC fitting plots for unreinforced SAC305 and SAC0307 solders and nanocomposite with 0.05 wt.% Al_2O_3 nanoparticles addition for bare Cu and Ni-P coated substrate are shown in Figure 5.9. The slope of the fitting line (n) and constant (k) values were found to be in the order $\text{SAC}/\text{Cu} > \text{SAC}+0.05\text{Al}_2\text{O}_3/\text{Cu} > \text{SAC}+0.05\text{Al}_2\text{O}_3/\text{Ni}$ -

P for all SAC solders and nanocomposites under different thermal conditions. The decrease in n and k values indicates the decrease in IMC growth rate and IMC layer thickness at the interface with the addition of Al₂O₃ nanoparticles in small weight percent and Ni-P coating on the Cu substrate.

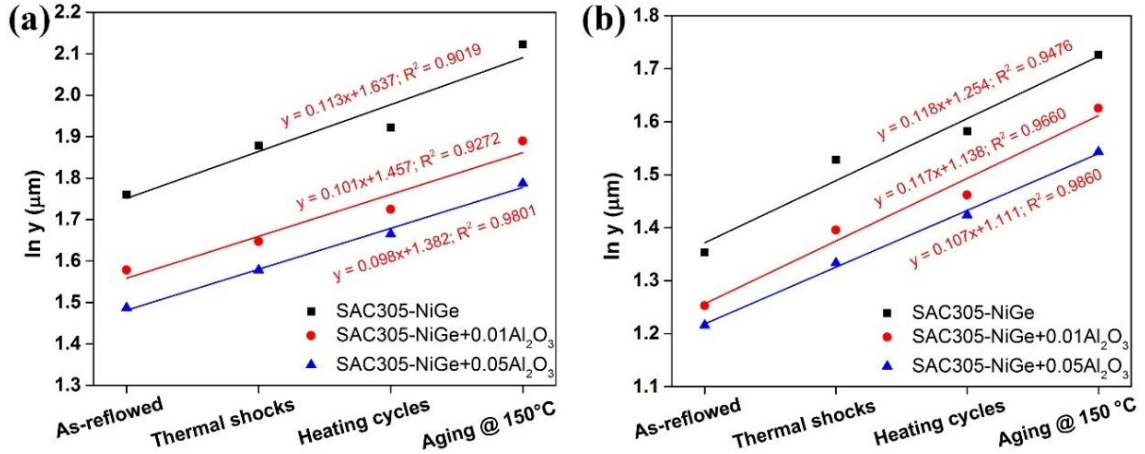


Figure 5.8: Natural log of Cu₆Sn₅ IMC thickness versus different thermal conditions for SAC305-NiGe solder nanocomposites on (a) uncoated-Cu substrate and (b) Ni-P coating

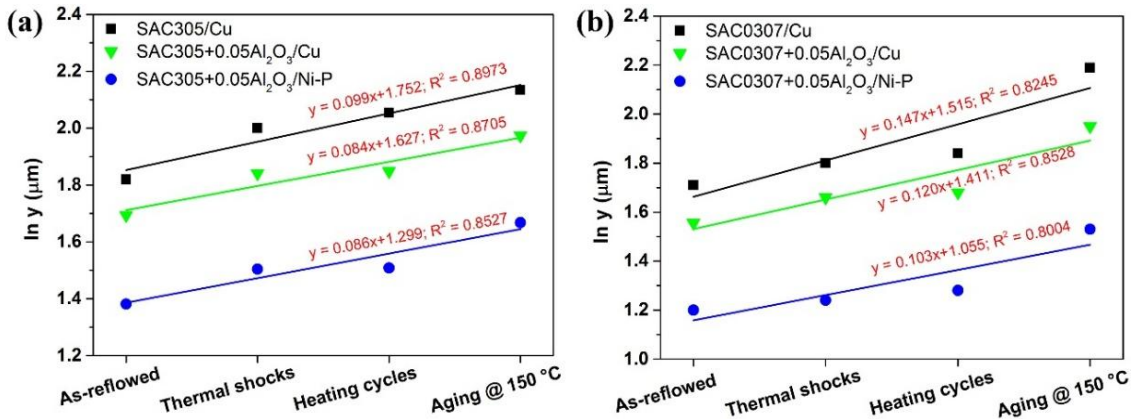


Figure 5.9: Natural log of Cu₆Sn₅ IMC thickness versus different thermal conditions for nanocomposites on the uncoated-Cu substrate and Ni-P coating for (a) SAC305 and (b) SAC0307 solder

The Ni-P coating acts as a strong barrier for the reaction and diffusion between Cu and Sn atoms at the interface under different thermal conditions. The Ni has a high solubility in Cu, hence, the Ni atoms from the coating take part during the formation of the Cu-Sn IMC

layer on the substrate and form the complex $(\text{Cu}, \text{Ni})_6\text{Sn}_5$ IMC layer at the interface. Besides, $(\text{Cu}, \text{Ni})_6\text{Sn}_5$ IMC has lower activation energy compared to Cu_6Sn_5 and Cu_3Sn IMCs. The presence of Ni-P coating causes fewer atoms to join the IMC formation reaction, which leads to the development of a thinner $(\text{Cu}, \text{Ni})_6\text{Sn}_5$ IMC layer at the interface. The slow diffusion rate of Ni atoms in Cu-Sn IMC was responsible for the suppression of $(\text{Cu}, \text{Ni})_6\text{Sn}_5$ IMC growth kinetics. The strong diffusion inhibition offered by the Ni-P layer helps in the formation of a thin IMC layer and the presence of Ni in IMC improves the uniformity of $(\text{Cu}, \text{Ni})_6\text{Sn}_5$ IMC layer at the interface. Hence, a thin and planar $(\text{Cu}, \text{Ni})_6\text{Sn}_5$ IMC was obtained under high-temperature aging conditions for samples with Ni-P coated substrate.

5.5 Performance and Reliability of the Solder Joints

The performance and reliability of the solder joint were determined in terms of the shear strength of the joint under varying thermal conditions. The performance of developed nanocomposites with small weight percent addition of Al_2O_3 nanoparticles for SAC305, SAC0307, and SAC305-NiGe solders under shear loading was found to be better than that of plain solders as well as the conventional Sn-Pb solder under the exposure of varying thermal conditions. The improvement in the joint shear strength was attributed to the refined grain structure and Ag_3Sn IMC precipitates, suppressed IMC layers at the interface, and dispersion of nanoparticles, which help to inhibit the grain boundary sliding, impede the dislocation movement and increase dislocation densities, leading to the enhancement of the solder joint strength (Xu et al. 2014a). Nanocomposites yielded higher microhardness compared to unreinforced solder regardless of the thermal condition, which could be attributed to the grain refinement and dispersion hardening. The existence of Al_2O_3 nanoparticles in the solder matrix inhibit dislocation glide, and microstructure refinement decreases the average grain size and spacing of the Ag_3Sn IMC particles in the matrix, which enhanced the microhardness. The decreasing trend in microhardness with exposure to the high-temperature environment was due to the β -Sn dendrites coarsening and the residual stress relaxation during the aging. The presence of Ag_3Sn IMC precipitates in the matrix provides more hardness to the SAC solder compared to the Sn-37Pb solder.

A thin and planar IMC layer at the joint interface along with the dispersion strengthening resulted in better performance and good reliability for the solder nanocomposite joints with Ni-P coated substrate compared to solder joints on bare Cu substrate under different thermal conditions. The rate of decrease in the shear strength for samples reflowed on Ni-P coating under all different thermal conditions was less compared to the samples reflowed on bare Cu substrate owing to the thin and planar IMC at the interface. This suggests that the solder joints could achieve better thermal stability under high-temperature environments with the use of Ni-P coating on Cu substrate. The performance and reliability of SAC305-NiGe solder were found to be higher compared to SAC305 and SAC0307 solders. It is noteworthy that the performance and reliability of low-silver content SAC0307 solder composite with the addition of Al₂O₃ nanoparticles in 0.05 wt.% were improved to the level of high-silver content SAC305 solder.

The decreasing trend in the joint shear strength under heating cycles and low-temperature aging conditions could be attributed to the microstructure coarsening. The decrease in joint strength and increase in brittleness of the joint under thermal shock was due to the thermal stresses produced at the interface between the solder matrix, IMC layer, and substrate, owing to the recrystallization of β -Sn at the sub-zero temperature and the difference in CTE values and crystal structure between bulk solder, IMC layers, and precipitates. These stresses promote the micro-crack formation at the interface, causing a decrease in the strength and brittle failure of the joint under loading. The increase in joint failure stress value under the aging condition at 75 °C and 150 °C could be due to the presence of thick but planar IMC layers at the interface and coarse precipitates in the matrix, which provides the resistance to the fracture propagation before cracking. The significant drop in the ductility of the joint under high-temperature aging condition justifies the rise in failure stress with a significant reduction in ductility of the joint. The high depletion of Sn from the matrix in coarsening the IMC precipitates and thickening the IMC layer at the interface under aging at 200 °C made the joint microstructure weak and brittle, which leads to a significant decrease in joint strength and ductility. Samples exposed to high-temperature (@ 200 °C) aging condition with Ni-P coated substrate showed growth of a brittle Ni-Sn-

P layer between the Ni-P substrate and $(\text{Cu, Ni})_6\text{Sn}_5$ IMC layer. These problems were well anticipated as the 200 °C aging temperature is very near to the solidus point of all SAC solders used in this study. Extreme high-temperature environment drastically accelerates the diffusion rate between respective elements and significantly increase the IMC growth, which considerably weakens the joint matrix strength and promotes brittle fracture.

The relationship between IMC thickness and shear strength of the solder joint under varying thermal conditions was studied by plotting the IMC thickness versus respective shear strength of the joint for different solder nanocomposites on bare Cu and Ni-P coated substrate. The obtained IMC thickness for plain SAC305 solder and SAC305+0.05Al₂O₃ composite on bare Cu and Ni-P coated substrates were plotted against respective joint shear strength under the different thermal conditions as shown in Figure 5.10.

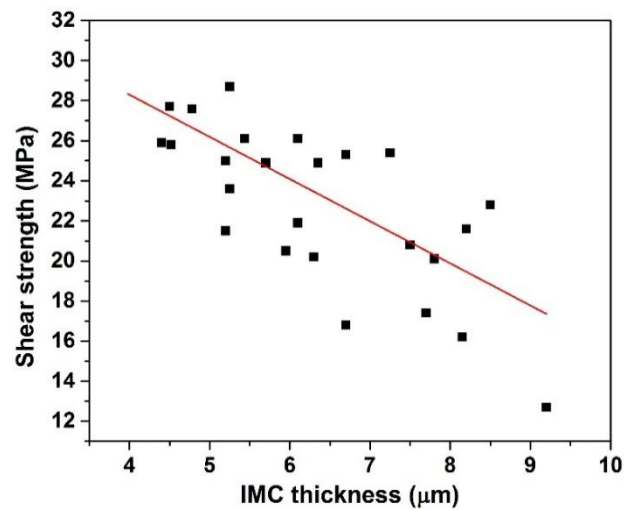


Figure 5.10: IMC thickness versus joint shear strength plot for plain SAC305 solder and SAC305+0.05Al₂O₃ composite reflowed on bare Cu and Ni-P coated substrate under different thermal conditions

The collective data plot showed that the joint shear strength decreases monotonically with the increase in IMC thickness under various thermal conditions for plain solder and nanocomposites. The IMC thickness versus joint shear strength relation showed similar behavior for SAC0307 and SAC305-NiGe solder nanocomposites under different thermal conditions. However, the detailed comparison between IMC thickness and respective shear strength showed that the maximum failure stress for the solder joint does not solely depend

on the IMC thickness at the joint interface. The thick IMC layer at the interface does not always result in lower failure stress. The solder joint strength was found to be weaker under thermal shocks due to induced thermal stresses at the interface despite having lesser IMC thickness than samples under heating cycles and aging conditions. On the other hand, joint strength was found to be very less for the samples aged at 200 °C, which has a duplex IMC layer structure at the interface and higher IMC thickness. This implies that the joint strength is not only affected by IMC thickness and its morphology at the interface but also collectively affected by the working environment temperature, solder bulk microstructure, precipitates in the matrix, and residual stresses at the joint interface caused by the exposure to the working environment. A very thick and uneven IMC layer indeed adversely affects the strength and ductility of the joint and majorly contributes to the brittle failure of the joint under loading conditions. Therefore, to optimize the performance of the solder joint, the IMC growth at the interface needs to be suppressed.

5.5.1 Weibull distribution analysis of the joint shear strength

The reliability of the solder joints under different high-temperature environments was quantitatively analyzed with the help of two-parameter Weibull analysis (Raghunathan et al. 2014; Tiryakioğlu and Hudak 2011; Weibull 1951). The joint shear strength data under different thermal conditions for different solders and nanocomposites on bare Cu and Ni-P coated substrate was fitted into Weibull distribution. The cumulative probability function of the two-parameter Weibull distribution is given by Equation 5.8.

$$P_f(\sigma_f) = 1 - \exp\left(\frac{-\sigma_f}{\sigma_0}\right)^m \quad 5.8$$

Where P_f is a probability of the joint failure when a stress σ_f is applied, σ_0 is the scale parameter, and m is the shape parameter, alternatively referred to as characteristic stress and Weibull modulus, respectively. Rearranging Equation 5.8 and by taking a natural log to both sides gives Equation 5.9.

$$\ln\left(\frac{1}{1 - P_f}\right) = \left(\frac{\sigma_f}{\sigma_0}\right)^m \quad 5.9$$

By taking a natural log again, Equation 5.9 turns into a straight line equation form as shown in Equation 5.10.

$$\ln\left(\ln\left(\frac{1}{1-P_f}\right)\right) = m\ln(\sigma_f) - m\ln(\sigma_0) \quad 5.10$$

The $(1-P_f)$ term is called the survival probability of the component when the applied stress reached the σ_f value. The survival probability is denoted by the letter S and replaced the $(1-P_f)$ term in Equation 5.10. Plotting $\ln\left(\ln\left(\frac{1}{S}\right)\right)$ versus $\ln(\sigma_f)$ gives the value for m and σ_0 with adj. R^2 value for data fitting. To plot the shear strength data, first, all samples were ranked in order of failure from small to a large value of failure stress, and P_f was determined by plotting the position formula as given in Equation 5.11.

$$P_f = (n - 0.5)/N \quad 5.11$$

Where, n is the n^{th} of order in failure, and N is the total number of samples, i.e. $N = 35$ in this study. The data of shear stress for joint failure under all different thermal conditions were considered together for each composition of respective solder. The $\ln\left(\ln\left(\frac{1}{S}\right)\right)$ vs. $\ln(\sigma_f)$ with S as a second Y-axis were plotted for all compositions. The Weibull distribution plots for the select nanocomposites of SAC0307 solder reflowed on bare Cu and Ni-P coated substrates are presented in Figure 5.11. The Weibull plots for SAC305 and SAC305-NiGe solder nanocomposites are shown in Appendix E and m , σ_0 , σ_{60} , and adjusted R^2 values obtained from the plots are tabulated in Table 5.4 and Table 5.5, respectively.

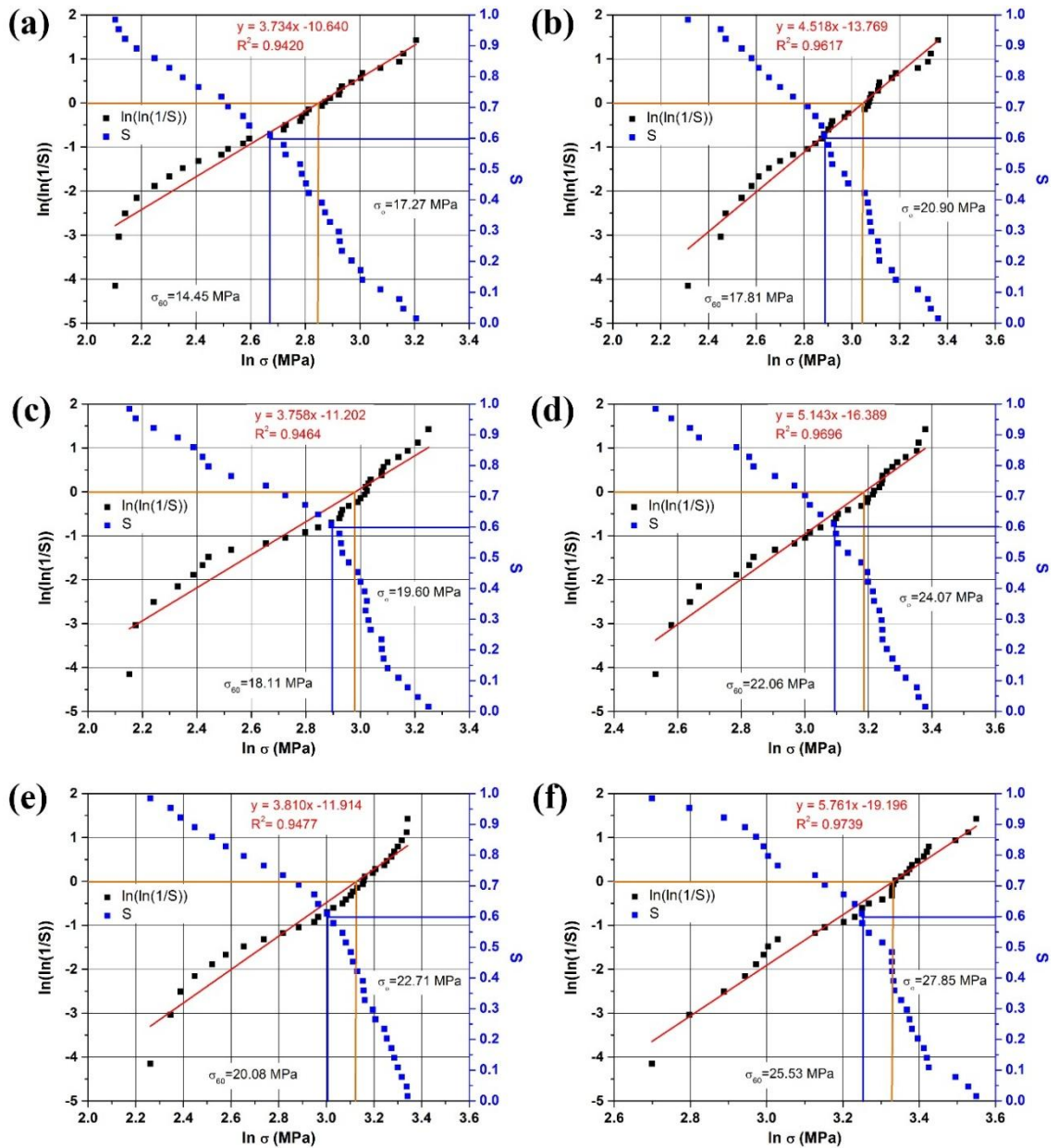


Figure 5.11: Weibull plots of joint shear strength for SAC0307, SAC0307+0.01Al₂O₃, and SAC0307+0.05Al₂O₃ solder compositions reflowed on (a), (c), (e) bare Cu substrate; and (b), (d), (f) on Ni-P coated substrate

The Weibull distribution analysis showed an increase in the Weibull module (m) i.e slope of the fitting line, characteristic stress (σ_0) and adjusted R^2 values for nanocomposite samples with Ni-P coated substrate, which indicates the improvement in the consistency of the performance and reliability of the joint with the narrower distribution of failure stress

data. The σ_0 i.e. characteristic stress value for the joint failure under the thermal environments considered in the present work for different solder nanocomposites with bare Cu and Ni-P coated substrate increased in the following order: SAC0307/Cu < SAC0307+0.01Al₂O₃/Cu < SAC0307/Ni-P < SAC0307+0.05Al₂O₃/Cu < SAC0307+0.01Al₂O₃/Ni-P < SAC0307+0.05Al₂O₃/Ni-P. The shear failure stress value for the 60% survival rate (σ_{60}) of the solder joints (i.e. up to 60% solder joint samples will survive from the total failure until that value of applied shear stress reached σ_{60} MPa) increased from 14.45 MPa for unreinforced SAC0307 solder joint with the bare copper substrate to 25.53 MPa for SAC0307+0.05Al₂O₃ nanocomposite joint on Ni-P coating. This implies that the nanocomposite solder joint with Ni-P coated substrate will fail at a much higher failure stress value than the plain solder joint with the bare copper substrate. The Weibull distribution analysis indicates the enhancement in the joint reliability of the SAC0307 solder with the small addition of Al₂O₃ nanoparticles and Ni-P coating on the substrate. Similar results were obtained for SAC305 and SAC305-NiGe solder nanocomposite joints under different thermal conditions.

Table 5.4: Characteristic parameters of Weibull analysis calculated from the fitting line for different nanocomposites of SAC305 solder reflowed on bare Cu and Ni-P coating

Solder composition	The slope of the fitting line (m) [Weibull modulus]	Y-intercept (c) [-m ln(σ_0)]	Characteristic stress (σ_0) (MPa)	σ_{60} (MPa)	Adj. R ² value
SAC305/Cu	6.22	-18.8	20.28	19.29	0.9102
SAC305/Ni-P	9.22	-29.01	23.24	21.32	0.9744
SAC305+ 0.01Al ₂ O ₃ /Cu	6.35	-19.77	22.42	20.49	0.9588
SAC305+ 0.01Al ₂ O ₃ /Ni-P	7.99	-25.59	24.60	21.97	0.9301
SAC305+ 0.05Al ₂ O ₃ /Cu	7.06	-22.62	24.77	22.19	0.9729
SAC305+ 0.05Al ₂ O ₃ /Ni-P	9.66	-32.12	27.93	26.04	0.9665

Table 5.5: Characteristic parameters of Weibull analysis calculated from the fitting line for different nanocomposites of SAC305-NiGe solder reflowed on bare Cu and Ni-P coating

Solder composition	The slope of the fitting line (m) [Weibull modulus]	Y-intercept (c) [-m ln(σ_0)]	Characteristic stress (σ_0) (MPa)	σ_{60} (MPa)	Adj. R ² value
SAC305-NiGe/Cu	4.62	-14.65	23.80	18.72	0.9147
SAC305-NiGe /Ni-P	4.90	-15.72	24.53	20.28	0.9229
SAC305-NiGe + 0.01Al ₂ O ₃ /Cu	4.66	-15.05	25.01	21.11	0.9211
SAC305-NiGe + 0.01Al ₂ O ₃ /Ni-P	4.90	-16.15	26.84	21.97	0.9261
SAC305-NiGe + 0.05Al ₂ O ₃ /Cu	5.14	-17.11	27.71	23.57	0.9474
SAC305-NiGe + 0.05Al ₂ O ₃ /Ni-P	5.33	-18.14	29.96	26.84	0.9662

5.5.2 Analysis of variance (ANOVA) experiment

The effect of different parameters on joint shear strength was studied using factorial experiments. The effect of individual parameters as well as the interaction of parameters on joint shear strength was analyzed with the help of the Analysis of Variance (ANOVA) method for the three-factor fixed effect model (Montgomery 2013). The joint shear strength was selected as the dependent variable. The independent variables were thermal condition (A) with seven levels, namely as-reflowed, heating cycles, thermal shocks, aging at room temperature, aging at 75 °C, aging at 150 °C, and aging at 200 °C; substrate coating (B) with two levels, viz. bare copper and Ni-P coated substrate; solder composition (C) with three levels, viz. SAC305, SAC305+0.01Al₂O₃ and SAC305+0.05Al₂O₃. The ANOVA results for SAC305 solder nanocomposites are summarized in Table 5.13. The results showed that the individual parameters as thermal condition (A), substrate coating (B), solder composition (C), and the interaction parameter between substrate coating and solder

composition (*BC*) are significant at a 99% confidence level, indicating a strong effect of these parameters on the joint shear strength. There is a significant interaction observed between thermal condition and solder composition (*AC*) as well as between thermal condition and substrate coating (*AB*) at a 95% confidence level; however, the significance of interaction parameters *AB* was found to be lower compared to parameter *AC* after comparing their p-values. The effect of interaction between all three parameters [thermal condition, substrate coating, and solder composition (*ABC*)] on joint shear strength, was found to be insignificant. The main effects and interaction plots for thermal condition, substrate coating, and solder composition are shown in Figure 5.12. The ANOVA table and the interaction plots clearly showed that the shear strength performance of the solder joint significantly depends on operating thermal conditions and the type of substrate as well as the solder composition used. The interaction plots suggest that the use of a combination of Ni-P substrate coating and solder composition with 0.05 wt.% Al₂O₃ nanoparticles can significantly enhance the solder joint strength and reliability under varying operating conditions. The ANOVA tables for SAC0307 and SAC305-NiGe solders are provided in Appendix F. The analysis showed a similar trend of significance for individual parameters and the relationship between parameters for SAC0307 and SAC305-NiGe solder nanocomposites as SAC305 under varying thermal condition.

Table 5.6: Analysis of Variance (ANOVA) table for joint shear strength of SAC305 solder nanocomposites

Source of Variation	Sum of Squares	Degrees of Freedom	Mean Square	F ratio (F_0)	F distribution value from table	P-Value	Remark
Thermal condition (A)	1440.1	6	240.02	113.21	$F_{0.01,6,84} = 3.025$	< 0.00001	Significant at $\alpha= 0.01$
Substrate coating (B)	224	1	224	105.66	$F_{0.01,1,84} = 6.946$	< 0.00001	Significant at $\alpha= 0.01$
Solder composition (C)	302.21	2	151.1	71.27	$F_{0.01,2,84} = 4.867$	< 0.00001	Significant at $\alpha= 0.01$
BC	33.76	2	16.88	7.96	$F_{0.01,2,84} = 4.867$	0.00069	Significant at $\alpha= 0.01$
AC	52.46	12	4.37	2.06	$F_{0.05,12,84} = 1.869$	0.0288	Significant at $\alpha= 0.05$
AB	29.89	6	4.98	2.35	$F_{0.05,6,84} = 2.208$	0.038	Significant at $\alpha= 0.05$
ABC	16.68	12	1.39	0.65	$F_{0.1,12,84} = 1.625$	0.7901	Insignificant
Error	178.67	84	2.12				
Total	2277.78	125					

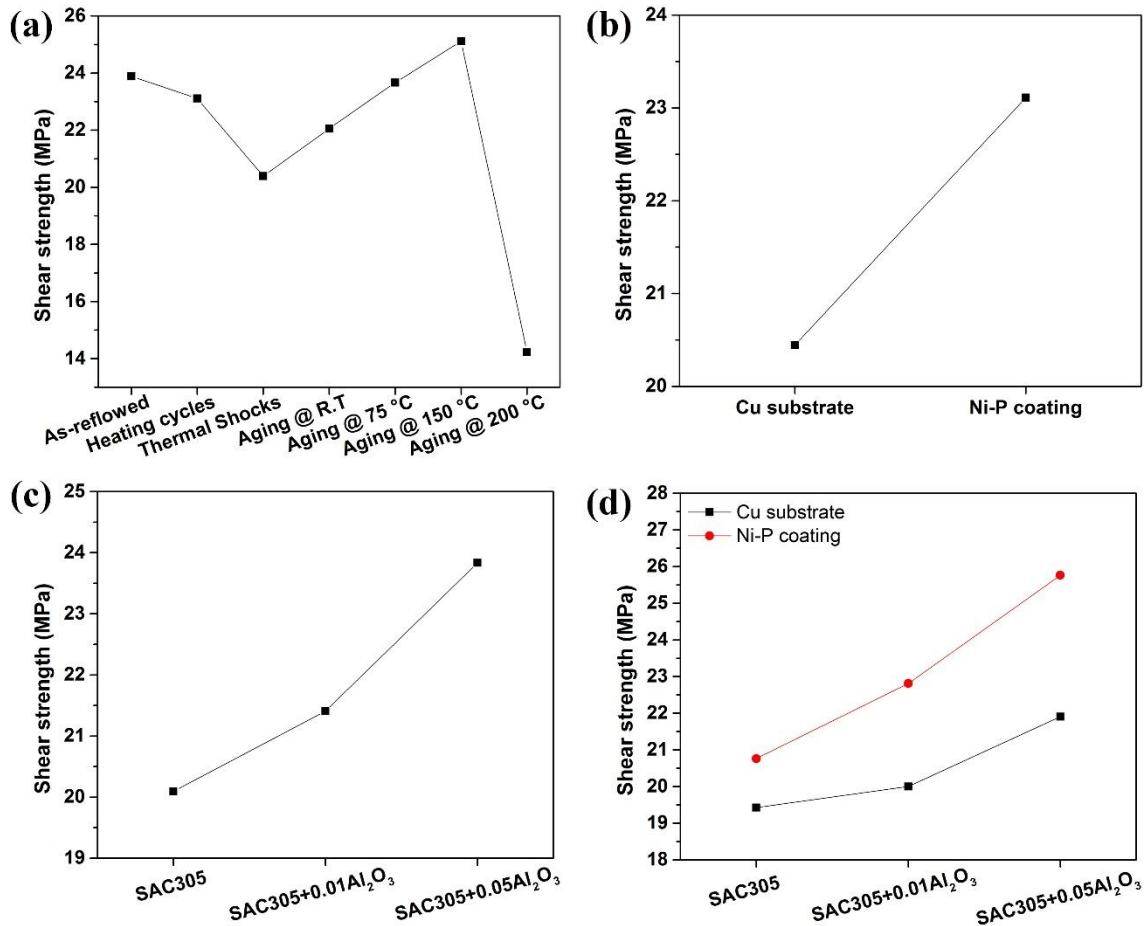


Figure 5.12: Main effect plots for (a) thermal condition, (b) substrate coating, (c) solder composition, and interaction plot for (d) substrate coating- solder composition

5.6 Fractography

There are three general modes of failure that can occur in solder joints under applied stress and strain condition. The different types of failure modes in the solder joint are illustrated in Figure 5.13. First is a solder mode, in which cracks initiate on the solder joint surface and propagate through bulk solder resulting in ductile failure. This mode of fracture occurs when the IMC layer thickness at the joint interface and the strength of the solder matrix are low. The higher strength of the IMC layer causes the fracture to propagate through the matrix. The second is mixed solder/IMC mode i.e. mixed-mode, where cracks originate on the joint surface, propagate across the bulk solder, and transit to the boundary of the IMCs which creates a detachment resulting in mixed partial ductile-brittle fracture surface. This

mode of failure is more common in the tensile-shear test. The thinner IMC layers at the interface promote longer crack propagation and more energy absorption, leading to a larger ductile fracture surface in mixed-mode failure. The third mode is IMC mode, which indicates a brittle fracture, where cracks develop at the IMC layer and propagate along the interface resulting in delamination of the interface and brittle fractured surface (Hu et al. 2014, 2016; Yazzie et al. 2012). Therefore, broken IMCs are easily visible on the fracture surface. This mode of failure is predominant when the thickness of the IMC layers is very high or the strength of the solder matrix is higher compared to the strength of the interfacial IMC layers. Although, these three failure modes may occur at the same time in the solder joint due to the microstructure changes, variations in morphology, and thickness of the IMC layer at the joint interface under varying temperature environments.

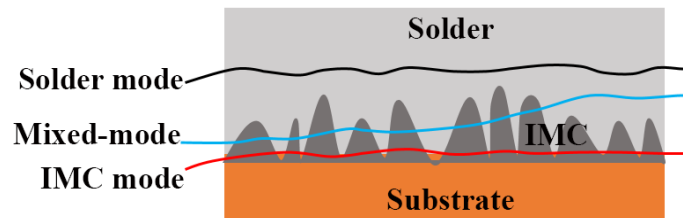


Figure 5.13: Different modes of failure in solder joint

In general, when the shear force is applied to the solder joint, more stress is concentrated at the interfacial region. The interfacial IMCs are inherently brittle, hence, the tendency for interfacial fracture is very high in solder joints. Therefore, the thickness of the IMC layers at the interface and the strength of the solder matrix are very influential in fracture mode. The elongated shear dimples and shear marks on the fracture surface (Figure 5.14-a) indicates a ductile failure with severe plastic deformation along the shear direction through the bulk solder for as-reflowed samples. The EDS analysis of the ductile fracture surface for the nanocomposite sample predominantly showed the presence of Sn with traces of Al_2O_3 nanoparticles. Elongated dimple formation is common in the shear test. The process of ductile dimple formation occurs by micro-void coalescence, i.e. voids nucleate at particles in the matrix (either by the particle cracking or separation at the particle/matrix interfaces). The growth of these voids is driven by applied stresses. The result is the coalescence of voids formed around particles in shear, which naturally results in elongated

dimples. The initial voids responsible for their micro-void coalescence ductile fracture are formed at inclusions. The ductile fracture surface for nanocomposites with small weight percent addition of nanoparticles showed refined grains with uniform distribution of small deep dimples over the fractured surface (Figure 5.14-c). The homogeneous distribution of Al_2O_3 nanoparticles increased the nucleation density in the solder matrix, which promotes the formation of dimples on the fractured surface. The ductile failure involves a high degree of plastic deformation. Some of the energy from stress concentration at the crack tips is dissipated by plastic deformation ahead of the crack as it propagates. The deep dimple signifies a better plastic property.

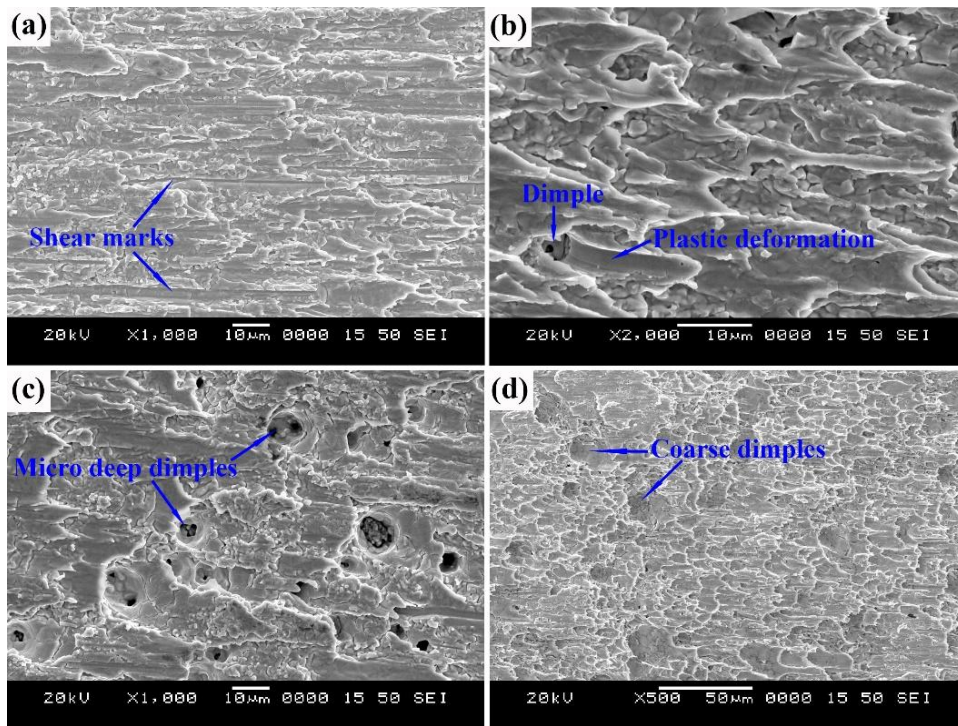


Figure 5.14: SEM images showing characteristics features of ductile failure for unreinforced solder and nanocomposites under different thermal conditions

Fracture surfaces for samples exposed to multiple heating cycles and aging conditions showed ductile fracture with a rough surface and coarser dimples (Figure 5.14-d). Samples aged at higher temperatures showed very rough dimples with exposed Cu_6Sn_5 IMC at the center of the dimple on the fractured surface. The Cu_6Sn_5 IMC exposure results from a combination of the low fracture toughness of the Cu_6Sn_5 layer and the stress concentration

at the solder/IMC interface. The fracture appears to transit from the bulk solder to the sub-micro IMC layer at the interface. The Ag_3Sn IMC particles are harder than the surrounding matrix leads to the stress and strain concentration during matrix deformation which produces voids due to matrix-particle decohesion or by fracture of IMC particle.

Figure 5.15-a shows details of a rough dimple with Ag_3Sn IMC particle arrangement inside the sheared dimple and a bulk solder-IMC interface separation plane on the fracture surface. Deep micro dimples with exposed Cu_6Sn_5 IMC and voids on fracture surface area are shown in Figure 5.15-b. The FESEM images showing the regional organization of micro dimples on ductile fracture surface (Figure 5.15-c) and magnified view of deep dimples reveals the broken Cu_6Sn_5 and Ag_3Sn IMC particles inside the dimple area Figure 5.15-d. Samples under thermal shocks and high-temperature aging conditions showed partial brittle fracture with a smooth surface. The fracture appears to be propagated from the bulk solder to the interface. The induced thermal stresses at the joint interface under thermal shocks are the main reasons for the brittle failure of the joint. The coarsening of IMC precipitates in the solder matrix and excessive IMC layer growth at the interface due to the long exposure to high-temperature environments are the prime reasons for the increase in the brittleness of the joint under aging conditions. The coarse IMC precipitates in the matrix are the favorable stress concentration sites under the loading conditions. These coarsen particles have a greater tendency of particle cracking and fragmentation under stress conditions. The cracked particles act as the discontinuous flow localization points in the matrix where micro-cracks initiate and propagate directly in the matrix, which promotes the brittle fracture in the joint. Thick and coarser IMC is more prone to the development of structural defects like micro-cracks and Kirkendall voids at the interface which weakens the joint strength and promotes brittle failure, hence affects the long term reliability of the solder joint. The micro-cracks and Kirkendall voids at the IMC interface decrease the effective area of resistance for failure which degrades the strength of the joint (Liu et al. 2016; Yu et al. 2014).

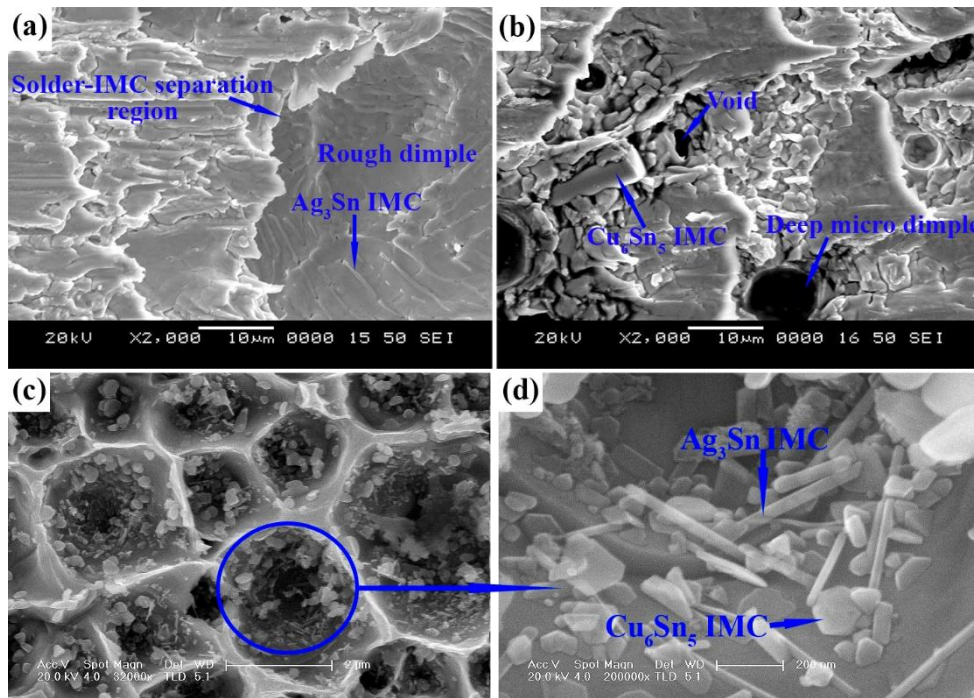


Figure 5.15: SEM micrographs showing (a) solder-IMC separation plane on fracture surface showing Ag₃Sn IMC particles inside the rough dimple, (b) deep dimples with exposed Cu₆Sn₅ IMC, and (c) FESEM images of the regional organization of micro dimples on the ductile fracture surface, (d) magnified view of deep dimple showing internal details of broken Cu₆Sn₅ and Ag₃Sn IMCs

The ductility of the solder joint was influenced by exposure to different high-temperature environments. The addition of nanoparticles in small amounts showed improvement in the ductility of the solder joint for the as-reflowed condition. The dispersion of nanoparticles, IMC suppression at the interface, and microstructure refinement are the main reasons behind improved joint strength and ductility. The solder joints under heating cycles and aging conditions showed a decrease in the ductility owing to the thickening of the IMC layer at the interface and coarsening of IMC precipitate in the matrix. Although the coarsening of Sn grains in the matrix makes the bulk solder softer, the hard and brittle IMC particles in the matrix resist and diverts the crack propagation towards the interface where the thick and brittle IMC layer promotes the brittle fracture. The resultant refined microstructure due to the addition of nanoparticles enhances the solder joint strength under high-temperature conditions with a slight reduction in ductility of the joint. The samples reflowed on Ni-P coated substrate showed a more ductile fracture area under different

thermal conditions compared to samples reflowed on the bare Cu substrate because of the planar and thin IMC layer at the interface. This suggests that the Ni-P coating on Cu substrate enhances the mechanical and thermal stability of the joint.

Chapter 6 CONCLUSIONS

The effects of MWCNT and Al_2O_3 nanoparticle reinforcement on physical, microstructural, and mechanical properties of Sn-3.6Ag, SAC0307, and SAC305 solders under multiple reflow cycles were investigated.

The best performing nanocomposites under multiple reflow conditions were selected and tested for their joint reliability under different thermal conditions using bare Cu and Ni-P coated substrates. The effects of process parameters on the performance and reliability of the joint were analyzed using factorial experiments. Based on the results and discussion, the following conclusions were drawn.

- 1) The preparation of nanocomposites through the blending of surfactant-treated nanoparticles paste and solder paste enhanced the uniformity of nanoparticle dispersion in the solder matrix and improved the flowability of the solder paste.
- 2) The addition of nanoparticles in small weight percent concentrations (0.01–0.05 wt.%) marginally affected the melting parameters of solders. The newly developed nanocomposite solders can be used in microelectronic packaging applications with the existing manufacturing setup and process designs.
- 3) The wetting area for different solders increased by about 30-55% on the addition of Al_2O_3 nanoparticles in the range of 0.01-0.5 wt.% concentrations. However, the rate of increase in the wetting area decreased with an increase in nanoparticle concentration. Nanocomposites showed higher wetting power than plain Sn-37Pb solder. The degree of enhancement in the wettability of Sn-3.6Ag solder was much lower than in SAC305 and SAC0307 solders.
- 4) The addition of MWCNT in 0.01-0.05 wt.% concentration showed improvement in the wetting area, while the addition above 0.05 wt.% significantly decreased the wettability of solders.
- 5) The addition of 0.05 wt.% Al_2O_3 nanoparticles was most effective in microstructure refinement and IMC suppression under multiple reflow cycles. The Cu_6Sn_5 IMC layer

thickness at the joint interface was suppressed by about 20% for SAC0307, 19% for SAC305, and 13% for Sn-3.6Ag solders with the addition of 0.05 wt.% Al_2O_3 nanoparticles. The extent of grain refinement of about 75% and 68% respectively in Ag_3Sn and Cu_6Sn_5 precipitates was achieved with the addition of 0.05 wt.% Al_2O_3 nanoparticles in the SAC305 solder. However, the addition of high content i.e. >0.05 wt.% concentration of nanoparticles showed a decline in the effectiveness of the nanoparticle reinforcement to obtain microstructure refinement and IMC suppression.

6) The addition of MWCNT in 0.05 wt.% concentration yielded about 10-16% reduction in IMC thickness for SAC0307 solder joint under multiple reflows. The IMC suppression with the addition of 0.05 wt.% MWCNT for SAC305 and Sn-3.6Ag solders was about 14% and 10%, respectively. However, the addition above 0.05 wt.% concentration of MWCNT was ineffective in suppressing IMC growth.

7) The IMC growth at the joint interface follows power-law growth behavior under the exposure of multiple reflow cycles. The obtained growth exponent values for nanocomposites confirmed the significant retardation in the IMC growth rate by the addition of nanoparticles. The effect of the addition of MWCNT in microstructure refinement and IMC suppression was weaker compared to Al_2O_3 nanoparticles.

8) The Al_2O_3 nanoparticles and MWCNT reinforcement considerably increased the microhardness of the solder alloys. SAC0307+0.5MWCNT nanocomposite showed about 59% higher microhardness than plain SAC0307 solder.

9) Irrespective of the solder composition, the joint strength improved with the second reflow cycle and gradually decreased with an increase in reflow cycles. The addition of Al_2O_3 nanoparticles and MWCNT in small weight percent (0.01-0.05 wt.%) concentrations yielded an appreciable increase in the joint shear strength. The 0.05 wt.% was the optimum concentration corresponding to higher solder joint strength under multiple reflow cycles. More than a 50% increase in the joint shear strength for the low-silver content SAC0307 solder was achieved with the addition of 0.05 wt.% Al_2O_3 nanoparticles. The increase in

shear strength for SAC305 and Sn-3.6Ag solder nanocomposites were obtained at about 12% under multiple reflow cycles.

10) The effectiveness of MWCNT addition in increasing the solder joint strength under multiple reflow cycles was lower compared to Al₂O₃ nanoparticles. About 20% increase in the joint shear strength was achieved with 0.05 wt.% MWCNT addition, whereas joint strength decreased by about 27% on the addition of 0.5 wt.% MWCNT.

11) The addition of small amounts of Al₂O₃ nanoparticles in solder improved the failure stress and strain of the joint. However, the addition of nanoparticles in high concentration decreased the shear strength and ductility of the joint.

12) The performance of SAC0307, SAC305, and SAC305-NiGe solders were found to be superior on both bare Cu and Ni-P coated substrates.

13) The use of electroless Ni-P coating on Cu substrate yielded about 26% reduction in interfacial IMC thickness for SAC solders. The use of 0.05 wt.% Al₂O₃ nanoparticles reinforced solder composites on Ni-P coated substrate produced the best results for microstructure refinement and yielded the highest joint shear strength under different high-temperature environments.

14) The joint shear strength under varying thermal conditions for 0.05 wt.% Al₂O₃ nanoparticle added composite for SAC0307, SAC305 and SAC305-NiGe solders with the copper substrate was about 28%, 17%, and 20% higher than respective unreinforced solders. The same composite solder joints yielded about 26-32% higher strength with Ni-P coated substrate. The extent of reduction in shear strength from as-reflowed to aging condition for samples with Ni-P coated substrate was about 40% lower compared to samples reflowed on Cu substrates. The nanocomposite solder joints with Ni-P coated substrate showed better mechanical and thermal stability compared to joints with the bare copper substrate.

15) The joint shear strength decreased monotonically with the increase in IMC thickness under various thermal conditions for all the SAC solders and nanocomposites considered

in this study. However, the strength of the solder joint is collectively influenced by IMC thickness and its morphology, bulk microstructure, the formation of IMC precipitates in the matrix, and the residual stresses at the interface developed due to varying high-temperature environments. The performance of the solder joint could be significantly improved by controlling the IMC growth at the interface.

16) The effect of nanoparticle addition on the development of physical, microstructural, and mechanical properties of the solder was more pronounced in SAC0307 solder compared to that in Sn-3.6Ag, SAC305, and SAC305-NiGe solders. The SAC0307+0.05Al₂O₃ composite showed excellent thermal stability, refined microstructure, smaller IMC growth rate, superior joint strength, and ductility compared to most preferred high-silver content SAC305 solder. This implies that the low-silver content solder can be successfully developed with the small amounts of Al₂O₃ nanoparticles addition and could be a preferable replacement for SAC305 solder in electronics packaging applications.

17) The Weibull distribution analysis of the joint shear strength showed that the reliability of the solder joint greatly improved with the small weight percent addition of Al₂O₃ nanoparticles in solders and Ni-P coating on the substrate.

18) The analysis of the variance (ANOVA) study showed that the solder joint strength is majorly affected by the operating environments, type of substrate coating, and solder composition at a 1% level of significance. The two-parameter interaction effect between the surface coating and solder composition was significant at a 1% level of significance, while the other two interactions (thermal condition and substrate coating, and thermal condition and solder composition) were significant only at a 5% level of significance. The three-parameter interaction effect between thermal conditions, substrate coating, and solder composition was found to be not significant.

19) The main effect and interaction plots from the ANOVA study suggest that the use of a combination of Ni-P substrate coating and solder composition with 0.05 wt.% Al₂O₃

nanoparticles significantly enhance the shear strength performance and reliability of the solder joint under varying operating conditions.

20) The increase in reflow cycles, thermal shocks, and long exposure to high-temperature environments increased the IMC coarsening and spalling leading to an increase in the brittleness of the joint. The composite solder joints failed with a mixed-mode of fracture. The brittle fracture area varied depending on exposure to different high-temperature environments.

21) Lead-free solder nanocomposites with 0.05 wt.% Al_2O_3 nanoparticles addition outperformed the unreinforced lead-free solders and conventional Sn-37Pb solder in terms of wetting, microhardness, and joint shear strength under different high-temperature working environments. In terms of both quality and reliability, the newly developed nanocomposites are an effective alternate for the existing lead-free and conventional Sn-Pb solders.

REFERENCES

- Abdelhadi, O. M., and Ladani, L. (2012). "IMC growth of Sn-3.5Ag/Cu system: Combined chemical reaction and diffusion mechanisms." *J. Alloys Compd.*, 537, 87–99.
- Abteu, M., and Selvaduray, G. (2000). "Lead-free solders in microelectronics." *Mater. Sci. Eng. R Reports*, 27(5), 95–141.
- Ahmed, S., Basit, M., Suhling, J. C., and Lall, P. (2016). "Effects of aging on SAC-Bi solder materials." *Proc. 15th Intersoc. Conf. Therm. Thermomechanical Phenom. Electron. Syst. ITherm 2016*, Institute of Electrical and Electronics Engineers Inc., 746–754.
- Amagai, M. (2008). "A study of nanoparticles in Sn-Ag based lead free solders." *Microelectron. Reliab.*, 48(1), 1–16.
- Anderson, I., Cook, B., Harringa, J., and Terpstra, R. (2002). "Microstructural Modifications and Properties of Sn-Ag-Cu Solder Joints Induced by Alloying." *J. Electron. Mater.*, 31(11), 1166–1174.
- Anderson, I. E., and Harringa, J. L. (2006). "Suppression of void coalescence in thermal aging of tin-silver-copper-X solder joints." *J. Electron. Mater.*, 35(1), 94–106.
- Anderson, M. P., Grest, G. S., Doherty, R. D., Li, K., and Srolovitz, D. J. (1989). "Inhibition of grain growth by second phase particles: Three dimensional Monte Carlo computer simulations." *Scr. Metall.*, 23(5), 753–758.
- Arafat, M. M., Haseeb, A. S. M. A., and Rafie Johan, M. (2011). "Interfacial reaction and dissolution behavior of Cu substrate in molten Sn-3.8Ag-0.7Cu in the presence of Mo nanoparticles." *Solder. Surf. Mt. Technol.*, 23(3), 140–149.
- Arenas, M. F., and Acoff, V. L. (2004). "Contact angle measurements of Sn-Ag and Sn-Cu lead-free solders on copper substrates." *J. Electron. Mater.*, 33(12), 1452–1458.
- ASTM Standards. (1999). "D1002-99." *Annu. B. ASTM Stand.*, ASTM International, West Conshohocken., 1–5.
- Chan, Y. H., Arafat, M. M., and Haseeb, A. S. M. A. (2013). "Effects of reflow on the interfacial characteristics between Zn nanoparticles containing Sn-3.8Ag-0.7Cu solder and copper substrate." *Solder. Surf. Mt. Technol.*, 25(2), 91–98.
- Che Ani, F., Jalar, A., Saad, A. A., Khor, C. Y., Ismail, R., Bachok, Z., Abas, M. A., and Othman, N. K. (2018). "The influence of Fe₂O₃ nano-reinforced SAC lead-free solder in the ultra-fine electronics assembly." *Int. J. Adv. Manuf. Technol.*, 96(1–4), 717–733.
- Che, F. X., Zhu, W. H., Poh, E. S. W., Zhang, X. W., and Zhang, X. R. (2010). "The study of mechanical properties of Sn-Ag-Cu lead-free solders with different Ag contents and Ni doping under different strain rates and temperatures." *J. Alloys Compd.*, 507(1), 215–224.
- Chen, G., Huang, B., Liu, H., Chan, Y. C., Tang, Z., and Wu, F. (2016). "An investigation of microstructure and properties of Sn_{3.0}Ag_{0.5}Cu-XAl₂O₃ composite solder." *Solder. Surf. Mt. Technol.*, 28(2), 84–92.

- Chen, G., Wu, F., Liu, C., Xia, W., and Liu, H. (2015a). "Effects of fullerenes reinforcement on the performance of 96.5Sn-3Ag-0.5Cu lead-free solder." *Mater. Sci. Eng. A*, 636, 484–492.
- Chen, L.-Y., Xu, J.-Q., and Li, X.-C. (2015b). "Controlling phase growth during solidification by nanoparticles." *Mater. Res. Lett.*, 3(1), 43–49.
- Chen, S. W., Wang, C. H., Lin, S. K., Chiu, C. N., and Chen, C. C. (2007). "Phase transformation and microstructural evolution in solder joints." *Jom*, 59(1), 39–43.
- Cheng, F., Gao, F., and Zhang, J. (2011). "Tensile properties and wettability of SAC0307 and SAC105 low Ag lead-free solder alloys." *J. Mater. Sci.*, 46, 3424–3429.
- Cheng, F., Nishikawa, H., and Takemoto, T. (2008). "Microstructural and mechanical properties of Sn-Ag-Cu lead-free solders with minor addition of Ni and/or Co." *J. Mater. Sci.*, 43(10), 3643–3648.
- Cheng, S., Huang, C.-M., and Pecht, M. (2017). "A review of lead-free solders for electronics applications." *Microelectron. Reliab.*, 75, 77–95.
- Chuang, T. H., Wu, M. W., Chang, S. Y., Ping, S. F., and Tsao, L. C. (2011a). "Strengthening mechanism of nano-Al₂O₃ particles reinforced Sn_{3.5}Ag_{0.5}Cu lead-free solder." *J. Mater. Sci. Mater. Electron.*, 22(8), 1021–1027.
- Chuang, T. H., Wu, M. W., Chang, S. Y., Ping, S. F., and Tsao, L. C. (2011b). "Strengthening mechanism of nano-Al₂O₃ particles reinforced Sn_{3.5}Ag_{0.5}Cu lead-free solder." *J. Mater. Sci. Mater. Electron.*, 22(8), 1021–1027.
- Cotell, C. M., Sprague, J. A., and Fred A. Smidt, J. (1994). *ASM handbook volume 5-surface engineering*. ASM International.
- Crawla, N., Shen, Y. L., Deng, X., and Ege, E. S. (2004). "An evaluation of the lap-shear test for sn-rich solder/Cu couples: Experiments and simulation." *J. Electron. Mater.*, 33(12), 1589–1595.
- Dele-Afolabi, T. T., Azmah Hanim, M. A., Norkhairunnisa, M., Yusoff, H. M., and Suraya, M. T. (2015). "Growth kinetics of intermetallic layer in lead-free Sn–5Sb solder reinforced with multi-walled carbon nanotubes." *J. Mater. Sci. Mater. Electron.*, 26(10), 8249–8259.
- Deng, X., Sidhu, R. S., Johnson, P., and Chawla, N. (2005). "Influence of reflow and thermal aging on the shear strength and fracture behavior of Sn-3.5Ag solder/Cu joints." *Metall. Mater. Trans. A Phys. Metall. Mater. Sci.*, 36 A(1), 55–64.
- Desmarest, S. G. (2012). "Reliability of Pb-free solders for harsh environment electronic assemblies." *Mater. Sci. Technol.*, 28(3), 257–273.
- Dudek, M. A., and Chawla, N. (2010). "Effect of rare-earth (La, Ce, and Y) additions on the microstructure and mechanical behavior of Sn-3.9Ag-0.7Cu solder alloy." *Metall. Mater. Trans. A Phys. Metall. Mater. Sci.*, 41(3), 610–620.
- Dudek, M. A., Sidhu, R. S., Chawla, N., and Renavikar, M. (2006). "Microstructure and mechanical behavior of novel rare earth-containing Pb-free solders." *J. Electron. Mater.*,

35(12), 2088–2097.

Dutta, I., Kumar, P., and Subbarayan, G. (2009). “Microstructural coarsening in Sn-Ag-based solders and its effects on mechanical properties.” *Jom*, 61(6), 29–38.

El-Daly, A. A., Desoky, W. M., Elmosalami, T. A., El-Shaarawy, M. G., and Abdraboh, A. M. (2015a). “Microstructural modifications and properties of SiC nanoparticles-reinforced Sn-3.0Ag-0.5Cu solder alloy.” *Mater. Des.*, 65, 1196–1204.

El-Daly, A. A., El-Hosainy, H., Elmosalami, T. A., and Desoky, W. M. (2015b). “Microstructural modifications and properties of low-Ag-content Sn-Ag-Cu solder joints induced by Zn alloying.” *J. Alloys Compd.*, 653, 402–410.

El-Daly, A. A., El-Taher, A. M., and Dalloul, T. R. (2014a). “Improved creep resistance and thermal behavior of Ni-doped Sn-3.0Ag-0.5Cu lead-free solder.” *J. Alloys Compd.*, 587, 32–39.

El-Daly, A. A., El-Taher, A. M., and Gouda, S. (2015c). “Development of new multicomponent Sn-Ag-Cu-Bi lead-free solders for low-cost commercial electronic assembly.” *J. Alloys Compd.*, 627, 268–275.

El-Daly, A. A., Hammad, A. E., Al-Ganainy, G. S., and Ragab, M. (2014b). “Properties enhancement of low Ag-content Sn-Ag-Cu lead-free solders containing small amount of Zn.” *J. Alloys Compd.*, 614, 20–28.

Ely, D. R., Edwin García, R., and Thommes, M. (2014). “Ostwald-Freundlich diffusion-limited dissolution kinetics of nanoparticles.” *Powder Technol.*, 257, 120–123.

Fallahi, H., Nurulakmal, M. S., Arezodar, A. F., and Abdullah, J. (2012). “Effect of iron and indium on IMC formation and mechanical properties of lead-free solder.” *Mater. Sci. Eng. A*, 553, 22–31.

Flanders, D. R., Jacobs, E. G., and Pinizzotto, R. F. (1997). “Activation energies of intermetallic growth of Sn-Ag eutectic solder on copper substrates.” *J. Electron. Mater.*, 26(7), 883–887.

Fouzder, T., Chan, Y. C., and Chan, D. K. (2014). “Influence of cerium oxide (CeO₂) nanoparticles on the microstructure and hardness of tin–silver–copper (Sn–Ag–Cu) solders on silver (Ag) surface-finished copper (Cu) substrates.” *J. Mater. Sci. Mater. Electron.*, 25(12), 5375–5387.

Gain, A. K., Chan, Y. C., and Yung, W. K. C. (2011a). “Effect of additions of ZrO₂ nanoparticles on the microstructure and shear strength of Sn-Ag-Cu solder on Au/Ni metallized Cu pads.” *Microelectron. Reliab.*, 51(12), 2306–2313.

Gain, A. K., Fouzder, T., Chan, Y. C., Sharif, A., Wong, N. B., and Yung, W. K. C. (2010). “The influence of addition of Al nano-particles on the microstructure and shear strength of eutectic Sn-Ag-Cu solder on Au/Ni metallized Cu pads.” *J. Alloys Compd.*, 506(1), 216–223.

Gain, A. K., Fouzder, T., Chan, Y. C., and Yung, W. K. C. (2011b). “Microstructure,

kinetic analysis and hardness of Sn-Ag-Cu-1 wt% nano-ZrO₂ composite solder on OSP-Cu pads." *J. Alloys Compd.*, 509(7), 3319–3325.

Gain, A. K., and Zhang, L. (2016). "Microstructure, mechanical and electrical performances of zirconia nanoparticles-doped tin-silver-copper solder alloys." *J. Mater. Sci. Mater. Electron.*, 27, 7524–7533.

Gao, F., Takemoto, T., and Nishikawa, H. (2006). "Effects of Co and Ni addition on reactive diffusion between Sn-3.5Ag solder and Cu during soldering and annealing." *Mater. Sci. Eng. A*, 420(1–2), 39–46.

Gao, H., Wei, F., Lin, C., Shu, T., Sui, Y., Qi, J., and Zhang, X. (2019). "Growth behavior of intermetallic compounds on Sn-10Bi-0.7Cu-0.15Co/Co interface under multiple reflows." *Mater. Lett.*, 252, 92–95.

Goh, Y., Haseeb, A. S. M. A., Liew, H. L., and Sabri, M. F. M. (2015). "Deformation and fracture behaviour of electroplated Sn–Bi/Cu solder joints." *J. Mater. Sci.*, 50(12), 4258–4269.

Hamilton, C., Snugovsky, P., and Kelly, M. (2007). "Have High Cu Dissolution Rates of SAC305/405 Alloys Forced a Change in the Lead Free Alloy Used during PTH Processes?" *Proc. PanPacific*

Han, R., Xue, S., Hu, Y., Wang, Z., and Ja, J. (2012). "Development of flux for Sn–Zn lead-free solder." *Trans. China Weld. Inst.*, 33(10), 101–104.

He, M., Lau, W. H., Qi, G., and Chen, Z. (2004). "Intermetallic compound formation between Sn-3.5Ag solder and Ni-based metallization during liquid state reaction." *Thin Solid Films*, 462–463(SPEC. ISS.), 376–383.

Ho, C. E., Kuo, T. T., Wang, C. C., and Wu, W. H. (2012). "Inhibiting the growth of Cu₃Sn and Kirkendall voids in the Cu/Sn-Ag-Cu system by minor Pd alloying." *Electron. Mater. Lett.*, 8(5), 495–501.

Hu, X., Li, Y., Liu, Y., Liu, Y., and Min, Z. (2014). "Microstructure and shear strength of Sn37Pb/Cu solder joints subjected to isothermal aging." *Microelectron. Reliab.*, 54(8), 1575–1582.

Hu, X., Xu, T., Keer, L. M., Li, Y., and Jiang, X. (2016). "Microstructure evolution and shear fracture behavior of aged Sn3Ag0.5Cu/Cu solder joints." *Mater. Sci. Eng. A*, 673, 167–177.

Huang, H. Y., Yang, C. W., and Pan, S. Z. (2013). "Wetting and the reaction of multiwalled carbon nanotube-Reinforced composite solder with a copper substrate." *Sci. Eng. Compos. Mater.*, 20(4), 301–306.

J-STD-020D.1. (2008). *IPC/JEDEC J-STD-020D.1 March 2008*.

Jiang, D. S., Wang, Y. P., and Hsiao, C. S. (2006). "Effect of minor doping elements on lead free solder joint quality." *Proc. Electron. Packag. Technol. Conf. EPTC*, 385–389.

Kamrani, S., Hübler, D., Ghasemi, A., and Fleck, C. (2019). "Enhanced strength and

- ductility in magnesium matrix composites reinforced by a high volume fraction of nano- and submicron-sized SiC particles produced by mechanical milling and hot extrusion.” *Materials (Basel)*, 12(20), 3445.
- Kanlayasiri, K., and Ariga, T. (2010). “Influence of thermal aging on microhardness and microstructure of Sn-0.3Ag-0.7Cu-xIn lead-free solders.” *J. Alloys Compd.*, 504(1), 5–9.
- Kanlayasiri, K., and Kongchayasukawat, R. (2018). “Property alterations of Sn – 0 . 6Cu – 0 . 05Ni – Ge lead-free solder by Ag , Bi , In and Sb addition.” *Trans. Nonferrous Met. Soc. China*, 28(6), 1166–1175.
- Kanlayasiri, K., Mongkolwongrojn, M., and Ariga, T. (2009). “Influence of indium addition on characteristics of Sn-0.3Ag-0.7Cu solder alloy.” *J. Alloys Compd.*, 485(1–2), 225–230.
- Kariya, Y., Hosoi, T., Kimura, T., Terashima, S., Tanaka, M., and Suga, T. (2004). “Fatigue life enhancement of low silver content Sn-Ag-Cu flip-chip interconnects by Ni addition.” *Thermomechanical Phenom. Electron. Syst. -Proceedings Intersoc. Conf.*, 2, 103–108.
- Keller, J., Baither, D., Wilke, U., and Schmitz, G. (2011a). “Mechanical properties of Pb-free SnAg solder joints.” *Acta Mater.*, 59, 2731–2741.
- Keller, J., Baither, D., Wilke, U., and Schmitz, G. (2011b). “Mechanical properties of Pb-free SnAg solder joints.” *Acta Mater.*, 59(7), 2731–2741.
- Kim, J. Y., Yu, J., and Kim, S. H. (2009). “Effects of sulfide-forming element additions on the Kirkendall void formation and drop impact reliability of Cu/Sn-3.5Ag solder joints.” *Acta Mater.*, 57(17), 5001–5012.
- Kim, K. S., Huh, S. H., and Sukanuma, K. (2003). “Effects of intermetallic compounds on properties of Sn-Ag-Cu lead-free soldered joints.” *J. Alloys Compd.*, 352(1–2), 226–236.
- Kim, S. H., Park, M. S., Choi, J. P., and Aranas, C. (2017). “Improved electrical and thermo-mechanical properties of a MWCNT/In-Sn-Bi composite solder reflowing on a flexible PET substrate.” *Sci. Rep.*, 7(1), 1–14.
- Kotadia, H. R., Howes, P. D., and Mannan, S. H. (2014). “A review: On the development of low melting temperature Pb-free solders.” *Microelectron. Reliab.*, 54(6–7), 1253–1273.
- Kotadia, H. R., Mokhtari, O., Clode, M. P., Green, M. A., and Mannan, S. H. (2012). “Intermetallic compound growth suppression at high temperature in SAC solders with Zn addition on Cu and Ni-P substrates.” *J. Alloys Compd.*, 511(1), 176–188.
- Kumar, G., and Prabhu, K. N. (2007). “Review of non-reactive and reactive wetting of liquids on surfaces.” *Adv. Colloid Interface Sci.*, 133(2), 61–89.
- Kumar, K. M., Kripesh, V., and Tay, A. A. O. (2008). “Single-wall carbon nanotube (SWCNT) functionalized Sn–Ag–Cu lead-free composite solders.” *J. Alloys Compd.*, 450, 229–237.
- Lalonde, A., Emelander, D., Jeannette, J., Larson, C., Rietz, W., Swenson, D., and

- Henderson, D. W. (2004). "Quantitative metallography of β -Sn dendrites in Sn-3.8Ag-0.7Cu ball grid array solder balls via electron backscatter diffraction and polarized light microscopy." *J. Electron. Mater.*, 33(12), 1545–1549.
- Laurila, T., Hurtig, J., Vuorinen, V., and Kivilahti, J. K. (2009). "Effect of Ag, Fe, Au and Ni on the growth kinetics of Sn-Cu intermetallic compound layers." *Microelectron. Reliab.*, 49(3), 242–247.
- Laurila, T., Vuorinen, V., and Kivilahti, J. K. (2005). "Interfacial reactions between lead-free solders and common base materials." *Mater. Sci. Eng. R Reports*, 49, 1–60.
- Laurila, T., Vuorinen, V., and Paulasto-Kröckel, M. (2010a). "Impurity and alloying effects on interfacial reaction layers in Pb-free soldering." *Mater. Sci. Eng. R Reports*, 68(1–2), 1–38.
- Laurila, T., Vuorinen, V., and Paulasto-Kröckel, M. (2010b). "Impurity and alloying effects on interfacial reaction layers in Pb-free soldering." *Mater. Sci. Eng. R Reports*, Elsevier.
- Lee, C. J., Moon, J. J., Jung, K. H., and Jung, S. B. (2017). "Thermal Characteristic of Sn-MWCNT Nanocomposite Solder in LED Package." *Proc. - Electron. Components Technol. Conf.*, 2225–2230.
- Lee, L. M., and Mohamad, A. A. (2013). "Interfacial Reaction of Sn-Ag-Cu Lead-Free Solder Alloy on Cu: A Review." *Adv. Mater. Sci. Eng.*, 2013, 1–11.
- Leong, J. C., Tsao, L. C., Wu, M. W., and Chang, S. Y. (2011). "Effect of nano-TiO₂ addition on the microstructure and bonding strengths of Sn_{3.5}Ag_{0.5}Cu composite solder BGA packages with immersion Sn surface finish." *J. Mater. Sci. Mater. Electron.*, 22, 1443–1449.
- Lewis, D., Allen, S., Notis, M., and Scotch, A. (2002). "Determination of the eutectic structure in the Ag-Cu-Sn system." *J. Electron. Mater.*, 31(2), 161–167.
- Li, J. F., Agyakwa, P. A., and Johnson, C. M. (2012). "Effect of trace Al on growth rates of intermetallic compound layers between Sn-based solders and Cu substrate." *J. Alloys Compd.*, 545, 70–79.
- Li, J. F., Agyakwa, P. A., and Johnson, C. M. (2014). "Suitable thicknesses of base metal and interlayer, and evolution of phases for Ag/Sn/Ag transient liquid-phase joints used for power die attachment." *J. Electron. Mater.*, 43(4), 983–995.
- Li, L., and An, M. (2008). "Electroless nickel-phosphorus plating on SiCp/Al composite from acid bath with nickel activation." *J. Alloys Compd.*, 461(1–2), 85–91.
- Li, X., Ma, Y., Zhou, W., and Wu, P. (2017). "Effects of nanoscale Cu₆Sn₅ particles addition on microstructure and properties of SnBi solder alloys." *Mater. Sci. Eng. A*, 684, 328–334.
- Liang, J., Dariavach, N., and Shangguan, D. (2007). "Solidification Condition Effects on Microstructures and Creep Resistance of Sn-3 . 8Ag-0 . 7Cu Lead-Free Solder." *Metall.*

Mater. Trans. A, 38A, 1530–1538.

Lim, R. (2010). *Investigation into Lead-Free Solder in Australian Defence Force Applications*.

Lin, D. C., Wang, G. X., Srivatsan, T. S., Al-Hajri, M., and Petraroli, M. (2003). “Influence of titanium dioxide nanopowder addition on microstructural development and hardness of tin-lead solder.” *Mater. Lett.*, 57(21), 3193–3198.

Lin, K. S., Huang, H. Y., and Chou, C. P. (2009). “Interfacial reaction between Sn{single bond}1Ag{single bond}0.5Cu({single bond}Co) solder and Cu substrate with Au/Ni surface finish during reflow reaction.” *J. Alloys Compd.*, 471(1–2), 291–295.

Lin, Y. C., Wang, K. J., and Duh, J. G. (2010). “Detailed phase evolution of a phosphorous-rich layer and formation of the Ni-Sn-P compound in Sn-Ag-Cu/electroplated Ni-P solder joints.” *J. Electron. Mater.*, 39(3), 283–294.

Liu, J., Chen, Z., Zhang, F., Ji, G., Wang, M., Ma, Y., Ji, V., Zhong, S., Wu, Y., and Wang, H. (2018). “Simultaneously increasing strength and ductility of nanoparticles reinforced al composites via accumulative orthogonal extrusion process.” *Mater. Res. Lett.*, 6(8), 406–412.

Liu, P., Yao, P., and Liu, J. (2009). “Evolutions of the interface and shear strength between SnAgCu-xNi solder and Cu substrate during isothermal aging at 150 ??C.” *J. Alloys Compd.*, 486(1–2), 474–479.

Liu, W., Wang, Y., Ma, Y., Yu, Q., and Huang, Y. (2016). “Interfacial microstructure evolution and shear behavior of Au-20Sn/(Sn)Cu solder joints bonded at 250°C.” *Mater. Sci. Eng. A*, 651, 626–635.

Liu, Y., Sun, F., and Liu, X. (2010). “Improving Sn-0.3Ag-0.7Cu low-Ag lead-free solder performance by adding Bi element.” *2010 Int. Forum Strateg. Technol. IFOST 2010*, 343–346.

Liukkonen, M., Havia, E., Leinonen, H., and Hiltunen, Y. (2011). “Quality-oriented optimization of wave soldering process by using self-organizing maps.” *Appl. Soft Comput. J.*, 11(1), 214–220.

Ma, H. R., Kunwar, A., Shang, S. Y., Jiang, C. R., Wang, Y. P., Ma, H. T., and Zhao, N. (2018). “Evolution behavior and growth kinetics of intermetallic compounds at Sn/Cu interface during multiple reflows.” *Intermetallics*, 96(November 2017), 1–12.

Ma, H., and Suhling, J. C. (2009a). “A review of mechanical properties of lead-free solders for electronic packaging.” *J. Mater. Sci.*, 44(5), 1141–1158.

Ma, H., and Suhling, J. C. (2009b). “A review of mechanical properties of lead-free solders for electronic packaging.” *J. Mater. Sci.*

Ma, Z. L., Belyakov, S. A., and Gourlay, C. M. (2016). “Effects of cobalt on the nucleation and grain refinement of Sn-3Ag-0.5Cu solders.” *J. Alloys Compd.*, 682, 326–337.

Mavoori, H., and Jin, S. (1998). “New, creep-resistant, low melting point solders with

- ultrafine oxide dispersions.” *J. Electron. Mater.*, 27(11), 1216–1222.
- Mayappan, R., Hassan, A. A., Ab Ghani, N. A., Yahya, I., and Andas, J. (2016). “Improvement in intermetallic thickness and joint strength in carbon nanotube composite Sn-3.5Ag lead-free solder.” *Mater. Today Proc.*, 3(6), 1338–1344.
- Mei, Z., Kaufmann, M., Eslambolchi, A., and Johnson, P. (1998). “Brittle interfacial fracture of PBGA packages soldered on electroless nickel/immersion gold.” *Proc. - Electron. Components Technol. Conf.*, Part F1334, 952–961.
- Mohan Kumar, K., Kripesh, V., and Tay, A. A. O. (2006). “Sn-Ag-Cu lead-free composite solders for ultra-fine-pitch wafer-level packaging.” *Proc. - Electron. Components Technol. Conf.*, 237–243.
- Mohd Salleh, M. A. A., McDonald, S. D., Gourlay, C. M., Yasuda, H., and Nogita, K. (2016). “Suppression of Cu₆Sn₅ in TiO₂ reinforced solder joints after multiple reflow cycles.” *Mater. Des.*, 108, 418–428.
- Montgomery, D. C. (2013). *Design and analysis of experiments*. John Wiley & Sons, Inc.
- Mookam, N., Tunthawiroon, P., and Kanlayasiri, K. (2018). “Effects of copper content in Sn-based solder on the intermetallic phase formation and growth during soldering.” *IOP Conf. Ser. Mater. Sci. Eng.*, 361(1).
- Moon, K. W., Boettinger, W. J., Kattner, U. R., Biancaniello, F. S., and Handwerker, C. A. (2000). “Experimental and thermodynamic assessment of Sn-Ag-Cu solder alloys.” *J. Electron. Mater.*, 29(10), 1122–1136.
- Nai, S. M. L., Han, Y. D., Jing, H. Y., Tan, C. M., Wei, J., and Gupta, M. (2009). “Using Nanoparticles and Carbon Nanotubes to Enhance the Properties of a Lead-free Solder.” *Nanotech Conf. Expo 2009, Vol 2, Tech. Proc. - Nanotechnol. 2009 Life Sci. Med. Diagnostics, Bio Mater. Compos.*, 538–541.
- Nai, S. M. L., Wei, J., and Gupta, M. (2006). “Improving the performance of lead-free solder reinforced with multi-walled carbon nanotubes.” *Mater. Sci. Eng. A*, 423, 166–169.
- Nai, S. M. L., Wei, J., and Gupta, M. (2008). “Effect of carbon nanotubes on the shear strength and electrical resistivity of a lead-free solder.” *J. Electron. Mater.*, 37(4), 515–522.
- Nakata, Y., Hashimoto, T., Kurasawa, M., Hayashi, Y., and Shohji, I. (2017). “Formation mechanism of pillar-shaped intermetallic compounds dispersed lead-free solder joint.” *IOP Conf. Ser. Mater. Sci. Eng.*, 257(1).
- Niranjani, V. L., Chandra Rao, S., Sarkar, R., and Kamat, S. V. (2012). “The influence of addition of nanosized molybdenum and nickel particles on creep behavior of Sn-Ag lead free solder alloy.” *J. Alloys Compd.*, 542, 136–141.
- Nogita, K., McDonald, S. D., Tsukamoto, H., Read, J., Suenaga, S., and Nishimura, T. (2009). “Inhibiting Cracking of Interfacial Cu₆Sn₅ by Ni Additions to Sn-based Lead-free Solders.” *Trans. Japan Inst. Electron. Packag.*, 2(1), 46–54.

- Nogita, K., and Nishimura, T. (2008). "Nickel-stabilized hexagonal (Cu, Ni)₆Sn₅ in Sn-Cu-Ni lead-free solder alloys." *Scr. Mater.*, 59(2), 191–194.
- Optronics, S. S. (2015). *Application Note 103: Pb-Free Solder Process Guidelines Application*.
- Pan, H., Wang, Y., Luo, W., Gao, L., and Li, M. (2018). "Effect of Ni thickness on the IMC and reliability of ultrathin ENEPIG." *Proc. - 2018 19th Int. Conf. Electron. Packag. Technol. ICEPT 2018*, 667–671.
- Pandher, R. S., Lewis, B. G., Vangaveti, R., and Singh, B. (2007). "Drop shock reliability of lead-free alloys - Effect of micro-additives." *Proc. - Electron. Components Technol. Conf.*, 669–676.
- Paramsothy, M., Chan, J., Kwok, R., and Gupta, M. (2012). "Al₂O₃ Nanoparticle Addition to Commercial Magnesium Alloys: Multiple Beneficial Effects." *Nanomaterials*, 2(2), 147–162.
- Paul, A., Ghosh, C., and Boettinger, W. J. (2011). "Diffusion parameters and growth mechanism of phases in the Cu-Sn system." *Metall. Mater. Trans. A Phys. Metall. Mater. Sci.*, 42(4), 952–963.
- Peng, H., Huang, B., Chen, G., Wu, F., Liu, H., and Chan, Y. C. (2015). "Effect of 0.8 wt% Al₂O₃ nanoparticles addition on the microstructures and electromigration behavior of Sn-Ag-Cu solder joint." *16th Int. Conf. Electron. Packag. Technol. ICEPT 2015*, 1014–1017.
- Peng, W., Monlevade, E., and Marques, M. E. (2007). "Effect of thermal aging on the interfacial structure of SnAgCu solder joints on Cu." *Microelectron. Reliab.*, 47(12), 2161–2168.
- Perez, M. (2005). "Gibbs-Thomson effects in phase transformations." *Scr. Mater.*, 52(8), 709–712.
- Prasad, L. C., and Mikula, A. (2006). "Surface segregation and surface tension in Al-Sn-Zn liquid alloys." *Phys. B Condens. Matter*, 373(1), 142–149.
- Raghunathan, R., Prabhu, K. N., and Hegde, T. G. (2014). "Two parameter Weibull analysis of the effect of chemical modification of Al-7Si-0.3 Mg alloy on ultimate tensile strength." *Trans. Indian Inst. Met.*, 67(6), 997–1000.
- Ramli, M. I. I., Saud, N., Salleh, M. A. A. M., Derman, M. N., and Said, R. M. (2016). "Effect of TiO₂ additions on Sn-0.7Cu-0.05Ni lead-free composite solder." *Microelectron. Reliab.*, 65, 255–264.
- Reid, M., Punch, J., Collins, M., and Ryan, C. (2008). "Effect of Ag content on the microstructure of Sn-Ag-Cu based solder alloys." *Solder. Surf. Mt. Technol.*, 20(4), 3–8.
- Rohrer, G. S. (2010). "introduction to grains, phases, and interfaces-an interpretation of microstructure," *Trans. AIME, 1948, vol. 175, pp. 15-51, by C.S. Smith. Metall. Mater. Trans. A Phys. Metall. Mater. Sci.*
- Schaefer, M., Fournelle, R. A., and Liang, J. (1998). "Theory for intermetallic phase

growth between Cu and liquid Sn-Pb solder based on grain boundary diffusion control.” *J. Electron. Mater.*, 27(11), 1167–1176.

Shao, H., Li, M., and Hu, A. (2019). “The effect of Ag₃Sn and Cu₃Sn nanoparticles on the IMC morphology of Sn-3.0Ag-0.5Cu solder.” *2019 20th Int. Conf. Electron. Packag. Technol. ICEPT 2019*, Institute of Electrical and Electronics Engineers Inc.

Shen, J., Liu, Y. C., Han, Y. J., Tian, Y. M., and Gao, H. X. (2006). “Strengthening effects of ZrO₂ nanoparticles on the microstructure and microhardness of Sn-3.5Ag lead-free solder.” *Mater. Sci. Eng. A*, 441(1–2), 135–141.

Shnawah, D. A. A., Said, S. B. M., Sabri, M. F. M., Badruddin, I. A., and Che, F. X. (2012a). “Microstructure, mechanical, and thermal properties of the Sn-1Ag-0.5Cu solder alloy bearing Fe for electronics applications.” *Mater. Sci. Eng. A*, 551, 160–168.

Shnawah, D. A., Said, S. B. M., Sabri, M. F. M., Badruddin, I. A., and Che, F. X. (2012b). “High-reliability low-Ag-content Sn-Ag-Cu solder joints for electronics applications.” *J. Electron. Mater.*, 41(9), 2631–2658.

Shohji, I., Tsunoda, S., Watanabe, H., Asai, T., and Nagano, M. (2005). “Reliability of solder joint with Sn-Ag-Cu-Ni-Ge lead-free alloy under heat exposure conditions.” *Mater. Trans.*, 46(12), 2737–2744.

Siewert, T. A., and Handwerker, C. . . (2002). *Test Procedures for Developing Solder Data*. National Institute of Standards and Technology.

Sohn, Y., Yu, J., Kang, S. K., Shih, D., and Lee, T. (2004). “Study of spalling behavior of intermetallic compounds during the reaction between electroless Ni-P metallization and lead-free solders.” *Electron. Components Technol. Conf.*, 75–81.

Song, H. Y., Zhu, Q. S., Wang, Z. G., Shang, J. K., and Lu, M. (2010). “Effects of Zn addition on microstructure and tensile properties of Sn-1Ag-0.5Cu alloy.” *Mater. Sci. Eng. A*, 527(6), 1343–1350.

Song, J. M., Lin, J. J., Huang, C. F., and Chuang, H. Y. (2007). “Crystallization, morphology and distribution of Ag₃Sn in Sn-Ag-Cu alloys and their influence on the vibration fracture properties.” *Mater. Sci. Eng. A*, 466(1–2), 9–17.

Suganuma, K. (2001). “Advances in lead-free electronics soldering.” *Curr. Opin. Solid State Mater. Sci.*, 5(1), 55–64.

Sun, L., Zhang, L., Xu, L., Zhong, S. J., Ma, J., and Bao, L. (2016). “Effect of nano-Al addition on properties and microstructure of low-Ag content Sn-1Ag-0.5Cu solders.” *J. Mater. Sci. Mater. Electron.*, 27(7), 7665–7673.

Szárász, Z., Trojanová, Z., Cabbibo, M., and Evangelista, E. (2007). “Strengthening in a WE54 magnesium alloy containing SiC particles.” *Mater. Sci. Eng. A*, 462(1–2), 225–229.

Tan, A. T., Tan, A. W., and Yusof, F. (2015). “Influence of nanoparticle addition on the formation and growth of intermetallic compounds (IMCs) in Cu/Sn-Ag-Cu/Cu solder joint during different thermal conditions.” *Sci. Technol. Adv. Mater.*, 16, 033505.

- Tang, Y., Li, G. Y., and Pan, Y. C. (2014). "Effects of TiO₂ nanoparticles addition on microstructure, microhardness and tensile properties of Sn-3.0Ag-0.5Cu-xTiO₂ composite solder." *Mater. Des.*, 55, 574–582.
- Ting Tan, A., Wen Tan, A., and Yusof, F. (2015). "Influence of nanoparticle addition on the formation and growth of intermetallic compounds (IMCs) in Cu/Sn-Ag-Cu/Cu solder joint during different thermal conditions." *Sci. Technol. Adv. Mater.*, 16(3), 1–18.
- Tiryakioğlu, M., and Hudak, D. (2011). "Guidelines for two-parameter weibull analysis for flaw-containing materials." *Metall. Mater. Trans. B Process Metall. Mater. Process. Sci.*, 42(6), 1130–1135.
- Tsao, L. C., and Chang, S. Y. (2010). "Effects of Nano-TiO₂ additions on thermal analysis, microstructure and tensile properties of Sn_{3.5}Ag_{0.25}Cu solder." *Mater. Des.*, 31(2), 990–993.
- Tsao, L. C., Chang, S. Y., Lee, C. I., Sun, W. H., and Huang, C. H. (2010). "Effects of nano-Al₂O₃ additions on microstructure development and hardness of Sn_{3.5}Ag_{0.5}Cu solder." *Mater. Des.*, 31(10), 4831–4835.
- Tsao, L. C., Wu, R. W., Cheng, T. H., Fan, K. H., and Chen, R. S. (2013a). "Effects of nano-Al₂O₃ particles on microstructure and mechanical properties of Sn_{3.5}Ag_{0.5}Cu composite solder ball grid array joints on Sn/Cu pads." *Mater. Des.*, 50, 774–781.
- Tsao, L. C., Wu, R. W., Cheng, T. H., Fan, K. H., and Chen, R. S. (2013b). "Effects of nano-Al₂O₃ particles on microstructure and mechanical properties of Sn_{3.5}Ag_{0.5}Cu composite solder ball grid array joints on Sn/Cu pads." *Mater. Des.*, 50, 774–781.
- Tseng, C. F., Jill Lee, C., and Duh, J. G. (2013). "Roles of Cu in Pb-free solders jointed with electroless Ni(P) plating." *Mater. Sci. Eng. A*, 574, 60–67.
- Tu, K. N., and Zeng, K. (2001). "Tin-lead (SnPb) solder reaction in flip chip technology." *Mater. Sci. Eng. R Reports*, 34(1), 1–58.
- Tu, P. L., Chan, Y. C., Hung, K. C., and Lai, J. K. L. (2001). "Growth kinetics of intermetallic compounds in chip scale package solder joint." *Scr. Mater.*, 44(2), 317–323.
- Wang, H., Hu, X., Li, Q., and Qu, M. (2019). "Effect of flux doped with Cu₆Sn₅ nanoparticles on the interfacial reaction of lead-free solder joints." *J. Mater. Sci. Mater. Electron.*, 30(12), 11552–11562.
- Wang, S. J., and Liu, C. Y. (2003). "Retarding growth of Ni₃P crystalline layer in Ni(P) substrate by reacting with Cu-bearing Sn(Cu) solders." *Scr. Mater.*, 49(9), 813–818.
- Wang, Y. W., Chang, C. C., and Kao, C. R. (2009). "Minimum effective Ni addition to SnAgCu solders for retarding Cu₃Sn growth." *ASE Technol. J*, Elsevier BV.
- Watanabe, H., Shimoda, M., Hidaka, N., and Shohji, I. (2011). "Effect of interfacial reaction in Sn-Ag-Cu solder alloy with Ni addition." *Key Eng. Mater.*, Trans Tech Publications Ltd, 247–252.
- Weibull, W. (1951). "Wide applicability." *J. Appl. Mech.*, 103, 293–297.

- Wu, C. M. L., Yu, D. Q., Law, C. M. T., and Wang, L. (2004). "Properties of lead-free solder alloys with rare earth element additions." *Mater. Sci. Eng. R Reports*, Elsevier Ltd.
- Wu, J., Xue, S., Wang, J., Wu, M., and Wang, J. (2018). "Effects of α -Al₂O₃ nanoparticles-doped on microstructure and properties of Sn-0.3Ag-0.7Cu low-Ag solder." *J. Mater. Sci. Mater. Electron.*, 29(9), 7372–7387.
- Xie, H., Chawla, N., and Mirpuri, K. (2012). "Thermal and mechanical stability of Ce-containing Sn-3.9Ag-0.7Cu lead-free solder on Cu and electroless Ni-P metallizations." *J. Electron. Mater.*, 41(12), 3249–3258.
- Xing, W. qing, Yu, X. ye, Li, H., Ma, L., Zuo, W., Dong, P., Wang, W. xian, and Ding, M. (2017). "Effect of nano Al₂O₃ additions on the interfacial behavior and mechanical properties of eutectic Sn-9Zn solder on low temperature wetting and soldering of 6061 aluminum alloys." *J. Alloys Compd.*, 695, 574–582.
- Xu, R., Liu, Y., and Sun, F. (2019). "Effect of isothermal aging on the microstructure, shear behavior and hardness of the Sn58Bi/Sn3.0Ag0.5Cu/Cu solder joints." *Results Phys.*
- Xu, S., Chan, Y. C., Zhang, K., and Yung, K. C. (2014a). "Interfacial intermetallic growth and mechanical properties of carbon nanotubes reinforced Sn3.5Ag0.5Cu solder joint under current stressing." *J. Alloys Compd.*, 595, 92–102.
- Xu, S., Hu, X., Yang, Y., Chen, Z., and Chan, Y. C. (2014b). "Effect of carbon nanotubes and their dispersion on electroless Ni-P under bump metallization for lead-free solder interconnection." *J. Mater. Sci. Mater. Electron.*, 25(6), 2682–2691.
- Yakymovych, A., Plevachuk, Y., Švec, P., Švec, P., Janičkovič, D., Šebo, P., Beronská, N., Roshanghias, A., and Ipser, H. (2016). "Morphology and shear strength of lead-free solder joints with Sn3.0Ag0.5Cu solder paste reinforced with ceramic nanoparticles." *J. Electron. Mater.*, 45(12), 6143–6149.
- Yang, C., Song, F., and Lee, S. W. R. (2011). "Effect of interfacial strength between Cu₆Sn₅ and Cu₃Sn intermetallics on the brittle fracture failure of lead-free solder joints with OSP pad finish." *Proc. - Electron. Components Technol. Conf.*, 971–978.
- Yang, L., Liu, H., and Zhang, Y. (2018). "Study on the tensile creep behavior of carbon nanotubes-reinforced Sn-58Bi solder joints." *J. Electron. Mater.*, 47(1), 662–671.
- Yang, L., Quan, S., Liu, C., and Shi, G. (2019). "Aging resistance of the Sn-Ag-Cu solder joints doped with Mo nanoparticles." *Mater. Lett.*
- Yao, P., Liu, P., and Liu, J. (2008). "Effects of multiple reflows on intermetallic morphology and shear strength of SnAgCu-xNi composite solder joints on electrolytic Ni/Au metallized substrate." *J. Alloys Compd.*, 462, 73–79.
- Yazzie, K. E., Fei, H. E., Jiang, H., and Chawla, N. (2012). "Rate-dependent behavior of Sn alloy-Cu couples: Effects of microstructure and composition on mechanical shock resistance." *Acta Mater.*, 60(10), 4336–4348.
- Yen, Y. W., Chiang, Y. C., Jao, C. C., Liaw, D. W., Lo, S. C., and Lee, C. (2011).

- “Interfacial reactions and mechanical properties between Sn-4.0Ag-0.5Cu and Sn-4.0Ag-0.5Cu-0.05Ni-0.01Ge lead-free solders with the Au/Ni/Cu substrate.” *J. Alloys Compd.*, 509(13), 4595–4602.
- Yin, L., Wentlent, L., Yang, L., Arfaei, B., Oasaimh, A., and Borgesen, P. (2012). “Recrystallization and precipitate coarsening in Pb-Free solder joints during thermomechanical fatigue.” *J. Electron. Mater.*, 41(2), 241–252.
- Yoon, J. W., Chun, H. S., and Jung, S. B. (2007). “Investigation of interfacial reaction and joint reliability between eutectic Sn-3.5Ag solder and ENIG-plated Cu substrate during high temperature storage test.” *J. Mater. Sci. Mater. Electron.*, 18(5), 559–567.
- Yoon, J. W., Noh, B. I., and Jung, S. B. (2010). “Comparison of interfacial stability of Pb-free solders (Sn-3.5Ag, Sn-3.5Ag-0.7Cu, and Sn-0.7Cu) on ENIG-plated Cu during aging.” *IEEE Trans. Components Packag. Technol.*, 33(1), 64–70.
- Yoon, J. W., Noh, B. I., Kim, B. K., Shur, C. C., and Jung, S. B. (2009). “Wettability and interfacial reactions of Sn-Ag-Cu/Cu and Sn-Ag-Ni/Cu solder joints.” *J. Alloys Compd.*, 486(1–2), 142–147.
- Yu, D. Q., Wu, C. M. L., Law, C. M. T., Wang, L., and Lai, J. K. L. (2005). “Intermetallic compounds growth between Sn-3.5Ag lead-free solder and Cu substrate by dipping method.” *J. Alloys Compd.*, 392(1–2), 192–199.
- Yu, S. P., Lin, H. J., Hon, M. H., and Wang, M. C. (2000). “Effects of process parameters on the soldering behavior of the eutectic Sn-Zn solder on Cu substrate.” *J. Mater. Sci. Mater. Electron.*, 11(6), 461–471.
- Yu, X., Hu, X., Li, Y., Liu, T., Zhang, R., and Min, Z. (2014). “Tensile properties of Cu/Sn-58Bi/Cu soldered joints subjected to isothermal aging.” *J. Mater. Sci. Mater. Electron.*, 25(6), 2416–2425.
- Yuan, Y., and Lee, T. R. (2013). “Contact angle and wetting properties.” *Springer Ser. Surf. Sci.*, 51(1), 3–34.
- Z.H. Li, Y. Tang, Q.W.Guo, G. Y. L. (2019). “Effects of CeO₂ nanoparticles addition on shear properties of low-silver Sn-0.3Ag-0.7Cu-xCeO₂ solder alloys.” *J. Alloys Compd.*, 789, 150–162.
- Zeng, K. (2009). “Lead-free soldering: Materials science and solder joint reliability.” *Jom*, 61(6), 28.
- Zeng, K., and Tu, K. N. (2002). “Six cases of reliability study of Pb-free solder joints in electronic packaging technology.” *Mater. Sci. Eng. R Reports*, 38(2), 55–105.
- Zhang, F., Li, M., Chum, C. C., and Shao, Z. C. (2003). “Effects of substrate metallization on solder/under-bump metallization interfacial reactions in flip-chip packages during multiple reflow cycles.” *J. Electron. Mater.*, 32(3), 123–130.
- Zhang, L., He, C. W., Guo, Y. H., Han, J. G., Zhang, Y. W., and Wang, X. Y. (2012). “Development of SnAg-based lead free solders in electronics packaging.” *Microelectron.*

Reliab., 52(3), 559–578.

Zhao, N., Liu, X. Y., Huang, M. L., and Ma, H. T. (2013). “Characters of multicomponent lead-free solders.” *J. Mater. Sci. Mater. Electron.*, 24(10), 3925–3931.

Zhao, X., Wen, Y., Li, Y., Liu, Y., and Wang, Y. (2016a). “Effect of γ -Fe₂O₃ nanoparticles size on the properties of Sn-1.0Ag-0.5Cu nano-composite solders and joints.” *J. Alloys Compd.*, 662(662), 272–282.

Zhao, X., Wen, Y., Li, Y., Liu, Y., and Wang, Y. (2016b). “Effect of γ -Fe₂O₃ nanoparticles size on the properties of Sn-1.0Ag-0.5Cu nano-composite solders and joints.” *J. Alloys Compd.*, 662, 272–282.

Zhong, X. L., and Gupta, M. (2008a). “Effect of type of reinforcement at nanolength scale on the tensile properties of Sn-0.7Cu solder alloy.” *10th Electron. Packag. Technol. Conf. EPTC 2008*, 669–674.

Zhong, X. L., and Gupta, M. (2008b). “Development of lead-free Sn–0.7Cu/Al₂O₃ nanocomposite solders with superior strength.” *J. Phys. D. Appl. Phys.*, 41, 1–7.

Zhong, Y., An, R., Wang, C., Zheng, Z., Liu, Z. Q., Liu, C. H., Li, C. F., Kim, T. K., and Jin, S. (2015). “Low Temperature Sintering Cu₆Sn₅ Nanoparticles for Superplastic and Super-uniform High Temperature Circuit Interconnections.” *Small*, 11(33), 4097–4103.

**APPENDIX A: MELTING PARAMETERS OBTAINED FROM THE DSC TEST
FOR DIFFERENT SOLDER NANOCOMPOSITES**

Table A.1: Melting parameters for SAC0307 solder with the addition of Al₂O₃ nanoparticles and MWCNT in different weight percent concentrations

Solder Composition	T _{Onset, Heating} (°C) A	T _{Peak, Heating} (°C) B	T _{End, Heating} (°C) C	T _{Onset, Cooling} (°C) D	Pasty Range (°C) (C-A)	Undercooling (°C) (A-D)
SAC0307	223.53	229.01	231.71	213.06	8.18	10.47
SAC0307 +0.01Al ₂ O ₃	223.36	228.99	231.56	213.14	8.2	10.22
SAC0307 +0.05Al ₂ O ₃	221.58	228.03	231.16	214.02	9.58	7.56
SAC0307 +0.1Al ₂ O ₃	222.5	228.88	231.41	214.98	8.91	7.52
SAC0307 +0.3Al ₂ O ₃	223	228.94	231.48	215.01	8.48	7.99
SAC0307 +0.5Al ₂ O ₃	223.42	229	231.69	215.06	8.27	8.36
SAC0307 +0.01MWCNT	223.77	228.09	231.21	213.21	7.44	10.56
SAC0307 +0.05MWCNT	222.42	228.78	230.28	214	7.86	8.42
SAC0307 +0.1 MWCNT	222.88	229.17	230.46	215.45	7.58	7.43
SAC0307 +0.3 MWCNT	223.05	230.1	231.58	216.5	8.53	6.55
SAC0307 +0.5 MWCNT	223.2	228	232.06	217.05	8.86	6.15

Table A.2: Melting parameters for Sn-3.6Ag solder with the addition of Al₂O₃ nanoparticles and MWCNT in different weight percent concentrations

Solder Composition	T _{Onset, Heating} (°C) A	T _{Peak, Heating} (°C) B	T _{End, Heating} (°C) C	T _{Onset, Cooling} (°C) D	Pasty Range (°C) (C-A)	Undercooling (°C) (A-D)
Sn-3.6Ag	221.84	225.77	228.17	184.8	6.33	37.04
Sn-3.6Ag +0.01Al ₂ O ₃	221.44	224.99	226.98	185.15	5.54	36.29
Sn-3.6Ag +0.05Al ₂ O ₃	220.58	224.05	226.01	187.76	5.43	32.82
Sn-3.6Ag +0.1Al ₂ O ₃	220.6	224.21	226.52	187.11	5.92	33.49
Sn-3.6Ag +0.5Al ₂ O ₃	220.71	224.66	227.19	188.2	6.48	32.51
Sn-3.6Ag +0.01MWCNT	221.12	225	228.02	184.87	6.9	36.25
Sn-3.6Ag +0.05MWCNT	221.01	224.87	227.5	185.24	6.49	35.77
Sn-3.6Ag +0.1MWCNT	221.22	226.15	228.11	186.68	6.89	34.54
Sn-3.6Ag +0.5MWCNT	221.54	227.21	228.42	187.8	6.88	33.74

Table A.3: Melting parameters for SAC305-NiGe solder with the addition of Al₂O₃ nanoparticles in different weight percent concentrations

Solder Composition	T _{Onset, Heating} (°C) A	T _{Peak, Heating} (°C) B	T _{End, Heating} (°C) C	T _{Onset, Cooling} (°C) D	Pasty Range (°C) (C-A)	Undercooling (°C) (A-D)
SAC305-NiGe	217.92	222.55	225.61	193.99	7.69	23.93
SAC305-NiGe +0.01 Al ₂ O ₃	217.90	222.4	225.51	194.01	7.61	23.89
SAC305-NiGe +0.05 Al ₂ O ₃	217.71	221.02	224.83	195	7.12	22.71

APPENDIX B: WETTING AREA AND TIN-CLIMB FOR DIFFERENT SOLDER NANOCOMPOSITES

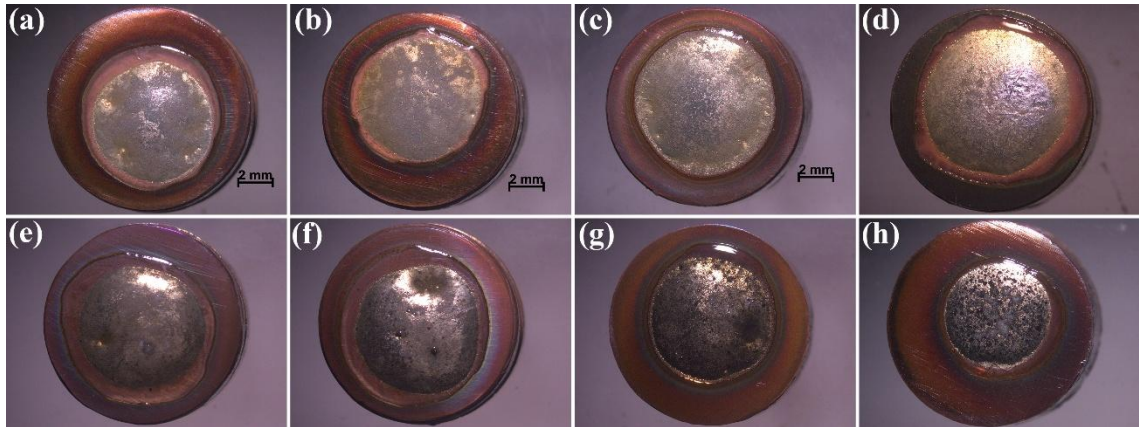


Figure B.1: The stereomicroscopic images of reflowed samples on bare Cu substrate for SAC305 solder nanocomposites reinforced with (a) 0, (b) 0.05, (c) 0.1, (d) 0.5 wt.% Al_2O_3 nanoparticles, and (e) 0.01, (f) 0.05, (g) 0.1, (h) 0.5 wt.% MWCNT

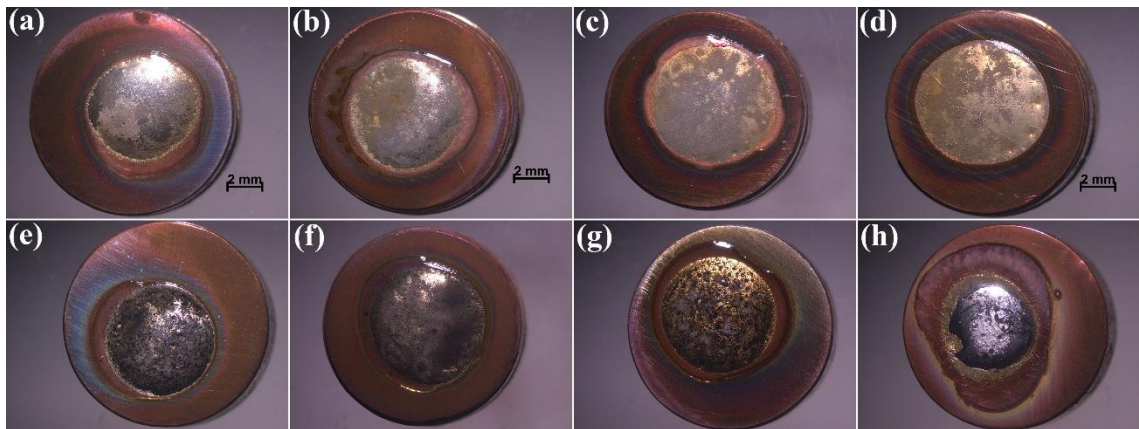


Figure B.2: The stereomicroscopic images of reflowed samples on bare Cu substrate for Sn-3.6Ag solder nanocomposites reinforced with (a) 0, (b) 0.05, (c) 0.1, (d) 0.5 wt.% Al_2O_3 nanoparticles, and (e) 0.01, (f) 0.05, (g) 0.1, (h) 0.5 wt.% MWCNT

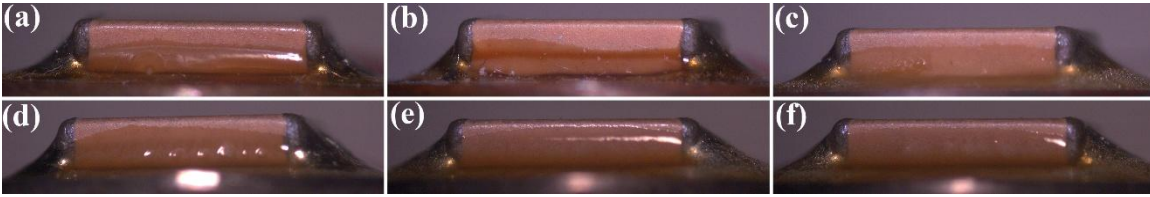


Figure B.3: The stereomicroscopic images of capacitor samples showing tin-climb on the capacitor terminals for SAC0307, SAC0307+0.01Al₂O₃, and SAC0307+0.05Al₂O₃ solder compositions reflowed on (a), (b), (c) bare copper substrate, and (d), (e), (f) Ni-coated substrate, respectively

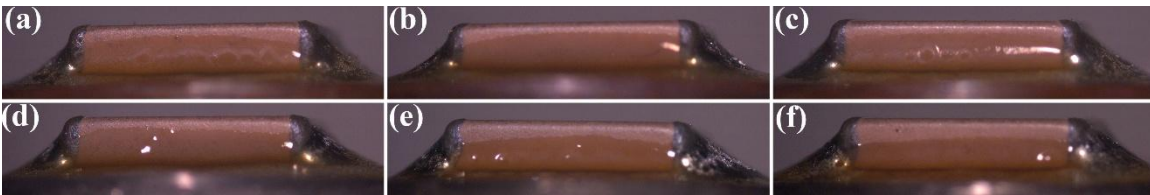


Figure B.4: The stereomicroscopic images of capacitor samples showing tin-climb on the capacitor terminals for SAC305, SAC305+0.01Al₂O₃, and SAC305+0.05Al₂O₃ solder compositions reflowed on (a), (b), (c) bare copper substrate, and (d), (e), (f) Ni-coated substrate, respectively

APPENDIX C: MICROSTRUCTURE OF SOLDER JOINT FOR DIFFERENT SOLDER NANOCOMPOSITES UNDER MULTIPLE REFLOW CYCLES

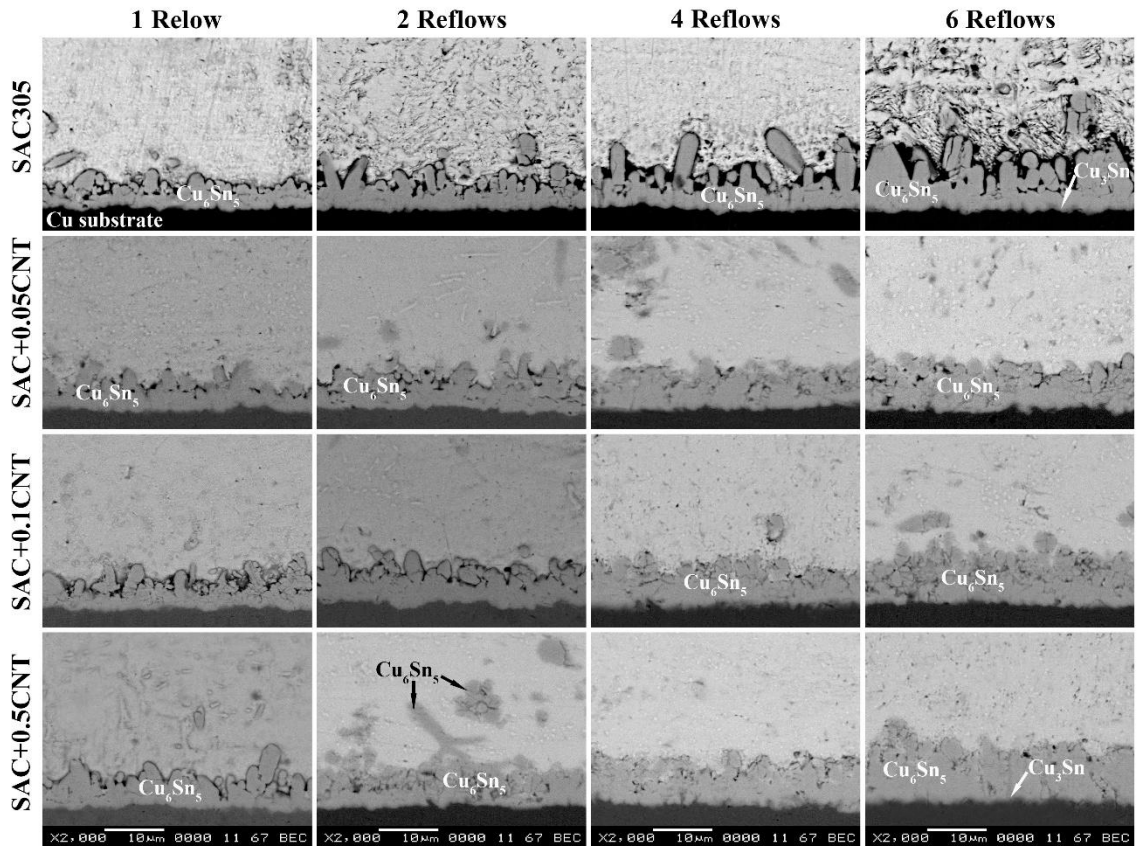


Figure C.1: SEM micrographs of the joint interface for SAC305 solder with the addition of MWCNT in different weight percent concentrations on the copper substrate under multiple reflow cycles

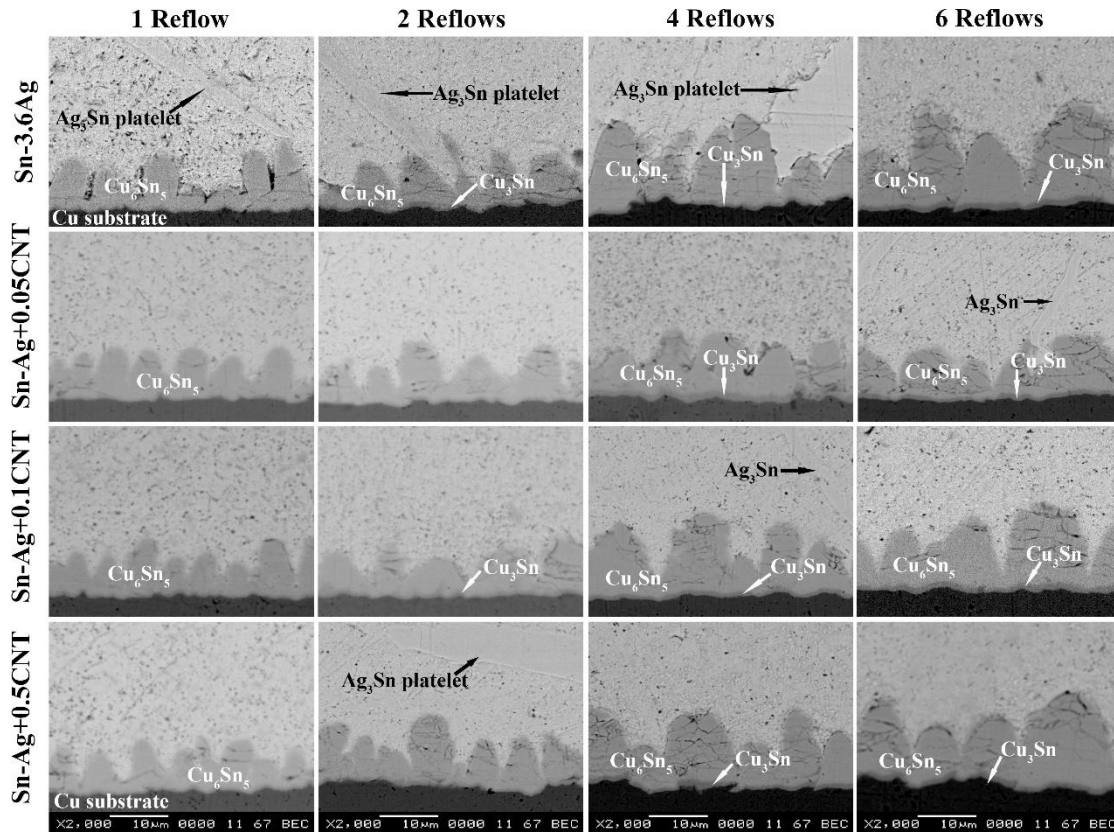


Figure C.2: SEM micrographs of the joint interface for Sn-3.6Ag solder with the addition of MWCNT in different weight percent concentrations on the copper substrate under multiple reflow cycles

APPENDIX D: STRESS-STRAIN CURVES AND MICROHARDNESS FOR DIFFERENT SOLDER NANOCOMPOSITES UNDER VARYING THERMAL CONDITIONS

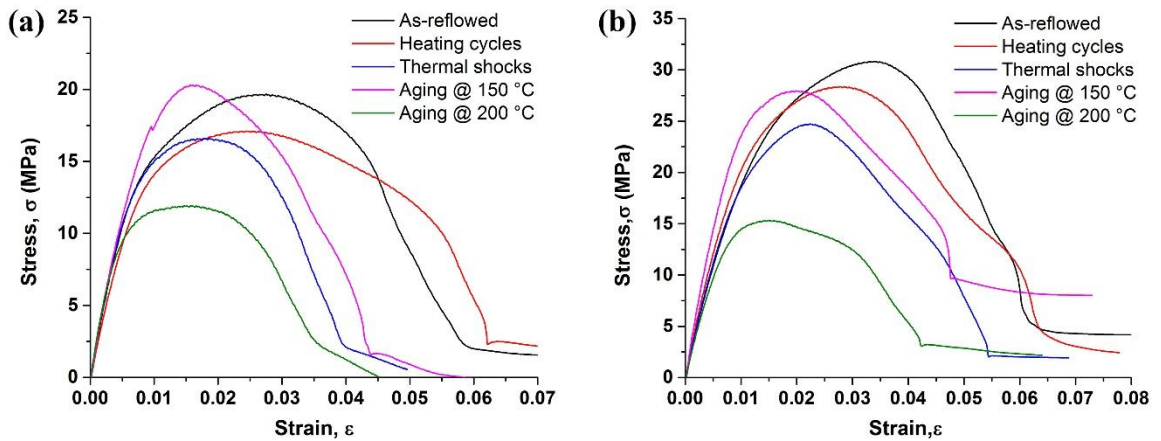


Figure D.1: Stress-strain plots for single-lap-joint samples under different thermal conditions for (a) SAC0307 on Cu substrate and (b) SAC0307+0.05Al₂O₃ solder composition on Ni-P coated substrate

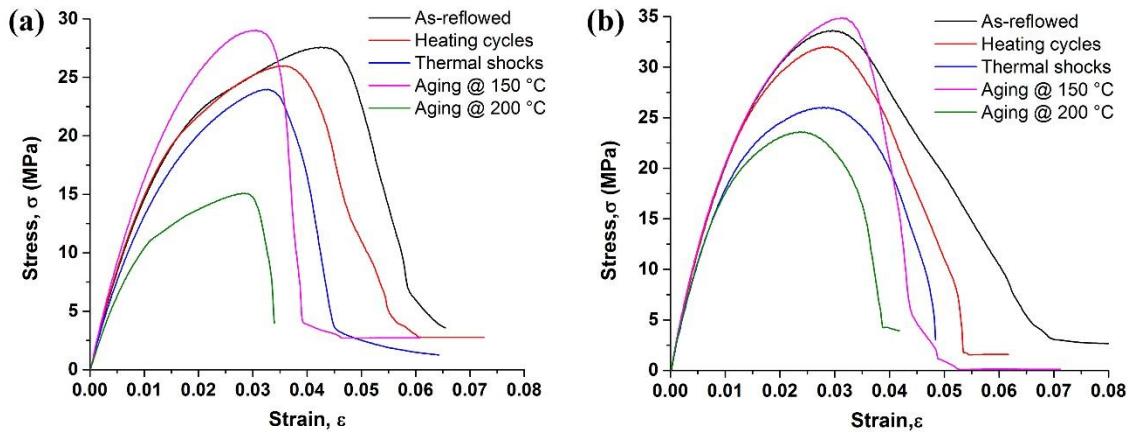


Figure D.2: Stress-strain plots for single-lap-joint samples under different thermal conditions for (a) SAC305-NiGe on Cu substrate and (b) SAC305-NiGe+0.05Al₂O₃ solder composition on Ni-P coated substrate

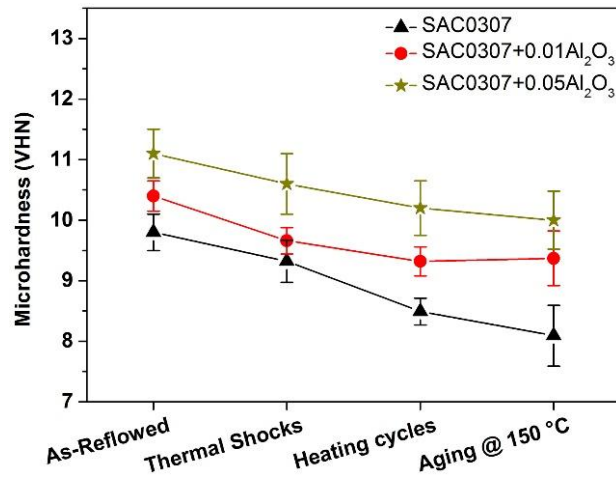


Figure D.3: Microhardness for SAC0307 solder nanocomposites under varying high-temperature environments

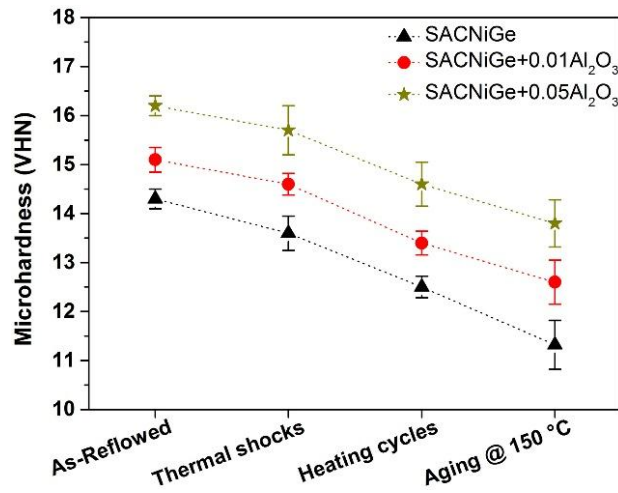


Figure D.4: Microhardness for SAC305-NiGe solder nanocomposites under varying high-temperature environments

APPENDIX E: WEIBULL PLOTS OF JOINT SHEAR STRENGTH FOR DIFFERENT SOLDER NANOCOMPOSITES

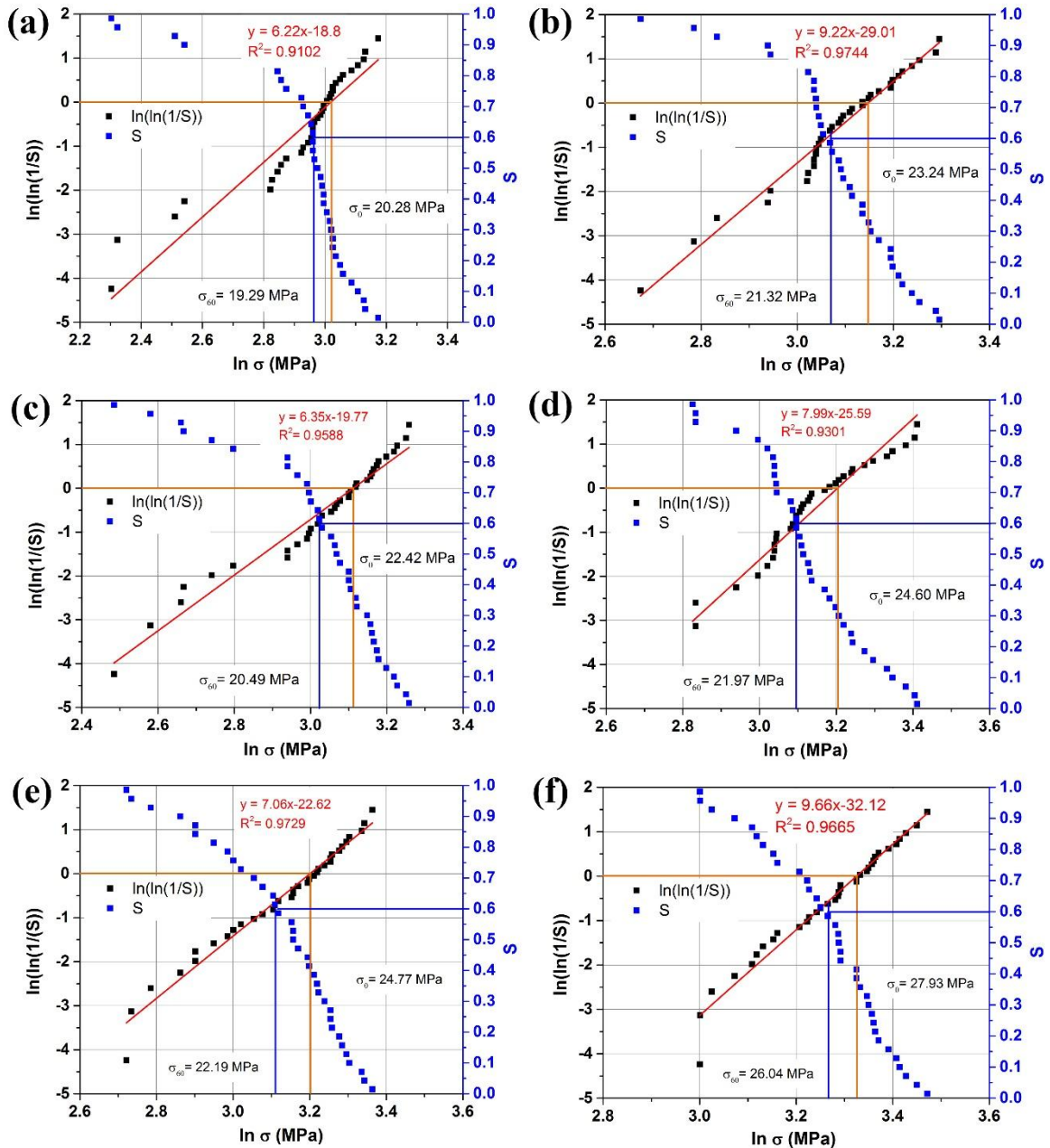


Figure E.1: Weibull plots of joint shear strength for SAC305, SAC305+0.01Al₂O₃, and SAC305+0.05Al₂O₃ solder compositions reflowed on (a), (c), (e) bare Cu substrate; and (b), (d), (f) on Ni-P coated substrate

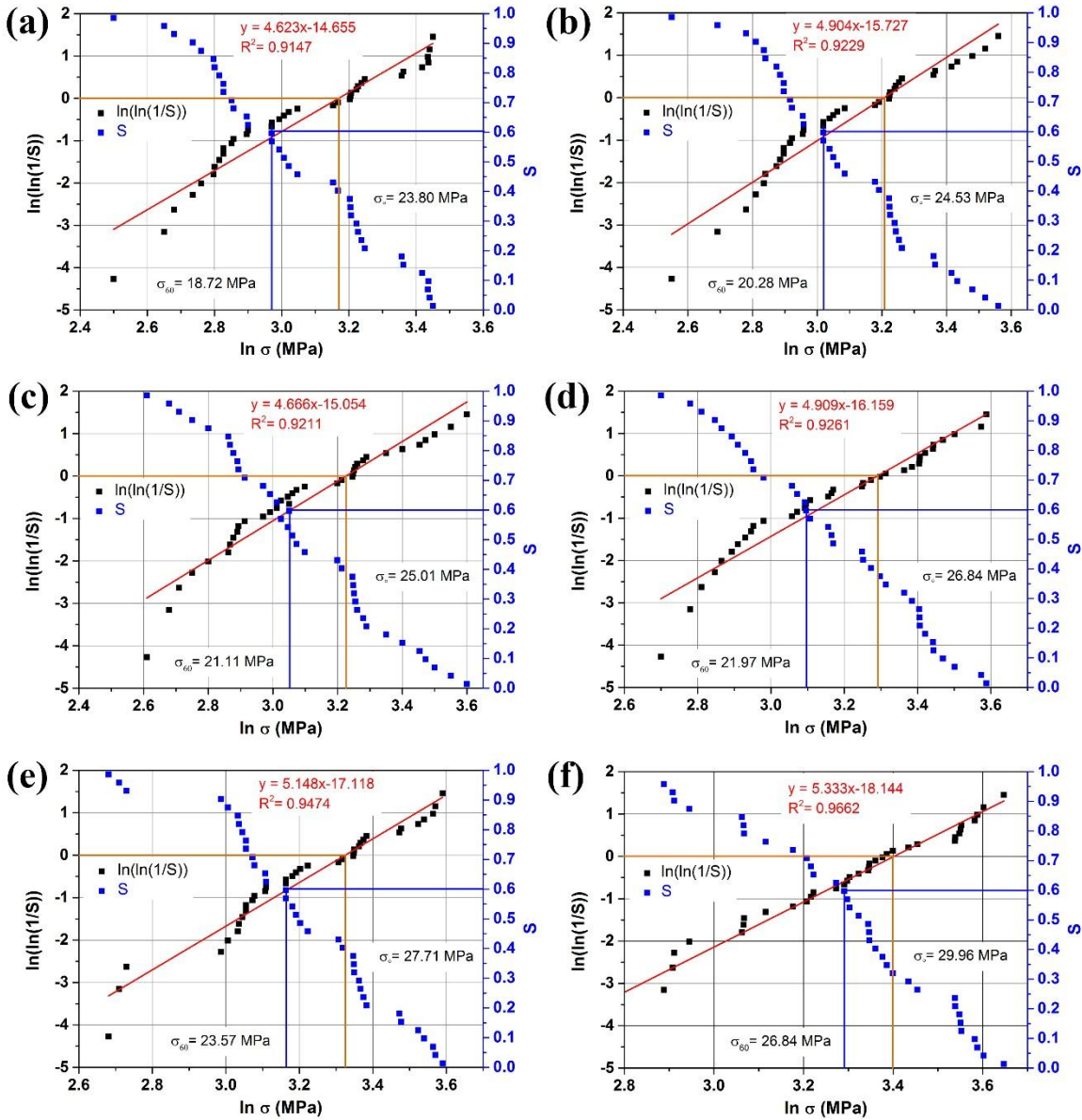


Figure E.2: Weibull plots of joint shear strength for SAC305, SAC305+0.01Al₂O₃, and SAC305+0.05Al₂O₃ solder compositions reflowed on (a), (c), (e) bare Cu substrate; and (b), (d), (f) on Ni-P coated substrate

APPENDIX F: ANOVA TABLES FOR JOINT SHEAR STRENGTH

Table F.1: Analysis of Variance (ANOVA) table for joint shear strength of SAC0307 solder nanocomposites

Source of Variation	Sum of Squares	Degrees of Freedom	Mean Square	F ratio (F_0)	F distribution value from table	P-Value	Remark
Thermal condition (A)	1811.09	6	301.8	161.84	$F_{0.01,6,84} = 3.025$	< 0.00001	Significant at $\alpha = 0.01$
Substrate finish (B)	210.86	1	210.9	113.05	$F_{0.01,1,84} = 6.946$	< 0.00001	Significant at $\alpha = 0.01$
Solder composition (C)	631.63	2	315.8	169.33	$F_{0.01,2,84} = 4.867$	< 0.00001	Significant at $\alpha = 0.01$
BC	18.39	2	9.198	4.93	$F_{0.01,2,84} = 4.867$	0.009	Significant at $\alpha = 0.01$
AC	43.47	12	3.623	1.94	$F_{0.05,12,84} = 1.869$	0.04	Significant at $\alpha = 0.05$
AB	25.19	6	4.198	2.25	$F_{0.05,6,84} = 2.208$	0.046	Significant at $\alpha = 0.05$
ABC	12.71	12	1.06	0.568	$F_{0.1,12,84} = 1.625$	0.86	Insignificant
Error	156.66	84	1.865				
Total	2910.03	125					

Table F.2: Analysis of Variance (ANOVA) table for joint shear strength of SAC305-NiGe solder nanocomposites

Source of Variation	Sum of Squares	Degrees of Freedom	Mean Square	F ratio (F_0)	F distribution value from table	P-Value	Remark
Thermal condition (A)	1581.82	6	263.6	218.54	$F_{0.01,6,84} = 3.025$	< 0.00001	Significant at $\alpha= 0.01$
Substrate finish (B)	232.07	1	232.1	192.37	$F_{0.01,1,84} = 6.946$	< 0.00001	Significant at $\alpha= 0.01$
Solder composition (C)	663.30	2	331.7	274.92	$F_{0.01,2,84} = 4.867$	< 0.00001	Significant at $\alpha= 0.01$
BC	13.90	2	6.952	5.763	$F_{0.01,2,84} = 4.867$	0.0045	Significant at $\alpha= 0.01$
AC	30.03	12	2.503	2.074	$F_{0.05,12,84} = 1.869$	0.0272	Significant at $\alpha= 0.05$
AB	20.87	6	3.479	2.883	$F_{0.05,6,84} = 2.208$	0.0132	Significant at $\alpha= 0.05$
ABC	22.317	12	1.86	1.54	$F_{0.1,12,84} = 1.625$	0.1255	Insignificant t
Error	101.33	84	1.206				
Total	2665.65	125					

LIST OF PUBLICATIONS

Journal Publications (Based on Ph.D. work)

- 1] Tikale, S., and Prabhu, K. N. (2021) “Bond shear strength of Al₂O₃ nanoparticles reinforced 2220-capacitor/SAC305 solder interconnects reflowed on bare and Ni-coated copper substrate.” *J. Mater. Sci. Mater. Electron.*, 32(3), 2865-2886.
- 2] Tikale, S., and Prabhu, K. N. (2020). “Development of low-silver content SAC0307 solder alloy with Al₂O₃ nanoparticles.” *Mater. Sci. Eng. A*, 787, 139439.
- 3] Tikale, S., and Prabhu, K. N. (2020). “Performance and reliability of Al₂O₃ nanoparticles doped multicomponent Sn-3.0Ag-0.5Cu-Ni-Ge solder alloy.” *Microelectron. Reliab.*, 113, 113933.
- 4] Tikale, S., and Narayan Prabhu, K. (2019). “The effect of multi-walled carbon nanotubes reinforcement and multiple reflow cycles on shear strength of SAC305 lead-free solder alloy.” *Mater. Perform. Charact.*, 8(3), 421–433.
- 5] Tikale, S., and Narayan Prabhu, K. (2018). “Effect of Multiple Reflow Cycles on the Shear Strength of Nano-Al₂O₃ Particles Reinforced Sn_{3.6}Ag Lead-Free Solder Alloy.” *Trans. Indian Inst. Met.*, 71(11), 2855–2859.
- 6] Tikale, S., and Prabhu, K. N. (2018). “Effect of multiple reflow cycles and Al₂O₃ nanoparticles reinforcement on performance of SAC305 lead-free solder alloy.” *J. Mater. Eng. Perform.*, 27(6), 3102–3111.
- 7] Tikale, S., and Prabhu, K. N. (2018). “Performance of MWCNT-reinforced SAC0307/Cu solder joint under multiple reflow cycles.” *Trans. Indian Inst. Met.*, 71(11), 2693–2698.

Other Journal Publications

- 8] Panikar, R. S., Amogha Skanda, V., **Tikale, S.**, and Narayan Prabhu, K. (2020). “The effect of reflow temperature on time at the end of the gravity zone (TGZ) of Sn-3.8Ag-0.7Cu solder alloy.” *Mater. Perform. Charact.*, 9(1), 190–203.
- 9] Sona, M., **Tikale, S.**, and Prabhu, N. (2019). “Wettability, Interfacial Intermetallic Growth and Joint Shear Strength of Eutectic Sn–Cu Solder Reflowed on Bare and Nickel-Coated Copper Substrates.” *Trans. Indian Inst. Met.*, 72(6), 1579–1583.

- 10]** Samuel, A., **Tikale, S.**, and Prabhu, K. N. (2018). “Assessment of the Performance of Sn-3.5Ag/Cu Solder Joint Under Multiple Reflows, Thermal Cycling, and Corrosive Environment.” *Trans. Indian Inst. Met.*, 71(11), 2687–2691.
- 11]** **Tikale, S.**, Sona, M., and Narayan Prabhu, K. (2017). “Effect of Cooling Rate on Joint Shear Strength of Sn-9Zn Lead-Free Solder Alloy Reflowed on Copper Substrate.” *Mater. Perform. Charact.*, 6(1), MPC20160058.
- 12]** **Tikale, S.**, Sona, M., and Prabhu, K. N. (2015). “Wettability and bond shear strength of Sn-9Zn lead-free solder alloy reflowed on a copper substrate.” *Mater. Sci. Forum*, 830–831, 215–218.

BIO-DATA



Name : SANJAY VINAYAK TIKALE
Date of Birth : 25-10-1988
Permanent Address : 167, Kokadi, Teh: Desaiganj (Wadsa),
Dist: Gadchiroli, State: Maharashtra, 441207, India
Email : Sanjaytikale@gmail.com

Academic qualification

Bachelor of Engineering (B.E) : Mechanical Engineering; (2012)
Jawaharlal Nehru Engineering College, Aurangabad,
Maharashtra.
Master of Technology (M.Tech) : Materials Engineering; (2015)
National Institute of Technology Karnataka.
Work Experience: Graduate Engineer Trainee (July 2012- July 2013),
Weir BDV Valves, Hubli, Karnataka.